Thermohydraulic and Mechanical Modeling of Printed Circuit Heat Exchangers for Next Generation Nuclear Service

By

Ian William Jentz

A dissertation submitted in partial fulfillment of
the requirements for the degree of

Doctor of Philosophy
(Nuclear Engineering and Engineering Physics)

at the

UNIVERSITY OF WISCONSIN-MADISON

2021

Date of final oral examination: October 21st, 2021

The dissertation is approved by the following members of the Final Oral Committee:

Mark Anderson, Professor, Mechanical Engineering
Gregory Nellis, Professor, Mechanical Engineering
Xiaoping Qian, Professor, Mechanical Engineering
Jennifer Franck, Professor, Engineering Physics
Riccardo Bonazza, Professor, Engineering Physics

Executive Summary

In this work an approach to thermodyraulic and mechanical modeling of a full 3-dimensional Printed Circuit Heat Exchanger (PCHE) is presented. A new approach to Finite Element (FE) analysis of the fluid and structure using homogenization of micro-channel behavior is developed. The accuracy of the thermohydrualic model is verified against experiment for a large range of flow conditions. Using the results from the thermohydraulic model as input to the mechanical FE model allows loading and stress within the PCHE to by resolved. Coupling of the thermodynamic and mechanical models allows the performance and mechanical integrity of all parts of the PCHE to be evaluated simultaneously. Motivation for using airfoil PCHEs in supercritical carbon-dioxide (s-CO_2) applications is given and the design of PCHEs are briefly discussed.

A thermohydraulic model using a homogenized heat exchanger thermohydraulics (HHXT) approach has been developed for PCHE applications [1]. The HHXT model provides a fully resolved PCHE model without the complexity inherent in resolving all facets of the micro-channel geometry throughout the core. The HHXT approach expands on previous work by Urquiza in homogenizing the PCHE micro-channel core as an anisotropic media[2]. Flow distribution in the PCHE is determined using a porous media approach. Heat transfer between fluids is modeled using heat transfer coefficients and is coupled to a conduction model of the solid PCHE body. The Homogenized Heat Exchanger Thermohydraulics (HHXT) model properly resolves American Society of Mechanical Engineers (ASME) Boiler and Pressure Vessel Code (BPVC) Sec-3 loading conditions without the complexity inherent in resolving all facets of the PCHE geometry.

The accuracy of the model is verified through experimental validation. A purpose designed zig-zag channel test PCHE was tested over a wide range of flow, using 60 separate tests with Reynolds number ranging from 1,790 to 64,200. Embedded fiber-optic temperature sensors measured 2-dimensional temperature distribution within the test recuperator. Along with measurement of inlet and outlet conditions, the internal temperature measurements provide 7,542 distributed measurements for each flow rate tested. This allowed the verification of HHXT against a large set of data. Combined modelling and measurement allowed for better insight into PCHE performance. The interaction of side entrance and transition regions could be resolved. Flow redistribution within the cold CO_2 of the zig-zag PCHE was found to be a major factor in the distribution of temperature.

Mechanical analysis per BPVC Sec. III Div. 5 design by analysis rules is demonstrated. Linearized stress analysis was used to break the stress within micro-channel walls into membrane and bending components needed in BPVC stress intensity calculations. A homogenized approach to modeling mechanical loads in the full 3-dimensional PCHE is used. The method consisted of separate micro-channel structure and PCHE structure analyses. The resulting model resolved pressurization and thermal stresses within the zig-zag test PCHE. Stress intensities within 108,000 distinct micro-channel walls could be determined. Thermal stress

arising from the differential expansion of the PCHE body was found to contribute the most stress. The zig-zag test PCHE meets BPVC Sec. III Div. 5 stress intensity limits at design operating conditions.

Additionally the measurement of airfoil micro-channel heat transfer and hydraulic performance is made. As direct internal measurement of bulk CO_2 or fluid-wall temperatures within the channels of the airfoil PCHE is not possible, convective heat transfer is calculated from inlet and outlet CO_2 conditions and simple models of heat transfer within the recuperator. Since CO_2 properties changed over the length of the recuperator, a 1D discrete model of the recuperator for calculating localized values of j and f is presented.

Acknowledgements

I would like to acknowledge my adviser Dr. Mark Anderson, who has guided my research career over the past ten years. I worked with Mark on a multitude of projects through both my undergraduate and graduate years and am looking forward to extending our collaboration into the future.

The Finite Element model that I developed would not have been possible without the excellent instruction in FE methods that I received from Prof. Robert Witt.

I also thank Dr. Gregory Nellis for providing extensive help with my heat transfer models, editing of my writing, and assistance in developing computational methods.

I acknowledge the contributions of the University of Wisconsin Thermohydrualics group. The knowledge I have obtained regarding PCHEs would not have been possible without extensive work done by previous students Matt Carlson and Alan Kruizenga. My experimental work would not have been possible without Paul Brooks. I also extend gratitude to all of my office-mates, as they are generally reasonable people and have tolerated my unhinged nature for some time.

I am grateful for the support of my family, in particular my wife Stephanie, and for long time college friends who have stayed in Madison as I've ground through grad school.

Table of Contents

List of Tables

List of Figures

Nomenclature

Symbol	Units	Description
A	m^2	area
c_p	J kg^{-1} K^{-1}	constant pressure heat capacity
C_f	-	drag coefficient
$\dot{C}$	W K^{-1}	Heat capacitance flow
C_d	-	Drag coefficient
D	m	diameter
D_h	m	hydraulic diameter
E	Pa	modulus of elasticity
$\mathbf{E}$	Pa	orthotropic elasticity matrix
$\hat{E}$	-	dimensionless elastic modulus
f_D, f_F	-	Darcy and Fanning friction factor
$\mathbf{f}$	-	directional friction factor
F	m^2	Frontal area
G	Pa	shear modulus
$\hat{G}$	-	dimensionless shear modulus
h	W m^{-2} K^{-1}	local dimensional heattransfer coefficient
H	J kg^{-1}	enthalpy
$\mathbf{I}$		Identity matrix
j	-	Colburn heat transfer coefficient
j_m	kg m^{-2} s^{-1}	mass flux
k	W m^{-1} K^{-1}	thermal conductivity
$\mathbf{k}$	W m^{-1} K^{-1}	Orthotropic thermal conductivity, or fluid permeability
K	-	minor contraction coefficient
$\mathbf{K}_{\text{perm.}}$	m^{-1}	permeability
$\mathbf{K}$	Pa	stiffness matrix
L	m	characteristic length, channel length
$\dot{m}$	kg s^{-1}	mass flow
NTU	-	number of transfer units
Nu	-	Nusselt number heat transfer coefficient
ΔP	Pa or psi	pressure drop
P	Pa or psi	absolute pressure
Pr	-	Prandtl number
Pe	-	Peclet number
$\dot{q}$	W	heat flow
r	m	local radius

Continued on next page

Table 1 – *Continued from previous page*

Symbol	Units	Description
R	m	radius of pipe
$R_{V_{1,\ell}}$	W m^3 K^{-1}	Volumetric thermal resistance
Re	-	Reynolds number
Re_{ch}	-	Reynolds number (within zig-zag channel)
RR	-	relative roughness
S_{ij}	s^{-1}	rate-of-strain tensor
t	s or min	time
T	°C or °K	temperature
$\Delta T_{ch.}$	°C or °K	temperature difference between the fluid channel walls
∇T	C m^{-1}	temperature gradient
u	m s^{-1}	fluid velocity in x direction
UA	W K^{-1}	heat exchanger UA
UA	K W^{-1}	heat exchanger conductance
v	m s^{-1}	fluid velocity in y direction
$\mathbf{v}$, $\mathbf{v_{ch.}}$	m s^{-1}	Channel velocity
$\mathbf{v_D}$	m s^{-1}	Darcy velocity
V	m^3	Volume
y	m	position
x	m	position

Greek Symbol	Units	Description
α	°, -, m^2 s^{-1}	zig-zag angle, or aspect ratio, or thermal diffusivity
γ	-	shear strain
δ	m	boundary layer thickness
Δ	-	difference or change in
ϵ	mm/mm,	strain or surface roughness
ε	-	heat exchanger effectiveness
ζ	-	coefficient of contraction
η	-	fin effectiveness coefficient
Λ		Transformation matrix
μ	kg m^{-1} s^{-1}	dynamic viscosity
∇	m^{-1}	gradient operator
ν	-, m^2 s^{-1}	Poisson's ratio or kinematic viscosity
ϕ	-	Volume fraction, porosity
ρ	kg m^{-3}	density
σ	Pa, -	stress, or uncertainty

Continued on next page

Table 2 – *Continued from previous page*

Greek Symbol	**Units**	**Description**
τ	Pa m^{-2}	shear stress
χ	-	surface area fraction
ω		specific turbulent dissipation rate

Subscript	**Description**
b	property of base material
c	evaluated over a cross-section
C	within the cold channel side
$cond$	Anisotropic conductivity matrix
H	within the hot channel side
i	section or summation index
ij	matrix indices
j	section or summation index
k	evaluated at the k^{th} cycle
m	membrane
obs	obstruction
$perm$	permeability
R	ratio
s	evaluated over a surface
S	within unit cell solid, micro-channel solid
t	thermal
w	evaluated at a wall
∞	free stream
ℓ	Stream index

Bracket	**Description**
{ }	Column vector
⌊ ⌋	Row vector
[ ]	Matrix
⌈ ⌋	Diagonal matrix
| |	Magnitude of vector, absolute value of constant

Acronyms and Abbreviations

American Society of Mechanical Engineers (ASME)
Boiler and Pressure Vessel Code (BPVC)
Carbondioxide (CO_2)
Finite Elements (FE)
Finite Element Analysis (FEA)
Homogenized Heat Exchanger Thermohydraulics (HHXT)
Printed Circuit Heat Exchanger (PCHE)
Partial Differential Equation (PDE)
Stress Classification Line (SCL)

Chapter 1

Introduction

1.1 Motivation

The supercritical carbon-dioxide (s-CO_2) Brayton power cycle shows promise as a power conversion system for advanced nuclear reactors including the High-Temperature Gas-cooled Reactor (HTGR), the Sodium Fast Reactor (SFR), and the Fluoride Salt High-temperature Reactor (FHR). Coupling the s-CO_2 Brayton cycle to these advance nuclear plants reduces cost and enhances performance[3][4]. In order to achieve high thermal efficiencies, the cycle must recuperate the heat it receives several times, thus requiring a large number of heat exchangers. Reducing the size and cost of the heat exchangers within the s-CO_2 Brayton cycle is critical in demonstrating its usefulness in nuclear applications. Along with reducing cost and size, nuclear reactor systems require increased safety over other thermal power systems (fossil and solar) and there are more strict regulations that components in the nuclear systems need to adhere to.

Printed Circuit Heat Exchanger (PCHE)s are the best candidates for recuperators and heat exchangers within the s-CO_2 Brayton power cycles. PCHEs can achieve the better thermal inefficiencies of higher source temperature reactors such as the HTGR[5][6], SFR[4][7], and FHR. In these reactor systems PCHEs would be used as Intermediate Heat Exchangers between the reactor coolant the s-CO_2 working fluid and as well as recuperators to recovering heat in the circulating s-CO_2. PCHEs fulfil this role better than traditional shell and tube heat exchangers by being more compact and having greater heat transfer surface area per unit volume. Novel PCHE designs have the potential to increase heat transfer while decreasing pressure drop across the heat exchanger. Experimental work at the University of

Wisconsin has identified these benefits in airfoil-fin channels PCHEs[8][9].

PCHEs can handle high pressures and operating temperatures required by generation IV nuclear plants. Advanced nuclear reactors will require the certification of a nuclear service PCHE design by construction codes, such as American Society of Mechanical Engineers (ASME) Boiler and Pressure Vessel Code (BPVC) Sec-3. Compliance with this standard requires a detailed analysis of expected mechanical loads. In particular the distribution of secondary loads, such as differential thermal expansion, within the monolithic PCHE structure is required.

Realizing such analysis in PCHEs requires a simplified and modeling approach for both thermohydraulics and mechanics. Something that can be run over dozens of transients for multiple heat exchanger geometries, while maintaining enough complexit to resolve the full loading within a 3-dimensional PCHE.

The Homogenized Heat Exchanger Thermohydraulics (HHXT) model has been developed to provide a full PCHE model needed to properly resolve ASME BPVC Sec-3 loading conditions without the complexity inherent in resolving all facets of the PCHE geometry. This work introduces the thermohydraulic model that is the core of the HHXT model. An example problem modeling an experimental scaled PCHE is presented. The ability of the HHXT model to simulate fluid flow through a directional varying microchannel core of two heat exchanging streams is demonstrated. The HHXT model resolves PCHE thermohydraulics using simple model definitions and minimum computational overhead, making it an ideal design tool.

A homogenized approach to modeling PCHE mechanics is demonstrated. The method uses a similar homogenization approach as the HHXT thermohydraulic model. However instead of homogenizing heat-transfer and hydraulics, the stiffness and stress-concentration of the micro-channel is homogenized. This allowed the stress intensity within the thousands of internal micro-channel walls of a test PCHE to be evaluated by BPVC BPVC Sec. III

Div. 5.

1.2 Objectives and Contributions

This work focuses on modeling thermohydraulics and mechanics of two PCHE designs, the airfoil and zig-zag micro-channel. The first objective was to understand the behavior of flow at the channel level, asses the heat transfer and pressure drop within the channels, and use these results to model thermohydraulics and temperature distribution within the heat exchanger. The second objective was to determine what mechanical stresses resulted from this combined thermal and hydraulic loading.

1.3 Organization

Following the objectives of this work, this report is composed of five chapters.

The first of the five chapters, Section 2, provides background on the zig-zag and airfoil recuperators, a review of Thermohydraulic analysis approaches used for PCHEs, and a review of pressure drop and heat transfer correlations that are relevant to the airfoil PCHE channels.

The second chapter details a custom Finite Element (FE) thermohydraulic method for PCHE, Section 3. Here the formulation of the HHXT model is presented. A comparison of the model to experimental data is made in Section 3.2, with a close match between model and experiment being found.

The third chapter validates the thermohydraulic model by comparing model predicition of internal temperature of the zig-zag PCHE to measurements. A novel in-situ fiber-optic temperature measurement system was used to provide a 2-dimensional evaluation of PCHE operation. The HHXT model was able to replicate thermal distributions with a good degree of accuracy.

Mechanical analysis is presented in the fourth chapter. Here the test zig-zag PCHE is

evaluated at tested pressure and temperature loads. Stress classification lines are defined at the thinnest micro-channel walls and analyzed using stress linearization as required by BPVC Sec. III Div. 5. Pressure and thermal expansion loads are evaluated for the full size 3-dimensional PCHE and the resulting stress state mapped to each of 108,000 unique micro-channel walls. The zig-zag PCHE is found to be within BPVC Sec. III Div. 5 stress intensity limits and thermal expansion is identified as the largest contributor to micro-channel wall stress.

Experimental performance quantification for the airfoil PCHE is presented in the fifth chapter, Sectionsec:Experiment. Within the experimental work, Section 6.1.1 presents the measurement of pressure drop across a airfoil PCHE. Darcy friction factor results are presented and are analyzed and compared to known correlations. Also under the experimental chapter, Section 6.1.2, presents recuperative testing of a airfoil PCHE. The challenge of calculating a local convective heat transfer coefficient from experiment is specifically addressed in this section and two methods of calculation are discussed. Colburn convective heat transfer results are presented and compared to correlation.

Chapter 2

Background

2.1 Geometry of zig-zag channel test recuperator

2.1.1 Zig-Zag Test Recuperator

A test PCHE recuperator containing zig-zag micro-channels was designed for experimental testing of heat transfer performance and demonstration of embedded fiber-optic temperature instrumentation. Sizing of the PCHE recuperator was based on previous experience testing an industry partner's recuperator design. The zig-zag recuperator has similar surface area and cross section as the industry partner's and was expected to achieve similar performance. Performance at the design point and the extremes of mass flow is given in Table 5.1 The recuperator was designed to operate in CO_2 flows at Reynolds number from 2,000-50,000.

The zig-zag PCHE features semi-circular micro-channels which periodically change direction, which increases mixing of fluid stream, increasing both heat transfer and pressure drop[10, 11]. The zig-zags are primarily described by their angle, with higher angle leading to larger heat transfer and pressure drop. An 80° zig-zag was chosen as it is comparable to commonly manufactured zig-zag PCHEs, such as those made by Heatric[12] that have

Table 2.1: Recuperator Performance

	lowest flow	design flow	high flow
$\dot{m}$ (kg/s)	0.0123	0.0336	0.1086
$\dot{q}$ (kW)	6.28	18.00	42.70
Re_C	1888	5131	17,295
Re_H	2309	6097	19,818
ε (%)	95.6	95.0	90.0
UA (W/K)	214	477	756

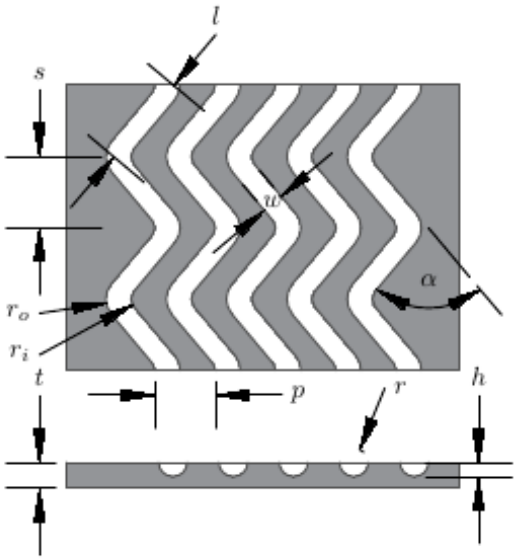

Figure 2.1: Zig-zag micro-channel geometric parameters

been preciously tested[8, 9]. The 80° zig-zag is comparable to the "medium" Heatric zig-zag channel investigated experimentally by Moisseytsev et. al. [13].

The pattern us in the test PCHE is shown in Figure 2.1. The zig-zag pattern is described by the bend-to-bend length (l), the bend angle (α), the width of the channel (w), the depth of the channel (h), and the lateral pitch between neighboring channels (p). In sizing the array, the lateral pitch of the channels was kept relatively large so that 20 MPa operating pressure could be contained by the relatively thick micro-channel walls. Values chosen for the zig-zag pattern that was constructed are listed in Table 2.4. These values are similar to those used in previous experimental analysis of Kruizenga and Carlson[8, 9]. The zig-zag angle used is slightly greater than the 74° in concurrent studies by Katz and Aakre[14].

recuperator layout

The recuperator is bonded out of a stack of 22×1.5 mm thick plates. A diagram of the stacking order is shown in Figure 2.4. Etched plates, each containing 28 zig-zag channels,

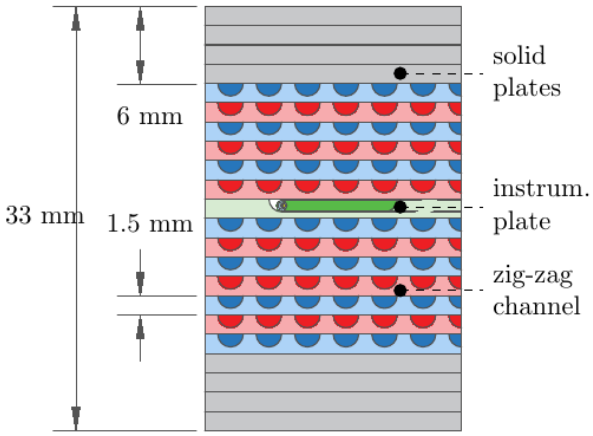

Figure 2.2: Zig-zag diffusion-bonded core stack

make up the core of the recuperator. These are alternated between cold and hot CO_2 streams and contain a central instrumented plate. The core is sandwiched between 4 solid plates at the top and bottom of the stack. These provide additional mechanical support and solid material onto which headers can be welded.

A diagram of the cold CO_2 channel layout is shown in Figure 5.4. Cold CO_2 enters from within an attached side header at the top right and exits at the bottom left. Hot CO_2 flows in the opposite direction, entering at the top left and exiting bottom right. An outline of modeling regions is overlayed on the pattern for the etched plate, and region types are identified.

A solid side wall is maintained around the micro-channels. This ensures that diffusion-bond edge defects are away from the micro-channels and provides a solid foundation for welded headers.

The semicircular headers are made out of a 3/4 inch schedule 160 pipe, which is and welded to the diffusion bonded block. Nozzles made of 1/2 inch 0.085 inch wall tube and pressure ports made of 1/4 tube are attached to each header.

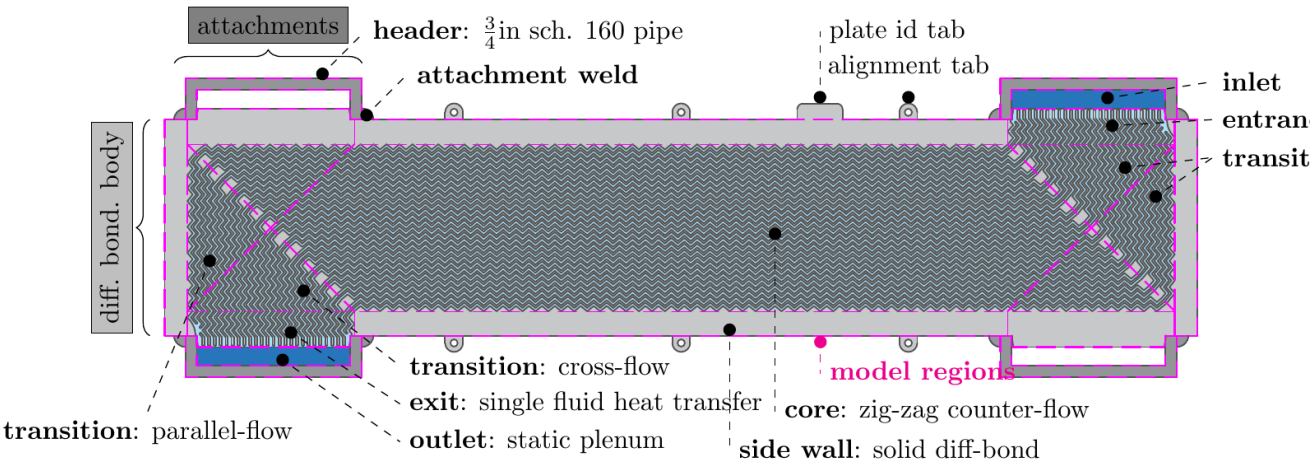

Figure 2.3: Regions within the cold CO_2 channel of the Zig-Zag test recuperator

zig-zag micro-channels

The topology of the zig-zag micro-channels was reconstructed from white light scans of the etched plates prior to diffusion bonding. White light scans were made over a 74×63 mm patch of etched channels, capturing roughly 315 zig-zag bends. Of these, 60 bends were analyzed and their geometry measured relative to the geometric parameters shown in Figure 2.1 and listed in Table 2.4. Uncertainty in each measurement is taken as the standard deviation of the measurements made over each of the 60 analyzed bends. The photo-etching process is highly accurate at locating features but has some difficulty in controlling the depth and radius of etch.

Hydraulic diameter, volume fraction and frontal area were determined by reconstructing the channel in CAD using the dimensions shown in Figure 2.1. Here the hydraulic diameter is determined by comparing the fluid volume to the wetted area of the channel surface,

$$D_h = \frac{4V}{A_{surf.}} \tag{2.1}$$

Table 2.2: Zig-zag channel geometry

description	**symbol**	**value,** (mm)		
		design	**measured**	
bend angle [deg]	α	80	80	
bend-to-bend length	l	4.724	4.727	$\pm$ 0.007
axial pitch	s	3.619	3.621	$\pm$ 0.005
lateral pitch	p	3.277	3.282	$\pm$ 0.018
channel width	w	1.456	1.482	$\pm$ 0.073
channel depth	h	1.000	0.829	$\pm$ 0.027
inner radius	r_i	0	0.399	$\pm$ 0.042
outer radius	r_o	0	0.825	$\pm$ 0.077
profile radius	r	0.728	0.741	$\pm$ 0.037
hydraulic diameter	D_h	1.010	1.012	
plate thickness	t	1.50	1.50	
volume fraction $(-)$	ϕ	0.251	0.262	
frontal area (mm^2)	A_{fr}	1.234	1.296	

2.2 Geometry of airfoil channel test recuperator

The University of Wisconsin Madison created a test PCHE recuperator containing airfoil micro channels. It was designed for experimental testing of heat transfer performance and demonstration of embedded fiber-optic temperature instrumentation. Sizing of the PCHE recuperator was based on previous experience testing an industry partners recuperator design. The airfoil recuperator has similar surface area and cross section as the industry partners and is expected to achieve similar performance. The performance design point is given in Table 5.1 The recuperator was designed to operate in a flow regime of 1490-16600 Re, .

Table 2.3: Recuperator Design Performance

	lowest mass flow	highest mass flow
Re	1402	16600
Effectiveness %	93.1	82.6
UA	61.6	219.3

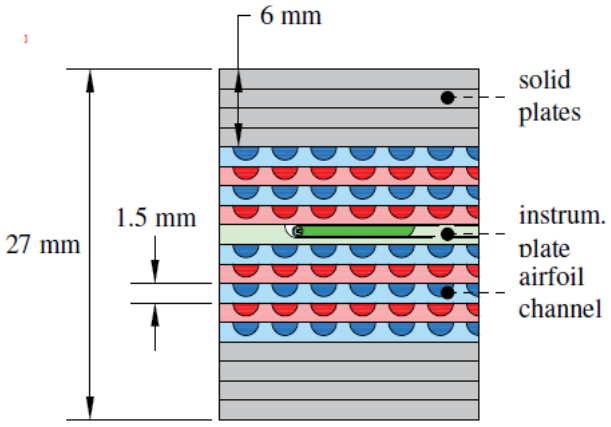

Figure 2.4: Plate stacking order in the airfoil recuperator, hot channels are red, cold channels blue.

The PCHE is made of a number of stacked counter flow channels, top and bottom solid channel-less plates, and a central instrumentation plate. Plates are 1.5 mm thick 316 Stainless Steel and are chemically etched to a depth of 0.95 mm. The stacking of the airfoil plates is shown in Figure 2.4. In flow channels the resulting profile is semicircular as the etch is produced from one direction. Channeled plates are stacked alternatively in counter flow with the outmost plates being the cold side. Solid plates bonded to the top and bottom of the stack are un-etched, so that when bonded 4 thick, they form 6 mm of solid wall within the recuperator. The 6 mm is needed primarily as a weld region so headers can be attached without damaging the fragile internal micro-channels.

Inlets and outlets to the hot and cold channels are brought together in a manifold and linked to plumbing through four separate headers. Headers are placed on the sides of the recuperator as show in the diagram of the airfoil recuperator in Figure 4.

The PCHE core, headers, and nozzles were designed to ASME BPVC Sec IIX standards. The choice of airfoil fin density and header wall thickness allow operation at pressures up to 29.6 MPa at 200 C and 11.3 MPa at 650 C.

2.2.1 Airfoil Micro Channel

The airfoil PCHE features an geometry that is unique among etched channel designs. The channels of the airfoil PCHE contain an array of offset airfoil shaped fins. The fins are patterned in alternating rows with the airfoils facing the direction of flow in the channel. In this fashion flow through the channel isnt constrained to a singular flow path, as in the typical straight and zig-zag channel designs. Flow is free to pass through the entirety of the air foil array without the usual constraint that is induced by repeating channel walls present in straight channel and zig-zag PCHE designs. Moving around each individual airfoil in the channel, the fluid becomes well mixed and transfers heat as well as the standard zig-zag channel design without as much of a pressure drop [9].

The pattern considered is shown in Table 2.4. The airfoils are described by the camber-less NACA airfoil equation. The pattern is described by the chord length of the airfoil, the width of the airfoil at its girth, the lateral pitch between airfoil columns (perpendicular to flow), and the axial pitch between airfoil rows (in the direction of flow). In sizing the array, chord length and axial pitch are set so that the most uniform hydraulic diameter is achieved, which occurs when the ratio of axial pitch to chord length (s/c) is 0.86 [8]. Values chosen for the airfoil pattern that was constructed are shown in Table 2.4. These values were chosen to be the same as those used in previous experimental analysis of Kruizenga and Carlson[8, 9].

The effect of chemical etching on the topology of the airfoil-fin channel was considered. The depth of etch and filleting of the channel features was anticipated and factored into initial estimates of the Hydraulic diameter. Optical topography of the etched airfoil channels revealed a geometry that came close to design, see Figure 2.5a. At 0.977 mm channel depth was marginally deeper than design while the etch filleting radius of 1.150 mm was considerably larger, see Figures 2.5b & 2.5b. Further optical topographically measured values are given in Table 2.4. The resulting hydraulic diameter was found to be 1.498 mm.

Table 2.4: Airfoil channel geometry

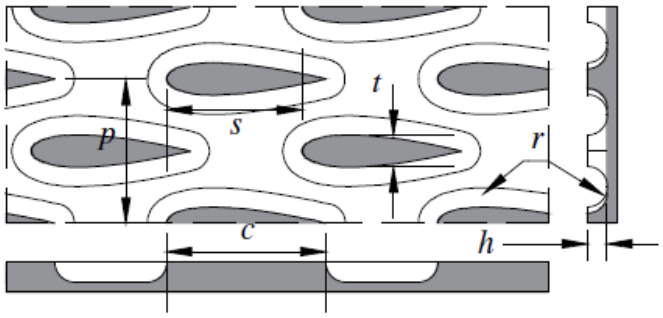

description	symbol	value, $[mm]$		
		design	measured	
axial pitch	s	6.9	6.9	
lateral pitch	p	7.3	7.3	
chord length	c	8.1	8.508	$\pm$ 1.766
airfoil width	t	1.62	1.738	$\pm$ 0.484
channel depth	h	0.95	0.977	$\pm$ 0.005
fillet radius	r	0.95	1.150	$\pm$ 0.043
hydraulic dia.	D_h	1.536	1.498	
volume fract.	ϕ	0.549	0.528	
frontal area	A_{fr}	1.917	2.190	

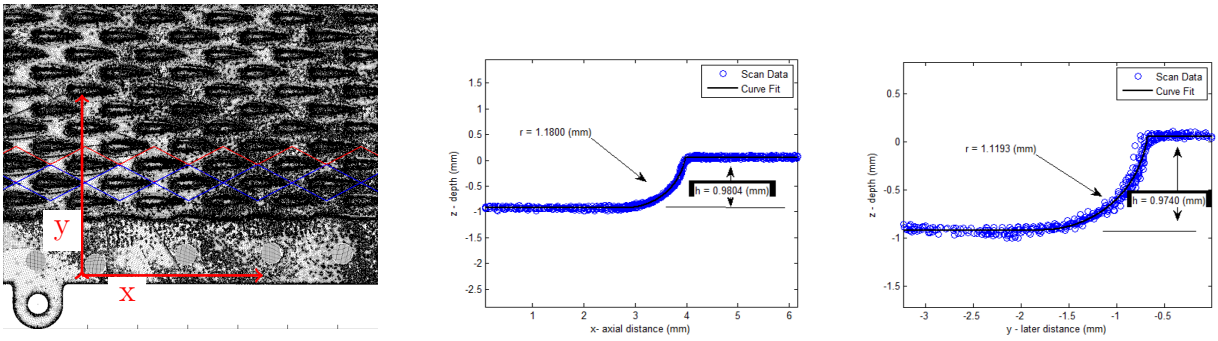

(a) scan section **(b)** profile along x **(c)** profile along y

Figure 2.5: Optical scan of etched Airfoil Channel gives an average etch radius of 1.150±0.043 mm

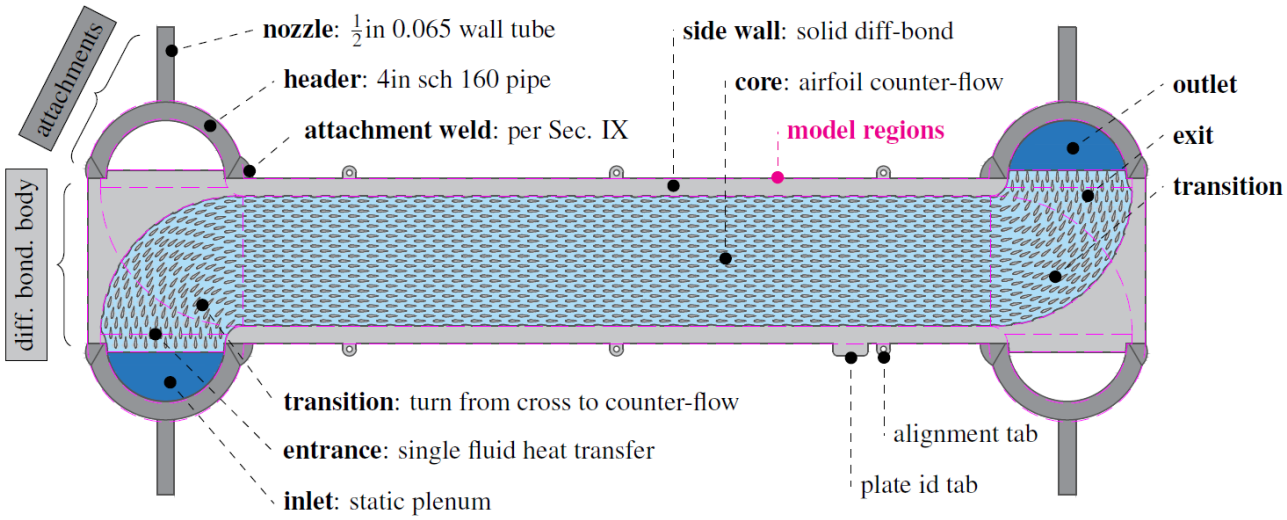

Figure 2.6: Common PCHE region types are illustrated for the cold carbon-dioxide (CO_2) channel of an airfoil test recuperator

2.3 Review of Thermohydraulic Analysis Approaches

As with other types of heat exchanger, it is most elementary and convenient to model the Printed Circuit Heat Exchanger (PCHE) using effectiveness-NTU methods. This is sufficient when the application doesn't require detail within the PCHE and the design of the PCHE is in a preliminary stage. Sizing and economic analysis of a PCHE design are two applications, run during the preliminary design phase of the PCHE application, that are adequately addressed using effectiveness-NTU methods. For instance when designing a He to supercritical carbon-dioxide (s-CO_2) Intermediate Heat Exchanger to be used in an High Temperature Gas Reactor, Kim and Ho[15] used effectiveness-NTU methods, combined with CFD analysis of micro-channel heat transfer, to find a cost optimum channel design and PCHE size. With sizing completed, the detailed component level design of the PCHE can begin.

Component level analyses of a PCHE require models that more accurately capture thermal performance, and resolve thermal gradients, within the PCHE body. Fluid property

variation, channel geometry changes, and the transition between fluid inlets, outlets, and the cross-flow core, all affect the thermal the performance in ways not capture by simple effectiveness-NTU methods. Furthermore they generate thermal gradation and secondary stresses, threatening the mechanical integrity of the PCHE through fatigue and ratcheting. Insufficient attention to detail within the modeling phase can overlook problematic geometry features and loading scenarios. If design margins are tight, in service failure of the PCHE can result.

2.3.1 Modeling Features

Ultimately it is the job of the designer to ensure that all relevant aspects of PCHE geometry are addressed within the thermal and mechanical analysis. While designs and channel arrangements will vary, the process of etching, bonding, and assembling of a PCHE will result common features which should be considered:

- **Inlet**: this is a relatively open fluid area that is not constructed of micro-channels. Flow is static relative to higher velocity flow in the channels. In practice this is the fluid within external or internally constructed headers.

- **Entrance**: a micro-channel region that connects the inlet to the interior of the PCHE. This region contains channels of only one fluid stream and thus heat transfer is just between the entering fluid and the PCHE solid. Thermohydraulics here are largely driven by the inlet conditions.

- **Transition**: a multi stream micro-channel region which transitions the channels from their inlets/outlets into pure counter flow. This is where heat-transfer between streams through the solid body first occurs. These regions are the drivers of non-axial temperature distributions.

- **Core**: the largest portion of the PCHE, channels in counter flow. The best designed PCHE will maximize the percentage of core in the PCHE body as this improves performance and reduces non-axial thermal gradients.

- **Exit**: a single stream similar to an entrance that connects a transition to an outlet plenum. Different than an entrance in that thermohydraulics are driven by conditions in the upstream transition region and relatively independent of conditions within the outlet.

- **Outlet**: like the inlet this is an open fluid area, but unlike the inlet the outlet conditions are driven by upstream flow.

- **Side Wall**: a solid portion of the diffusion bonded body. These exist as primary pressure boundaries and more importantly as a solid region onto which headers and attachments can be welded. Thermally these solid regions conduct and store more heat than the core.

- **Top/Bottom Wall**: (not shown) thick plates placed at the bottom and top of the diffusion bonded body. Like the side wall, these provide a pressure boundary and material to weld to. However the thickness of the top/bottom wall is dictated by the need for thick plates to distribute compressive loads within the diffusion bonding press.

- **Headers & Attachments**: material that is welded onto the diffusion bonded body. Thermally these can store heat during transients and interact with the inlet and outlet fluid plenums.

These features are identified in Figure 5.4 for an experimental Airfoil micro-channel PCHE that was constructed for CO_2 recuperative testing at the University of Wisconsin[16]. The features exist in distinct regions of the PCHE (outlined by magenta lines in the figure).

Any model of PCHE thermodynamics needs to account for the variation of hydraulics and heat transfer from region to region. Unfortunately due to varying levels of sophistication across PCHE model approaches, some, or most, of these regions might be neglected.

2.3.2 PCHE modeling approaches

Approaches to PCHE modeling can be split between linearized analyses and homogenization methods. Both approaches use estimations of the pressure drop within, and the heat transfer to the PCHE from, the fluid streams. Modeling approaches can also choose to address conduction and heat storage within the PCHE body, and sometimes will do so for the fluid streams if necessary–i.e. sodium applications.

Use of a friction factor f, Darcy or Fanning, is commonly used to express the pressure drop performance of a PCHE microchannel. Heat transfer coefficients vary between the dimensional local heat transfer coefficient, h, and its dimensionless equivalents: Nusselt number, Nu, and Colburn factor, j. All these can be determined through experiment, with Computational Fluid Dynamic (CFD) simulations of the micro-channel, or a combination of both. Kruizenga and Li [17, 18] perform an evaluation of f and Nu for Zigzag microchannels in s-CO_2 using both experiment and CFD, while Chen et al. [19] do the same for straight channels in He.

Linearized methods

In linearized analysis only the PCHE Core and Transition regions are addressed, and their behavior is reduced along the axis of the PCHE. One dimensional descretization of fluid-to-fluid heat transfer is used, with finite difference and ad hoc methods being the most popular. Linearized analyses capture overall performance of the PCHE well and can account for variable fluid properties, e.g. CO_2 operating near the critical point[16]. Given their

simplicity and potential for rapid numerical evaluation, linearized PCHE models have also found use within plant system dynamics models such as that developed at Argonne National Laboratory for the AFR-100 Sodium-cooled Fast Reactor[13, 20].

Homogenized methods

Homogenization analyses address all PCHE regions within a single 2D or 3D model of the PCHE. They do so by homogenizing the behavior of micro-channeled regions within a representative volume. The PCHE thermohydraulic problem is presented as a system of partial differential equations that (PDEs) describe the flow, conduction, heat transfer etc., that all exist within the element. Regions of the model contain different homogenized volumes, e.g. the core region would be homogenized using a volume that captures both counter-flow streams such as that shown in Figure 2.7. The PDEs can be evaluated using finite difference or finite element (FE) methods.

So far only a finite difference homogenization method in 2D has been demonstrated by Urquiza[2]. Urquiza's model could capture entrance, transition, core, exit, and solid PCHE regions. Using a porous media model for the hydraulic equations, the model captured two dimensional flow. Urquiza's work proved the homogenization method's applicability in PCHE thermohydraulic modeling, but was limited in its finite difference implementation. Being finite difference based, meshes and geometries that could be used were limited to rectilinear space, and the assembly of boundary conditions in regions of non-linearity proved to be unstable[21].

While apparently similar to traditional fluid-solid FE implementations (Fluent, CFX), the homogenization method differs in its evaluation of the fluids and solid simultaneously within every element. Traditional FE must evaluate each fluid and the solid on separate elements, thereby requiring each fluid channel to be covered by at least one element. Pra et al.[22] provides an example where traditional FE was used in modeling transients in an

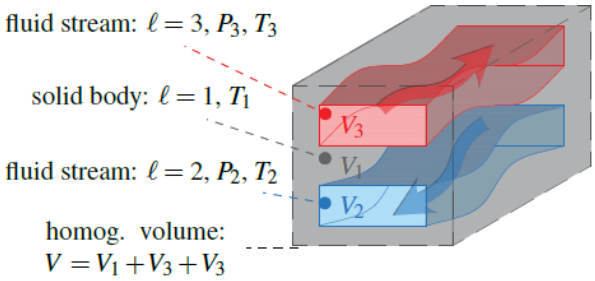

Figure 2.7: Homogenization of a two stream micro-channel

air-to-air PCHE. Here the modelers had to suffice with modeling a single pair of hot and cold air channels, instead of the 49 pairs that composed the block. This channel pair required a 132560 element mesh on a footprint of 196×896 mm, or 755 thousand elements per m^2. In comparison, the FE implementation of the homogenization presented in this paper was able to use a 2750 element mesh over a 774×121 mm footprint, which at roughly 29 thousand elements per m^2, is a marked improvement. By being able to homogenize over many fluid channels, the homogenization method can mesh using fewer larger elements.

2.4 Pressure drop in airfoil channels

2.4.1 Pressure drop due to wall friction

Pressure drop resulting from frictional shear with a channel wall is generally expressed in terms of a friction factor. The most useful form is the Darcy friction factor, as it is the factor that can be directly used in Darcy porous media models. Common correlations for the Darcy friction factor, f, exist for fully-developed internal flow through circular pipes and many other ducts. The dimensionless parameters Reynolds number, and relative roughness are used to simplify friction factor relations so that $f = F(Re, \epsilon/D)$. The Darcy friction

quantity of channel pairs is inferred: figures in Pra et al. show a 160 mm thick PCHE, assuming a common configuration of 1 mm deep micro-channels etched in 1.5 mm thick plates and 1/4in thick top & bottom plates would give 49.1 pairs of plates.

factor is related to pressure drop as follows [23, 24],

$$\Delta P = f\frac{L}{D}\tfrac{1}{2}\rho \mathrm{v}^2 \tag{2.2}$$

For fully developed flow the friction factor can also be written in terms of wall shear-stress,

$$f = \frac{8\tau_w}{\rho \mathrm{v}^2} \text{ , where } \tau_w = \left|\mu\frac{du}{dr}\right|_{r=R} \tag{2.3}$$

Laminar friction

For laminar flow the wall velocity distribution $u(r)$ is parabolic with no-slip at the wall and maximum velocity of $u_{max} = 2\mathrm{v}$ in the center of the flow, where v is average velocity within the channel. The highest velocity gradient is at the wall and can be expressed as [24],

$$\left|\frac{du}{dr}\right|_{r=R} = \left[\tfrac{1}{2}\frac{r}{\mu}\left(u_{max}\frac{4}{R^2}\right)\right]_{r=R} = \frac{2u_{max}\mu}{R} = \frac{8\mathrm{v}}{D} \tag{2.4}$$

The friction factor for laminar flow can be found from the velocity gradient at the wall.

$$f = \frac{8\left(\mu\frac{8\mathrm{v}}{D}\right)}{\rho \mathrm{v}^2} = \frac{64\mu}{\rho \mathrm{v} D} = \frac{64}{Re} \tag{2.5}$$

where the Reynolds number is simply

$$Re = \frac{\mathrm{v}D}{\nu} = \frac{\rho \mathrm{v} D}{\mu} \tag{2.6}$$

In laminar flow the friction factor is inversely related to Reynolds number. Stated otherwise, pressure drop is directly proportional to velocity in laminar flow.

Turbulent friction

A linear relation between flow and pressure-drop is not the case for turbulent flow. Here instabilities break up the laminar boundary layer, producing a smaller viscous sublayer that hugs the wall. In 1935 Prandtl used logarithmic law-of-the-wall correlations to compute the mean velocity of the turbulent viscous sublayer and arrived at the following relation: [25]

$$\frac{\mathrm{v}}{u^*} \approx 2.44 \ln\left(\frac{Ru^*}{\nu}\right) + 1.34, \text{ where } u^* = \sqrt{\frac{\tau_w}{\rho}} \tag{2.7}$$

which is useful because v/u^* is directly related to the Darcy friction factor,

$$\frac{\mathrm{v}}{u^*} = \sqrt{\frac{\rho \mathrm{v}^2}{\tau_w}} = \sqrt{\frac{8}{f}} \tag{2.8}$$

And the argument of the logarithm in equation 2.7 is equivalent to

$$\frac{Ru^*}{\nu} = \frac{\frac{1}{2}\mathrm{v}D}{\nu}\frac{u^*}{\mathrm{v}} = \frac{1}{2}Re\sqrt{\frac{f}{8}} \tag{2.9}$$

Substituting equations 2.8, 2.9 into equation 2.7 and changing the logarithm to base-10 results in the following formula for f:

$$\frac{1}{\sqrt{f}} \approx 1.99 \log_{10}\left(Re\sqrt{f}\right) - 1.02 \tag{2.10}$$

Prandtl took this smooth-wall correlation and adjusted the constants slightly to fit experimental data better. He arrived at the following formula for a smooth-walled pipe:

$$\frac{1}{\sqrt{f}} = 2.0 \log_{10}\left(Re\sqrt{f}\right) - 0.8 \tag{2.11}$$

Early turbulent flow experiments by Coulomb[26] revealed that surface roughness affects friction resistance. It was discovered that the effect of roughness is negligible for laminar

flow but a factor in turbulent flow. This is because surface features are much smaller than the laminar boundary layer but can affect the thinner turbulent viscous sublayer. The law-of-the-wall would indicate that the viscous sublayer only extends out to $y^+ = yu^*/\nu = 5$. Thus, compared to the diameter D, the sublayer thickness δ_s would only be:

$$\frac{\delta_s}{D} = \frac{5\nu/u^*}{D} = \frac{14.1}{Re\sqrt{f}} \tag{2.12}$$

Wall roughness could be a concern within the turbulent region when the viscous sub-layer becomes increasingly thin. Based on smooth pipe relation, at the beginning of the turbulent region (Re=3000 and f=0.0435) the viscous sublayer would be δ_s=0.022·D while at high turbulence (Re=10000 and f=0.0309) the viscous sublayer would be δ_s=0.00802·D. If the relative roughnes reaches these values, the break up of the sublayer will start. This would profoundly change the velocity distribution and rendered the law-of-the-wall void. This critical roughness is achievable in channel systems where hydraulic diameter is on the order of millimeters. With D_h=1.498 mm, the airfoil channels would require a wall roughness of 0.012 mm to break up the viscous sublayer at Re=10000. Optical measurements of etched PCHE plates at UW-Madison has found surface roughness to be in the range of 0.0022-0.0076 mm[9][8], which would break up the sublayer at Re above 76500 and 16900 respectively. See Section **??** for further analysis on roughness.

Prandtl's student Nikuradse made measurements of roughness's affect on friction and found that a roughness height ϵ forces the law-of-the-wall velocity profile outward by an amount approximately equal to $\ln\epsilon^+$, where $\epsilon^+ = \epsilon u^*/\nu$[27]. Flow is considered *hydraulically smooth* when $\epsilon^+ < 5$, *transitionally rough* when $5 < \epsilon^+ < 70$, and *fully rough* when $\epsilon^+ > 70$. With roughness the slope of the logarithmic law-of-the-wall remains the same, but the shift outward causes u^* to decrease by approximately $(1/\kappa)\ln\epsilon^+$. For fully rough flow, $\epsilon^+ > 70$, Nikuradse found the law of the wall to be:

$$u^+ = \frac{1}{\kappa}\ln y^+ + 8.5 - \frac{1}{\kappa}\ln\epsilon^+ = \frac{1}{\kappa}\ln\frac{y}{\epsilon} + 8.5 \tag{2.13}$$

The effect of viscosity vanishes, and thus fully rough flow is independent of Reynolds number. Equation 2.13 can be integrated to obtain the average velocity in the pipe.

$$\frac{\mathrm{v}}{u^*} = 2.44\ln\left(\frac{D}{\epsilon}\right) + 3.2 \text{ or } \frac{1}{\sqrt{f}} = -2.0\log_{10}\left(\frac{\epsilon/D}{3.7}\right) \tag{2.14}$$

The fully rough equation for f has no Reynolds effect and the thus pressure drop varies exactly as the square of velocity. Fully rough turbulent flow is completely independent of Re and follows equation 2.14. Hydraulically smooth turbulent flow is completely independent of roughness but depends on Re and is described by equation 2.11. The transitionally rough region of turbulent flow is a mix between these two regimes, depending somewhat on both roughness and Reynolds number.

To cover the the transitionally rough region Colebrook combined the smooth wall and fully rough relations into the Colebrook formula[28].

$$\frac{1}{\sqrt{f}} = -2.0\log_{10}\left(\frac{\epsilon/D}{3.7} + \frac{2.51}{Re\sqrt{f}}\right) \tag{2.15}$$

This is the most accepted design formula for turbulent friction and applies well to circular and non-circular pipe flows as well as open-channel flows. Solutions to the Colebrook equation were plotted by Moody[29] into what is know as the *Moody chart* of pipe friction and shown in Figure 2.8. Note that the roughness curves are horizontal at high Re. This is because flow has transitioned into the Reynolds independent fully rough regime. The transition point to fully rough flow is demarcated by the dashed line.

The shaded area in the Moody chart indicates the range where flow transitions from laminar to turbulent. Prediction of pressure-drop in this range is impossible as turbulence

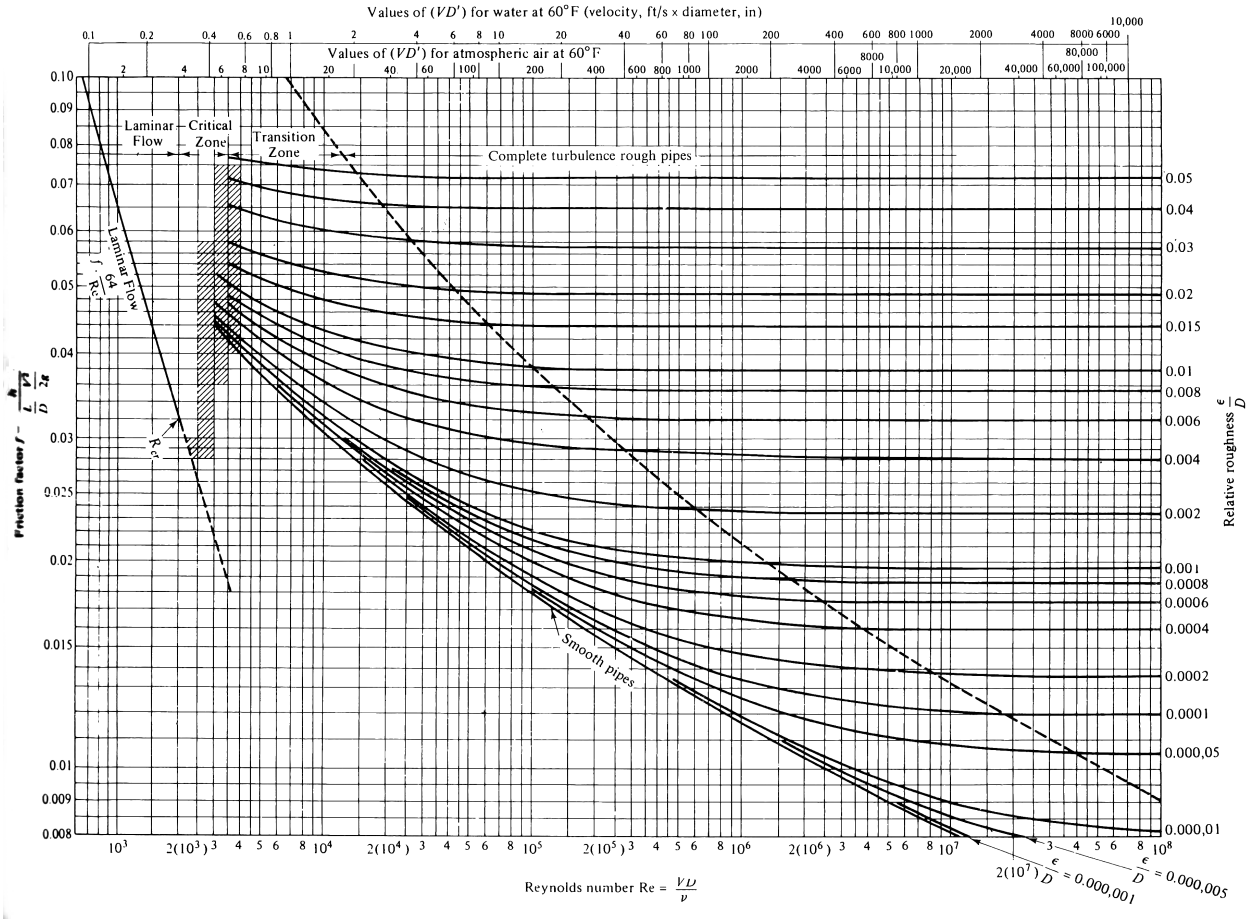

Figure 2.8: The Moody chart for pipe friction with smooth and rough walls[29].
This chart is identical to equation 6.3 for turbulent flow.

can burst in and out of existence. This transition region spans $2000 < Re < 4000$ for pipe flow. Inclusion of turbulence inducing mechanisms, such as spacer grids in nuclear reactor cores or fins in heat exchangers, can shorten the transition region by generating turbulence sources. Because of their complex geometries and highly non-uniform flow, the transition region in channel heat exchangers begins at lower Reynolds number than that shown in the Moody chart. Furthermore the complex geometry of these heat exchangers can create pressure drops in excess of that predicted by the pipe-flow relations.

2.4.2 Pressure drop from minor losses

Standard pipe-flow pressure drop models are not sufficient for modeling flow through the airfoil recuperator channels. Flow through the recuperator channels is much more complex than that of an equally sized pipe. Flow directional changes, obstructions, and header entrance and exit regions all contribute to pressure drop. These must be considered when evaluating flow in the recuperator.

Pressure drop is also highly influence by the shape of recuperator channels. For instance the evaluation of pressure-drop in straight channels would only have to consider entrance and exit effects in addition to frictional contributions. Zig-Zag channels on the other hand would require an additional evaluation of pressure loss through flow bends, while airfoil channels require an evaluation of drag induced pressure-drop accross each airfoil. The affect of entrance and exit losses and airfoil drag are considered for the airfoil channels

Entrance and exit losses

The flow transition between PCHE headers and their internal channels is an abrupt contraction of flow. This presents a significant flow resistance that must be accounted for when calculating pressure drop through a channel, see Figure 2.9a. Increased pressure drop from

contraction is slightly offset by pressure increase in the downstream header due to expansion from the channels back into the larger header volume , see Figure 2.9b.

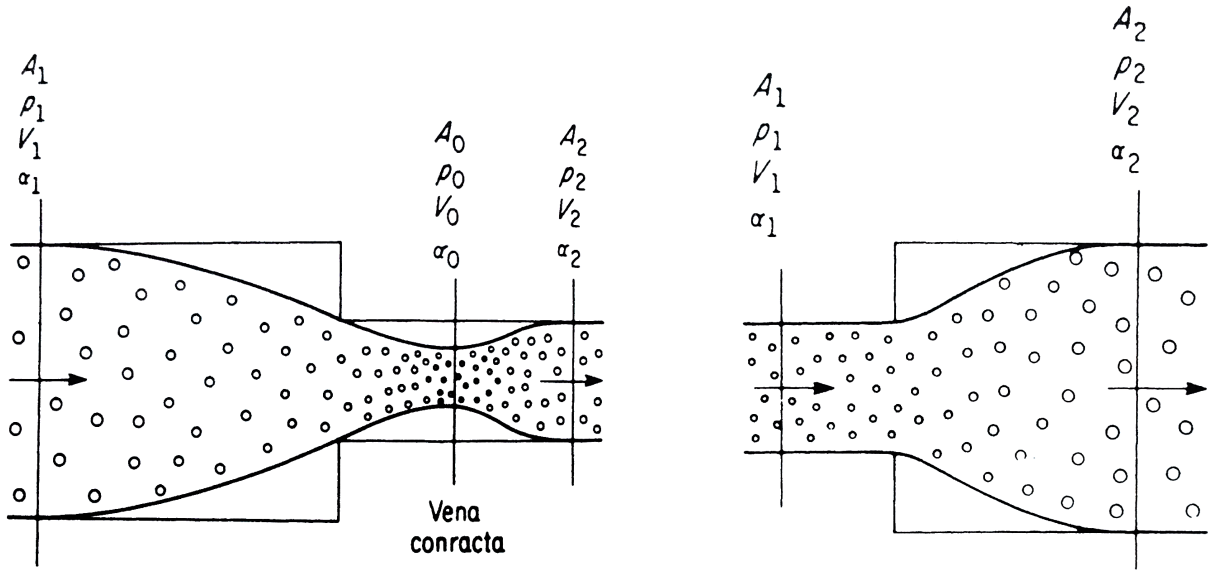

(a) Contraction at inlet. **(b)** Expansion at outlet.

Figure 2.9: Pressure drop minor losses diagram[30]
Minor losses occur at the entrance and exit of the channel block.

Pressure changes from expansion are the simplest to consider, as the recirculating regions downstream of the contraction do not dissipate much energy from the flow. Figure 2.9b gives a schematic of flow expansion in sharp edged geometries. Here the flow coming from the channels is upstream at cross-section 1 while established flow in the header occurs at cross-section 2. It can be assumed that pressure p_1 still acts on the expanded area A_2 since the flow lines there are essentially the same as at cross-section 1. Applying a momentum balance with this assumption leads to,

$$P_1 A_2 - P_2 A_2 = \dot{m}_t(v_2 - v_1) \tag{2.16}$$

With the help of the continuity equation $\dot{m}_t = \rho A_s v_2$, Equation 2.16 can be written and rearranged to give the Borda-Carnot equation for pressure increase during expansion [30],

$$P_2 - P_1 = \rho v_1^2 \left[\frac{A_1}{A_2} - \left(\frac{A_1}{A_2} \right)^2 \right] = -\Delta P_{expansion} \tag{2.17}$$

In the upstream contraction of flow from header to channel streamlining is prevented by the abrupt change in flow area, leading to a *vena contracta* that occurs after the contraction, shown at cross-section 0 in Figure 2.9a. Not much pressure is lost when moving from before the contraction, at cross-section 1, to the *vena contracta*, at cross-section 0. But their are substantial losses between the *vena contracta* and the downstream channel at cross-section 2. These head losses can be expressed using the Borda-Carnot expression for flow contraction [25],

$$\Delta P_{contraction} = \tfrac{1}{2}\rho v_2^2 \left(\frac{1}{\zeta} - 1 \right)^2 = \tfrac{1}{2}\rho v_1^2 \left(\frac{1}{\zeta} - 1 \right)^2 \left(\frac{A_1}{A_2} \right)^2 \tag{2.18}$$

where ζ is the coefficient of contraction. According to Weisbach, the contraction coefficient for a sharp-edged contraction is approximately [25],

$$\zeta = 0.63 + 0.37 \left(\frac{A_2}{A_1} \right)^3 \tag{2.19}$$

The Borda-Carnot expressions for contraction and expansion losses are the most simple of the minor loss formula and are generally applicable to most flow cases. However they assume contraction and expansion between singular whole cross-sections that are not like that seen between headers and PCHE channels where a large homogeneous flow area breaks up into many smaller channels. The coefficient of contraction ζ used in the Borda-Carnot expression is meant for contraction and expansion to a singular flow-cross-section. Borda-Carnot underestimates pressure-drop in the case where a large perimeter of sharp-edged contraction exists and the *vena contracta* within small PCHE channels takes up much more

area than it would in large pipe or rectangular duct.

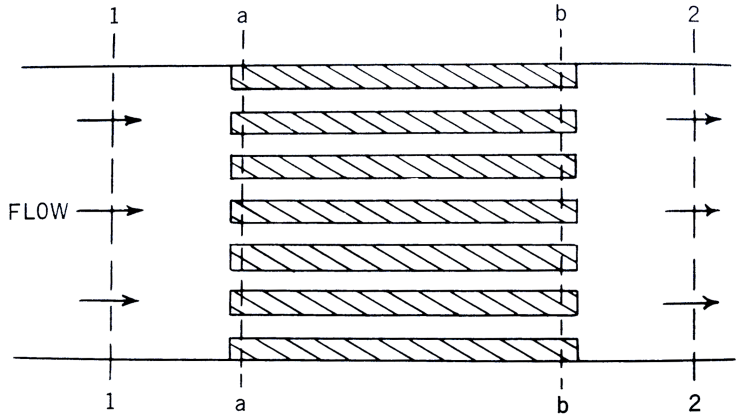

Figure 2.10: Heat exchanger core model for pressure-drop analysis [31].

Because of these inaccuracies in the Borda-Carnot expressions, minor-loss equations have been specifically developed for flow in heat-exchanger channels. Kays and London propose an experimentally derived minor loss equation for flow through multiple-square-tube heat exchanger cores. An illustration of the flow scenario is given in Figure 2.10 where flow is entering from the header (cross-section 1), flowing through the core of the heat exchanger (cross-section a→b), and exiting to a downstream header (cross-section 2). Although obtained for the relatively larger brazed-plate heat exchangers, minor loss equations from Kays-London are more applicable to PCHE channels than the Borda-Carnot equations. The Kay-London equation for all pressure drop through the heatexchanger is [31],

$$\Delta P = \frac{1}{2}\rho \mathrm{v}_m^2 \left[\underbrace{\left(K_c + 1 - \sigma^2\right)}_{\text{Entrance contraction}} + \underbrace{2\left(\frac{\mathrm{v}_2}{\mathrm{v}_1} - 1\right)}_{\text{Flow acceleration}} + \underbrace{f\frac{L}{D_h}}_{\text{Core friction}} - \underbrace{\left(1 - \sigma^2 - K_e\right)}_{\text{Exit expansion}} \right] \tag{2.20}$$

where v_m is the velocity of flow in the heat exchanger channels. σ is the ratio of free-flow to the frontal area of one side of the heat exchanger, i.e. $\sigma = A_c/A_{f,entrance}$. In the case of the airfoil heat exchanger σ=3.006 cm^2/22.867 cm^2=0.1315 on the hot CO_2 side and σ=3.758

$cm^2/22.867\ cm^2$=0.1643 on the cold CO_2 side. v_1, v_2, and v_m are the velocities before contraction, after expansion, and in the heat exchanger core respectively. As experimental data was taken with little variation in s-CO_2 temperature, and change in absolute pressure is small, it can be assumed that $v_1 = v_2 = v_m$. Thus the Kays-London equation reduces to,

$$\Delta P = \frac{\rho v^2}{2}\left[\underbrace{\left(K_c + 1 - \sigma^2\right)}_{\text{Entrance contraction}} + \underbrace{f\frac{L}{D_h}}_{\text{Core friction}} - \underbrace{\left(1 - \sigma^2 - K_e\right)}_{\text{Exit expansion}}\right] \tag{2.21}$$

Entrance and exit loss coefficients, K_c and K_e, are given in graphical form for a multiple-square-tube heat exchanger core by Kays and London in Figure 2.11. Polynomial fits to the Re=∞ curves results in the following correlations for K_c and K_e,

$$K_c = 0.4 - 0.4\sigma^2, \text{ with fit quality } R^2 = 0.992 \tag{2.22}$$

$$K_e = 1.0 - 1.9\sigma + 0.9\sigma^2, \text{ with fit quality } R^2 = 0.993 \tag{2.23}$$

For the airfoil recuperator the Kays and London minor loss term add an additional $1.159\times\rho v^2/2$ pressure drop, which is negligible in comparison to the core friction factor term.

Obstructions in flow

Obstructions in flow such presented by the airfoil-fins of the airfoil channel, present an additional source of pressure drop. Unlike contraction/expansion effects or channel bends, the flow obstruction contribution is expressed as an obstructional friction factor f_{obs} that acts in addition to the standard pipe friction factor f_{frict} from equation 6.3. The obstruction factor f_{obs} is not a standard minor loss factor, as it is applied along the channel length L/D_h to obtain pressure-drop. Thus the pressure drop over a core section is:

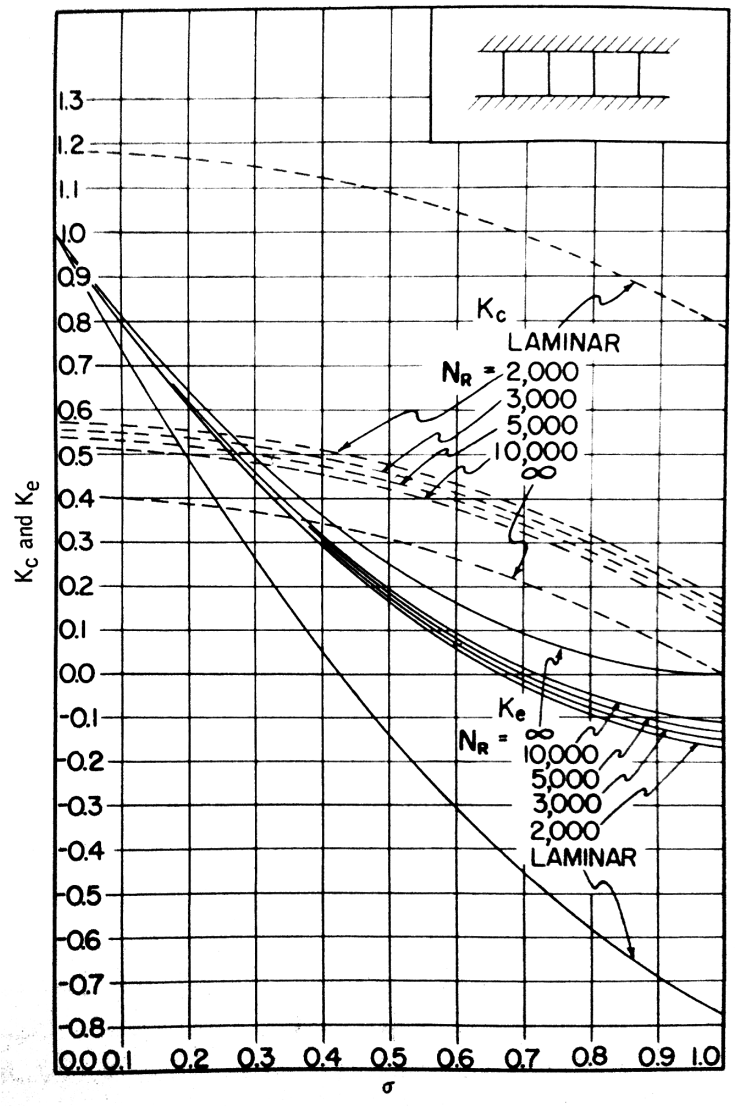

Figure 2.11: Entrance contraction, K_c, and exit expansion, K_e, loss coefficients for the Kays-London pressure drop correlation [31].
Correlations are shown in Equations 2.20, 2.21

$$\Delta P = (f_{frict} + f_{obs}) \frac{L}{D_h} \frac{1}{2} \rho \mathrm{v}^2 \tag{2.24}$$

The obstruction factor f_{obs} is only dependent on the geometry of the obstructions. Dependence on flow parameters such as Re or roughness is not needed since these are taken care of by f_{frict}. Geometrical considerations can include: channel shape, channel aspect ratio, obstruction shape, obstruction size, number of obstructions, obstruction pattern and placement as well as dis-similar surface conditions on obstructions and the channel walls. Idelchik's *Handbook of Hyrdaulic Resistance* provides experimentally determined correlations for f_{obs} for most imaginable combinations of geometrical parameters[23].

The airfoils within the channel will add a drag loss to the pressure drop. The drag of many airfoils act along the entire length of the channel, making it convenient to express the drag contribution as an obstruction factor f_{obs}. By considering the pressure drop occurring through the small volume $\frac{1}{2}p \times h \times 2s$ surrounding an individual airfoil, the obstruction factor can be related to the airfoil's drag coefficient C_d.

$$\begin{aligned} \frac{1}{2} \frac{2s}{D_h} f_{obs} \rho v^2 = \Delta P &= \frac{A_{fr}}{\frac{1}{2}ph} C_d \frac{1}{2} \rho v^2 \\ f_{obs} &= \frac{D_h A_{fr}}{sph} C_d \end{aligned} \tag{2.25}$$

Taking a common C_d=0.045 for NACA0200 airfoils and the optical scan measurements in Table 2.4, the obstruction factor in the straight airfoil channels is f_{obs}=0.0030.

Additional drag within the transition region results from the airfoil's angle of attack increasing in the turn. Drag as a function of attack-angle for the NACA0200 is known, becoming much greater at angles of attack above 10° [32]. Airfoils at the inside of the turn have a higher angle of attack than those at the periphery. An average drag coefficient within the turn, $\bar{C}_{d,turn}$, is found by integrating the attack-angle dependent drag coefficient over the

turn.

$$\bar{C}_{d,turn} = \int_{r_i}^{r_o} \int_{0}^{\pi/2} C_d \left(\frac{2s}{r}\right) r d\theta dr = 0.1215 \tag{2.26}$$

This results in an average obstruction coefficient within the turn of $\bar{f}_{obs,turn}$=0.0081. As the recuperator consists of 547.5 mm of straight airfoil channel and 179.0 mm of turning airfoil channel, a mean obstruction factor, $\bar{f}_{obs}$=0.0043, for the entire 726.5 mm length can be used.

2.5 Heat transfer in airfoil channels

2.5.1 Heat transfer correlations

Laminar and turbulent heat transfer

Convective heat transfer in fully turbulent systems is commonly expressed in terms of the Colburn factor. The Colburn factor is preferred for s-CO_2 analysis over other heat transfer coefficients as it better captures fluid property variation through its dependence on Prandtl number. The Colburn factor can be either expressed in terms of the Nusselt number Nu or related to the dimensional heat transfer coefficient h as follows,

$$\begin{aligned} j &= NuRe^{-1}Pr^{-\frac{1}{3}} \\ &= \frac{hD_h}{k}Re^{-1}Pr^{-\frac{1}{3}} \end{aligned} \tag{2.27}$$

The most common convection correlation for turbulent flow in smooth pipes and ducts is the Dittus-Boelter equation[33]. The Dittus-Boelter equation is valid for $0.6 \leq Pr \leq 160$, $Re \gtrsim 10000$, $L/D \gtrsim 10$ and is expressed as,

$$Nu = 0.023 Re^{4/5} Pr^{n} \tag{2.28}$$

$$j = 0.023 Re^{-1/5} Pr^{n-1/3} \tag{2.29}$$

where $n = 0.4$ for heating and $n = 0.3$ for cooling of the fluid.

For rough tubes the Gnielinski correlation can be used. This correlation utilizes the assumption that the thermal boundary layer behaves much like the hydraulic boundary layer and thus that j can be related to the the friction factor f[33]. This is a valid assumption for surfaces without flow impingement or significant forced mixing within the thermal boundary layer. The Gnielinski correlation is valid for $0.5 \leq Pr \leq 2000$, $3000 \leq Re \leq 1 \times 10^6$ and is expressed as,

$$Nu = \frac{\frac{f}{8}\left(Re - 1000\right) Pr}{1 + 12.7\left(\frac{f}{8}\right)^{1/2}\left(Pr^{2/3} - 1\right)} \tag{2.30}$$

$$j = \frac{\frac{f}{8}\left(1 - \frac{1000}{Re}\right) Pr^{2/3}}{1 + 12.7\left(\frac{f}{8}\right)^{1/2}\left(Pr^{2/3} - 1\right)} \tag{2.31}$$

where f is the friction factor of a rough tube determined either through the Moody Chart (fig. 2.8) or Colebrook equation 6.3.

Behavior of j in rough tubes and ducts is similar to that of f. Kays and London provide comparisons of experimentally determined j and f for rectangular ducts of various aspect ratio[31]. The rectangular aspect ratio of the airfoil channel can be considered as that formed between two laterally neighboring airfoils and is $\alpha^* = 3.74$. Experimental j from Kays and London are given for similar aspect ratios $\alpha^* = 3.0$ in Figure 2.12 and $\alpha^* = 8.0$ in Figure 2.13.

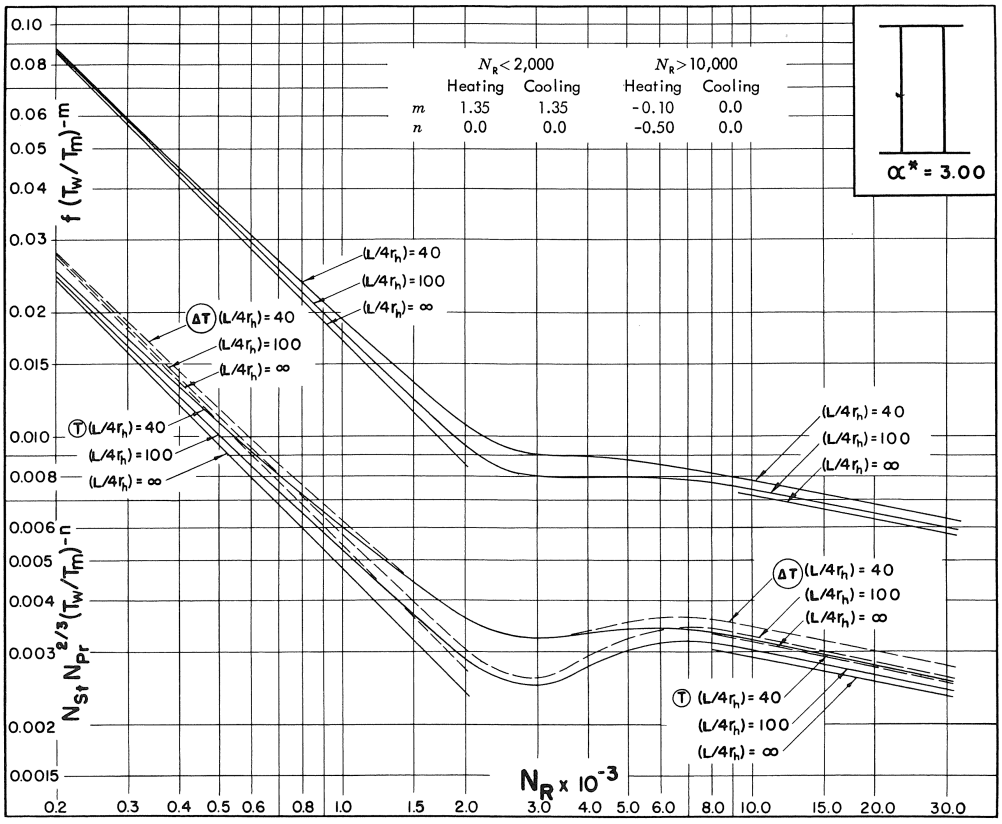

Figure 2.12: Heat transfer within rectangular channel of aspect ratio $\alpha = 3.0$[31]. *Note x-axis is Reynolds number and y-axis is Colburn heat transfer factor j for the lower grouping of lines and friciton factor f for the upper grouping.*

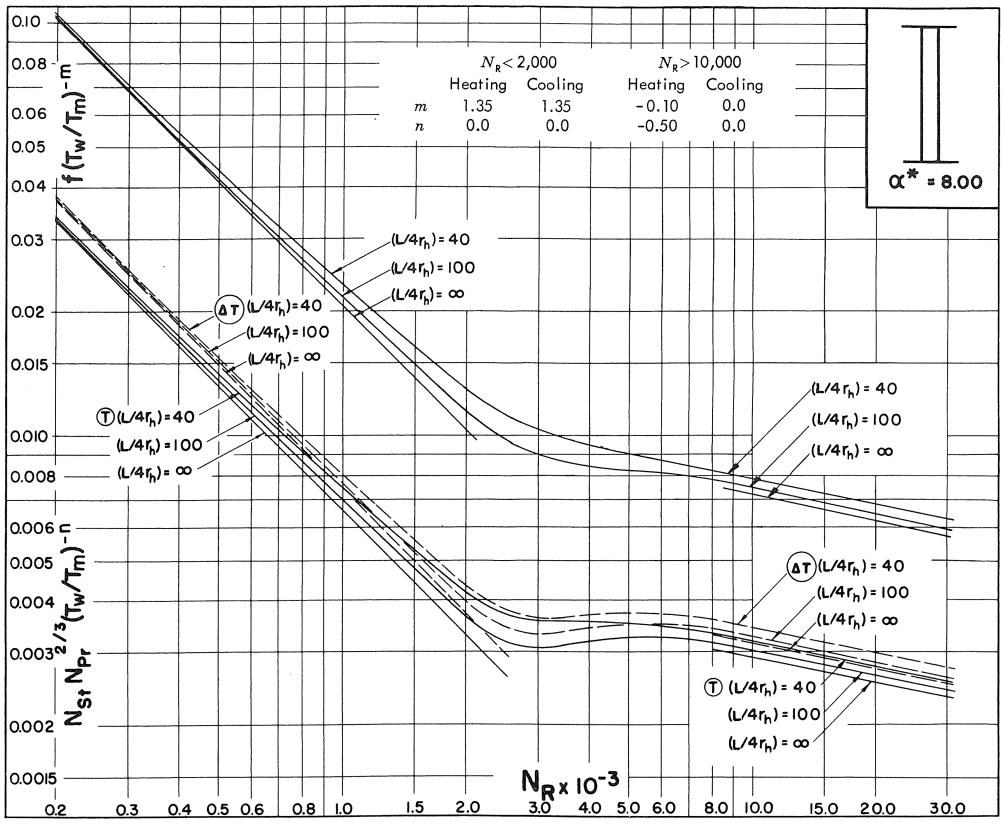

Figure 2.13: Heat transfer within rectangular channel of aspect ratio $\alpha = 8.0$[31]. *Note x-axis is Reynolds number and y-axis is Colburn heat transfer factor j for the lower grouping of lines and friciton factor f for the upper grouping.*

As duct relations, the Kays and London experimental j and f in Figures 2.12 and 2.13 should be lower than that expected in the airfoil channels. As in the Moody chart, the transition region shown in the Kays and London j relation occurs between Reynolds numbers 2000 to 4000. Within the turbulent region ($Re > 4000$) j falls along with f. This turbulent trend is characteristic of the Dittus-Boelter and other j correlations.

Heat transfer in obstructed channels

Heat transfer in the airfoil channel is enhanced by the presence of airfoil-fins within the flow. These fins enhance heat transfer by both churning the flow and by breaking and reforming fluid boundary layers. Unobstructed j correlations such as Dittus-Boelter and Gnielinski do not capture the enhanced heat transfer of the airfoil channel. Heat transfer in the airfoil channel can be compared to that of the off-set-fin channel shown in Figure 2.14.

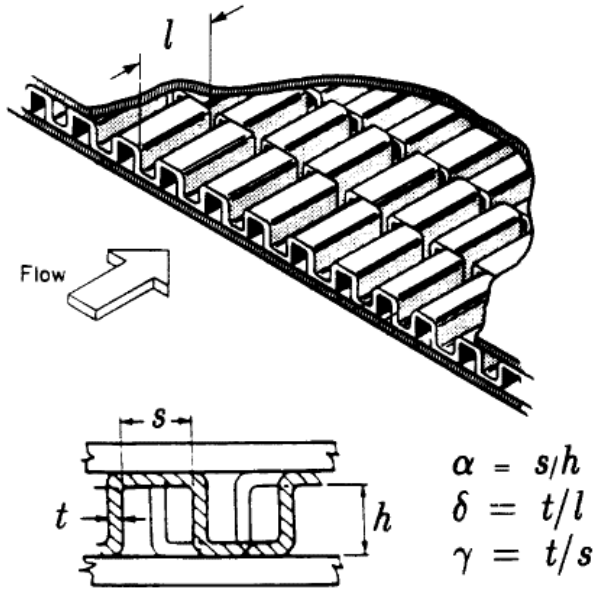

Figure 2.14: Off-set-fin channel diagram.

The airfoil-fins can be approximated as off-set-fins. Although off-set-fin channels have

more closely packed flow obstructions than the airfoil channel, flow in the off-set-fin channel is more comparable to flow in the airfoil channel than any of the other unobstructed channel relations. The off-set-fin channel experiences the same constantly breaking and recombining flow as the airfoil channel. Geometric off-set-fin parameters can be used to approximate the geometry of the airfoil-fins. Expressed as the parameters shown in Figure 2.14, the airfoil channel would have geometric parameters $h = 0.98$ mm, $l = 8.51$ mm, $s = 1.91$ mm, and $t = 1.74$ mm. Dimensionless aspect parameters would then be,

$$\begin{aligned} \alpha &= s/h &&= 1.95 \\ \delta &= t/l &&= 0.204 \\ \gamma &= t/s &&= 0.911 \end{aligned} \tag{2.32}$$

The Wieting off-set-fin correlation for heat transfer is a power law fit made to experimental data from 22 geometries. It has been a widely used correlation since its introduction in 1975 and covers both the laminar and turbulent regimes well. Although it is not good in the transition region[34].

$$j = \begin{cases} 0.483\,(l/D_h)^{-0.162}\,\alpha^{-0.184} Re^{-0.536} & Re < Re_j^* \\ 0.242\,(l/D_h)^{-0.322}\,(t/D_h)^{0.089}\,Re^{-0.368} & Re \geq Re_j^* \end{cases} \tag{2.33}$$

where the cutoff Reynolds Re_j^* is

$$Re_j^* = 61.9\,(l/D_h)^{0.95}\,\alpha^{-1.1}\,(t/D_h)^{-0.53} \tag{2.34}$$

which for the airfoil channel evaluates to $Re_j^* = 2599$.

The Manglik-Bergles off-set-fin correlation is a newer correction of the Wieting correlation. It is based on fits to 18 experimental geometries that were tested with air ($Pr = 0.7$). Accounting for more geometric parameters than the Wieting correlation the Manglik-Bergles

correlation is also relevant in deep laminar, and fully turbulent flow regions, but not in the band of transition flow from $Re^* \leq Re < 1000 + Re^*$[35].

$$j = \begin{cases} 0.6522 Re^{-0.5403} \alpha^{-0.1541} \delta^{0.1499} \gamma^{-0.0678} & Re < Re^* \\ 0.2435 Re^{-0.4063} \alpha^{-0.1037} \delta^{0.1955} \gamma^{-0.1733} & Re \geq 1000 + Re^* \end{cases} \tag{2.35}$$

where the cutoff Reynolds Re^* is 65.8

$$Re^* = 257 \left(l/s\right)^{1.23} \delta^{0.58} D_h \left[t + 1.328 \left(\frac{Re^*}{l D_h} \right)^{-0.5} \right]^{-1} \tag{2.36}$$

which for the airfoil channel evaluates to $Re^* = 493$.

Chapter 3

Thermohydraulic Modeling of PCHE

3.1 Finite Element Approach to PCHE Thermohydraulics

The FE approach used in the Homogenized Heat Exchanger Thermohydraulics (HHXT) model evaluates a homogenized thermodynamic model of the Printed Circuit Heat Exchanger (PCHE) structure. Here the internal micro-channel regions of the PCHE are homogenized within a volume of interest, V, as shown in Figure 2.7. The modeler must consider the different homogenized regions that would appear in the PCHEs e.g., two stream, single stream, and no stream (solid) regions.

Within the homogenized volume, interaction of the separate fluid streams and PCHE body is described using a system of connected non-linear PDEs. The problem can be reduced to a few degrees of freedom: the temperature of the core, the pressure of each fluid stream, and the temperature of each fluid stream. With multiple fluid streams the number of DoFs is increased.

Table 3.1: Model's system of PDEs

stream index	DoF	PDE
$\ell = 1$	T_1	Solid Conduction PDE
$\ell = 2$	P_2	Darcy Porous Media PDE
	T_2	Fluid Heat Advection PDE
$\ell = 3$	P_3	Darcy Porous Media PDE
	T_3	Fluid Heat Advection PDE
...	...	...

We adopt a stream notation, ℓ, where the first stream, $\ell = 1$, corresponds to the solid PCHE body that occupies a fraction of physical space, $\phi_1 = V_1/V$. As a solid, this first "stream" only has a temperature DoF, T_1. All further streams, $\ell = 2, 3, ...$, correspond to

different fluid channels occupying their own fraction of space $\phi_\ell = V_\ell/V$. Each fluid stream has both pressure and temperature DoFs, P_ℓ, and T_ℓ.

The system of PDEs solved in the FE model consists of three different PDEs repeated to capture any number of fluid streams, see Table 3.1. The model contains a PDE for conduction in the solid body, along with PDEs representing the hydraulics and heat transport within each fluid stream. A nonlinear Darcy porous media PDE is used for hydraulics along with another incompressible heat advection PDE for each fluid stream.

3.1.1 Solid Conduction PDE

The Solid Conduction PDE combines anisotropic conduction, heat storage, and heat loss through heat transfer to the fluid streams. Anisotropic conduction is the result of the PCHE core's perforated nature. Simple FE thermal analysis on a micro-channel core structure reveals a favored conduction direction that aligns with the micro-channel run. Heat loss to the fluids is driven by the volumetric resistance between core and fluid, $R_{V_{1,\ell}}$. This can either be constant, or dependent on a heat transfer coefficient such as the Colburn j coefficient.

$$\underbrace{\phi_1 \left(\rho c_p\right)_1 \frac{\partial T_1}{\partial t}}_{\text{heat storage}} - \underbrace{\nabla \cdot \left([\mathbf{k}]_{cond} \nabla T_1\right)}_{\text{anisotropic conduction}} + \underbrace{\sum_{\ell=2}^{L} \left(\frac{1}{R_{V_{1,\ell}}}\right) T_1 - \sum_{\ell=2}^{L} \left(\frac{1}{R_{V_{1,\ell}}} T_\ell\right)}_{\text{heat transfer to fluids}} = 0 \tag{3.1}$$

3.1.2 Darcy Porous Media PDE

The Darcy Porous Media PDE provides the hydraulic solution. Instead of modeling flow through each individual micro-channel, the core is approximated as a porous medium of many fluid streams each with a porosity of ϕ_ℓ.

Laminar flow through porous media is described by Darcy's Law which relates flux in the porous media and pressure drop using a permeability term. In isotropic media, permeability takes a constant form, k_{perm}. For orthotropic media, permeability is a diagonal matrix,

$\lceil \mathbf{k} \rfloor_{perm}$; giving the following form of Darcy's law [36],

$$\{\mathbf{v_D}\} = -\frac{1}{\mu} \lceil \mathbf{k} \rfloor_{perm} \nabla P = -\frac{1}{\mu} \lceil \mathbf{k} \rfloor_{perm} \begin{Bmatrix} P_{,x} \\ P_{,y} \\ P_{,z} \end{Bmatrix} \tag{3.2}$$

here the Darcy Flux, $\mathbf{v_D}$, is related to the fluid velocity in the channel $\mathbf{v}$ by

$$\{\mathbf{v_D}\} = \phi \{\mathbf{v}\} \tag{3.3}$$

Flow in every fluid stream is incompressible, allowing the Darcy flow in Eqn. (3.2) to be assembled into the following Darcy Porous Media PDE,

$$\underbrace{-\nabla \cdot \left(\left(\frac{\rho}{\mu} \right)_{\ell} \lceil \mathbf{k} \rfloor_{perm,\ell} \nabla P_{\ell} \right)}_{\text{nonlinear \& anisotropic porosity}} = 0 \tag{3.4}$$

A nonlinear form of the Darcy porous media equation is used where the permeability matrix is determined from a prescribed Darcy friction factor, f, and is thus a function of velocity and fluid properties. In order to model the directional flow that occurs in micro-channels, the permeability matrix is also anisotropic.

The Darcy friction factor relation can be written in 3D in terms of flux $\{\mathbf{v_D}\}$,

$$\begin{aligned} \begin{Bmatrix} |P_{,x}| \\ |P_{,y}| \\ |P_{,z}| \end{Bmatrix} &= \frac{\rho}{2D_h} \underbrace{\begin{bmatrix} f_x & & \\ & f_y & \\ & & f_z \end{bmatrix}}_{\lceil \mathbf{f} \rfloor} \underbrace{\begin{bmatrix} v_x & & \\ & v_y & \\ & & v_z \end{bmatrix}}_{\lceil \mathbf{v} \rfloor} \underbrace{\begin{Bmatrix} v_x \\ v_y \\ v_z \end{Bmatrix}}_{\{\mathbf{v}\}} \\ &= \frac{\rho}{2D_h \phi^2} \lceil \mathbf{f} \rfloor \lceil \mathbf{v_D} \rfloor \{\mathbf{v_D}\} \end{aligned} \tag{3.5}$$

where D_h is the internal hydraulic diameter of the micro-channel. This can be expressed either as the ratio of fluid volume to channel surface area, or the ratio of the homogenized volume to surface area–i.e. surface area density,

$$D_h = \frac{4V_\ell}{A_{surf,\ell}} = \frac{4\phi_\ell V}{A_{surf,\ell}} \tag{3.6}$$

If flow is laminar ($f = \frac{64}{Re}$) Eqn. (3.5) will only have one $\{\mathbf{v_D}\}$ term. Substituting this into Eqn. (3.2) results in constant permeability; thereby returning the original laminar definition of Darcy's Law.

However with turbulent flow the permeability tensor remains dependent on $\lceil \mathbf{f} \rfloor$ and $\{\mathbf{v_D}\}$. This is seen by combining Eqns. (3.2) & (3.5). The resulting permeability tensor components are expressed in terms of the Darcy friction factor and the pressure gradient.

$$\mathbf{k}_{ii_{perm}} = \sqrt{\frac{2D_h\phi^2\mu^2}{\rho}\frac{1}{|P_{,i}\,|\,\mathbf{f}_{ii}}} \tag{3.7}$$

If the friction factor isn't constant, the permeability tensor must be implicitly solved for. This is the case for most micro-channels, where f increases at lower velocity. Such variation is best captured with the flow's Reynolds number, Re. To be most practical, the PCHE model accepts input of Re dependent functional definitions of f as well as constant and laminar definitions.

3.1.3 Fluid Heat Advection PDE

The Fluid Heat Advection PDE provides the fluid thermal solution. Heat in the fluid streams is stored, advected with flow, and transferred to the solid core. Velocity dependence of the heat transfer and advection terms is treated non-linearly using the stream's Darcy flux as computed from the previous P solution,

$$\{\mathbf{v_D}\}_\ell = -\frac{1}{\mu_\ell}\left[\mathbf{k}\right]_{perm,\ell}\nabla P_\ell \tag{3.8}$$

This results in a PDE who's FE formulation must be iterated at each solution step until a sufficiently low residual is achieved,

$$\underbrace{\phi_\ell\left(\rho c_p\right)_\ell\frac{\partial T_\ell}{\partial t}}_{\text{heat storage}} - \underbrace{\nabla\cdot\left(\left[\mathbf{k}\right]_{cond,\ell}\nabla T_\ell\right)}_{\text{conduction}} - \underbrace{\left(\rho c_p\right)_\ell\left\{\mathbf{v_D}\right\}_\ell\cdot\nabla T_\ell}_{\text{nonlinear heat advection}} - \underbrace{\tfrac{1}{R_{V_1,\ell}}T_1 + \tfrac{1}{R_{V_1,\ell}}T_\ell}_{\text{heat transfer to solid body}} = 0 \tag{3.9}$$

Table 3.2: PCHE Model Inputs & Allowed Dependencies

PCHE Body Properties, $\ell = 1$	**units**	**spatial dependence**†	**state dependence**†
volume fraction, ϕ_1	$[-]$	region, position	
thermal conductivity‡, $[\mathbf{k}]_{cond}$	$\left[\frac{W}{m-K}\right]$	region, position, time	temperature
density, ρ_1	$\left[\frac{kg}{m^3}\right]$	region, position, time	temperature
specific heat, c_{p_1}	$\left[\frac{J}{kg-K}\right]$	region, position, time	temperature
Fluid Properties, $\ell = 2, 3, ...$	**units**	**spatial dependence**†	**state dependence**†
volume fraction, ϕ_ℓ	$[-]$	region, position	
hydraulic diameter, D_{h_ℓ}	$[m]$	region, position	
thermal conductivity‡, $[\mathbf{k}]_{cond,\ell}$	$\left[\frac{W}{m-K}\right]$	region, position, time	temperature, pressure
density, ρ_ℓ	$\left[\frac{kg}{m^3}\right]$	region, position, time	temperature, pressure
specific heat, $c_{p\ell}$	$\left[\frac{J}{kg-K}\right]$	region, position, time	temperature, pressure
viscosity, μ_ℓ	$\left[\frac{kg}{m-s}\right]$	region, position, time	temperature, pressure
Darcy friction factor‡, $\lceil \mathbf{f} \rfloor_\ell$	$[-]$	region, position, time	Reynolds number
· OR permeability‡, $[\mathbf{k}]_{perm,\ell}$	$[m^2]$	region, position, time	temperature, pressure
Colburn heat transfer coefficient, $j_{1,\ell}$	$[-]$	region, position, time	Reynolds number
· OR local heat transfer coefficient, $h_{1,\ell}$	$\left[\frac{W}{m^2-K}\right]$	region, position, time	temperature, pressure
· OR Nusselt number, $Nu_{1,\ell}$	$[-]$	region, position, time	Reynolds number, Prandtl number
· OR volumetric thermal resistance, $R_{V_{1,\ell}}$	$\left[\frac{K-m^3}{W}\right]$	region, position, time	temperature, pressure

† dependencies must be interpreted as having SI units.
‡ can be input as tensors or constants.

3.1.4 Heat Transfer Specification

The volumetric resistance between the fluid stream and solid core, $R_{V_{1,\ell}}$, can either be set as a constant or derived from a heat transfer coefficient. The dimensional heat transfer coefficient, h, is the easiest to use and allows the volumetric resistance to be written in terms of the micro-channel hydraulic diameter given in Eqn. (3.6),

$$R_{V_{1,\ell}} = \frac{1}{h_\ell A_{surf,\ell}} * V = \frac{1}{4}\left(\frac{D_h}{\phi h}\right)_\ell \tag{3.10}$$

For heat exchanger problems where fluid velocity and fluid properties are changing, dimensionless heat transfer coefficients such as the Colburn heat transfer coefficient, j, or the Nusselt number, Nu, are more useful than the dimensional h.

$$j = \frac{h}{\rho c_p \left|\mathbf{v}\right|} Pr^{\frac{2}{3}} = \frac{h\phi}{\rho c_p \left|\mathbf{v_D}\right|} Pr^{\frac{2}{3}} \tag{3.11}$$

$$Nu = \frac{hD_h}{k} \tag{3.12}$$

Combining Eqn. (3.10) with Eqns (4.8) & (3.12), gives the volumetric thermal resistance between stream ℓ and the PCHE body,

$$R_{V_{1,\ell}} = \tfrac{1}{4}\left(\frac{D_h Pr^{\frac{2}{3}}}{j\rho c_p}\right)_\ell \frac{1}{\left|\mathbf{v_D}\right|_\ell} \tag{3.13}$$

$$R_{V_{1,\ell}} = \tfrac{1}{4}\left(\frac{D_h^2}{\phi k Nu}\right)_\ell \tag{3.14}$$

3.1.5 FE Implementation & Stabilization

The PDEs are assembled using a mix of Galerkin and Streamline Upwind Petrov Galerkin (SUPG) methods, then integrated element-wise using Gaussian Quadrature. The Crank-Nicholson method is used for time integration. Currently only 2D triangular and 3D tetrahedral meshes of linear or quadratic order are supported. Standard Garlekin formulation is used for the Solid Conduction and Darcy Porous Media PDE's, Eqns. (3.1,3.4). The Galerkin formulation cannot be used on the Fluid Heat Advection PDE, Eqn. (3.9), as the heat advection term contains first order temperature dependencies which introduce instability. Evaluating this PDE using an advective method, i.e the SUPG method, elliminates the instability but introduces some additional complexity.

The SUPG method adds a correction by perturbing elemental approximating functions in the upwind direction of the streamline. The correction is implemented element wise, and depends on the advective term from Eqn. (3.9) and a stabilization parameter τ. Many examples of the SUPG method's use in mass transport problems exist. For interested readers, a paper by Cui[37] provides an example of the numerical implementation while a book by Donea[38] details the theory of common stabilization techniques.

When used in mass transport problems the advective term is simply the velocity, but in the PCHE model it becomes a heat advection term,

$$\{\mathbf{b}\}_\ell = (\rho c_p)_\ell \{\mathbf{v_D}\}_\ell \tag{3.15}$$

Choice of the stabilization parameter, τ, influences the quality of the solution and has been subject to extensive research within the FE community e.g., the review [39]. A general "optimal" definition of τ does not exist, resulting in multiple differing and valid interpretations of τ to be used.

Formulation of τ in the PCHE FE model follows the methodology outlined by Knobloch

[40], which involves extending a common 1D formulation into 2D and 3D elements. Here the stabilization parameter is calculated from streamlines of length, s, and Peclet number, Pe, that exist within each element of the mesh.

$$\tau = \frac{s}{2\,|\mathbf{b}|}\left(coth(Pe) - \frac{1}{Pe}\right) \text{ with } Pe = \frac{|\mathbf{b}|\,s}{2\alpha} \tag{3.16}$$

where α is the thermal diffusivity of the fluid in the streamline direction. Since fluid conductivity can be orthotropic in the PCHE model, the diffusivity along s accounts for the directionality of $\mathbf{b}$,

$$\alpha = \frac{1}{\rho c_p}\left|[\mathbf{k}]_{cond,\ell}\,\frac{\{\mathbf{b}\}}{|\mathbf{b}|}\right| \tag{3.17}$$

3.1.6 Model Input

The PCHE model is implemented in MATLAB® and integrated into its existing Partial Differential Equation Toolbox. MATLAB® PDE tools are used in model preparation and post processing. Geometry input, meshing, setting initial and boundary condition definitions, and material property inputs are all familiar to the experienced MATLAB® user. Likewise postprocessing operations such as mesh based plotting, solution interpolation, and the formatting of solution result files are similar to other MATLAB® PDE models.

The definition of PCHE properties is not limited to simple cases. All fluid and solid body properties can be position, time, temperature and pressure dependent. A list of all manipulatable material properties and their allowed dependencies are given in Table 3.2. This allows modeling of variable property problems e.g., a s-CO_2 recuperator operating near the critical point. This also presents a way for the user to input external property routines, such as NIST real gas properties, into their heat exchanger model. Finally, there are also no geometric limitations on the PCHE model. Geometries can be 2D or 3D, can contain any

number of regions, and can include non-rectilinear features.

Hydraulic and heatransfer properties of the PCHE core channels are directly input into the model. The PCHE model accepts input of the either a porous media permeability or the Darcy friction factor for hydraulics, and a choice between the Colburn, local dimensional, or Nusselt heat transfer coefficient. These can be position, time, and Reynolds number dependent.

3.2 Modeling an Experimental Airfoil Micro-channel PCHE

Experimental investigations into PCHE performance have been made as a means of validating the HHXT model[16]. A scaled airfoil micro-channel CO_2-CO_2 recuperative PCHE was made for this purpose. The airfoil PCHE features novel embedded fiber-optic temperature sensors, enabling experimental internal temperatures to be mapped and compared to the modeling effort.

3.2.1 Model Definition

The airfoil PCHE consists of 5 cold CO_2, 4 hot CO_2, and 1 instrumented 1.5 mm thick plates. The CO_2 plates contain a 1 mm deep etched, 94.3 mm wide, airfoil channel, containing 8.1 mm long NACA0020 airfoils spaced at 3.65 mm intervals across the flow and 6.9 mm along the flow direction. The channel pattern for the cold CO_2 is depicted in Figure 5.4. The hot side channel is simply the mirror image of this about the vertical.

CO_2 flows through the cold and hot streams as shown in Figure 3.1. Within the transition region, and in parts of the entrance and exit regions, the airfoil channels curve, directing flow from the side mounted inlets and outlets to the horizontally oriented counter-flow core.

As the Airfoil PHCE is constructed out of 316 Stainless Steel, model solid properties are taken as the following constants: $k = 17.6[W/m\text{-}K]$, $\rho = 8030[kg/m^3]$, and $c_p = 533[J/kg\text{-}$

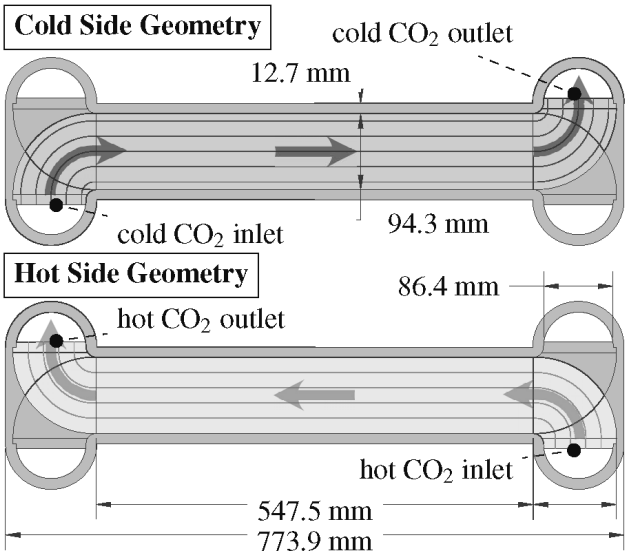

Figure 3.1: Flow configuration of the Airfoil PCHE model

K].

flow and heat transfer

To match the experimental conditions, the two fluid streams are modeled as CO_2 at 6 MPa. Temperature dependent functions for k, ρ, c_p, and μ were input into the PCHE model. Property values were pre-determined for the isobar over a 22-250 C temperature range as shown in Figure 3.2. The Span-Wagner equation of state for CO_2 was used to calculate ρ and c_p[41], Vesovic's method was used in determining k[42], and a correlation proposed by Fenghour defined μ[43].

The Airfoil micro-channels were evaluated in a separate experimental study from which the comparative case was also taken[16]. Optical scans of the etched airfoil plates found a D_h of 1.498 mm. Once bonded, the plates formed a PCHE core with a ϕ of 0.264 on the cold side and 0.211 on the hot side. An average Colburn heat transfer coefficient of j=0.003911 was determined from a 1D analysis of the recuperator's experimental performance. For flows

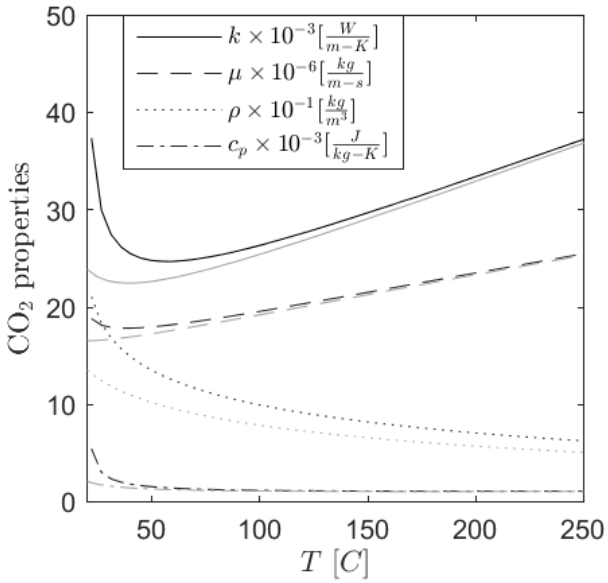

Figure 3.2: CO_2 properties along 4.9 & 6 MPa isobar (gray and black lines).

of $Re > 2000$ the channels were found to have a friction factor fitting the following modified Colebrook equation[16],

$$\frac{1}{\sqrt{f}} = -2.0log_{10}\left(80.68e-3+\frac{43.1}{Re\sqrt{f}}\right) \tag{3.18}$$

The friction factor could only be determined in the flow direction. Crossflow can occur in airfoil micro-channels but couldn't be experimentally measured. As a result the Airfoil PCHE model assumes a relatively large, although not infinite, resistance to flow across the stream. A cross-flow f could be obtained through a purpose designed experiment or a CFD study, results of which did not exist at the time the Airfoil PCHE model was made. Thus the cross-flow was arbitrarily defined as having an f of 10 in the y direction of the micro-channel core. Thus the directional friction factor tensor used in the model is,

$$\lceil \mathbf{f} \rfloor_x = \lceil f(Re), 10 \rfloor \tag{3.19}$$

orthotropic channels

The core of the airfoil PCHE favors both flow and conduction along the axis of the recuperator (x direction in all Figures). Heat can be conducted in all directions within the airfoil core, but the stacked nature of the etched plates greatly favors conduction in the x and y while limiting it in z. Heat can be conducted within the CO_2, but can only do so in x and y, as z lies perpendicular to the plane of fluid flow within the channel plates. Conduction in the cold and hot CO_2 also differs as there is slightly more cold fluid, with 5 plates of cold channels and 4 plates of hot.

When homogenized, the conductivity of the Airfoil PCHE core becomes orthotropic. This was determined through a separate FE study on the conductivity of the airfoil micro-channel structure and fluid passages. When compared to a fully solid conducting volume, a reduction in conductivity through the structure and through the fluid channels is observed, resulting in the following relations for the orthotropic conductivities,

$$\begin{aligned} [\mathbf{k}]_s &= k_{316} \lceil 0.482, 0.413 \rfloor \\ [\mathbf{k}]_c &= \tfrac{5}{9} k_{CO_2} \lceil 0.476, 0.170 \rfloor \\ [\mathbf{k}]_h &= \tfrac{4}{9} k_{CO_2} \lceil 0.476, 0.170 \rfloor \end{aligned} \tag{3.20}$$

The directional friction factor and orthotropic conductivity given in Eqns. (3.19) and (3.20) apply to the Airfoil PCHE's core (region I in Figure 3.3). Entrance, transition, and exit regions (regions III-XII) of the PCHE contain airfoil channels which gradually turn 90 degrees. The extent of the airfoil channel's turn is evaluated using transform matrices,$[\Lambda]$, which apply a rotation about one of four centers (magenta points Λ_{1-4} in Figure 3.3).

The volume fraction, conductivity, and directional friction factor, are defined for each region within the model. The values and transformations used at each region are given in

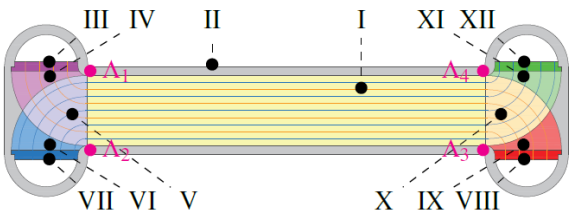

Figure 3.3: Regions of varying micro-channel geometry within the Airfoil PCHE model

Table 4.2. As the FE model accepts region and position variable inputs, the turning nature of the airfoil PCHE micro-channels can be captured.

Table 3.3: Definition of Airfoil PCHE Model by Region, see Figure 3.3

model	**solid body,** $\ell = 1$		**cold** CO_2**,** $\ell = 2$			**hot** CO_2**,** $\ell = 3$		
re-	ϕ	$[\mathbf{k}]_{cond}$	ϕ	$[\mathbf{k}]_{cond}$	$\lceil \mathbf{f} \rfloor$	ϕ	$[\mathbf{k}]_{cond}$	$\lceil \mathbf{f} \rfloor$
gion	0.525	$[\mathbf{k}]_s$	0.264	$[\mathbf{k}]_c$	$\lceil \mathbf{f} \rfloor_x$	0.211	$[\mathbf{k}]_h$	$\lceil \mathbf{f} \rfloor_x$
II	1.000	$k \lceil \mathbf{I} \rfloor$						
III	0.789	$\frac{4}{9} [\Lambda]_{90} [\mathbf{k}]_s + \frac{5}{9} k \lceil \mathbf{I} \rfloor$				0.211	$[\Lambda]_{90} [\mathbf{k}]_h$	$[\Lambda]_{90} \lceil \mathbf{f} \rfloor_x$
IV	0.789	$\frac{4}{9} [\Lambda]_1 [\mathbf{k}]_s + \frac{5}{9} k \lceil \mathbf{I} \rfloor$				0.211	$[\Lambda]_1 [\mathbf{k}]_h$	$[\Lambda]_1 \lceil \mathbf{f} \rfloor_x$
V	0.525	$\frac{4}{9} [\Lambda]_1 [\mathbf{k}]_s + \frac{5}{9} [\Lambda]_2 [\mathbf{k}]_s$	0.264	$[\Lambda]_2 [\mathbf{k}]_c$	$[\Lambda]_2 \lceil \mathbf{f} \rfloor_x$	0.211	$[\Lambda]_1 [\mathbf{k}]_h$	$[\Lambda]_1 \lceil \mathbf{f} \rfloor_x$
VI	0.736	$\frac{5}{9} [\Lambda]_2 [\mathbf{k}]_s + \frac{4}{9} k \lceil \mathbf{I} \rfloor$	0.264	$[\Lambda]_2 [\mathbf{k}]_c$	$\lceil \mathbf{f} \rfloor = [\Lambda]_2 \lceil \mathbf{f} \rfloor_x$			
VII	0.736	$\frac{5}{9} [\Lambda]_{90} [\mathbf{k}]_s + \frac{4}{9} k \lceil \mathbf{I} \rfloor$	0.264	$[\Lambda]_{90} [\mathbf{k}]_c$	$\lceil \mathbf{f} \rfloor = [\Lambda]_{90} \lceil \mathbf{f} \rfloor_x$			
VIII	0.789	$\frac{4}{9} [\Lambda]_{90} [\mathbf{k}]_s + \frac{5}{9} k \lceil \mathbf{I} \rfloor$				0.211	$[\Lambda]_{90} [\mathbf{k}]_h$	$[\Lambda]_{90} \lceil \mathbf{f} \rfloor_x$
IX	0.789	$\frac{4}{9} [\Lambda]_3 [\mathbf{k}]_s + \frac{5}{9} k \lceil \mathbf{I} \rfloor$				0.211	$[\Lambda]_3 [\mathbf{k}]_h$	$[\Lambda]_3 \lceil \mathbf{f} \rfloor_x$
X	0.525	$\frac{4}{9} [\Lambda]_3 [\mathbf{k}]_s + \frac{5}{9} [\Lambda]_4 [\mathbf{k}]_s$	0.264	$[\Lambda]_4 [\mathbf{k}]_c$	$[\Lambda]_4 \lceil \mathbf{f} \rfloor_x$	0.211	$[\Lambda]_3 [\mathbf{k}]_h$	$[\Lambda]_3 \lceil \mathbf{f} \rfloor_x$
XI	0.736	$\frac{5}{9} [\Lambda]_4 [\mathbf{k}]_s + \frac{4}{9} k \lceil \mathbf{I} \rfloor$	0.264	$[\Lambda]_4 [\mathbf{k}]_c$	$[\Lambda]_4 \lceil \mathbf{f} \rfloor_x$			
XII	0.736	$\frac{5}{9} [\Lambda]_{90} [\mathbf{k}]_s + \frac{4}{9} k \lceil \mathbf{I} \rfloor$	0.264	$[\Lambda]_{90} [\mathbf{k}]_c$	$[\Lambda]_{90} \lceil \mathbf{f} \rfloor_x$			

† transformation matrices $[\Lambda]_1$, $[\Lambda]_2$, $[\Lambda]_3$, and $[\Lambda]_4$ are rotations of angle equal to that formed between the evaluated position and the vertical from the centers shown in Figure 3.3. Transform $[\Lambda]_{90}$ is a 90 degree rotation.

Table 3.4: Conditions of experimental low mass flow case

	cold CO_2 side	**hot CO_2 side**
P_{inlet}	5.990 $[MPa]$	4.892 $[MPa]$
ΔP	4.087 $[kPa]$	7.250 $[kPa]$
T_{inlet}	22.5 $[C]$	202.3 $[C]$
T_{outlet}	144.0 $[C]$	39.1 $[C]$
$\dot{m}$	0.05378 $[kg/s]$	0.05378 $[kg/s]$

operating conditions

In experiment, the airfoil PCHE was designed to operate at CO_2 mass flows of 0.08-0.10 $[kg/s]$, achieving a design effectiveness of 91-93.7%. However when operated at a lower mass flow of 0.05378 $[kg/s]$ the airfoil PCHE effectiveness decreased to 88.9%. At this lower mass flow the PCHE is over-sized, and heat transfer becomes unbalanced, with the heat being transferred being shifted toward one end of the PCHE and the CO_2 streams starting to pinch at the outlet. Furthermore turning cross-flow within the transition betweent the inlets and the core (regions V & X) shift heat transfer off-axis toward the hot inlet (bottom of the model). The resulting PCHE temperature distribution at steady state was observed in experiment using a novel method of distributing fiber optic temperature probes within the PCHE[16].

The fiber optic measurements offer a point of comparison for the FE model. While multiple steady state PCHE temperature distributions were measured, the low mass flow case is chosen for modeling as its 2D temperature distributions are more non-linear and difficult to capture in a model. Experimental conditions for the low mass flow case are summarized in Table 3.4. The inlet pressures and temperatures were applied as Dirichlet boundary conditions at the inlets of the FE model. Massflow was fixed at the inlet and outlets using Neumann boundary conditions.

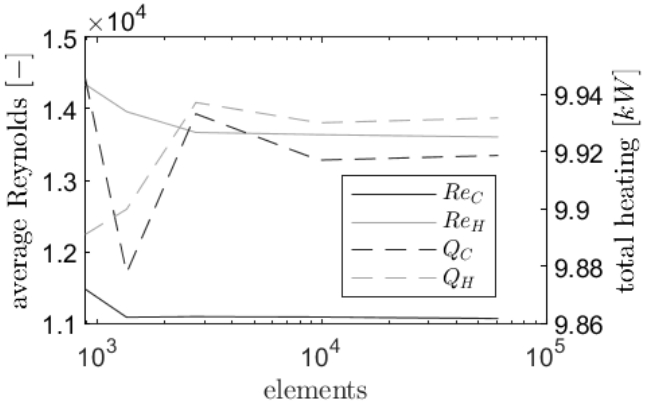

Figure 3.4: Mesh convergence study

3.2.2 Steady State Solution

The FE problem was assembled on a 2750 element, 1520 node, mesh. The mesh is shown, along with the PCHE body temperature, in Figure 3.5. Mesh convergence was studied by examining the total heat transferred and the average Reynolds number in the cold and hot streams for various mesh resolutions. This is shown for 884, 1352, 2750, 9722, and 61158 element meshes in Figure 3.4. Results from the 2750 element mesh are shown in this paper as the solution is sufficiently converged without being so over meshed as to make printed figures such as Figures 3.6 & 3.5 illegible.

Solution of the steady state proceeds in an iterative fashion with non-linear components of the FE model reassembled at each iteration. Non-linearity results from variable CO_2 properties, velocity, and heat transfer terms. Convergence to a residual $< 1 \times 10^{-6}$ is reached within 8 iterations, using 209 seconds of CPU time. Faster solution times are expected in future implementations, as the FE model is in the design phase and can benefit from the streamlining and pre-compilation of large portions of the toolbox.

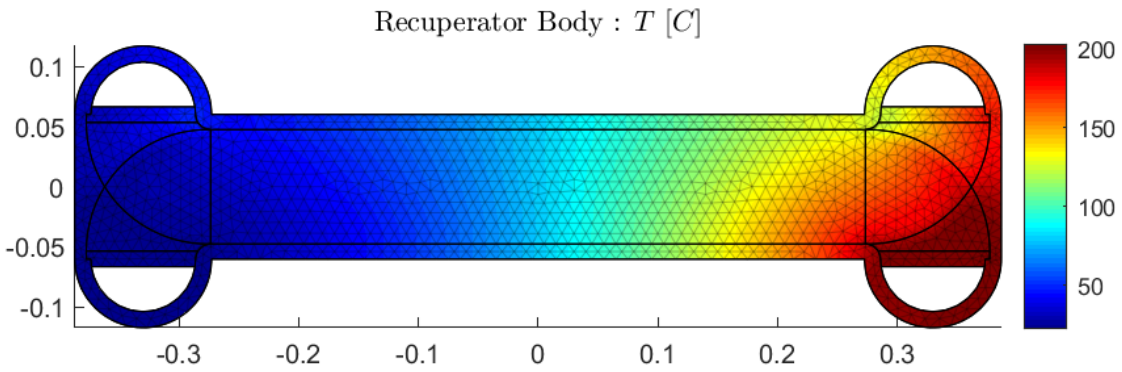

Figure 3.5: Temperature of the solid body and mesh used in the Airfoil PCHE model

comparison to experimental conditions

Results from the homogenized model compare reasonably with experiment. Experimentally only the inlet and outlet conditions, mass flow, and heat transfer are well known. The model operates using f and j values that were backed out from a one dimensional simplification of the recuperator[16]. As a result some play in the actual values of f and j is expected. A comparison of the model results and experiment is given in Table 3.5.

Table 3.5: Results of model compared to experiment

	experiment		**model**
$T_{C,out}$ $[C]$	143.96	$\pm$ 0.95	147.92
$T_{H,out}$ $[C]$	39.05	$\pm$ 0.29	40.58
Re_C	11340	$\pm$ 230	11060
Re_H	13780	$\pm$ 330	13610
$\dot{m}_C$ $[kg/s]$	0.0538	$\pm$ 0.0006	0.0544
$\dot{m}_H$ $[kg/s]$	0.0538	$\pm$ 0.0006	0.0550
Q_C $[kW]$	9.60	$\pm$ 0.33	9.94
Q_H $[kW]$	-10.01	$\pm$ 0.11	-9.95
ΔP_C $[Pa]$	4090	$\pm$ 920	3000
ΔP_H $[Pa]$	7250	$\pm$ 230	8150

Model results for the average Reynolds number, mass flow, and total heat transfer fall

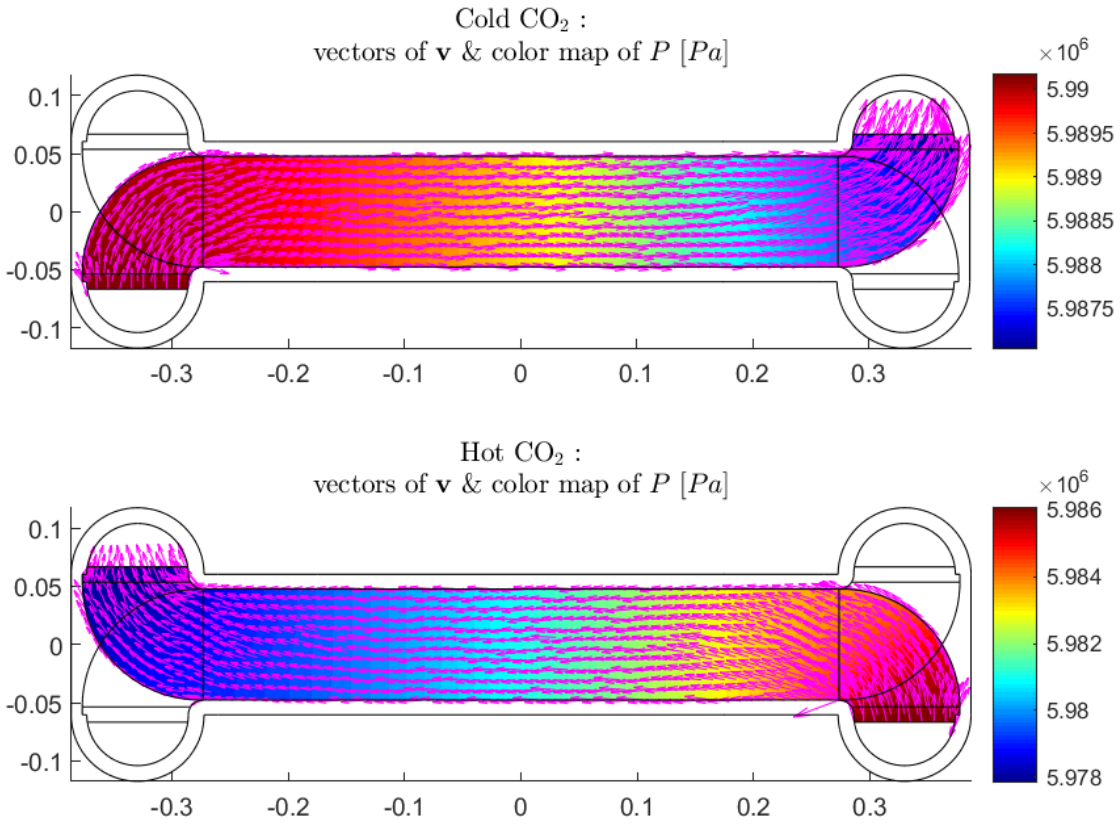

Figure 3.6: CO_2 flow solution for the cold side of the Airfoil PCHE model

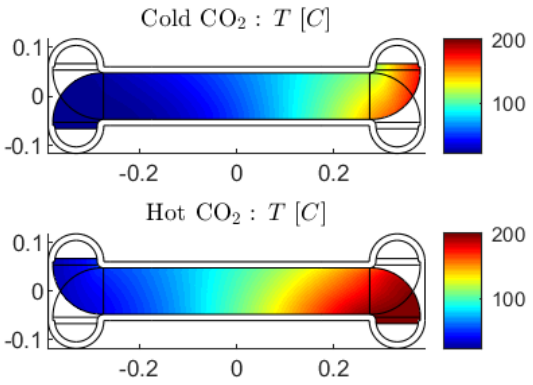

(a) CO_2 Stream temperatures

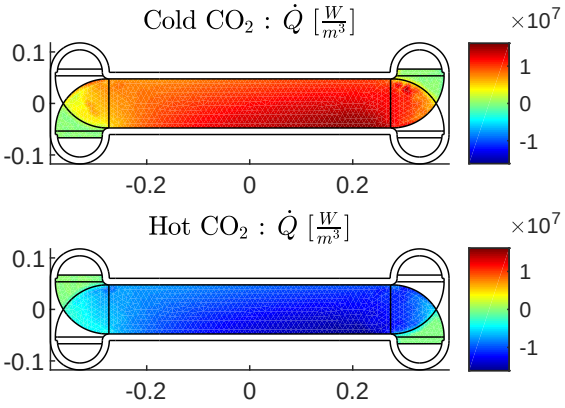

(b) Thermal results for the Airfoil PCHE model

Figure 3.7: Thermal results for the Airfoil PCHE model

within, or just on the edge of, experimental values and their uncertainties. Outlet temperatures and pressure drops are close to experimental values, but slightly outside of measured experimental uncertainty. The differences are attributed to a few experimental unknowns with require investigation, and that are discussed at the end of Sec. 3.2.2.

flow and stream heat transfer

The hydraulic solution is shown for both the cold CO_2 and hot CO_2 sides in Figure 3.6. Here the stream pressure is shown as a colormap and vectors of the resulting velocity are superimposed. Turning of the flow through the entry, exit, and transition regions can be seen. There is also a degree of flow acceleration at the inside of the turns, as the airfoil channel allows cross flow, and hence redistribution, to occur.

Temperatures within the CO_2 streams are shown in Figure 3.7a. The stream temperatures are well separated at the hot side of the PCHE, but after transferring heat gradually approach each other within the PCHE core. The hot and cold stream start to pinch within region V, this can be seen in their similar temperature at left in Figure 3.7a and the near zero

heat transfer at left in Figure 3.7b. This is the behavior expected in a lower mass flow case. There is also temperature variation across the channel as some streamlines spend longer runs within the transition regions (regions V and X).

The fluid temperatures do not change much within the entrance and exit regions (regions III, IV, VI, VII, VIII, IX, XI, and XII). This is due to the single channeled nature of these regions, where heat transfer is only between one stream and the solid body. To heat or cool the fluid in these entrance and exit regions, heat must first be conducted through the solid body from further away. The lack of much heat transfer in the entrance and exit regions is apparent when the volumetric heating of the streams is examined.

The distribution of heating and cooling within the CO_2 streams is shown in Figure 3.7b. Here red in the colormap indicates heating, blue cooling, and green no heating or cooling. It is apparent that the cold CO_2 is only heated and the hot CO_2 only cooled. Furthermore no heating occurs in the hot entrance or cold exit region. An axial shift of more heat transfer occurring near the hot inlet side of the recuperator is apparent. Hot fluid entering the PCHE at the bottom-right must turn into the heat exchanger core. Streamlines at the bottom (-y) of the core spend less time in the transition (region X) and thus enter the core hotter, shifting heat transfer to the bottom of the core.

body temperature

The solution for the PCHE solid body temperature, T_1, is shown along with the mesh in Figure 3.5. Since the model is of a lower mass flow case, the more temperature change occurs at the hot end of the PCHE (right side). Heat transfer starts in the transition region (region X) as the hot CO_2 first encounters the cold stream. The density of heat being transferred increases as the hot stream turns into the PCHE core (boundary between region I & X). Here at the right side of the core, the heat transfer peaks, as can be seen in Figure 3.7b. As the hot CO_2 continues to flow from right-to-left through the core, the streams reach a

pinched condition and heat transfer is gradually reduced.

Thermal gradients within the PCHE solid body are greatest where heat transfer changes from single stream-to-body to two stream-through-body. Even in this lower mass flow case, the high heat transfer coefficient and large surface area density of the airfoil micro-channels create heating of the solid body that dominates any diffusion of temperature through the core structure. Structure temperature largely follows the temperature of the fluid it is interacting with. Thus the body temperature within the hot CO_2 entrance region follows the temperature of the hot inlet. When the hot entrance abruptly enters the transition region, the core body equilibrates to a temperature between the hot and cold streams.

The airfoil test recuperator was constructed to exacerbate these thermal gradients between entrance and transition region. In designing a service PCHE these regions would be reduced as much as possible, although it would be impossible to eliminate them entirely.

comparison to fiberoptic data

Comparison of the model's body temperature to that measured with embedded fiberoptic temperature probes proves the model's accuracy. Figure 3.8 plots model recuperator body temperatures along the position of the eight fiberoptic temperature probes with the fiber's experimental reading. The eight comparisons are staggered by 100 C to aid in visualization. It should be noted that the dips in measured temperature at the end of the PCHE (right side of plot) are due to local cooling action of protruding capillaries used to house the fibers. These dips in temperature only exist within the fiber sensors and not within the PCHE itself.

A position-by-position comparison between the measured fiber temperatures and corresponding model temperatures are shown in Figure 3.9. The linearity of the comparison is noteworthy and most values fall within a ±20% error band. Only two lines (blue and grey) fall within the larger ±30% error band. These lines correspond to the bottom most and top most lines in Figure 3.8, which are for fibers embedded within at the edges of the recuperator

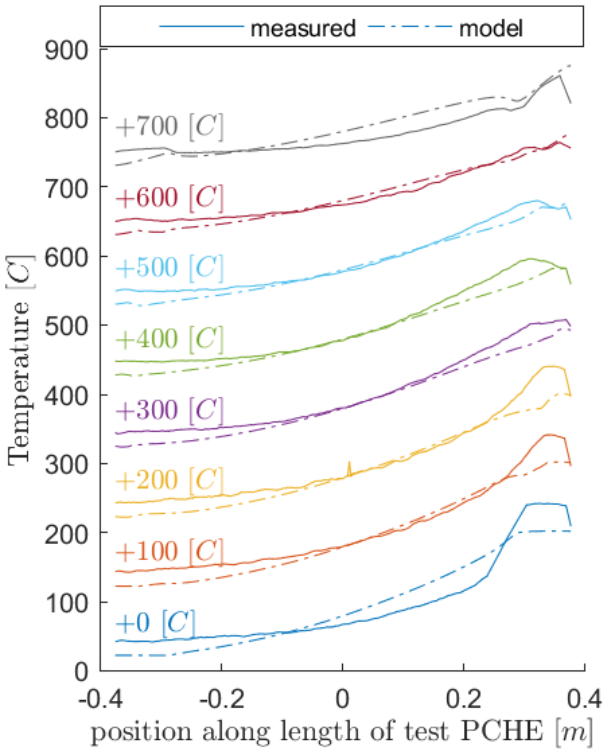

Figure 3.8: Comparison of model and measurement along the 8 instrumentation fibers

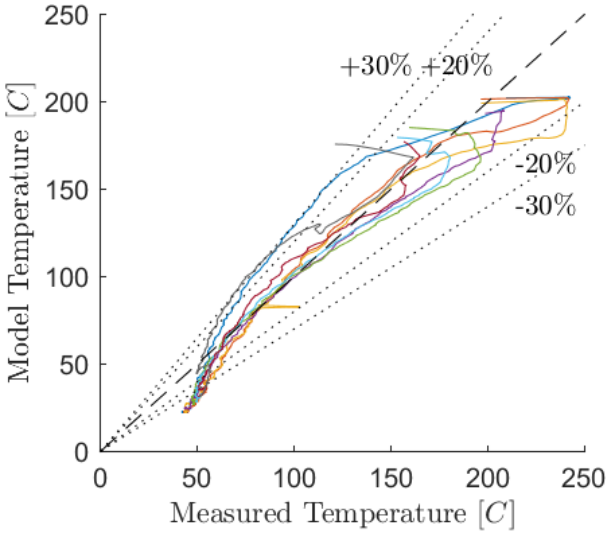

Figure 3.9: Model predicted temperatures fall within ±20% of measured values

(along the interface between regions I and II). Heat loss through insulation and attachments at these sides are contributing factors at these locations.

A better match between the model and experiment requires a few experimental unknowns to be investigated and incorporated into the model.

1. The cross flow friction factor (f_y) in Eqn. 3.19 needs to be properly evaluated. This could be achieved with either a CFD simulation or purpose designed experiment looking at flow in the turning transition (regions V, VI, X & XI).

2. Heat loss through insulation and nozzle connections needs to be measured and implemented as boundary conditions within the model. Insulation heat loss was not quantified during the experiment. Furthermore the extent that heat was transferred to or from external attachments such as nozzles and mounting brackets needs investigation.

3. An expansion of f and j testing. This should both increase the range of Re tested for the j data and attempt to account for channel turning and cross-flow effects in the calculation of f and j .

4. The thermal resistance between embedded fiber-optic instrumentation and the recuperator block needs to be quantified. In this analysis the fiber temperature sensors were assumed to directly measure the solid PCHE temperature.

Chapter 4

Experimental Validation of Thermodynamic Model

4.1 Experimental Measurements

4.1.1 Measurements

Each steady state data point is taken as a 2 minute average of data taken at 0.5 Hz. Variation of measurements over this period is included in the reported uncertainty.

mass flow rate

The mass flow rate through the both the hot and cold streams is the same and was measured using a Coriolis flow meter. The flow meter was positioned down stream of the hot outlet in order to maintain its cooler allowed operational temperature. A Siemens Sitrans F 2000 with a 6 mm tube diameter was used. The meter is factory calibrated for a measurement range of 0-0.278 kg/s

inlet and outlet fluid conditions

Static pressure is measured from taps installed at each inlet and outlet header. Separate absolute pressure transducers were used to measure the hot and cold inlet pressure. Differential pressure transducers were used to measure the pressure drop across the hot and cold streams, but could only measure up to 480 kPa. Above that, an absolute pressure transducer measured the outlet in order to calculate pressure drop.

Fluid bulk temperatures were measured within the inlets and outlets of both streams. Thermocouples were inserted down the center of the nozzles attached to the inlet and outlet headers. Positioning of thermocouples within the nozzles, as opposed to within the static

plenum of the headers, gives a measurement of the CO_2 in a well mixed state. Each thermocouple was calibrated within a cell against a NIST ITS-90 standard platinum resistance detector over a range of 18 to 900 °C.

fiber-optic temperature probe

The zig-zag recuperator was designed to demonstrate a novel method of measuring the thermal gradients within a Printed Circuit Heat Exchanger (PCHE). A fiber optic temperature probe is built into the central instrumentation plate shown in Figure 2.4, allowing temperature readings to be made along the length of the recuperator. A fiber is passed up and down the length of the recuperator through 8 passes. Passes are spaced 15.1 mm apart across the width of the instrumented plate. Temperature measurements are made every 0.6125 mm along the snaking fiber, giving 7542 spatially distinct temperature measurements. The fiber is held fixed at the cold end of the recuperator, creating an index from which a planar map of temperatures can be reconstructed.

An in house code, FiberMap, for obtaining and interpreting fiber data was created. Data acquisition consists of LabVIEW® codes that interface with the Luna ODiSI® fiber sensor system to create .csv databases of experimental data. A set of MATLAB® scripts within FiberMap are then used to read and assemble the .csv database, convert fiber data to temperature readings, and create final 2D maps of temperature in the recuperator over time. An example of fiber readings made in a low mass flow run is shown in Figure 4.8.

collocated reference thermocouples

Additional thermocouples are embedded to a depth of 61 mm from either end of the recuperator. Each end contains four 0.8 mm diameter K type thermocouples spaced 30.18 mm apart, so that their tips are collocated with neighboring fibers. This provides redundant measurement and a way to check the calibration of the fiber. These are shown as circular

points along with fiber measurements, see Figure 4.8. The embedded thermocouples were calibrated between 0-900 °C against the standard platinum resistance detector.

4.1.2 Test Conditions

The zig-zag recuperator was operated over a wide range of CO_2 mass flow, from 0.012 to 0.265 kg/s. This covered flows in the transition region, starting with channel Reynolds number 1790, and continued through to highly turbulent flow, with a maximum Reynolds number of 64200. This exceeded the maximum Re =17,056 tested in a concurrent study by Katz[14]. High mass flow cases developed pressure drops peaking at 1260 kPa.

Operation was maintained in the supercritical region of CO_2, with inlet pressures ranging from 7.99 to 20.08 MPa. Cold inlet temperatures range from 53 to 141°C and hot inlet temperatures range from 278 to 448°C. Higher temperatures could not be reached as the system was driven by a nitrate salt pool based heat source with a 550°C decomposition point. This limited the ability to transfer heat to the CO_2 stream at temperatures above 550°C.

The 60 experimentally measured steady state conditions are given in Appendix Tables B.1 & B.2 in order of increasing mass flow.

Heat duty in each stream is calculated as the difference in enthalpy between the outlet and inlet, using the Span-Wagner equation of state for CO_2 [41],

$$\dot{q}_C = \dot{m}\left(H(T_{C_{out}}, P_{C_{out}}) - H(T_{C_{in}}, P_{C_{in}})\right) \tag{4.1}$$

$$\dot{q}_H = \dot{m}\left(H(T_{H_{out}}, P_{H_{out}}) - H(T_{H_{in}}, P_{H_{in}})\right) \tag{4.2}$$

The heat transfer from the hot CO_2 stream is somewhat greater than the heat transfer to the cold CO_2. This imbalance is heat loss through insulation and from conduction through nozzles and supports.

4.1.3 Uncertainty Quantification

Uncertainty in the measurement of steady state operating conditions is a combination of the instruments precision and the variation of measurement over the 2 minute period.

Uncertainty in the measurement of pressure drop depended on whether a single differential pressure transducer was used or a pair of less accurate absolute pressure transducers. At pressure drops above 480 kPa the pressure drop had to be measured as the difference between two absolute pressure readings. This gives a much greater error in ΔP as absolute pressure transducers are less accurate and their errors are compounded when determining ΔP.

4.2 Thermohydraulic Finite Element Model

structure conductivity and porosity

For modeling purposes, the micro channel structure can be simplified by looking at a unit cell. The cell is taken as a piece of the 33 mm thick diffusion-bonded core stack and is a CAD reconstruction of the 80° zig-zag channels described in Table 2.4. A cell footprint of $2p \times 2s$ captures the periodically repeating structure of the counter-flow micro-channel core. Analysis of the structure allows solid and fluid volumes, volume fractions, and internal surface areas to be calculated. These are given, along with a diagram of the unit cell, in Table 4.1.

Resistance to thermal conduction between the hot and cold fluid walls was quantified using a conduction model of the counterflow unit cell. A 100°C gradient was applied between the hot and cold channel fluid walls. The resulting heat flow through the 316 stainless steel micro-channel structure was calculated. The combination of heat flow and temperature drop yield a conduction resistance for this micro-channel structure. The conduction resistance is then normalized by the volume of the unit cell, giving a volumetric resistance that allows

Table 4.1: Unit Cell Analysis

volumes (mm^3)	
V	1568.7
V_S	1325.8
V_C	130.8
V_H	121.1
areas (mm^2)	
$A_{surf.C}$	517.1
$A_{surf.H}$	443.2
volume fraction	
ϕ_S	0.8452
ϕ_C	0.0834
ϕ_H	0.0715

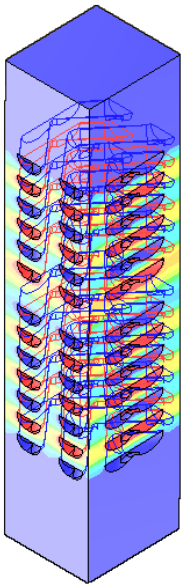

scaling to larger models. The unit cell analysis yielded volumetric conduction resistances, $R_{V,cond.}$, of 0.1986-0.1239 K-m^3/MW for 316 temperatures of 20-600°C.

The effect of zig-zag channels on the effective conductivity through the structure and fluid channels was also considered. Porosity and orientation of the micro-channel result in orthotropic effective conductivity through the unit cell. Conduction through the unit-cell is reduced relative to a purely solid volume 316 stainless steel. Conduction in the fluid streams is modeled as an effective conductivity of the fluid which is reduced and only in the channel direction, x. Effective conductivity of the fluid across channels (in y and z) is zero, as heat would first have to be transfered to the fluid walls and conducted through the solid. Orthotropic effective conductivity of counter-flow the solid structure, k_S, and the hot and

cold CO_2 channels, k_H and k_C, were also determined through conduction models,

$$[\mathbf{k}]_S = k_{316} \lceil 0.8186, 0.7966, 0.6420 \rfloor \tag{4.3}$$

$$[\mathbf{k}]_C = k_{CO_2} \lceil 0.0977, 0, 0 \rfloor \tag{4.4}$$

$$[\mathbf{k}]_H = k_{CO_2} \lceil 0.0837, 0, 0 \rfloor \tag{4.5}$$

balance of heat transfer

The Fluid Heat Advection PDE provides the fluid thermal solution. Heat in the fluid streams is stored, advected with flow, and transferred to the solid core. Heat transfer between the CO_2 and the solid is described using a thermal resistance network comprising the convective resistance and conductive resistance between the fluid walls,

$$T_C - T_S = \dot{q}_{V,C} \left(R_{V_{conv.}} + \tfrac{1}{2} R_{V_{cond.}} \right) \tag{4.6}$$

$$T_H - T_S = \dot{q}_{V,H} \left(R_{V_{conv.}} + \tfrac{1}{2} R_{V_{cond.}} \right) \tag{4.7}$$

The standard definition of the Colburn heat transfer coefficient j can be reformulated to use the Darcy velocity of the porous media model,

$$j = \frac{h}{\rho c_p \mathrm{v}} Pr^{\frac{2}{3}} = \frac{h\phi}{\rho c_p \left| \mathrm{v}_D \right|} Pr^{\frac{2}{3}} \tag{4.8}$$

The convective resistance in Equation 4.6 is then formulated in terms of the Colburn coefficient,

$$R_{V_{conv.}} = \frac{V}{h A_{surf.}} = \tfrac{1}{4} \frac{D_h Pr^{2/3}}{j \rho c_p} \frac{1}{\mathrm{v}_D} \tag{4.9}$$

The Darcy friction factor and Colburn heat transfer coefficient in Equations 3.7 and 4.9 can be taken from known Zig-Zag channel correlations.

4.2.1 Zig-Zag Channel Performance

model implementation of correlations

Hydraulic performance is often reported as a Fanning friction factor, f_F, calculated from the pressure drop over the internal length of the zig-zag channel.

$$\frac{\Delta P}{L_{ch}} = \frac{2\rho}{D_h} f_F \mathrm{v}_{ch}^2 \tag{4.10}$$

Due to the zig-zag angle, the internal length of the zig-zag channel is longer than that of the micro-channel core, and the fluid velocity within the zig-zag channel is greater than that of the porous media approximation.

$$L_{ch} = \cos^{-1}(\alpha/2) L_{core} \tag{4.11}$$

$$\mathrm{v}_{ch} = \cos^{-1}(\alpha/2) \tfrac{1}{\phi} \mathrm{v}_D \tag{4.12}$$

The Homogenized Heat Exchanger Thermohydraulics (HHXT) model requires a directional Darcy friction factor that relates pressure drop to the Darcy flux.

$$\frac{\Delta P}{L_{core}} = \frac{\rho}{2 D_h \phi^2} f_D \mathrm{v}_D^2 \tag{4.13}$$

Correlations for f_F are often a function of the channel Reynolds number, Re_{ch}, which differs from the Reynolds number used by the porous media approximation in the HHXT model,

$$Re_{ch} = \frac{\rho \mathrm{v}_{ch} D_h}{\mu} \tag{4.14}$$

$$Re = \frac{\rho \mathrm{v}_D D_h}{\mu \phi} \tag{4.15}$$

The model and channel Reynolds number are related by the zig-zag angle,

$$Re_{ch} = \cos^{-1}(\alpha/2)Re \tag{4.16}$$

A transform must be applied in order to use zig-zag correlations in the HHXT model. Combining Equations (4.10)-(4.13) and accounting for the Reynolds relations in Eqn. (4.16), the functional form of the Darcy friction factor input into the HHXT model becomes,

$$f_D(Re) = 4\cos^{-3}(\alpha/2) f_F\left(\cos^{-1}(\alpha/2)Re\right) \tag{4.17}$$

A simpler transform is applied to heat transfer correlations, which like the Fanning friction factor, are given relative to the channel Reynolds number.

$$Nu(Re\ ,\ Pr) = Nu_{ch}\left(\cos^{-1}(\alpha/2)Re\ ,\ Pr\right) \tag{4.18}$$

$$j(Re) = j_{ch}\left(\cos^{-1}(\alpha/2)Re\right) \tag{4.19}$$

f and j correlations

Moisseytsev et. al.[13] provide comprehensive correlations for the Fanning friction factor and Colburn heat transfer coefficient of zig-zag channels that are defined over a wide range of channel Reynolds number and account for variation in the zig-zag angle α. These are fits to vendor supplied data sets for three different zig-zag angles and one set of straight channel data over a range of 10 to 100,000 Reynolds number.

The correlations proposed by Moisseytsev et. al. separate behavior in the laminar, $Re_{ch} < 1700$, and turbulent,$Re_{ch} > 2300$, regions. A linear interpolation is used for flows within the transition region.

The Fanning friction factor of the zig-zag channel is based a straight channel correlation,

$$f_0 = \begin{cases} 16Re_{ch}^{-1} & , \quad Re_{ch} < 1700 \\ 0.0791Re_{ch}^{-0.25} & , \quad Re_{ch} > 2300 \end{cases} \tag{4.20}$$

this is then enhanced by another factor which accounts for the contribution of the zig-zag angle α,

$$\frac{f}{f_0} = \begin{cases} 1 + a_f(Re_{ch} + 50) & , \quad Re_{ch} < 1300 \\ kRe_{ch}^{c} & , \quad Re_{ch} \geq 1300 \end{cases} \tag{4.21}$$

where a_f =0.0038, k=11.3575, and c=-0.0867 for a zig-zag of $\alpha = 80°$.

The Fanning friction factor correlation combines the straight correlation and the enhancement,

$$f_F(Re_{ch}) = \frac{f}{f_0} f_0 \tag{4.22}$$

The heat transfer correlation is developed separately for the laminar and turbulent regions. Angle-dependent parameters are introduced to control the behavior,

$$j_{ch}(Re_{ch}) = \begin{cases} 4.1Re_{ch}^{-1} j_{lam.} & , \quad Re_{ch} < 1700 \\ j_{turb.} & , \quad Re_{ch} > 2300 \end{cases} \tag{4.23}$$

$$j_{lam.} = 1 + a_{j,lam.}(Re_{ch} + 50) \tag{4.24}$$

$$j_{turb.} = 0.1341 a_{j,turb.} Re_{ch}^{-0.3319} \tag{4.25}$$

where $a_{j,lam.}$ =0.0022 and $a_{j,turb.}$ =1.0195 for a zig-zag of $\alpha = 80°$.

Friction factor and heat transfer correlations for 80° are used in the model. The model was initially run using unmodified correlations, but a better match to experimental data was possible with a correction to Moisseytsev et. al.'s friction factor correlation and the incorperation of seperate correlations for heat transfer on the hot and cold CO_2 sides.

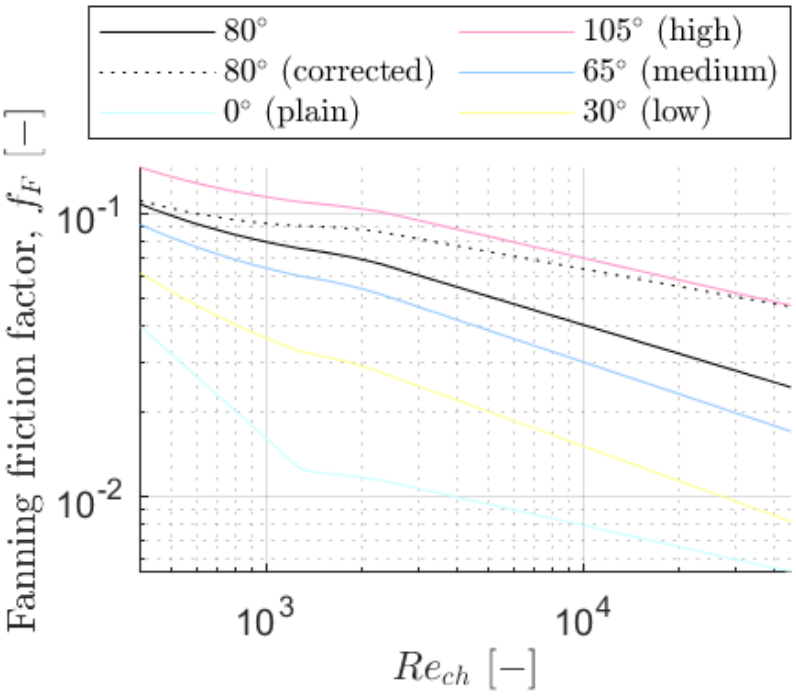

Figure 4.1: Comparison of Fanning friction factor correlations. The model used the 80° correlation in both an uncorrected (Equations 4.20-4.21) and corrected form(Equation 4.26). "plain", "high", "medium", and "low" angle channel correlations from Moisseytsev et al. are provided for comparison[4].

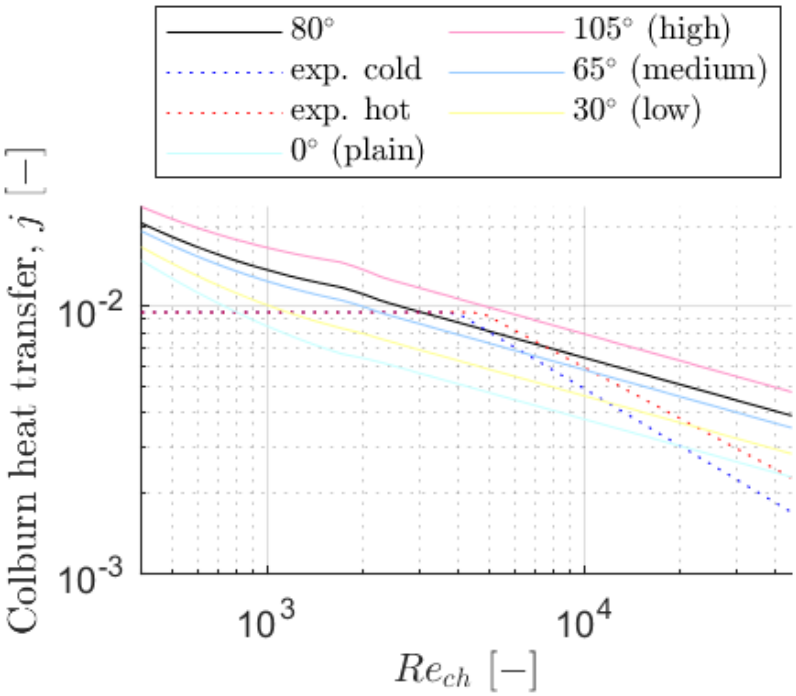

Figure 4.2: Comparison of Colburn correlations. The model used both th 80° correlation (Equations 4.23-4.25) and a corrected hot and cold experimental correlations (Equations 4.28 & 4.29). "plain", "high", "medium", and "low" angle channel correlations from Moisseytsev et al. are provided for comparison[4].

The friction factor correction which produced the best match in mass flow and heat transfer is as follows,

$$f_F^*(Re_{ch}) = 0.4834 Re_{ch}^{0.1322} f_F(Re_{ch}) \tag{4.26}$$

$$\tag{4.27}$$

The heat transfer coefficients are taken as fits to experimentally determined j data shown in Figure 4.3.

$$j_H = 2.331 Re_{ch.}^{-0.6330} \text{ , for } j_H \leq 0.009528 \tag{4.28}$$

$$j_C = 3.946 Rech.^{-0.7083} \text{ , for } j_C \leq 0.009528 \tag{4.29}$$

The uncorrected and corrected forms of the 80° correlations are plotted over the range of experimental channel Reynolds numbers in Figures 4.1 and 4.2. These are compared to other "high", "medium", and "low" zig-zag channels detailed in Moisseytsev et al.'s report[4]. These correspond roughly to α of 105°, 65°, and 30°. The report supplies data for "plain" straight channels as well.

The correlations provided by Moisseytsev et al. require some adaptation to be used with the homogenized model. Equations 4.22 and 4.23 define the micro-channel friction, f_{ch}, and heat transfer, j_{ch}, relative to the Reynolds number of the flow within the channel,Re_{ch}. These definitions are different than those used in Equations 3.7 and 4.6 of the homogenized model. The transforms given in Equations 4.17 and 4.18 are applied when implementing the correlations within the homogenized model.

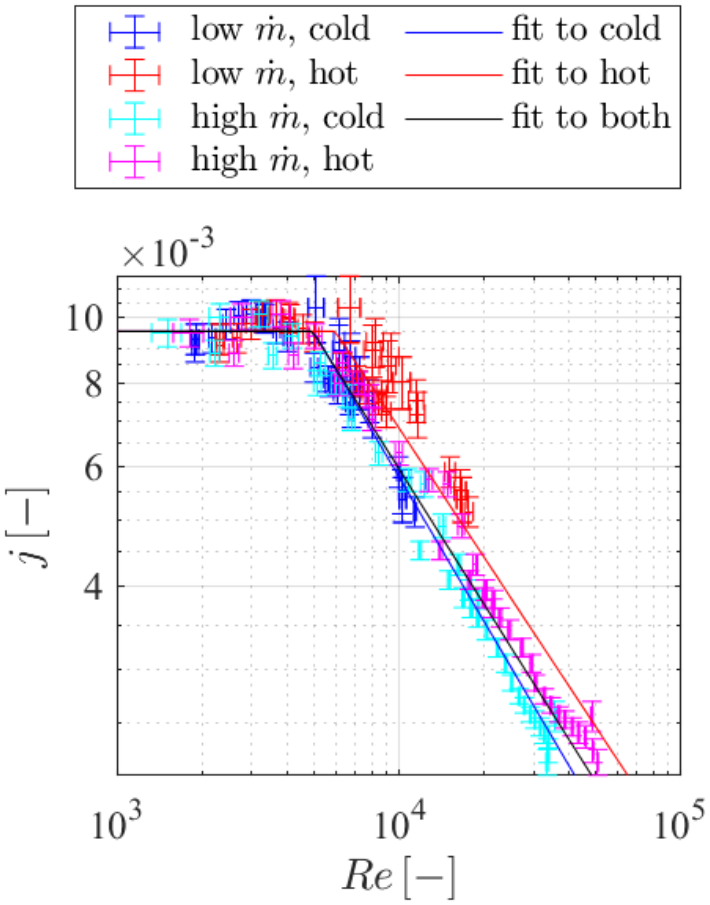

Figure 4.3: Experimental heat transfer coefficients for the hot and cold CO_2 sides. Fits to the data are given in Equations (4.28 & 4.29).

4.2.2 Model Geometry

A 2-dimensional approximation of the recuperator is used in the model. In Figure 5.4, an outline of the modeling regions are overlayed on the pattern for the etched plate, and region types are identified. The simplified model geometry is show in Figure 4.4.

Volume fraction, ϕ, orthotropic conductivity, $[\mathbf{k}]$, and directional friction factor, $\lceil \mathbf{f} \rfloor$, differ in the model regions. Their assignment by region is detailed in Table 4.2. Orthotropic conductivities were determined from the unit cell model, see Equations 4.3-4.5.

Table 4.2: Definition of Zig-Zag PCHE Model by Region, see Figure 4.4

model	**solid body**		**cold CO_2**			**hot CO_2**		
re-	ϕ	$[\mathbf{k}]_{cond}$	ϕ	$[\mathbf{k}]_{cond}$	$\lceil\mathbf{f}\rfloor$	ϕ	$[\mathbf{k}]_{cond}$	$\lceil\mathbf{f}\rfloor$
gion	0.8452	$[\mathbf{k}]_S$	0.0834	$[\mathbf{k}]_C$	$\lceil\mathbf{f}\rfloor_x$	0.0715	$[\mathbf{k}]_H$	$\lceil\mathbf{f}\rfloor_x$
II	1.000	$k_{316}\lceil\mathbf{I}\rfloor$						
III,VIII	0.9286	$\frac{6}{22}[\Lambda]_{90}[\mathbf{k}]_S + \frac{7}{22}k_{316}\lceil\mathbf{I}\rfloor$				0.0715	$[\Lambda]_{90}[\mathbf{k}]_H$	$[\Lambda]_{90}\lceil\mathbf{f}\rfloor_x$
IV,IX	0.9286	$\frac{6}{22}[\Lambda]_{90}[\mathbf{k}]_S + \frac{7}{22}k_{316}\lceil\mathbf{I}\rfloor$				0.0715	$[\Lambda]_{90}[\mathbf{k}]_H$	$[\Lambda]_{90}\lceil\mathbf{f}\rfloor_x$
V,X	0.8452	$[\Lambda]_{90}[\mathbf{k}]_S$	0.0834	$[\Lambda]_{90}[\mathbf{k}]_C$	$[\Lambda]_{90}\lceil\mathbf{f}\rfloor_x$	0.0715	$[\Lambda]_{90}[\mathbf{k}]_H$	$[\Lambda]_{90}\lceil\mathbf{f}\rfloor_x$
VI,XI	0.9167	$\frac{7}{22}[\Lambda]_{90}[\mathbf{k}]_S + \frac{6}{22}k_{316}\lceil\mathbf{I}\rfloor$	0.0834	$[\Lambda]_{90}[\mathbf{k}]_C$	$\lceil\mathbf{f}\rfloor = [\Lambda]_{90}\lceil\mathbf{f}\rfloor_x$			
VII,XII	0.9167	$\frac{7}{22}[\Lambda]_{90}[\mathbf{k}]_S + \frac{6}{22}k_{316}\lceil\mathbf{I}\rfloor$	0.0834	$[\Lambda]_{90}[\mathbf{k}]_C$	$\lceil\mathbf{f}\rfloor = [\Lambda]_{90}\lceil\mathbf{f}\rfloor_x$			

† transformation matrix $[\Lambda]_{90}$ is a 90 degree rotation. $\lceil\mathbf{I}\rfloor$ is the identity matrix.

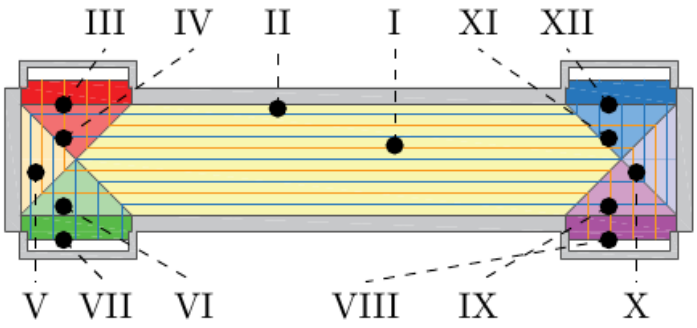

Figure 4.4: Model geometry and regions

The majority of the recuperator consists of a counter-flow core, region I in Figure 4.4. Side mounted headers distribute flow to micro-channel entrance regions (III & XII), which in turn bring the flow into the heat exchanger. Similarly exit regions (VII & VIII) bring flow out. Entrance and exit from the side necessitates turning of the zig-zag channels, creating transitions which contain both parallel-flow (V & X), and cross-flow (IV, VI, IX, & XI).

4.2.3 Material Definitions

CO_2 fluid

The two fluid streams are modeled as CO_2 with real gas properties. Temperature and pressure dependent functions for k, ρ, c_p, and μ were input into the model. Property values were pre-determined for several isobars over a 20-700 °C temperature range. During runtime the real gas properties were interpolated from these isobars. The Span-Wagner equation of state for CO_2 was used to calculate ρ and c_p[41], Vesovic's method was used in determining k[42], and a correlation proposed by Fenghour defined μ[43].

316 stainless steel solid

Properties of 316 stainless steel were used for the model's solid body. Properties were taken from the physical property tables within the American Society of Mechanical Engineers

(ASME) code Section II, Part D. A constant 8030 kg/m^3 density is used. Temperature dependent conductivity was implemented, with k_{316} varying from 14.6 to 20.5 W/m-K over 50-450°C.

4.2.4 Boundary Conditions

Two boundary condition configurations are considered for the homogenized model, a uniform mass flux and uniform pressure drop configuration.

Both configurations apply experimentally measured values of inlet temperature and pressure as Dirichlet conditions. These are applied at the model's cold and hot inlet boundaries, which are the top edges of regions XII and III of Figure 4.4 respectively.

The configurations differ in their treatment of hydraulic boundary conditions at the inlets and outlets of the model. Outlet boundary conditions are applied to the cold and hot outlet boundaries, which are the bottom edges of regions VII and VIII of Figure 4.4 respectively.

uniform mass flux BC

A uniform mass flux assumption is often used in PCHE analysis, and arises based on the following arguments. Pressure variation within open headers is small in comparison to that of the pressure drop within the micro-channels, thus the pressure drop across any given micro-channel is the same. Given that each individual zig-zag channel has the same geometry and internal length, it presents the same resistance to flow as any other channel. Therefor if the pressure drop is the same, and the resistance is the same, then mass flow is the same in all channels.

The uniform mass flux configuration assumes that a mass flux, j_m, is evenly distributed across the inlet and outlet boundaries. This is applied as a Neumann boundary condition for both the hot and cold CO_2 inlets and outlets.

$$j_m = \rho \mathrm{v}_D = -\frac{\rho}{\mu} \lceil \mathbf{k} \rfloor \nabla P \tag{4.30}$$

where the magnitude of mass flux, j_m, is simply the experimental $\dot{m}$ divided by the area of the inlet/outlet boundary, 30.8273 cm^2. The sign is changed so that flow is into the system at the inlets, and out of the system at the outlets.

This is a convenient form for the hydraulic boundary condition as it fixes the mass flow within the model. Any inaccuracy in the friction factor correlations used would only alter the pressure drop within the model, which only weakly affects the thermal solution.

However, the uniform mass flux assumption is flawed due to the 2-D temperature distribution inherent in a PCHE and the impact of temperature on CO_2 properties. Since density and viscosity of CO_2 vary with temperature, the flow resistance of micro-channels will vary with temperature. This isn't a problem if the temperature distribution along the length of the channels is the same, as the resulting flow resistance will still be the same for each channel. This result, and the effect of temperature variation along the PCHE length, has been addressed in multiple 1D discretized modeling efforts[13, 14]. However, temperature can vary across the PCHE–i.e. perpendicular to the flow direction. Channel layout, header orientation, cross-flow region heat transfer, and conduction in the PCHE solid are all factors that contribute to variation in temperature profiles between channels. The result is that CO_2 within the channels on one side of a PCHE are on average hotter than in the channels on another side and therefore have much different flow resistance.

uniform pressure drop BC

As uniform mass flux cannot be assumed in a PCHE, a different boundary condition must be considered that allows for flow variation. Application of a uniform pressure drop across the micro-channels allows for flow variation and is a more natural boundary condition as it

mimics the conditions within the PCHE headers.

The uniform pressure drop configuration boundary condition applies the experimentally measured pressure drop directly. This is applied by setting the pressure at the inlets and outlets using Dirichlet conditions. The inlet pressures are taken as the measured pressure of the inlet nozzle. The outlet pressure is taken as the measured inlet pressure minus the measured pressure drop. In this manner the flow is free to distribute itself in the model, as it would in practice.

With pressure drop fixed, the resulting mass flow and heat transfer become sensitive to changes in friction factor. Corrections to the friction factor can be made in order to match experimental mass flows, see Equation 4.26.

4.3 Results

4.3.1 Effect of Boundary Condition on Distribution of Flow and Temperature

This section compares the behavior and accuracy of the two boundary condition configurations. The uniform mass flux and uniform pressure drop boundary conditions were compared by running these models using the uncorrected f_D correlations (Equation 4.22).

fluid temperatures

CO_2 temperatures within the hot and cold streams are directly calculated in the HHXT model. An example is shown for the lowest mass flow test in Figure 4.5. Which are results for the 0.0123 kg/s test using both the uniform mass flux and uniform pressure drop boundary conditions. Flow is from right to left on the cold side, and left to right on the hot side. Cold side inlet conditions are 54.9°C and 12.1 MPa, hot side inlet conditions 451.3°C and 12.0

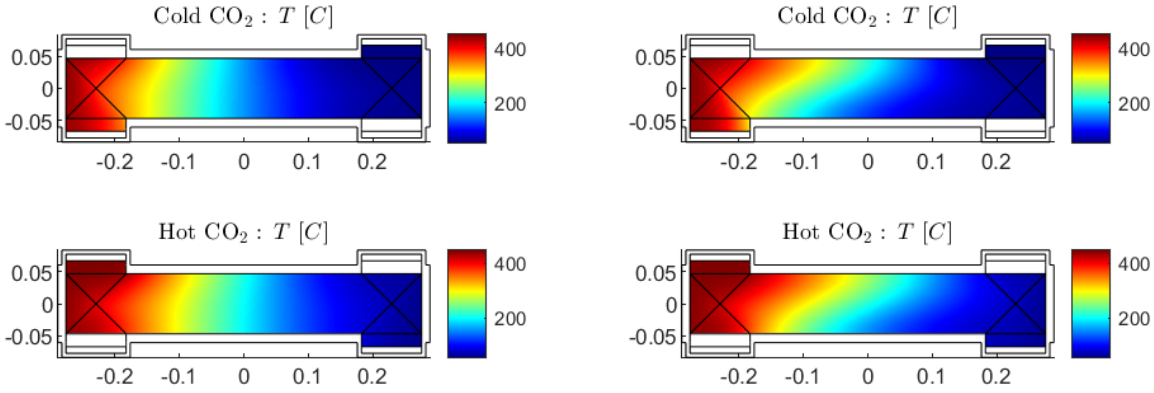

(a) uniform mass flux BC.

(b) uniform pressure drop BC.

Figure 4.5: CO_2 temperature distribution for both boundary conditions in the 0.0123 kg/s test.

MPa.

Use of a uniform mass flux boundary condition results in relatively 1-D temperature distributions, see Figure 4.5a. Here temperature change is along the length of the heat exchanger, in the flow direction.

The less restrictive uniform pressure drop boundary condition results in a 2-D temperature distribution, see Figure 4.5b. Mass flux is allowed to distribute, so that hotter channel receive less mass flow than colder ones, causing very different thermal behavior.

flow distribution

The difference in mass flux distribution when using the uniform mass flux or uniform pressure drop boundary conditions can be seen in Figure 4.6. Cold and hot CO_2 mass flux values are interpolated at 11 locations across the counter-flow core (region I in Figure 4.4). The lines are distributed across the core in the y direction, with positive y corresponding to the top end of the core, the side closest to the hot and cold CO_2 inlets. Note the interpolated lines contain non-continuous "steps". These occur because mass flux is defined as constant

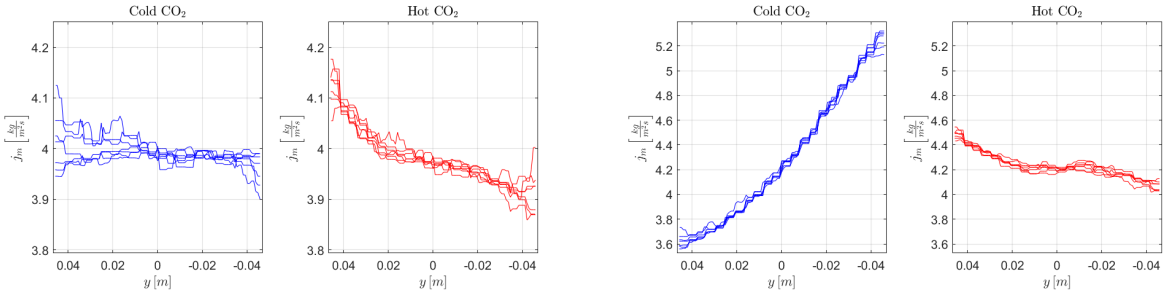

(a) uniform mass flux BC. **(b)** uniform pressure drop BC.

Figure 4.6: Mass flux distribution within micro-channel core in the 0.0123 kg/s test.

throughout each element and the interpolation is just slicing through elements.

Mass flux does not vary along the length zig-zag core. This can be seen as each of the 11 cross section lines have the same mass flux distribution. However variation across the core can occur.

Using a uniform pressure drop boundary condition allows mass flux to freely distribute within the core, see Figure 4.6b. Here the mass flux is higher at the bottom of the cold CO_2 side and the top of the hot CO_2 side, where streamlines are colder on average. Variation across the core is more substantial within the cold CO_2 side.

This variation of mass flux is caused by the variation of CO_2 properties, shown in Figure 3.2. Applying a constant pressure gradient to the definitions of mass flux in Equation 4.30 and permeability in Equation 3.7, we see that mass flux is proportional to the root of density over the friction factor,

$$j_m \propto \sqrt{\frac{\rho}{f_D(Re)}} \tag{4.31}$$

where the Darcy friction factor (Equations 4.16, 4.17, & 4.22) introduces viscosity dependence through its correlation to Reynold's number,

$$Re = \frac{\rho \mathrm{v}_D D_h}{\phi \mu} = \frac{j_m D_h}{\phi \mu} \tag{4.32}$$

The effect of CO_2 properties is simpler to illustrate if a constant friction factor for Equation 4.31 is considered. In this case the mass flux variation becomes solely dependent on density, $j_m \propto \sqrt{\rho}$. This relation is plotted from 50-450°C in Figure 4.7a. The rate of change in density with temperature is shown in Figure 4.7b.

Mass fluxes shown in Figure 4.6 for the 0.0123 kg/s test are the result of density variation along the central, 12 MPa, isobar plotted in Figure 4.7. CO_2 density is greatest at lower temperature, leading to greater mass flux in cold streamlines. Variation in mass flux on the cold CO_2 side is more pronounced than the hot CO_2 side as density changes more rapidly at colder temperatures.

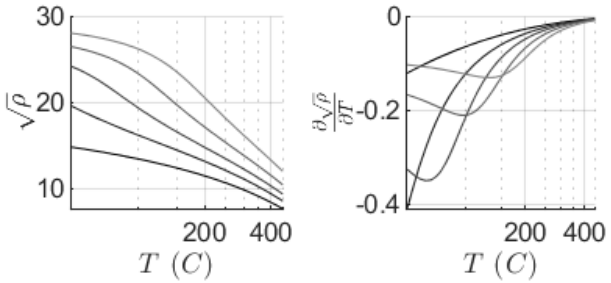

(a) variation of $\sqrt{\rho}$. **(b)** derivative of $\sqrt{\rho}$.

Figure 4.7: Variation of mass flux with temperature at constant pressure drop and friction factor is proportional to $\sqrt{\rho}$. Lines from black to gray given for 8, 10, 12, 15, and 20 MPa isobars.

body temperature distribution

The model directly calculates the homogenized body temperature, a representation of the temperature of the unit cell in Table 4.1. As this homogenizes the micro-channel walls and top/bottom solid plate structure, it represents the mean temperature of the PCHE solid. The homogenized body temperature falls between that of the hot and cold CO_2 streams, depending on the details of the resistance network (see equation 4.6).

The homogenized body temperature can be compared to fiber-optic temperature measurements, which are made within the instrumented plate, see Figure 2.4. As conduction resistance are low, the fiber measurement is made at a similar mean temperature as that calculated for the homogenized solid–i.e. the addition of the instrumentation plate has a small impact on the temperature distribution.

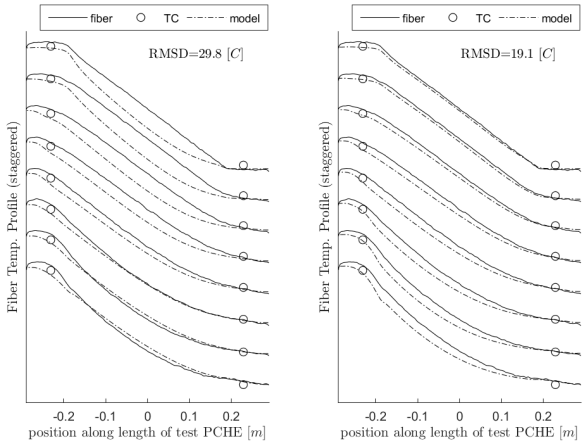

(a) uniform mass flux BC. **(b)** uniform pressure drop BC.

Figure 4.8: Comparison of modeled and measured body temperatures in the 0.0123 kg/s test.

The homogenized body temperature of the model can be interpolated to the points of measurement of the fiber and plotted against each of the 8 passes of the fiber, see Figure 4.8. Here 8 lines are staggered bottom to top representing the 8 fiber passes spaced 15.1 mm in y. The passes are separated vertically for better readability.

In this case the comparison is to fiber and embedded thermocouple measurements made in the 0.0123 kg/s test. The comparison is shown for models using the uniform mass flux and uniform pressure drop boundary conditions.

Accuracy of the model is quantified by looking at the root mean square difference (RMSD) of temperatures calculated by the model and those measured by the embedded fiber-optic

measurements. Each of the 7542 measurement points, i, of the the fiber-optic sensor is considered in the RMSD comparison,

$$\text{RMSD} = \sqrt{\frac{1}{7542}\sum_{i}^{7542}\left(T_S(x_i, y_i) - T_{fiber}(i)\right)^2} \tag{4.33}$$

here the model solid temperature T_S is interpolated at positions x_i and y_i of the fiber-optic measurement. The RMSD difference in temperature between the model and experiment is calculated for each experimental distribution. It is shown within comparison plots shown in Figures 4.8 & 4.17. The RMSD differences for all experimental data points falls below 40°C for most, see Figure 4.17.

Using a uniform pressure drop boundary condition gives a model that matches the measured internal temperature distribution more closely. Figure 4.8a shows a model result that is comparable to that of the embedded fiber-optic temperature probe. This is a considerable improvement when compared to the uniform mass flux condition. Uniform mass flux is unable to match the temperature distribution at the top of the heat exchanger, see Figure 4.8b.

Fiber-optic measured temperatures feature a linear temperature profile at the top ($+y$) of the PCHE and a curved temperature profile at the bottom ($-y$). A fully curved temperature profile is the result of uniform flow distribution. With uniform flow, the balance of heat transfer is consistent across the PCHE, and a curved temperature profile is maintained from top to bottom. The curved to linear profile transition that is seen experimentally can only be obtained with variation of mass flow across the core. A reduction in flow at the top of the PCHE relative to the bottom leads to less heat transfer, and an over all hotter condition, at the top of the PCHE. The flow and heat transfer reduction at the top of the PCHE results in the linear temperature profile that is measured.

4.3.2 Corrected and Uncorrected Correlations

This section shows the improvement in results made by correcting Moissetsev et al.'s friction factor correlation. The uncorrected f_D correlation is given in Equation (4.22). A correction is introduced in Equation (4.26), so that a better match to experimental conditions, heat transfer, and internal temperatures could be achieved. Uncorrected and corrected forms were run as two separate models, both of which used the uniform pressure drop boundary condition.

mass flow

Total mass flow in the model is sensitive to the friction factor correlation. Since a fixed uniform pressure drop boundary condition is used, changes in the f_D correlation result impact total mass flow.

The friction factor correlation for a 80° given by Moisseytsev et al. was too low, resulting in model mass flows which were higher than measured, see Figure 4.9a. The mass flow prediction was particularly far off at for high Reynolds cases. High Reynolds flow was chosen to be $Re_{ch} > 17,056$, the highest tested in a concurrent zig-zag channel study by Katz et al [14]. Tests with Re above this point are plotted with gray filled markers.

Applying a correction on the friction factor (Equation 4.26) increases the 80° friction factor, see Figure 4.1. The corrected friction factor correlation is closer to that of the "high" 105° zig-zag reported by Moisseytsev et al. The corrected correlation gives model mass flows that are within 20% of the measured value, see Figure 4.9b.

Figures 4.9, 4.10, and 4.11 plot the percent difference in the model value from the measured value of mass flow, heat transfer, and outlet temperature respectively. The percent

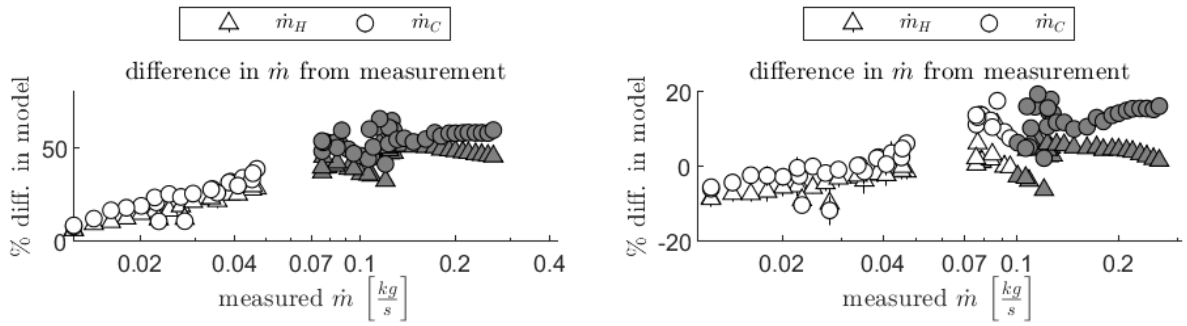

(a) uncorrected correlations. **(b)** corrected correlations.

Figure 4.9: Comparison of modeled and measured total mass flow for all tests. Gray fill indicates Re_{ch} >17,056.

difference is calculate for each value as,

$$\%\text{ diff. in model} = \frac{\text{model} - \text{measured}}{\text{measured}} \times 100\% \tag{4.34}$$

heat duty

Model calculated total heat transfer is given for all tests in Appendix Table B.3. Total heat transferred is calculated by adding up the heat going into the cold and out of the hot CO_2 over all elements in the model,

$$\dot{q}_C = \sum_e \dot{q}_{V,C} V_e \tag{4.35}$$

$$\dot{q}_H = \sum_e \dot{q}_{V,H} V_e \tag{4.36}$$

where the volumetric heat transfer within each element is described in Equations 4.6 & 4.7.

The difference in heat transferred in the model is compared to that measured in Figure 4.10. Measured $\dot{q}$ is based on the inlet and outlet conditions, see Equations 4.1 & 4.2.

Model heat transfer is largely affected by the total mass flow developed in the model.

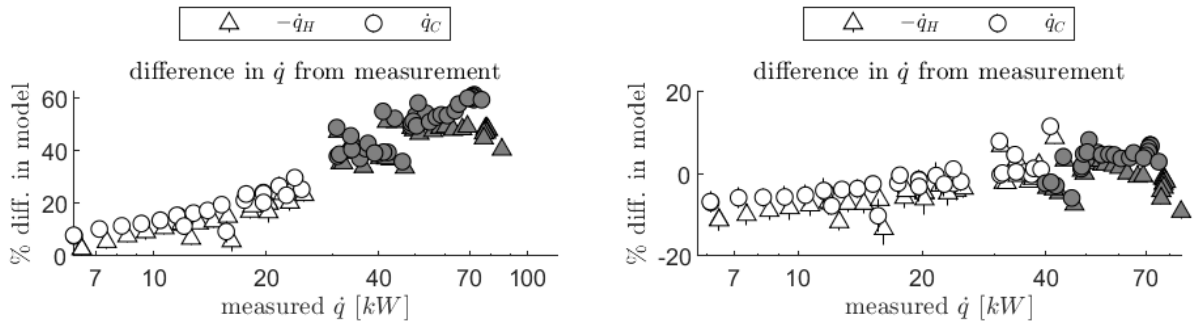

(a) uncorrected correlations. **(b)** corrected correlations.

Figure 4.10: Comparison of modeled and measured total heat transfer for all tests. Gray fill indicates Re_{ch} >17,056.

Higher evaluation of $\dot{m}$ in the uncorrected model results in $\dot{q}$ that are much higher than experiment, see Figure 4.10a. Using the corrected friction factor correlation gives model total heat transfer that is within 20% of the measured value, see Figure 4.10b.

outlet conditions

Outlet temperatures are evaluated as the bulk temperature at the outlet boundary. Bulk temperature is calculated by integrating the enthalpy and mass flux over the boundary to get the enthalpy of the adiabatically mixed fluid. Bulk temperature is then that of the adiabatically mixed fluid at the outlet pressure,

$$\dot{m}H(T_{out}, P_{out}) = \int_A j_m H(T, P) dA \tag{4.37}$$

The model's calculation of the outlet temperature is given for all tests in Appendix Table B.3. Outlet temperatures for the 0.0123 kg/s model were 397.6°C and 63.6°C for the cold and hot streams respectively.

The accuracy of model outlet temperature predictions is largely unchanged when using

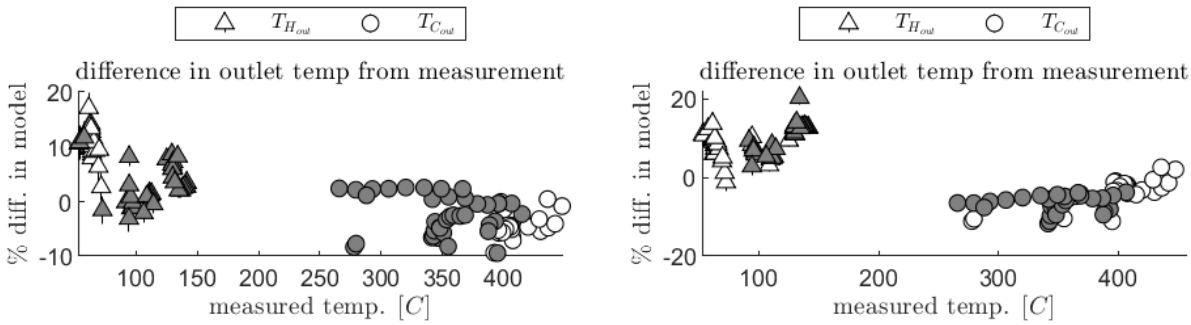

(a) uncorrected correlations. **(b)** corrected correlations.

Figure 4.11: Comparison of modeled and measured outlet temperatures for all test. Gray fill indicates Re_{ch} >17,056.

the corrected friction factor, see Figure 4.11. A slight improvement in hot outlet temperature is made for some of the Re <17,056 cases. The improvement being from a maximum 18% error in the uncorrected case to 14% using the corrected correlation.

Hot outlet temperatures have a larger % error because the hot outlet is at a lower temperature, 50-60°C. A 1°C difference in outlet temperature yields a higher percent error at the lower temperature hot outlet than the high temperature cold outlet.

Outlet temperature predictions of the model are more accurate at high Reynolds, $Re_{ch} > 17,056$. High Re test outlet temperatures are within 8% of experiments while lower Re tests are up to 18% off experiment. This is the result of low Re test having lower hot outlet temperatures, and therefore more percent error for degree that the model is off.

4.3.3 Selected Results

Results of the model using the corrected friction factor (Equation 4.26) and constant pressure drop boundary conditions are reported in Appendix Table B.3. Three tests representing the range of experimental mass flow are taken as representative subset of these model results. A test representing the designed flow operation of the PCHE, a high flow operation, and

Table 4.3: Summary of Performance for a Subset of Model Results

	design flow	high flow	extreme flow
run	14	37	60
$\dot{m}$ (kg/s)	0.0336	0.1086	0.2646
$\dot{q}$ (kW)	18.00	42.70	80.29
$T_{C_{in}}$ (C)	55.0	63.5	101.5
$P_{C_{in}}$ (MPa)	11.55	11.59	20.08
ΔP_C (kPa)	20.49	161.3	594.9
$T_{H_{in}}$ (C)	495.5	428.6	397.0
$P_{H_{in}}$ (MPa)	11.35	10.16	14.71
ΔP_H (kPa)	31.76	282.6	1261.6
Re_C	5131	17,295	53,326
Re_H	6097	19,818	64,234
ε (%)	95.0	90.0	83.7
UA (W/K)	477	756	1155

the most extreme flow operation experience in experiment are investigated further. The conditions of these tests are summarized in Table 4.3.

temperatures

At the designed flow rate the distribution of CO_2 temperatures is shown Figure 5.1. Hot CO_2 is cooled uniformly within the counter-flow core (region I in Figure 4.4). Temperature variation across the core occurs as some of the hot CO_2 entering from the top left makes a longer pass through the left side transition (regions IV-VI), where it is pre-cooled by cold CO_2 leaving the counter-flow core. Similarly, cold CO_2 entering from the top right is pre-heated in the right side transition (regions IX-XI). The PCHE body temperature falls between the hot and cold streams.

Inlet, and hence outlet, temperatures become closer to experiment as mass flow is increased, see Table 4.3. The hot inlet becomes colder because the heater installed between the cold outlet and hot inlet can only produce 10kW, limiting the temperature rise on the hot side of the heatexchanger. The cold inlet becomes warmer as more heat transfer occurs

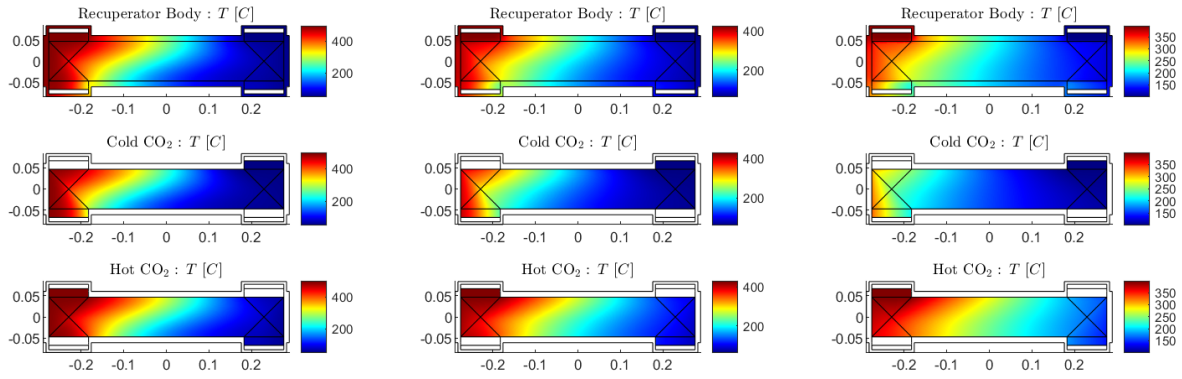

(a) design flow **(b)** high flow **(c)** extreme flow

Figure 4.12: Temperature distribution within the unit cell solid body, cold CO_2 steam, and hot CO_2 stream.

in the low temperature recuperator downstream of the test PCHE. As mass flow increases, hot outlet CO_2 is able to drive more heat transfer within the low temperature recuperator, warming the inlet CO_2.

As mass flow is increased heat transfer becomes more concentrated at the hot end of the heat exchanger, shifting temperature gradients further into the hot end transition region. The distribution of heat transfer is shown in Figure 4.14.

flow

The distribution of flow is shown in Figure 4.13. Here the model Reynolds number is given, which is 0.766 $\times$ smaller than channel Re_{ch}, see Equation 4.16. Cold CO_2 enters from the top right, flowing right to left within the counter-flow core (region I). Hot CO_2 enters from the top left, flowing left to right.

Mass flux redistribution results in higher cold CO_2 flow at the cooler bottom of the PCHE. CO_2 density varies significantly more at temperatures below 150°C, see Figure 4.7b. This drives variation in the mass flux distribution which is greatest at these lower temperatures.

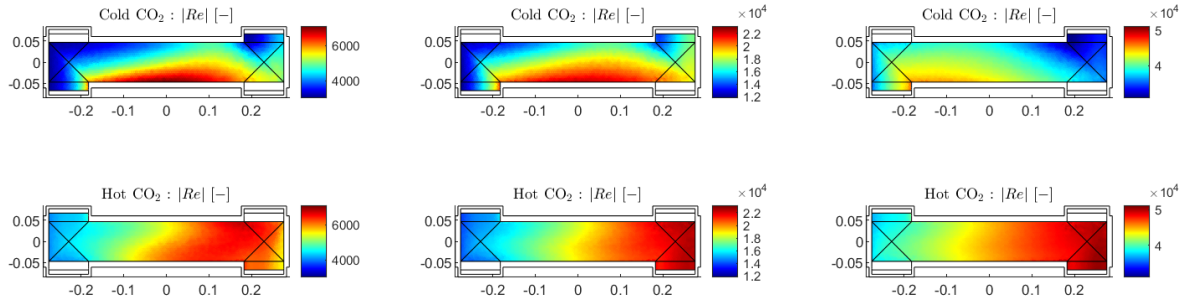

(a) design flow **(b)** high flow **(c)** extreme flow

Figure 4.13: Reynolds number within CO_2 streams. This shows model Re which is 0.766 $\times$ smaller than channel Re_{ch}, see Equation 4.16.

Flow variation is pronounced on the cold CO_2 side as temperatures dip below 150°C. There is less variation in flow on the hot side as CO_2 is hotter and density varies less.

As mass flow increases, cold inlet temperatures increase and reduce the mass flux redistribution. Mass flux variation is reduced as the variation of CO_2 density is less significant at temperatures above 150°C, see Figure 4.7b.

This variation in flow Reynolds translates into variation in the Colburn heat transfer coefficient (Equations 4.23-4.25).

distribution of heat transfer

Total heat transfer increases with mass flow and becomes more evenly distributed throughout the PCHE, see Figure 4.14. This is due to flow becoming more evenly distributed at higher mass flows. The majority of heat transfer occurs in the counter-flow core (region I) with the rest ocuring in the transitions (regions IV-VI & IX-XI).

At the design flow, heating in the transition region is limited and highly localized near the cold entrance and exit (regions VI & XI), see Figure 4.14a. This creates the imbalance in heat transfer across the flow that results in cross-core temperature variations seen in Figure

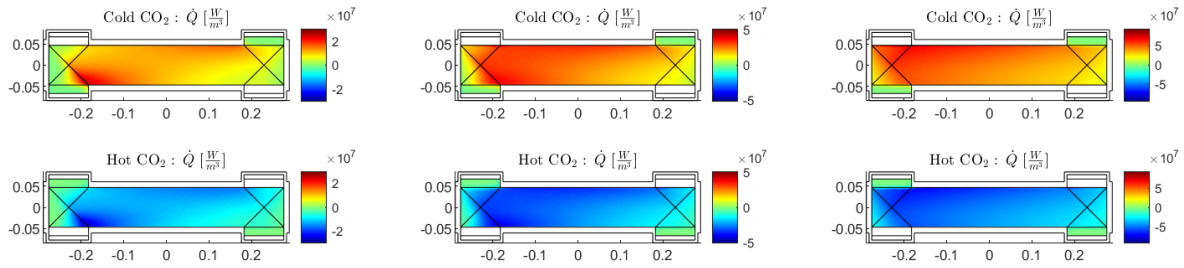

(a) design flow **(b)** high flow **(c)** extreme flow

Figure 4.14: Distribution of heat transfer, in W/m^3, within the hot and cold CO_2 streams.

5.1.

The share of heat transfer in the transition regions becomes greater and is better distributed as flow increases above the design condition. This results in more even heat transfer across the PCHE and less stratification within the counter-flow core, see Figures 4.14b and 4.14c. Heat transfer also shifts to the left, closer to the hot inlet.

Heat transfer is driven by the difference in hot and cold CO_2 temperatures, as described by the resistance network given in Equations 4.6-4.7. Concentrations of heat transfer are produced by greater differences between the hot and cold CO_2 streams, see the distribution of fluid bulk ΔT in Figure 4.15. The maximum ΔT between the hot and cold CO_2 remains at 100°C across mass flows, but is highly localized at the design flow conditions, becoming more spread out as mass flow is increased. This results from heat transfer becoming more evenly distributed at higher mass flow.

The temperature difference between the fluid walls can be determined by only considering the conductive resistance in Equations 4.6-4.7. This is shown as the fluid wall ΔT in Figure 4.15. At the design mass flow heat transfer is smaller, resulting in low fluid wall temperature differences ¡4.5°C which are concentrated close to the cold outlet. As flow is raised heat transfer increases and spreads out, creating higher temperature gradient between the hot

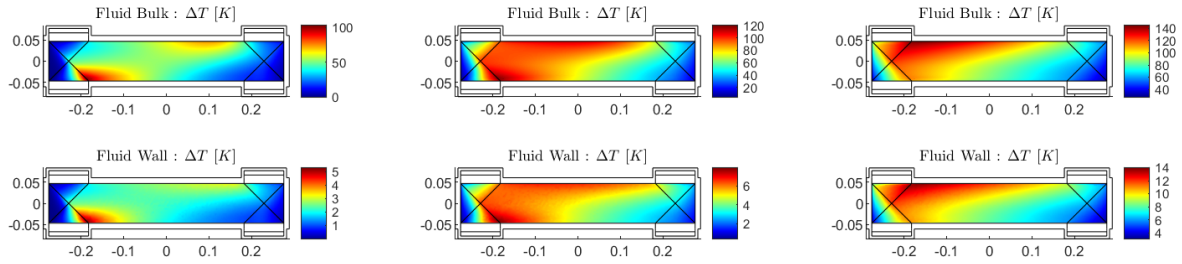

(a) design flow **(b)** high flow **(c)** extreme flow

Figure 4.15: Difference between hot and cold CO_2 stream bulk temperature (Fluid Bulk). Temperature drop between hot and cold walls (Fluid Wall).

and cold micro-channel walls. At extreme mass flow conditions ΔT between hot and cold walls reaches 15°C.

The difference in hot and cold CO_2 fluid walls is of concern as this results in thermal gradients, and thermal expansion, within the thin micro-channel walls which separate the fluids. The instantaneous coefficient of thermal expansion for 316 stainless steel at 250°C is 18.8×10^{-6} (mm/mm-K). With 0.671 mm of stainless steel separating the hot and cold streams, a 10°C ΔT between the fluid walls results in a 0.028% thermal strain in the micro-channel wall. By this estimation the thermal strain resulting from fluid wall temperature differences doesn't threaten the integrity of the stainless steel micro-structure, even at the extreme mass flow case.

internal temperatures

A comparison of internal temperatures, both modeled and measured, is given in Figure 4.16. These show the results of the model using the corrected friction factor (Equation 4.26) and plot against both fiber and embedded thermocouple measurements.

The fiber-optic temperature measurement is noisier at high mass flows. This is particularly notable in the extreme 0.2646 kg/s test shown in Figure 4.16c. Noise is due to increased

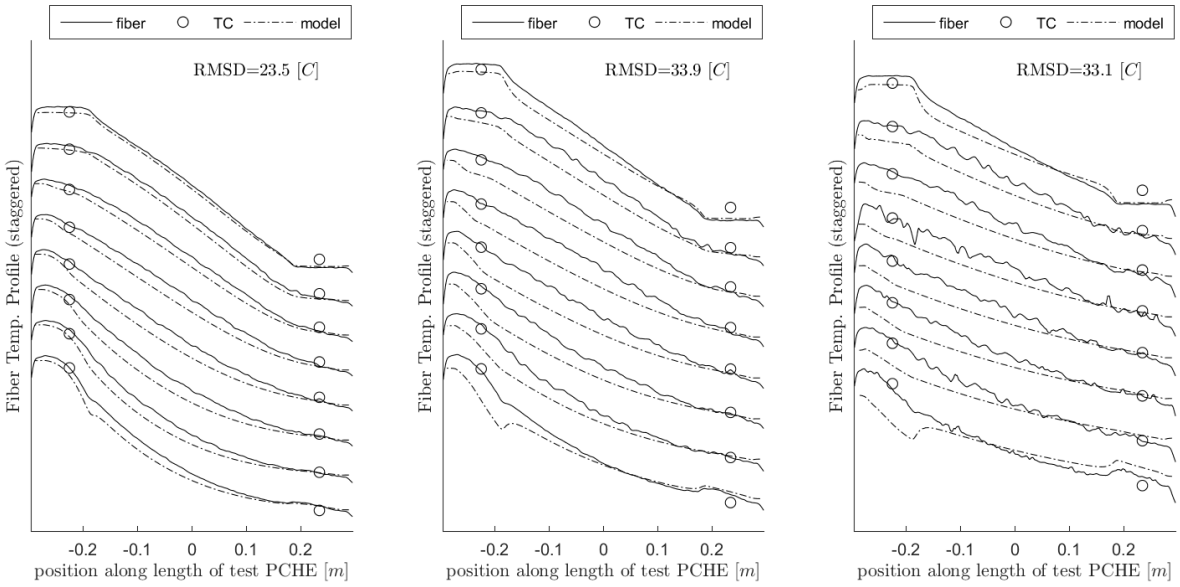

(a) design flow **(b)** high flow **(c)** extreme flow

Figure 4.16: Comparison of modeled and measured body temperatures.

flow driven vibration within the PCHE. A throttle valve positioned downstream of the cold outlet creates CO_2 expansion induced vibration that is communicated through piping to the PCHE. The position of this valve results in a higher concentration of noise near the cold outlet (bottom left of the PCHE and Figure 4.16c.

Accuracy of the model in matching internal temperatures increases with mass flow. This can be seen in Figure 4.16 but is most apparent when plotting the RMSD difference (Equation 4.33) against the total heat transfer as shown in Figure 4.17.

RMSD differences between the model and the fiber measurements are larger than the RMSD differences between the model and the 8 embedded thermocouples. This is because the model is a better match near ends of the heat exchanger where the thermocoouples are mounted than the center through which the fiber-optic sensors also pass.

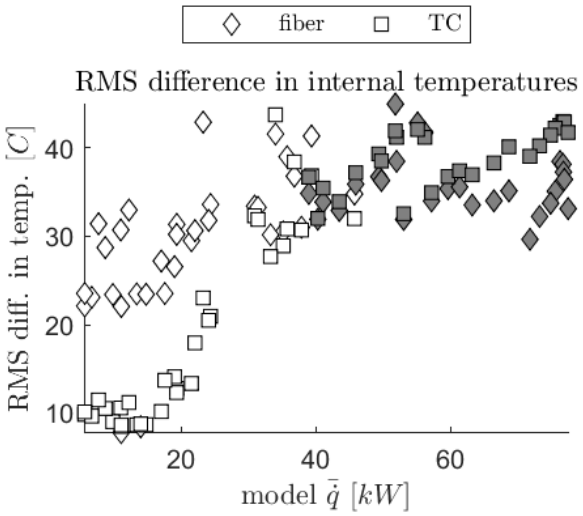

Figure 4.17: Comparison of modeled and measured body temperatures for all experiments. RMSD of fiber is for 7542 points and RMSD of thermcouples are for 8 TCs. Gray fill indicates Re_{ch} >17,056.

Chapter 5

Mechanical Analysis of PCHE Loading

5.1 Introduction

5.1.1 loading at design conditions

Measurement and thermohydraulic modeling resolved fluid and structural temperatures within the recuperator in Section 3.1. A small footprint of 120.7×577.4 mm allowed the recuperator to be run within an existing CO_2 loop and while performing over a large range of experimental extremes of mass flow, see Table 5.1.

At the designed flow rate CO_2 temperatures within the Printed Circuit Heat Exchanger (PCHE) are well distributed, see Figure 5.1. Hot CO_2 is cooled uniformly within the counter-flow core. Temperature variation across the core occurs as some of the hot CO_2 entering from the top left makes a longer pass through the left side transition, where it is pre-cooled

Table 5.1: Recuperator Design Performance

	design flow	high flow	extreme flow
run	14	37	60
$\dot{m}$ (kg/s)	0.0336	0.1086	0.2646
$\dot{q}$ (kW)	18.00	42.70	80.29
$T_{C_{in}}$ (C)	55.0	63.5	101.5
$P_{C_{in}}$ (MPa)	11.55	11.59	20.08
ΔP_C (kPa)	20.49	161.3	594.9
$T_{H_{in}}$ (C)	495.5	428.6	397.0
$P_{H_{in}}$ (MPa)	11.35	10.16	14.71
ΔP_H (kPa)	31.76	282.6	1261.6
Re_C	5131	17,295	53,326
Re_H	6097	19,818	64,234
ε (%)	95.0	90.0	83.7
UA (W/K)	477	756	1155

by cold CO_2 leaving the counter-flow core. Similarly, cold CO_2 entering from the top right is pre-heated in the right side transition. PCHE body temperature falls between the hot and cold streams.

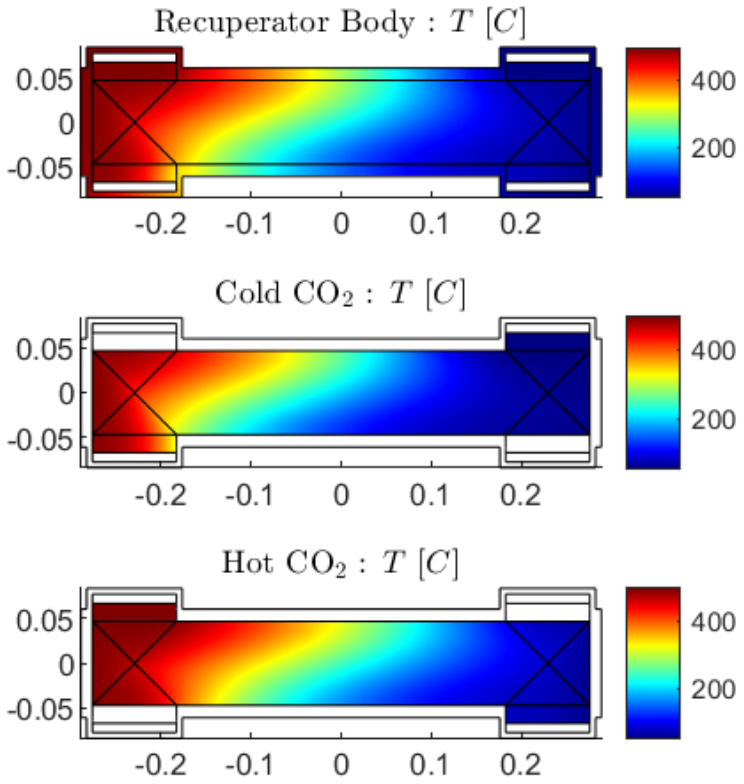

Figure 5.1: Temperature distribution within the unit cell solid body, cold CO_2 stream, and hot CO_2 stream.

Pressures within the hot and cold CO_2 streams are also determined in the thermohydraulic model. Pressure is directly applied to the inside of the headers. Insdide of the micro-channel, hot and cold pressures are averaged into a representative force at the micriochannel region boundary.

The PCHE body temperature is input into the mechanical model of the PCHE. This provides both the temperature at which to evaluate 316 properties and the basis for differential

thermal expansion within the PCHE model.

The difference between hot and cold CO_2 fluid channel walls is applied as a separate loading, which is internal to the micro-channel structure.

Areas of high thermal stress exist within the cold CO_2 exit and transition (bottom left of Figure 5.1). Thermal gradients are highest here as fairly uniform hot CO_2 flowing down and over from the hot inlet (top left) first encounters exiting cold CO_2. The cold CO_2 stream flow is not uniform, with flow maldistribution shifting a greater weight of flow, and thus heat transfer, to the bottom side of the PCHE. A detailed analysis of the PCHE thermohydraulic state is discussed in Section 3.1.

5.1.2 stress classification

Stress limits in the nuclear code vary based on the classification of the stress. Classification is dictated by two factors: the load which produces the stress, and the component of stress as evaluated using linearization techniques. In this way BPVC Sec. III Div. 5 assigns greater restrictions to mechanical loads, like pressure, that yield average through wall stress. Thermal loads that yield local stress concentrations are less restricted. Thermal loadings are considered less limiting as they can relax, unlike pressure loads.

load controlled stresses

Stress is the result of various loadings, which can be evaluated separately and combined to get the total stress at the diffusion bond,

$$\sigma_{total} = \sigma_P + \sigma_{\nabla T} + \sigma_{\Delta T_{ch.}} \tag{5.1}$$

Each stress component is evaluated separately, in the following manners,

- σ_P, stress from internal pressurization of the micro-channels. A thermohydraulic model

supplies the pressure loads that are applied at the PCHE scale model. Resulting stress at the micro-channel diffusion bond is resolved through stress mapping.

- $\sigma_{\nabla T}$, stress from differential expansion across the PCHE. The thermohydraulic model provides temperature variation throughout the PCHE solid, which is applied as a thermal expansion load in the PCHE scale model. Resulting stress at the micro-channel diffusion bond is resolved through stress mapping.

- $\sigma_{\Delta T_{ch.}}$, stress in the micro-channel walls from differential expansion of hot and cold channels. The thermohydraulic model provides the temperature difference between the hot and cold walls. Analysis of the micro-structure provides a relation between fluid wall ΔT and bondline stress.

When reporting stress, the Cauchy tensor for is implied,

$$\sigma = \lfloor \sigma_{11}, \sigma_{22}, \sigma_{33}, \tau_{12}, \tau_{23}, \tau_{31} \rfloor^T \tag{5.2}$$

When reporting equivalent stress, the von Mises stress is used,

$$2\sigma^2_{\text{eqv.}} = (\sigma_{11} - \sigma_{22})^2 + (\sigma_{22} - \sigma_{33})^2 + (\sigma_{33} - \sigma_{11})^2 + 6\left(\tau^2_{12} + \tau^2_{23} + \tau^2_{31}\right) \tag{5.3}$$

stress linearization

To check the load controlled stress limits of HBB-3220, SCLs are placed at ligaments of minimum thickness in the same-stream and cross-stream micro-channel walls, as shown in Figure 5.8. Stress linearization allows the through-thickness elastic field stress along the SCLs to be decomposed into equivalent membrane, bending, and peak stresses for comparison with appropriate allowable limits.

- Membrane stress is the average stress through the thickness

- Bending stress is the linearly varying stress through the thickness
- Peak stress is the total stress minus the membrane plus bending stress

Stress linearization was developed in the pressure vessel industry by Kroenke and Gordon in the 1970s[44, 45, 46]. A more recent overiew of stress linearization in elastic design by analysis is given by Mackenzie[47]. It was first implemented in BPVC Sec. III Div. 5 and BPVC Sec. VIII Div. 2 of the American Society of Mechanical Engineers (ASME) Boiler and Pressure Code.

The stress distribution along the SCL is approximated with an equivalent linear stress distribution, similar to what would be the result of an analysis using shell theory. Linearized membrane and bending stress components are resolved from the net forces and moments on a the micro-channel sub-unit. The linearized stress consists of six stress quantities representing the normal n, out-of-plane l, and tangential t components of the SCL.

$$\{\sigma_{nlt}\} = \begin{bmatrix} \sigma_{nn} & \sigma_{ll} & \sigma_{tt} & \tau_{nl} & \tau_{lt} & \tau_{nt} \end{bmatrix}^T \tag{5.4}$$

Membrane, bending, and secondary stresses are calculated in this frame.

5.1.3 Properties of 316 stainless steel

The recuperator is made of diffusion bonded 316 stainless steel plates. Properties for 316 are taken from BPVC Sec. II D. The modulus of elasticity and instantaneous coefficient of thermal expansion both depend on the steel temperature. These are plotted in Figures 5.2 & 5.3. The Poison's ratio is constant with temperature at 0.31.

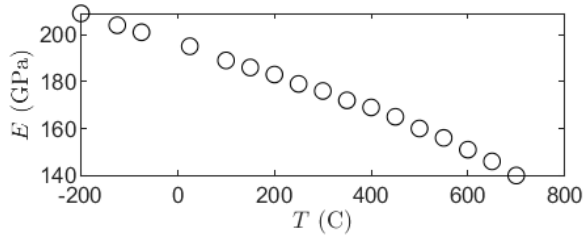

Figure 5.2: Elastic modulus of 316 stainless steel.

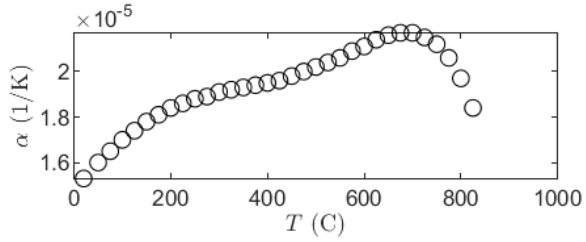

Figure 5.3: Instantaneous coefficient of thermal expansion for 316 stainless steel.

5.2 Mechanical Characterization of Micro-channel Structure

Considering the PCHE as a structure composed of representative sections simplifies the PCHE mechanical model. Modeling the full PCHE would require resolution of each of the 168 hot and 198 cold 1.01 mm diameter channels. It is simpler to separate the behavior of the micro-channel from that of the larger 120.7×577.4×33 mm PCHE. This is achieved by substituting in a model of the subunit micro-structure. Figure 5.4 shows a schematic of the test recuperator, identifing the regions of repeating micro-channel which can be modeled as subunits.

Two conditions must be met for the substitution of the micro-channel with subunits to be valid. First, the PCHE must contain sections of repeating micro-channel geometry from which a subunit can be withdrawn. The second condition is that the mechanical model of both the PCHE and subunits be linear-elastic. Sticking with linearly elastic materials allows for the superposition of stress states. This is necessary, as response of the subunit can be

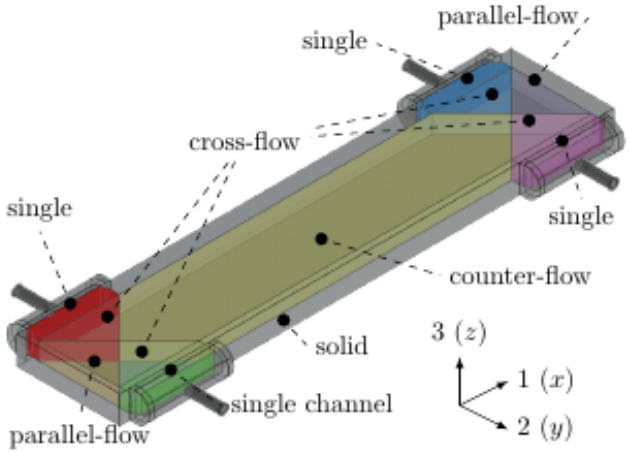

Figure 5.4: Regions consisting of repeating micro-channel structure within the 3D PCHE model. Each region's structure is described by a subunit from Figure 5.5.

separated into that of principal loadings, and the stress at SCLs evaluated as a superposition loadings.

The sections of repeated geometry are noted in Figure 5.4. The mechanical structure of each region can be characterized with a repeating subunit. The zig-zag PCHE consists of four repeating subunits as show in Figure 5.5: single channel, cross-flow, and counter-

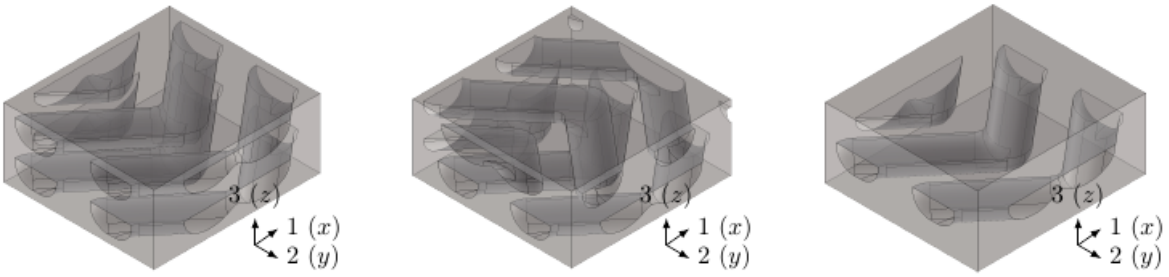

(a) counter-flow, parallel-flow (rotate 90° about z)

(b) cross-flow

(c) single channel

Figure 5.5: subunits of the repeating geometry. These correspond to the counter-flow & parallel-flow, cross-flow, and single channel regions of Figure 5.4.

Table 5.2: Stress classification within micro-channel subunit

	lowest flow	design flow	high flow
$\dot{m}$ (kg/s)	0.0123	0.0336	0.1086
$\dot{q}$ (kW)	6.28	18.00	42.70
Re_C	1888	5131	17,295
Re_H	2309	6097	19,818
ε (%)	95.6	95.0	90.0
UA (W/K)	214	477	756

flow and parallel-flow. The counter-flow and parallel flow regions contain the same micro-channel, just different flow orientation. The parallel-flow region is just a 90° rotation of the counter-flow micro-channel. As counter-flow and parallel-flow are geometrically the same, but orthogonally different, a single analysis of the common counter-flow is used.

Modeling the response of the micro-channel to principal deformations allows homogenized properties of the subunit to be deduced. The micro-channel can be replaced with a homogeneous orthogonal material who's deformation is governed by the stress tensor of Equation (5.5). This substitution is similar to a porous material substitution.

5.2.1 Orthogonal Material Simplification

The substitution of a homogeneous, orthogonal material for a material with geometry requires an evaluation of the orthotropic stiffness of the subunit. Deformation of the micro-channel subunit can be defined using an orthotropic stiffness tensor. Stresses applied to the subunit boundaries are born by the micro-channel structure. Deformation of the subunit depends on the orthotropic stiffness, [**K**], of the micro-channels,

$$\epsilon = \mathbf{K}\sigma \tag{5.5}$$

where σ is evaluated over the boundary faces of the subunit.

Equation (5.5) is the inverted form of Hooke's law, and thus the orthotropic elasticity tensor, $\mathbf{E}$ is simply the inverse of the stiffness tensor, $\mathbf{K}^{-1}$.

simplified methodology

Stiffness of the subunit can be analyzed using simple methods without having to evaluate a 3D finite element model of the subunit micro-structure. This can provide a quick estimate of orthotropic stiffness that is reasonably close to that obtained through full 3D analyses, see Table 5.4.

Considering the Zig-zag channel geometry of Table 2.4, the zig-zag core micro-channel structure would appear as shown in Figure 5.6. Here alternating layers of hot side (red) and cold side (blue) etched plates are stacked. A subunit representing the structure of the core micro-channel can be selected, as outlined in magenta. The sub unit has characteristic directions 1,2,3 along which the core structure repeats.

A conservative examination of the zig-zag micro-channel geometry establishes the orthotropic stiffness based on the wall thickness at the gross structural discontinuities of the micro-channel. These are the same-stream and cross-stream wall thicknesses, th_{ss} and th_{as}, show in Figure 5.6.

The orthotropic stiffness of the subunit is related to the mechanical properties of the base material from which it is made: the elastic modulus, E_b, shear modulus, G_b, and Poison ratio, ν_b.

Stiffness of the subunit in the 1 direction is related to the reduced area of material coverage within the 23 plane (bottom of Figure 5.6). Here the subtraction of the semi-circular etch profile is taken into account. A conservative estimate of stiffness in the 2 direction is taken by treating all deflection as occuring in the cross-stream wall, th_{as}. Stiffness in the 3 direction is dictated by the same-stream wall, th_{ss}. The contribution to orthotropic stiffness in the

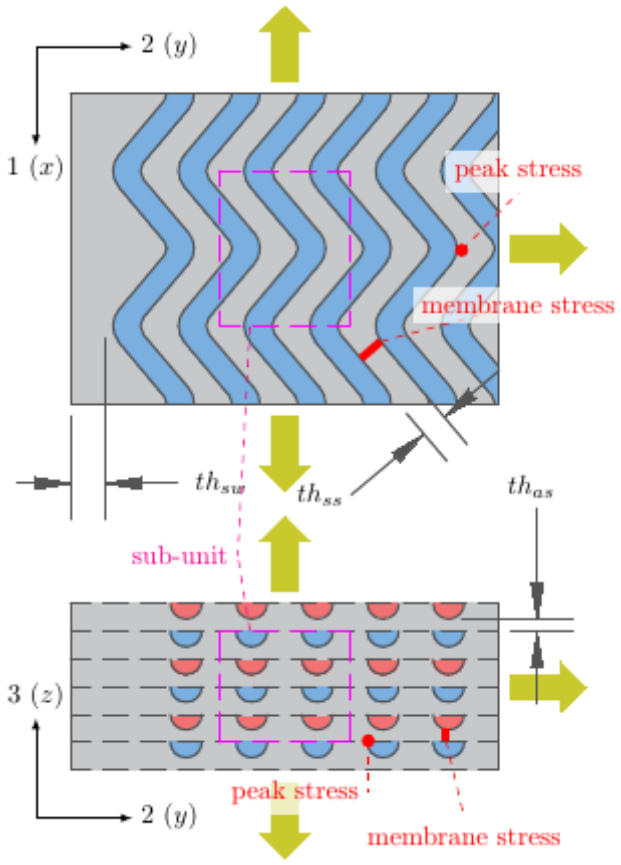

Figure 5.6: Breakdown of counter-flow zig-zag channel micro-structure.

normal directions are thus,

$$\begin{aligned} E_{11} = & \quad \tfrac{pt-0.5\pi h^2}{pt} E_b & = 0.781 E_b \\ E_{22} = & \quad \tfrac{th_{as}}{t} E_b & = 0.447 E_b \\ E_{33} = & \quad \tfrac{th_{ss}}{th_{ss}+w} E_b & = 0.411 E_b \end{aligned} \tag{5.6}$$

A simple analysis cannot predict the Poison ratio of the zig-zag structure, thus it is assumed to be constant,

$$\nu_{12} = \nu_{23} = \nu_{31} = \nu_b = 0.31 \tag{5.7}$$

A simple analysis does not account for bending in the micro-channel walls when considering the subunit's shear moduli. Shear vectors applied in the 23 and 13 planes are born by the same-stream walls. Shear vectors applied in the 12 plane are supported by the micro-channel cross-section whose area is somewhat reduced by the semicircular channels. Thus a simple approximation of the contribution to orthotropic stiffness for the shear is,

$$\begin{aligned} G_{12} = & \quad \tfrac{pt-0.5\pi h^2}{pt} G_b & = 0.781 G_b \\ G_{23} = G_{31} = & \quad \tfrac{th_{ss}}{th_{ss}+w} G_b & = 0.411 G_b \end{aligned} \tag{5.8}$$

micro-channel subunit model

Each component of the tensor is evaluated by modeling deflection in a 3D geometry subunit. Constant material properties for 316 Stainless Steel at 22°C are applied to the micro-channel structure. The subunit boundaries are constrained so that only primary tensile or shear deformation occurs. The unit–cell is exercised in the six primary deformations, three tensile (Figures 5.9a-5.9c) and three shear (Figures 5.9d-5.9f). The infinite repeating nature of the micro-channel structure dictates that subunit boundaries maintain their parallelism and do not experience bending. This is enforced through topological constraint equations, applied

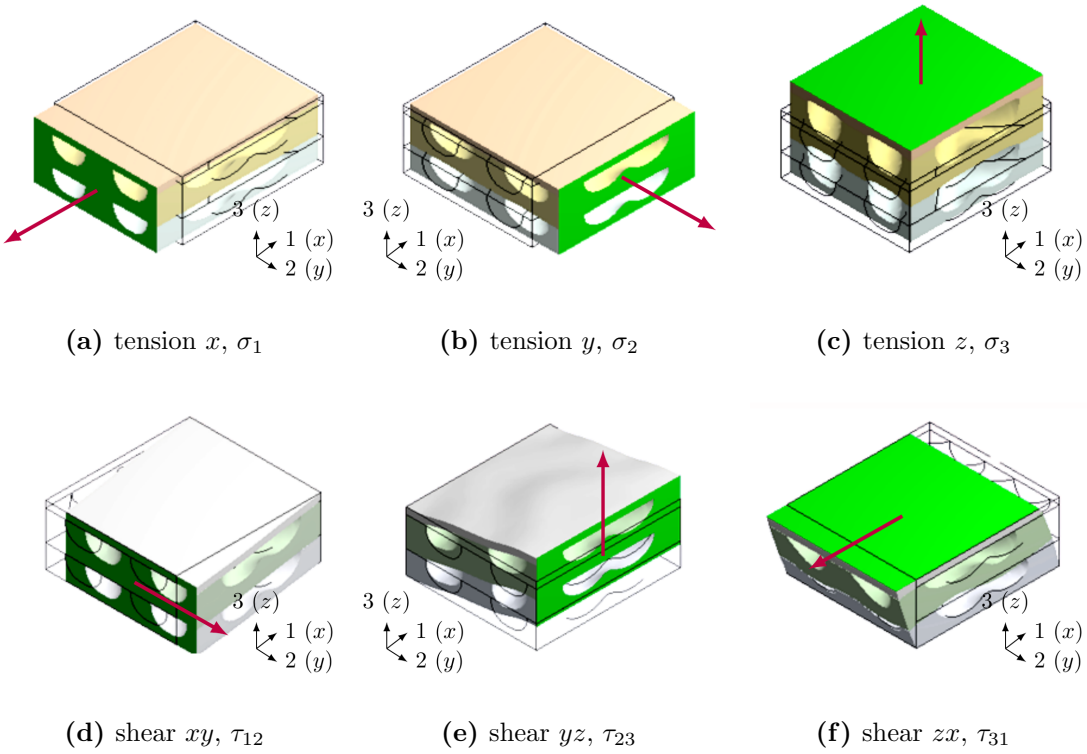

(a) tension x, σ_1 **(b)** tension y, σ_2 **(c)** tension z, σ_3

(d) shear xy, τ_{12} **(e)** shear yz, τ_{23} **(f)** shear zx, τ_{31}

Figure 5.7: Principal loadings and deformations in counter-flow subunit model.

at the subunit boundaries.

Normal and shear strains of 0.2% strain are applied and the reaction force is calculated. The cross-sectional area of the subunit in each orthogonal plane is recorded as well as the dimensions of the subunits bounding box. See Table 5.3.

Strain in the subunit volume is determined from the deflection of the subunit boundaries. Stress on the subunit volume is determined from the reaction forces and areas of subunit boundaries. This stress is used with the 0.2% strain to define a directional elasticity for each loading scenario. The elasticities are tabulated in Table 5.4 and normalized against the bulk material elasticity.

Each subunit model was exercised with the three primary tensile and shear loadings shown in Figure 5.7. The modeling of the counter-flow subunit is detailed for one tensile

Table 5.3: Deformations and Stresses of the counter-flow subunit model

	subunit dimensions			
	1 (x)	2 (y)	3 (z)	
length (mm)	7.24	6.56	3.00	
area (mm^2)	19.7	21.7	47.5	
	deformation (μm)			**reaction (kN)**
	1 (x)	2 (y)	3 (z)	
tension 1	**14.484**	-4.195	-1.543	4.956
tension 2	-4.327	**13.128**	-1.364	5.112
tension 3	-2.879	-2.467	**6.000**	9.248
shear 12	-0.003	**14.484**	0.000	1.278
shear 23	0.000	-0.018	**13.128**	0.557
shear 31	**6.000**	0.000	0.000	2.841
	strain (mm/m)			**stress (MPa)**
	1 (x)	2 (y)	3 (z)	
tension 1	**2.001**	-0.639	-0.514	251.8
tension 2	-0.598	**2.001**	-0.455	235.3
tension 3	-0.398	-0.376	**2.000**	194.7
shear 12	0.000	**2.001**	0.000	65.0
shear 23	0.000	-0.003	**2.001**	25.6
shear 31	**2.000**	0.000	0.000	59.8

and shear loading. Results for all six loadings of the counter-flow subunit are given in Table 5.3. Results for the cross-flow and single channel subunits are given in Appendix Tables C.1 & C.3.

Consider the counter-flow subunit model subject to tensile deformation in the x-direction as shown in Figure 5.9f. The face normal to the (+) x-axis is coupled by a remote point so all the x-positions in the plane are the same. This face is also displaced such that 0.2% strain in the (+) x-direction is maintained. The face normal to the (-) x-axis is fixed. The plane normal to the (+) y-axis is coupled by a remote point. The plane normal to the (-) y-axis is supported by a frictionless support. The plane normal the (+) z-axis is coupled in the y-direction. The plane normal to the (-) z-axis is supported by a frictionless support.

These boundary conditions reflect the allowed deformation of a piece of material embedded in a bulk material experiencing pure tensile deformation. The 0.2% axial strain is confirmed,

$$\epsilon = \frac{x \text{ deformation}}{x \text{ length}} = \frac{0.0145 \text{ mm}}{7.24 \text{ mm}} = 0.2\% \tag{5.9}$$

The subunit stress is calculated from the reaction force and area of the subunit face,

$$\sigma^*_{11} = \frac{\text{reaction force}}{\text{face area}} = \frac{4.956 \text{ kN}}{0.197 \text{ mm}^2} = 251.8 \text{ MPa} \tag{5.10}$$

where the star indicates that the stress is that on the subunit volume, and not the stress within the micro-channel geometry.

The modulus for the counter-flow subunit in the 11 tensile deformation is then,

$$E_{11} = \frac{\sigma^*_{11}}{\epsilon} = 125.9 \text{ GPa} \tag{5.11}$$

Shear deformation in the xy plane of the counter-flow subunit model is shown in Figure 5.9d. The face normal to the (+) x-axis is bounded by a remote point to couple the x-position of the face. Additionally, this plane is applied a deformation of 0.2% of the x-length of the subunit in the (+) y-direction such that 0.2% strain is maintained. The face normal to the (-) x-axis is fixed. The faces normal to the (+) and (-) z-axis are constrained such that the planes can shift but must stay parallel with the 13 (xz) plane. The faces normal to the (+) and (-) y-axis each have their points coupled such that the rotation about the z-axis is the same. These constraints isolate the subunits response to primary shear.

The orthogonal deformations in the moved plane, the resultant force, and relevant dimensions, are listed in Table 5.3. The 0.2% strain is confirmed,

$$\gamma = \frac{y \text{ deformation}}{x \text{ length}} = \frac{0.0145 \text{ mm}}{7.24 \text{ mm}} = 0.2\% \tag{5.12}$$

The subunit stress is calculated from the reaction force and area of the subunit face,

$$\tau_{12}^{*} = \frac{\text{reaction force}}{\text{face area}} = \frac{1.278 \text{ kN}}{0.197 \text{ mm}^2} = 65.0 \text{ MPa} \tag{5.13}$$

The modulus for the counter-flow subunit in the 12 shear deformation is,

$$G_{12} = \frac{\tau_{12}}{\gamma} = 32.5 \text{ GPa} \tag{5.14}$$

dimensionless and dimensional dtiffness

The orthotropic elasticity of the micro-channel structure is related to the isotropic elasticity of the material from which it is constructed. The dimensionless stiffness of the structure provides the relation between the two. As the PCHE structure is made of 316 stainless steel with temperature dependent elasticity, E_b the orthotropic elasticity of the micro-channel structure is modeled thus,

$$\mathbf{E}_{ortho.} = E_b(T)\hat{\mathbf{K}}^{-1} \tag{5.15}$$

where $\hat{\mathbf{K}}$ is the dimensionless stiffness tensor of the subunit,

$$\hat{\mathbf{K}} = \begin{bmatrix} \frac{1}{\hat{E}_{11}} & -\frac{\nu_{21}}{\hat{E}_{22}} & -\frac{\nu_{31}}{\hat{E}_{33}} & & & \\ -\frac{\nu_{12}}{\hat{E}_{11}} & \frac{1}{\hat{E}_{22}} & -\frac{\nu_{32}}{\hat{E}_{33}} & & & \\ -\frac{\nu_{13}}{\hat{E}_{11}} & -\frac{\nu_{23}}{\hat{E}_{22}} & \frac{1}{\hat{E}_{33}} & & & \\ & & & \frac{2(1+\nu)}{\hat{G}_{23}} & & \\ & & & & \frac{2(1+\nu)}{\hat{G}_{31}} & \\ & & & & & \frac{2(1+\nu)}{\hat{G}_{12}} \end{bmatrix} \tag{5.16}$$

the components of which are listed for each subunit model in Table 5.4.

The dimensionless components within Equation (5.16) are obtained by normalizing the

Table 5.4: Components of dimensionless stiffness tensor from different calculation methods.

	simplified analysis	**micro-channel subunit model**		
		counter-flow	cross-flow	Single Channel
$\hat{E}_{11}$	0.781	0.646	0.623	0.827
$\hat{E}_{22}$	0.447	0.604	0.627	0.805
$\hat{E}_{33}$	0.411	0.500	0.438	0.606
$\hat{G}_{23}$	0.168	0.172	0.175	0.257
$\hat{G}_{31}$	0.168	0.402	0.392	0.556
$\hat{G}_{12}$	0.298	0.437	0.455	0.544
ν_{12}	0.310	0.309	0.305	0.307
ν_{31}	0.310	0.228	0.225	0.181
ν_{23}	0.310	0.208	0.226	0.180
† parallel-flow is a 90° rotation of counter-flow x.				

tensile and shear moduli of the subunit. Normalization is relative to the isotropic elasticity, E, used in the subunit model.

$$\hat{E}_{ii} = \frac{E_{ii}}{E},\ \hat{G}_{ij} = \frac{G_{ij}}{E} \tag{5.17}$$

Take, for example, the primary tensile and shear loadings of the counter-flow subunit shown in Figures 5.9a & 5.9d. The tensile and shear moduli were calculated using model reactions in Equations (5.11 & 5.14), and are normalized by the elastic and shear moduli used in the model,

$$\hat{E}_{11} = \frac{E_{11}}{E} = \frac{125.9 \text{ GPa}}{195 \text{ GPa}} = 0.646 \tag{5.18}$$

$$\hat{G}_{12} = \frac{G_{12}}{G} = \frac{32.5 \text{ GPa}}{74.3 \text{ GPa}} = 0.437 \tag{5.19}$$

Poisson ratio terms describe the contraction in i resulting from the tensile strain in direction j. A symmetrical $\hat{\mathbf{K}}$ is used, so the orthotropic Poisson ration is taken as the

average of the ij and ji strains,

$$\nu_{ij} = -\frac{\epsilon_{ij} + \epsilon_{ji}}{2\epsilon_{jj}} \tag{5.20}$$

$$\nu_{12} = -\frac{-0.0598\% - 0.0639\%}{2 * 0.2\%} = 0.309 \tag{5.21}$$

5.2.2 Stress Classification and Mappping

The PCHE model uses an orthogonal material simplification to model micro-channel regions. Stress on the subunit volume must be mapped to the micro-channel to observe the local impact of geometry. This section details the stress map from global (heat exchanger size) to local (microchannel) stresses and the definition of the Von Mises Equivalent stress using ANSYS components.

Stress Classification Lines

Stress Classification Lines (SCL) are placed at gross structural discontinuities of the microchannel structure. In the zig-zag micro-channel the SCLs lie at the minimum wall thicknesses, the area with the highest stress and least support. Two SCLs were investigate, marked in Figure 5.8, for the same-stream and cross-stream walls. Local Structural Discontinuities exist at the corners of the zig-zag turns and at the sharp corners of the semicircular micro-channel cross-section, but are not considered in this analysis.

The same-stream SCL spans the micro-channel wall separating CO_2 of the same hot or cold stream. This SCL is oriented within the x, y plane of the PCHE, spanning the 1.032 mm thickness of the same-stream wall. Minor failures within this wall, such as a cracking and localize yielding, are allowed as these will not result in mixing of the fluid streams. Full rupture at this SCl is not tolerated, as this will lead to loss of structural support.

The cross-stream SCL bridges the micro-channel wall separating the hot and cold CO_2

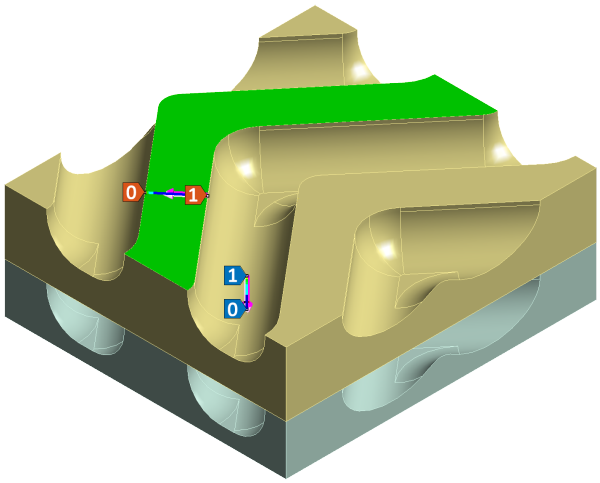

Figure 5.8: Stress Classification Lines (SCLs) and the diffusion bond interface within a subunit the zig-zag micro-channel core. Bondline of one zig-zag wall is highlighted green. SCLs are same-stream (horizontal orange) and cross-stream (vertical blue).

streams. This SCL is oriented along the z direction of the PCHE, spanning the 0.671 mm thickness of the cross-stream wall. In the case of this CO_2 to CO_2 recuperator, minor failures such as cracking or localized yielding is tolerated. However, in some PCHE applications this SCL might represent a chemical or radiological boundary. As with the same-stream SCL, the cross-stream wall is part of the PCHE structure and thus full rupture is not tolerated.

The linearized stress can be determined from the subunit stress using stress mapping. A stress map, $[\Lambda_\sigma]$, is made of each SCL within the micro-channel structure. This map transforms the subunit stress, $\{\sigma_{123}\}$, found in full-scale orthotropic analysis to the micro-channel SCL level,

$$\{\sigma_{nlt}\} = [\Lambda_\sigma]\,\{\sigma_{123}\} \tag{5.22}$$

mapping SCL stress

As a linear elastic model, the stress anywhere within the subunit is proportional to the stress applied at the boundaries of the subunit. Thus, any component of stress within an SCL, σ_{scl}, can be mapped from the global stress of the PCHE model, σ, using a transform Λ_σ,

$$\sigma_{\text{scl}} = [\Lambda_\sigma]\sigma \tag{5.23}$$

The stress map Λ_σ is built by collecting the tensor response to the six orthogonally applied loads of the subunit model. Each of the six columns of Λ_σ represents the stress response at the SCL normalized by the applied load,

$$\{\Lambda_\sigma\}_j = \frac{\sigma_{\text{scl}}}{\sigma_{ij}} \tag{5.24}$$

Response of the same-stream and cross-stream SCLs to the six principal loadings was obtained using the 3 micro-channel subunit models shown in Figure 5.5. Stress linearization of the elastic field gave an evaluation of the membrane, bending, peak, and total stress. The linearization terms were then normalized by the subunit stress per Equation (5.23), creating stress maps for each component. The calculated stress maps are given for both SCLs for the counter-flow subunit is Appendix Table C.4. Stress maps for the cross-flow and single-channel subunits are not given in the Appendices as these would append superfluous data.

Stress along the SCLs manifests differently in the same-stream and cross-stream micro-channel walls. Equivalent stresses within the counter-flow subunit model for same-stream and cross-stream SCLs are shown in orange and blue in Figure 5.9. Here the position along the SCL from start 0 to end 1 is plotted on the vertical and stress on the horizontal axes. Lines of total stress are shown along side dotted and dashed lines of the membrane and

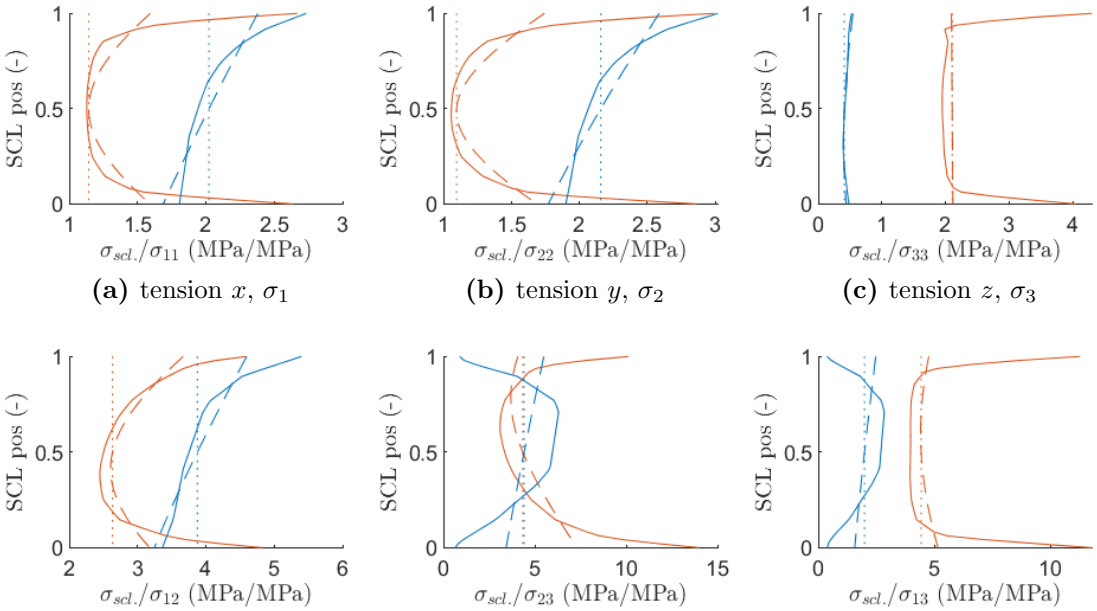

(a) tension x, σ_1 **(b)** tension y, σ_2 **(c)** tension z, σ_3

(d) shear xy, τ_{12} **(e)** shear yz, τ_{23} **(f)** shear zx, τ_{31}

Figure 5.9: Stress mapping within the counter-flow subunit model. Total (solid line), membrane (dotted line), and membrane + bending (dashed line), components of linearized stress are plotted along length of the same-stream SCL (orange) and cross-stream SCL (blue). See Figure 5.8 for SCL locations.

membrane + bending stress linearization.

Geometric discontinuities within the zig-zag micro-channel result in bending stresses that are higher in the the same-stream wall than the cross-stream wall.

The same-stream wall contains stress 90° corners which highly elevate the elastic field near the SCL edges. Linearization of this elastic field results in a high evaluation of bending stress within the same-stream SCL. As the cross-stream wall does not contain geometric stress concentrations, its linearization contains bending stresses which are closer to the elastic field.

Stress resulting from the six principal subunit loadings are,

tension x **&** y**,** σ_1 **&** σ_2 : (Figures 5.9a-5.9b) These primarily load the cross-stream SCL, who's micro-channel wall provides support in the x and y directions. Membrane stress is 2-2.2 $\times$ higher than the subunit stress. This ratio can be deduced by comparing the cross-stream wall's coverage in the x and y directions: $t/(h-t) = 2.24$. Some bending is introduced as arching micro-channel creates more stiffness at the end of the cross-stream wall. Stress in the same-stream SCL is small, with some membrane stress developing in reaction to Poison ratio shrinkage of the micro-structure in z.

tension z**,** σ_3 : (Figure 5.9c) This primarily loads the same-stream SCL, who' micro-channel wall provides support against z oriented loading. Membrane stress is 2.1 $\times$ higher than the subunit stress. This ratio can be deduced by comparing the bondline coverage. There is no bending about the same-stream wall as its structure is symetrical and balanced. A small amount of stress is realized in the cross-stream SCL due to the contraction of the structure in the xy plane.

shear xy**,** τ_{12} : (Figure 5.9d) The same-stream wall sees less shear in this mode as it is less stiff in y shear deflection than the cross stream wall. The x orientation of the channels makes the micro-structure the least stiff in this shear deformation. The cross-stream wall sees more stress at the top of its SCL as the arching micro-channel transfer some shear from the same-stream walls.

shear yz**,** τ_{23} : (Figure 5.9e) This is the stiffest shear orientation, with both SCLs see seing a 5 $\times$ multiplier on shear stress.

shear zx**,** τ_{31} : (Figure 5.9f Shear in this deformation is primarily resisted at the diffusion bond. This is seen in the high and uniform distribution of stress across the same-stream wall.)

fluid wall thermal stress

The contribution of internal thermal stress resulting from the difference in hot and cold CO_2 stream temperatures must also be accounted for. Fluid wall temperatures create a thermal gradient within the micro-channel structure, the reaction to which is entirely contained within the structure. The structure cannot relieve this thermal stress through relaxations, as neighboring channels within the repeating structure of the PCHE resist any non-uniform exansion or contraction.

A linear temperature gradient within a constrained homogeneous solid compresses material at the hot side, while putting the cold side in tension. The magnitude of compressive and tensile stresses are,

$$\tau = \frac{1}{2}\alpha E_b \left|T_{H,wall} - T_{C,wall}\right| \tag{5.25}$$

where α is the instananeous coefficient of thermal expansion, and E_b the modulus of elasticity, of the base material.

The driving temperature difference can be determined from the density of heat flow, $\dot{q}_V$, the conductivity of the base material, k, the thickness of the wall, and the hydraulic diameter,

$$\left|T_{H,wall} - T_{C,wall}\right| = \dot{q}_V \frac{th_{as}}{k}\frac{D_h}{4} \tag{5.26}$$

This formulation is most usefull as heat flow density within a CHX can be directly output

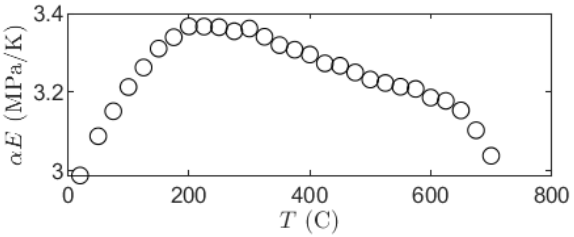

Figure 5.10: Combination of thermal expansion and elastic modulus which determines cross-stream thermal stress.

from CHX thermohydraulic models[48].

For 316 stainless steel the combination of thermal expansion and elasitic modulus, αE in Equation (5.25) is relatively stable with temperature. Figure 5.10 shows that αE doesn't vary much above 200°C. A conservative estimate for calculating the cross-stream thermal stress takes the maximal value of $\alpha E = 3.37$ MPa as a representative constant for all temperatures. Equation (5.25) would then give 1.87 MPa of thermal stress per °C of difference. This is a low estimation for the zig-zag micro-channel, as the void of the channel localizes the reaction to the thinner cross-steam wall.

A more accurate estimate of cross-stream thermal stress is obtained through the subunit models. This is modeled by assigning hot and cold temperature conditions to the fluid channel walls within a 3D conduction analysis. The resulting thermal gradient is largely across the cross-stream wall, with no gradient in the same-stream wall. Thermal expansion within the subunit model is constrained by boundaries that are kept planar and parallel, as would be in an infinitely repeating structure.

Stress accumulates at the expansion of the hot side channel structure is in opposition to contraction of the hot side. This puts the cross-stream wall in a state of balanced tension and compression. Figure 5.11 shows the equivalent stress across the cross-stream SCL. Here the change from compression to tension passes through an unstressed state bout 60% of the way through the SCL. Expansion and compression do not perfectly cancel , the asymmetry

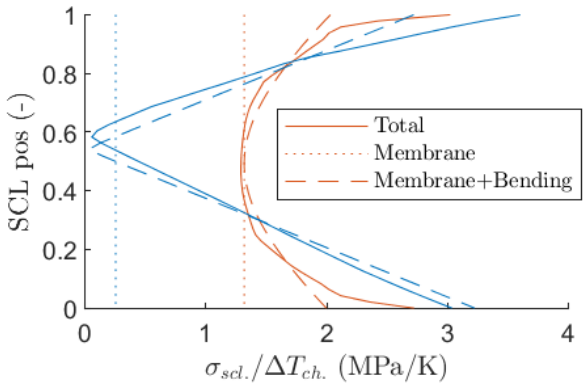

Figure 5.11: Fluid wall ΔT stress mapping within the counter-flow subunit model. Total, membrane, and membrane + bending, components of linearized stress are plotted along length of the same-stream SCL (orange) and cross-stream SCL (blue). See Figure 5.8 for SCL locations.

of the cross-stream wall leaving a slight membrane stress in the cross-stream SCL.

Stress within the same-stream SCL is more uniform and totally tensile or compressive in the cold and hot micro-channels. The symmetry of the structure and the cross-channel wall constrains the expansion and contraction of the same-stream SCL walls. As with the external loading of the subunit structure, stress concentrations at the ends of the same-stream SCL create large peak stresses.

Response of the same-stream and cross-stream SCLs to fluid-wall thermal expansions can be mapped in a similar fashion to that of the principal subunit loadings. Instead of using the stress state of the PCHE model, as in Equation (5.23), the fluid-wall thermal stress can be mapped to the difference in hot and cold wall temperature obtained in the thermohydraulic model.

$$\sigma_{\Delta T_{ch.}} = \Lambda_{\Delta T_{ch.}} \sigma \tag{5.27}$$

Stress linearization of the elastic field gave an evaluation of the membrane, bending, peak, and total stress. The linearization terms were then normalized by the temperature gradient,

elasticity, and thermal expansion coefficient of the subunit model,

$$\{\Lambda_{\Delta T_{ch.}}\}_j = \frac{\sigma^T_{\text{scl}}}{\alpha E_b \left|T_{H,wall} - T_{C,wall}\right|} \tag{5.28}$$

Calculated maps are given for both SCLs for the counter-flow, cross-flow and single channel subunits in Appendix Tables C.5-C.5.

5.2.3 Hot-Cold Channel Differential Expansion

5.3 3D Heat Exchanger Simulation

5.3.1 Geometry

The PCHE is modeled as a half geometry, with an xy plane of symmetry chosen at the center of the PCHE plate stack. The geometry and mesh are shown in Figure 5.12, with the micro-channel regions highlighted using the same color scheme as Figure 5.4. The hot inlet is at the top left, the cold outlet at the bottom left, the hot outlet at the bottom right, and the cold inlet at the top right.

The PCHE structure is meshed using a combination of linear tetrahedral and hexahedral elements. Hexahedral elements are used in the micro-channel regions as they best conform with coordinate definition of the subunit analysis. Hexahedral elements that align with the principal xyz of the micro-channel subunits approximate the stiffness of the micro-channel structure with less numerical error. The solid sides, top/bottom plates, headers, and nozzles are all modeled using tetrahedral elements for easier mesh conformity. As these are composed of solid isotropic 316, no accuracy is lost in using non-rectilinear elements.

Within the micro-channel regions a 28,432 element hexahedral mesh is used, with the base element being 1.625 mm square. Further mesh refinement is unnecessary as this does not

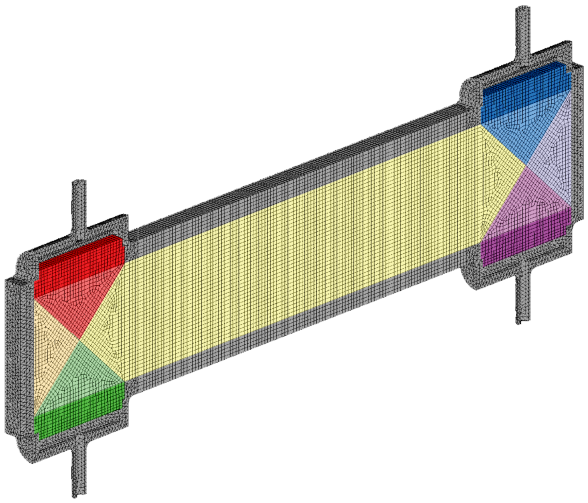

Figure 5.12: Mesh of the PCHE model. Regions of repeating micro-channel are modelled using orthotropic stiffness. Color coding corresponds to Figure 5.4.

improve results at geometric stress concentrations and nonlinearities. Any further resolution of the mesh will give a non-physical solution, as this would result in hexahedral elements smaller in volume than the micro-channel subunits which they are approximating.

The mesh was not optimized to capture the headers and nozzles perfectly, as these were not the focus of this analysis. The headers and nozzles are only included in the PCHE model insofar as the transfer pressure and thermal loading to the micro-channel regions of the PCHE. Future models could look at resolving the header and nozzle walls in more detail, and evaluate SCLs within these components.

5.3.2 Operational Temperatures and Pressures

The temperature loading of the material and pressure loading on the channels is imported and the mechanical response within the PCHE is found. The global stresses found in the PCHE model are then mapped back to the micro-channel's local stresses.

The designed operating condition of the PCHE is considered. Designed flow is 0.0336

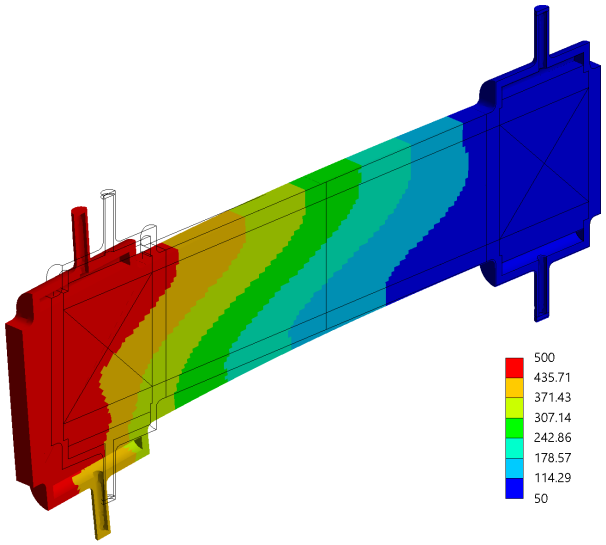

Figure 5.13: Temperature loading within the PCHE and resulting thermal expansion. Scale is 50→500 °C. Deformation shown is exaggerated by ×10.

kg/s of CO_2 at 11.5 MPa, with a 55→429°C rise in CO_2 temperature on the cold side and a 496→69°C drop on the hot side. Performance and other conditions are given in Table 5.1.

Temperature of the solid and micro-channel geometry is applied directly to the mechanical model of the PCHE. Temperatures are interpolated from the thermohydraulic model onto the element centers of the half PCHE model as shown in Figure 5.13. Temperature variation is predominately in the xy plane, as thermal gradients are flow and heat transfer driven. Little temperature variation exists in the z.

Thermal expansion creates deflection of the 500°C hot end of the PCHE. An exaggerated deformation 10× that of the real thermal deformation is shown in Figure 5.13. An undeformed wireframe is superimposed for comparison.

Differences in thermal expansion cause the PCHE to bend about the z axis. Here side entrance effects and flow maldistribution in the cold CO_2 side cause the top side ($+y$) of the PCHE to be hotter than the bottom ($-y$) side. The difference in temperature causes the top side of the PCHE to expand more than the bottom side, bending the hot side of the PCHE

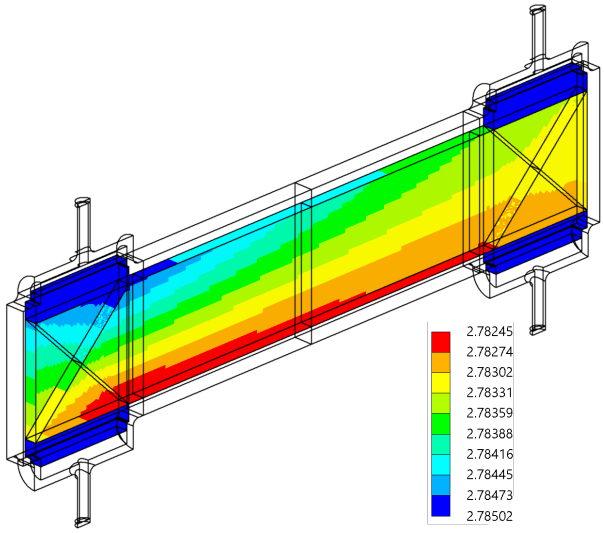

Figure 5.14: Pressure loading of the micro-channel region boundaries in MPa. Pressure is projected from internal hot and cold CO_2 fluid pressures as determined in Equation (5.29).

down in y. This bending forms a neutral axis roughly along the central x axis. Above this neutral axis the PCHE is in compression, and below this axis in tension. This drives large thermal stresses within the micro-channel core.

Pressure within the micro-channels can be applied as a representative pressure at the boundary of the micro channel region. The representative pressure accounts for the reduced volume of pressurized CO_2 in the micro-channel, ϕ, as well as the balance between the 6 hot and 7 cold plates,

$$P_{\text{boundary}} = \phi \left(\frac{6}{13} P_H + \frac{7}{13} P_C \right) \tag{5.29}$$

The magnitude and location of the applied micro-channel boundary pressure is shown in Figure 5.14.

Experimental inlet and outlet pressures are applied to the inside of the headers and nozzles. Inlet and outlet pressures are 11.55& 11.53 MPa within the cold side headers and 11.35& 11.32 MPa in the hot side headers.

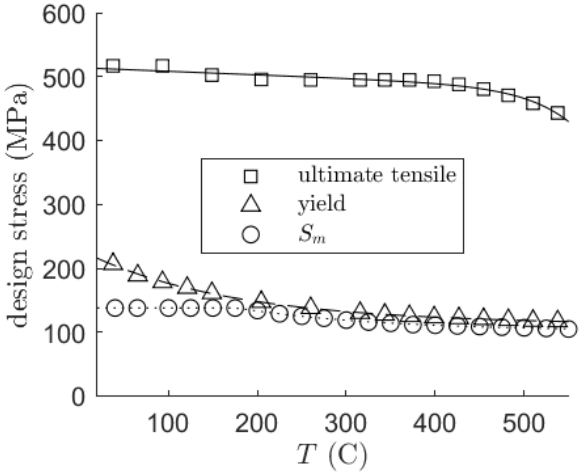

Figure 5.15: Stress limits for 316 stainless steel over 20-550°C PCHE operating range. Taken from BPVC Sec. II D Tables U, Y-1, and 5A.

5.3.3 design stress limits and safety factors

Evaluation of PCHE failure is dictated by the stress limits of 316 stainless steel. As stress limits decrease with temperature, they are evaluated locally over the temperature distribution show in Figure 5.13. Ultimate tensile strength, yields stress, and design stress intensity for 316 stainless steel are shown over the range of PCHE temperature in Figure 5.15.

Fits to the stress limits using T in °C were input into the PCHE model,

$$\sigma_{\text{uts}} = -0.001273e^{0.0194T} + 514.2e^{-0.000110T} \tag{5.30}$$

$$\sigma_{\text{y}} = 110.2e^{-0.006304T} + 119.0e^{-9.053\times10^{-5}T} \tag{5.31}$$

$$\sigma_{Sm} = min\left(138,\ 107.3e^{-0.005939T} + 100.2e^{2.1073\times10^{-5}T}\right) \tag{5.32}$$

Safety factors are calculated as the ratio of these stress limits to the equivalent stress

realized in the component,

$$\mathrm{SF_y} = \frac{\sigma_\mathrm{y}}{\sigma_\mathrm{eqv.}} \tag{5.33}$$

$$\mathrm{SF}_{Sm} = \frac{\sigma_{Sm}}{\sigma_\mathrm{eqv.}} \tag{5.34}$$

$$\tag{5.35}$$

5.4 Results

5.4.1 solid side walls, top/bottom plates

Stress within solid portions of the PCHE comes from a combination of pressure and thermal expansion loadings. The solid portions consist of the solid side wall, top/bottom plates, headers, and nozzles. Equivalent stress within these regions are shown in Figure 5.16. Here the total equivalent stress has distinct contributions from pressure and thermal loadings, shown in Figures 5.16b & 5.16c respectively.

Pressurization stress is highest in the headers and nozzles, where 11.32-11.55 MPa of internal pressure is contained. Stress on the solid side walls and top/bottom plates of the PCHE is negligible, as the internal pressure is born by the micro-channel regions.

Thermal expansion stresses are higher than pressurization stresses. All solid and micro-channel material are bonded together, leaving little room for stress relaxation. Three distinct regions of high thermal stress can be identified:

1. **stress in the core side walls:** Temperature differences between the top and bottom of PCHE cause the top side of the PCHE to expand more than the bottom side, bending the hot side of the PCHE down in y. This bending forms a neutral axis roughly along the central x axis. Above this neutral axis the PCHE is in compression, and below this axis in tension.

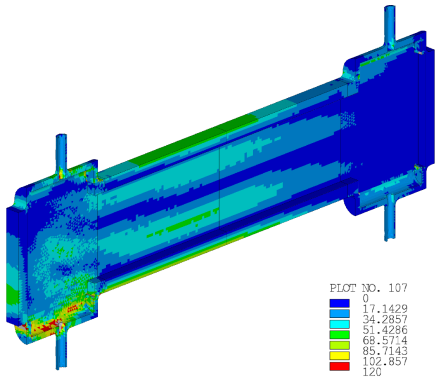

(a) total loading, σ_{total}, scale 0→120 MPa

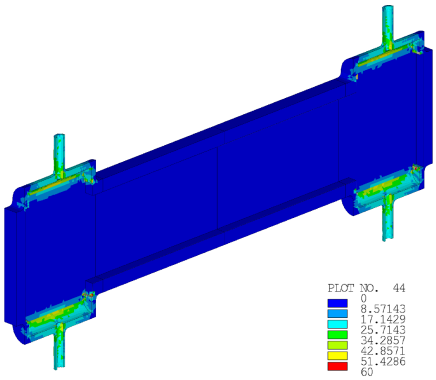

(b) pressure loading, σ_P, scale 0→60 MPa

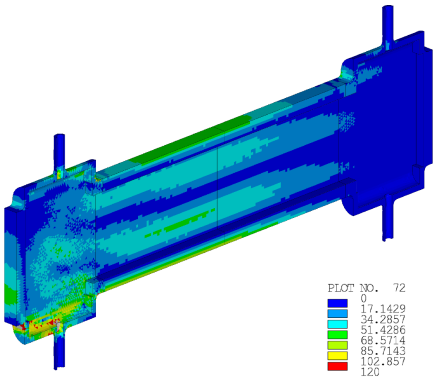

(c) PCHE thermal expansion, $\sigma_{\nabla T}$, scale 0→120 MPa

Figure 5.16: Solid side-wall von Mises stress in MPa. Total stress is a combination of individual loadings in equation (5.1).

2. **stress in the hot end counter-flow and transition region side walls:** Thermal gradients are caused by the cross-flow interaction of hot CO_2 entering, cold CO_2 leaving, the PCHE (left side of Figure 5.13). These are especially pronounced at the cold outlet (bottom left), as cold CO_2 is unevenly distributed, being higher at the cooler bottom side of the PCHE.

3. **stress within the header:** Thermal gradients across the cold outlet header (bottom left) arise from the temperature gradient across the cold exit to which it is welded. The header and exit region micro-channel conduct heat differently and thus develop different thermal expansion profiles. Overall the cold exit region is hotter than the cold outlet header, resulting in a net tensile load in the header.

Total equivalent stress within the solid material regions exceeds 120 MPa within the cold outlet header. This is of concern as the yield stress of 316 stainless is reduced at the higher temperatures experience in this header.

The extent of yielding is illustrated through the yield safety factor of Equation (5.33) and plotted in Figure 5.17. In this Figure any stress above yield gives a safety factor below 1 (colored dark blue). A minimum yield safety factor of 0.267 occurs at the sharp interior weld connecting the nozzle to the header at the cold outlet (bottom left). This stress is highly localized and not of great enough magnitude to reach the ultimate strength of the material. In practice this concentration likely yielded away. Failure was not seen during testing.

5.4.2 stress at the SCLs

Each etched plate contains 4,320 same-stream walls, and each pair of adjacent plates 4,320 cross-stream walls. Considering the 13 etched plates that make up the PCHE, there are 56,160 same-stream SCLs and 51,840 cross-stream SCLs where failure could occur. Stresses within all of these SCLs can be evaluated by mapping the stress in the 28,432 elements

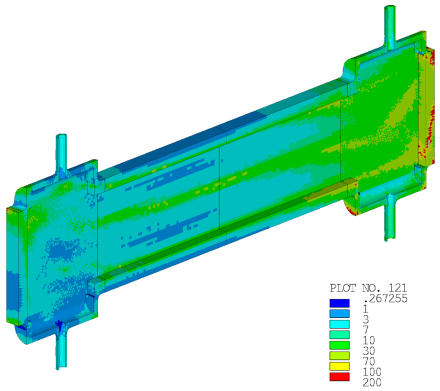

Figure 5.17: Yield safety factor within the solid side wall. Elements in dark blue are above yield stress.

within the micro-channel region of the PCHE model into the SCL space, see Equations (5.23-eq:Lambda2).

Stress due to internally restrained thermal expansion between the hot and cold CO_2 fluid walls can also mapped into each SCL using Eqautions (5.27-eq:Lambda4) and wall temperatures of the thermohydraulic model.

Stress linearization within the subunit model allows the loading of the SCLs to split into Membrane and Bending components. These components are evaluated for each of the 28,432 elements encompassing the counter-flow, parallel-flow, cross-flow, and single channel regions. The equivalent membrane and bending stresses are calculated for each contributing loading and for the total combined loading in Equation (5.1). The contributing loads are that of the pressure, σ_P, PCHE thermal gradient, $\sigma_{\nabla T}$, and cross-stream fluid wall temperature difference, $\sigma_{\Delta T_{ch.}}$.

membrane stress

The distribution of membrane stress within the cross-stream and same-stream SCLs is shown in the Figure 5.18. This histogram plots bars representing the percentage of SCL elements

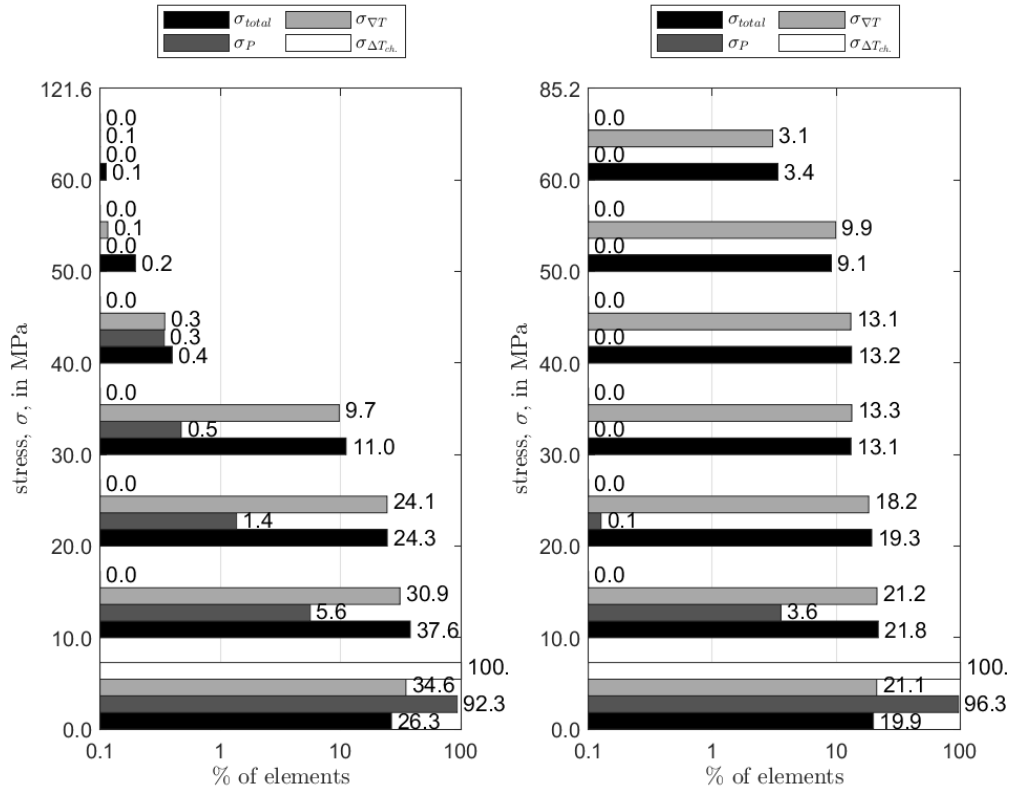

(a) Same-stream SCL **(b)** Cross-stream SCL

Figure 5.18: Distribution of SCL membrane stress within the PCHE. Total stress results from a combination of individual loadings in equation (5.1). See Figure 5.9 stress variation along the SCL.

with membrane stress falling within 10 MPa bins on the vertical axis. The top most bin encompasses all membrane stresses above 60 MPa. The horizontal scale of the bars is logarithmic, ranging from 0.1 to 100% of all 28,432 elements. Each bin is split into four bars representing the total membrane stress (black bar), and the contribution of each component stress : pressure (dark gray bar), PCHE thermal gradient (gray bar), and cross-stream fluid-wall temperature (white bar). Each loading contribution is considered in detail:

Membrane stresses due to internal fluid-wall temperature differences contribute little to the total SCL loading. Both the same-stream and cross-stream SCL do not have any elements experiencing $\sigma_{\Delta T_{ch.}}$ membrane stresses in excess of 10 MPa (see white bars). This is due to a combination of relatively close CO_2 stream approach temperatures and the nature of the SCLs reaction to internal thermal stress. The reaction to fluid-wall thermal stress is primarily bending, with little membrane stress developed in the SCLs, see Figure 5.11.

The same-stream micro-channel wall see's higher $\sigma_{\Delta T_{ch.}}$ membrane stress than the cross-stream wall. This membrane stress is highest in areas where heat transfer occurs, see Figures 5.19c & 5.20c. Heat transfer is highest near the interface of the hot end cross-flow to counter-flow transition. Larger separation in temperature between the entering hot and exiting cold CO_2 streams creates a local maximum membrane stress of 6.5 MPa in the same-stream wall and 1.7 MPa in the cross-stream wall.

Membrane stress from pressurization is primarily born by the same-stream micro-channel walls, which react most to tensile loads in the z direction (see Figure 5.9c). Although thinner than the same-stream wall, the cross-stream walls see less pressurization stress. Solid top/bottom plates provide a greater proportion of support against loads oriented in the xy plane than the solid side walls provide for loads in the z. As result there is less force on the cross-stream wall, which reacts most to xy tension (see Figures 5.9a & 5.9b).

The distribution of membrane pressurization stress, σ_P, is shown in Figures 5.19b &

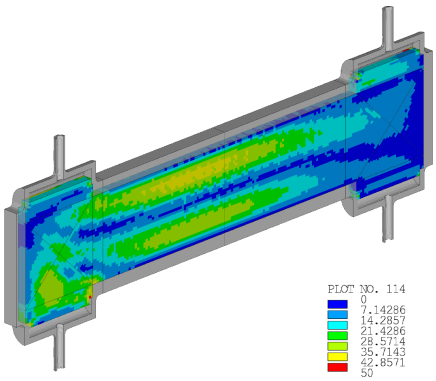

(a) total loading, σ_{total}, scale 0→50 MPa

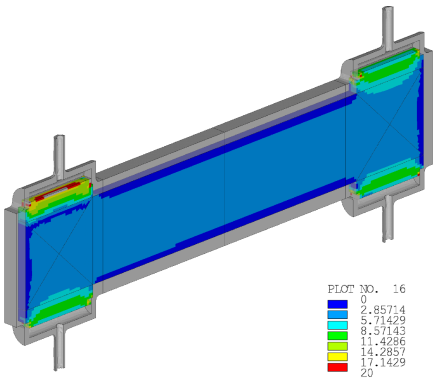

(b) pressure loading, σ_P, scale 0→20 MPa

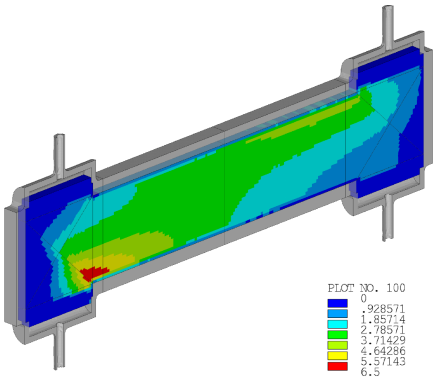

(c) fluid wall thermal expansion, $\sigma_{\Delta T_{ch.}}$, scale 0→6.5 MPa

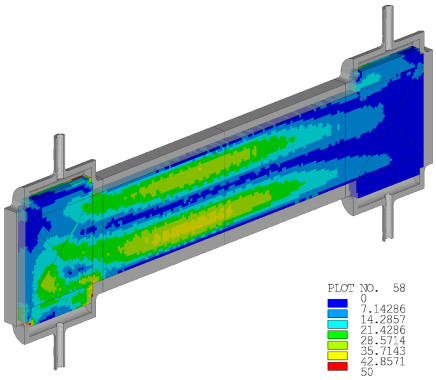

(d) PCHE thermal expansion, $\sigma_{\nabla T}$, scale 0→50 MPa

Figure 5.19: Same-stream SCL membrane stress in MPa. Total stress results from a combination of individual loadings in equation (5.1). See Figure 5.9 stress variation along the SCL.

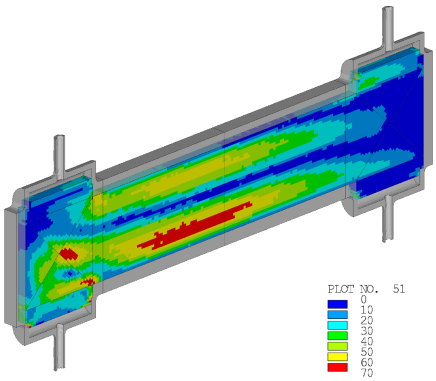

(a) total loading, σ_{total}, scale 0→70 MPa

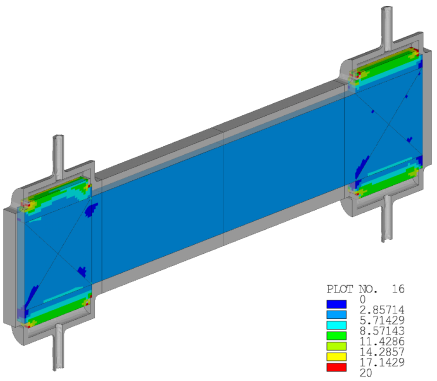

(b) pressure loading, σ_P, scale 0→20 MPa

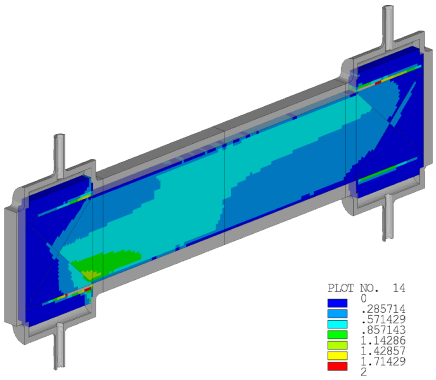

(c) fluid wall thermal expansion, $\sigma_{\Delta T_{ch.}}$, scale 0→2 MPa

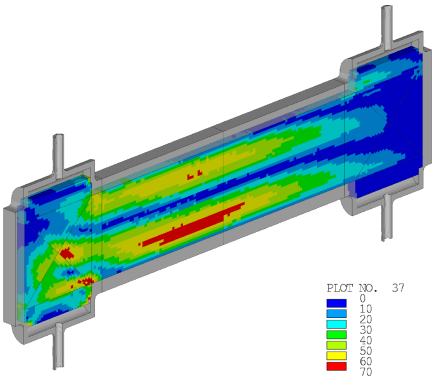

(d) PCHE thermal expansion, $\sigma_{\nabla T}$, scale 0→70 MPa

Figure 5.20: Cross-stream SCL membrane stress in MPa. Total stress results from a combination of individual loadings in equation (5.1). See Figure 5.9 stress variation along the SCL.

5.20b. Variation of pressurization stress is the result of two distinct features:

1. **interaction with the solid side wall :** Pressure stresses are evenly distributed throughout the counter-flow and cross-flow micro-channel regions. This stress is reduced near the interface between the micro-channel and stiffer solid side-wall. The solid-side wall and top/bottom plates provide localized support that relieves the stress on neighboring micro-channel walls. As a result we would expect failure from pressurization to begin within the center of the PCHE micro-channel region, and not at the edge of the core.

2. **reaction to header loading:** High micro-channel wall stresses occurring in the single-channel regions are the result of pressure loading of the headers, not internal pressure within the channels. The single-channel micro-channel regions support a portion of the 11.32-11.55 MPa contained by the headers. The semi-circular header geometry primarily loads the underlying PCHE block in z tension, resulting in higher membrane stress in the same-stream micro-channel wall.

Membrane stress from differential thermal expansion contributes the most to the total membrane stress within the micro-channel walls. These stresses are driven by differences in thermal expansion and are primarily oriented in the xy plane. This result in loading of the micro-channel structure which is supported by both the same-stream and cross-stream micro-channel walls. The cross-stream wall sees more stress as it is thinner than the same-stream wall.

The distribution of thermal expansion membrane stress, $\sigma_{\nabla T}$, is shown in in Figures 5.19c & 5.20c. All micro-channel material is bonded together, leaving little room for stress relaxation. Two regions of high thermal stress within the micro-channel can be identified:

1. **stress within the counter-flow core:** Temperature differences between the top and bottom of PCHE cause the top side of the PCHE to expand more than the bottom

side, bending the hot side of the PCHE down in y. This bending forms a neutral axis roughly along the central x axis. Above this neutral axis micro-channel volumes are in compression, and below this axis in tension. This x oriented tension and compression is born by both the same-stream and cross-stream micro-channel walls.

2. **stress in the hot end cross-flow and parallel micro-channels:** Thermal gradients are caused by the cross-flow interaction of hot CO_2 entering, cold CO_2 leaving, the PCHE (left side of Figure 5.13). These are especially pronounced at the cold outlet (bottom left), as cold CO_2 is unevenly distributed, being higher at the cooler bottom side of the PCHE. Being oriented in the xy plane, these thermal gradient load both the same-stream and cross-stream walls.

bending stress

The distribution of maximum bending stress within the cross-stream and same-stream SCLs is shown in the Figure 5.21. This histogram plots bars representing the percentage of SCL elements falling into bins of maximum bending stres son the vertical axis. Bins are 7.14 MPa for the same-stream SCL and 3.57 MPa for the cross-stream SCL. The maximum bending stress is taken as the greater value of bending stress at beginning (0) and end (1) of the SCL. Each bin is split into four bars representing the total membrane stress (black bar), and the contribution of each component stress : pressure (dark gray bar), PCHE thermal gradient (gray bar), and cross-stream fluid-wall temperature (white bar).

Geometric discontinuities within the zig-zag micro-channel result in bending stresses that are higher in the the same-stream wall than the cross-stream wall. The difference between SCls is seen by examining a 3% subset of the 28,432 micro-channel elements which experience the highest total bending stress. In the same-stream SCl, the top 2.9% of elements see total bending stress in excess of 35.7 MPa. In the cross-stream SCL the top 3.1% of elements only

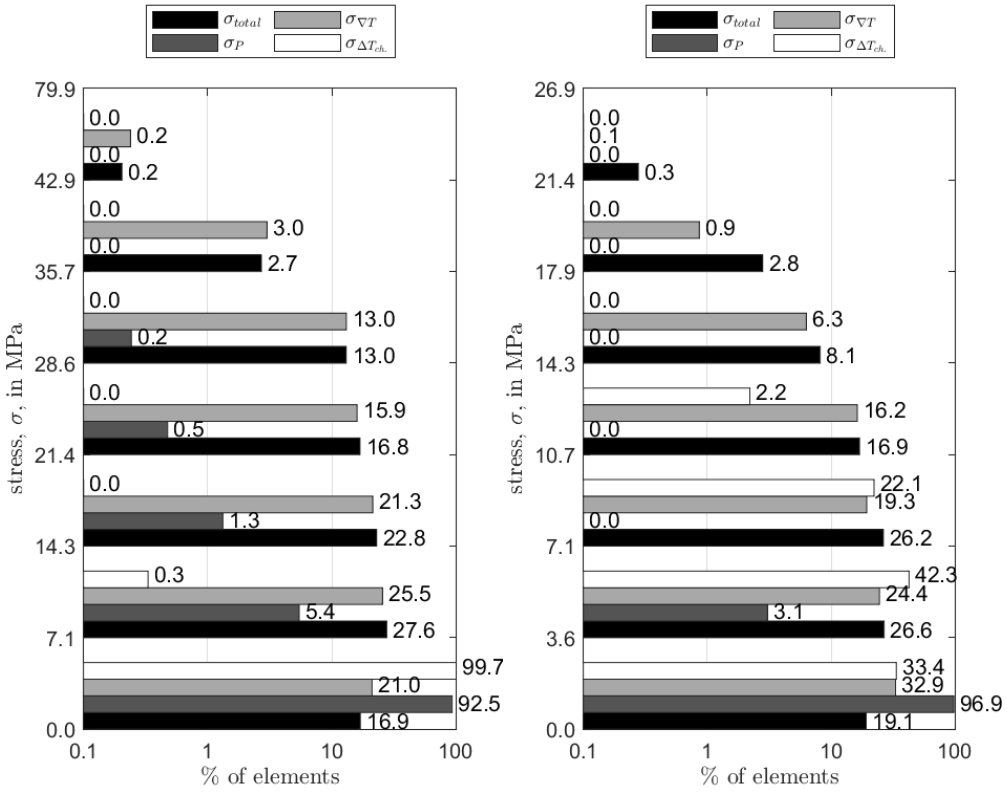

(a) Same-stream SCL **(b)** Cross-stream SCL

Figure 5.21: Distribution of SCL maximum bending stress within the PCHE. Total stress results from a combination of individual loadings in equation (5.1). See Figure 5.9 stress variation along the SCL.

see bending stress in excess of 17.9 MPa.

The total bending stress results from a combination of loadings, the contribution of each is considered in detail:

Bending stresses due to internal fluid-wall temperature differences make up a larger portion of total stress in the SCL loading. In this $\sigma_{\Delta T_{ch.}}$ loading the bending stress in greater than corresponding membrane stress shown in Figure 5.18. This is because the reaction to fluid-wall thermal stress is primarily bending, with little membrane stress developed in the SCLs, see Figure 5.11.

The cross-stream wall sees the greatest amount of bending, as most of the fluid-wall temperature gradient is realized across this SCL. The distribution of bending stress is higher in the cross-stream SCLs, where 24.3% of elements see a $\sigma_{\Delta T_{ch.}}$ in excess of 7.1 MPa. Only 0.3% of elements see a same-stream bending stress in excess of 7.1 MPa.

As with the membrane stress, the bending stress is highest in areas where heat transfer occurs, see Figures 5.22c & 5.23c. Heat transfer is highest near the interface of the hot end cross-flow to counter-flow transition. Larger separation in temperature between the entering hot and exiting cold CO_2 streams creates a local maximum bending stress of 8 MPa in the same-stream wall and 15 MPa in the cross-stream wall.

Bending stress from pressurization is primarily born by the same-stream micro-channel walls, which react most to tensile loads in the z direction and have higher bending stress (see Figure 5.9c). Elements within the single-channel regions see an especially elevated same-stream bending stress due to localized header loadings near the inlets and outlets.

The distribution of bending pressurization stress, σ_P, is shown in Figures 5.22b & 5.23b. Variation of pressurization stress is the result of two distinct features:

1. **difference in counter-flow and cross-flow structure :** The structure of the cross-flow micro-channel does not support loading in z as well as the counter-flow channel.

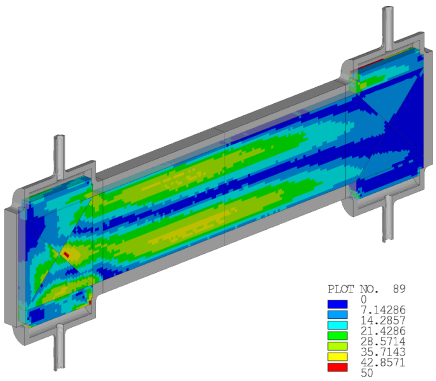

(a) total loading, σ_{total}, scale 0→50 MPa

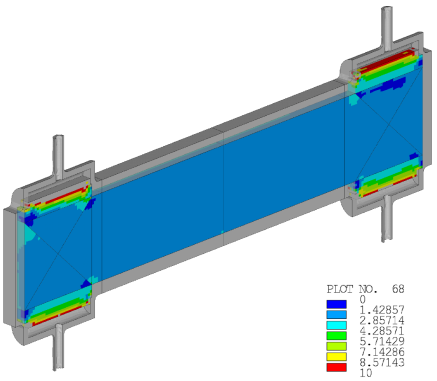

(b) pressure loading, σ_P, scale 0→10 MPa

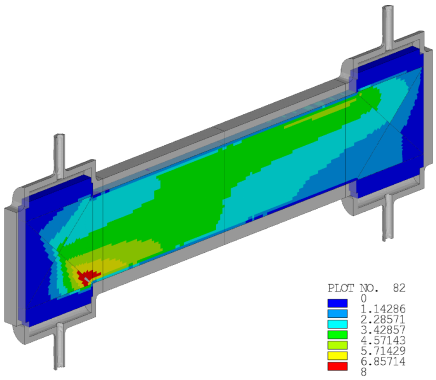

(c) fluid wall thermal expansion, $\sigma_{\Delta T_{ch.}}$, scale 0→8 MPa

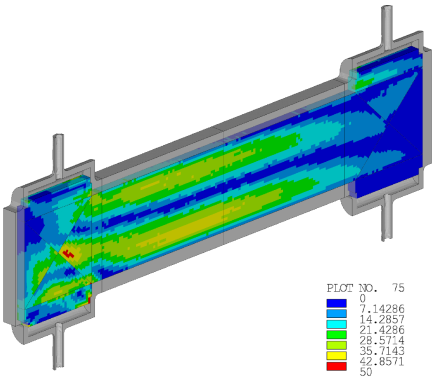

(d) PCHE thermal expansion, $\sigma_{\nabla T}$, scale 0→50 MPa

Figure 5.22: Same-stream SCL bending stress in MPa, maximum bending stress at end of SCL. Total stress results from a combination of individual loadings in equation (5.1). See Figure 5.9 stress variation along the SCL.

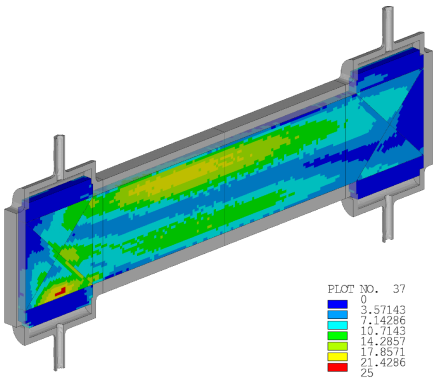

(a) total loading, σ_{total}, scale 0→25 MPa

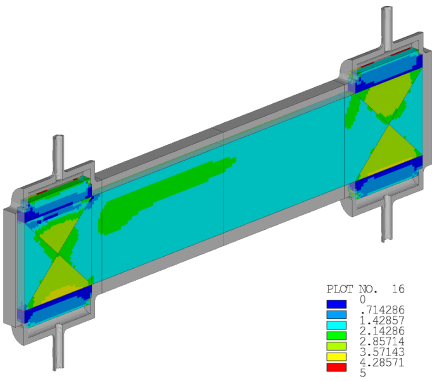

(b) pressure loading, σ_P, scale 0→5 MPa

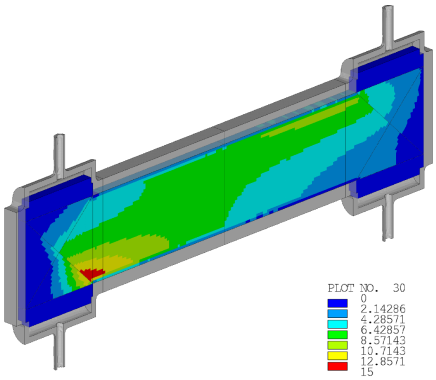

(c) fluid wall thermal expansion, $\sigma_{\Delta T_{ch.}}$, scale 0→15 MPa

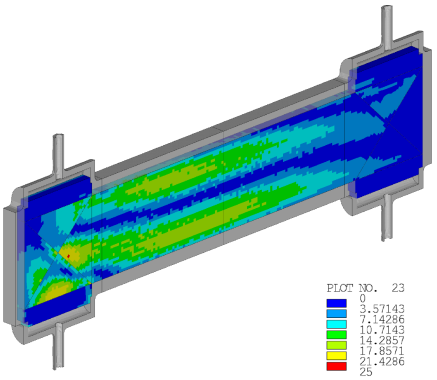

(d) PCHE thermal expansion, $\sigma_{\nabla T}$, scale 0→25 MPa

Figure 5.23: Cross-stream SCL bending stress in MPa, maximum bending stress at end of SCL. Total stress results from a combination of individual loadings in equation (5.1). See Figure 5.9 stress variation along the SCL.

This is because the 90° orientation of successive hot cold plates leads to less overlap of the same-stream channel wall. As a result the same-stream wall supports less z tensile load. The cross-stream wall then has to support a larger amount of the z loading, resulting in higher cross-stream bending stress in the counter-flow region.

2. **reaction to header loading:** The single-channel micro-channel regions support a portion of the 11.32-11.55 MPa contained by the headers. The semi-circular header geometry primarily loads the underlying PCHE block in z tension, resulting in higher bending stress in the same-stream micro-channel wall.

Bending stress from differential thermal expansion contributes the most to the total bending stress within the micro-channel walls. These stresses are driven by differences in thermal expansion and are primarily oriented in the xy plane. This result in loading of the micro-channel structure which is supported by both the same-stream and cross-stream micro-channel walls. Bending in the same-stream wall is higher because of stress concentrations formed at the micro-channel corner.

The distribution of thermal expansion bending stress, $\sigma_{\nabla T}$, is shown in in Figures 5.22c & 5.23c. Two regions of high thermal stress within the micro-channel can be identified:

1. **stress within the counter-flow core:** Temperature differences between the top and bottom of PCHE cause the top side of the PCHE to expand more than the bottom side, bending the hot side of the PCHE down in y. This bending forms a neutral axis roughly along the central x axis. Above this neutral axis micro-channel volumes are in compression, and below this axis in tension. This x oriented tension and compression is born by both the same-stream and cross-stream micro-channel walls.

2. **stress in the hot end cross-flow and parallel-flow micro-channels:** Thermal gradients are caused by the cross-flow interaction of hot CO_2 entering, cold CO_2 leaving,

the PCHE (left side of Figure 5.13). These are especially pronounced at the cold outlet (bottom left), as cold CO_2 is unevenly distributed, being higher at the cooler bottom side of the PCHE. Being oriented in the xy plane, these thermal gradient load both the same-stream and cross-stream walls.

5.4.3 Stress Classification

Classification of stress is performed for all micro-channel walls. The same-stream and cross-stream walls are considered.

Stress classifications in BPVC Sec. III Div. 5 are grouped into primary and secondary stresses. Primary stresses are,

- **General membrane** P_m **:** *"Average primary stress across solid section. Excludes effects of discontinuities and concentrations. Produced by pressure and mechanical loads."* This is the membrane stress of the micro-channel SCLs within uniform regions of the PCHE. Produced by pressurization.

- **Local membrane** P_L **:** *"Average stress across any solid section. Considers effects of discontinuities but not concentrations. Produced by pressure and mechanical loads."* This is the membrane stress of the micro-channel SCLs at the boundaries of the micro-channel regions where structure changes create discontinuity in the material, e.g where the core and solid walls meet. Produced by pressure.

- **Bending** P_b **:** *"Component of primary stress proportional to distance from centroid of solid section. Excludes effects of discontinuities and concentrations."* This is bending stress within the micro-channel SCLs within uniform regions of the PCHE. Produced by pressurization.

Secondary stresses are,

- **Membrane plus bending** Q **:** *"Self-equilibrating stress necessary to satisfy continuity of structure. Occurs at structural discontinuity. Can be cased by press, mechanical loads, or differential thermal expansion."* This is the membrane plus bending stress in the micro-channel SCLs which results from thermal expansion of the PCHE.

- **Peak** F **:** *"1. Increment added to primary or secondary stress by a conentration (notch) 2. Certain thermal stresses which may cause fatigue but not distortion."* 1. The peak stress from pressurization, occurring at the ends of the same-stream SLC, a stress concentration. 2. This is the thermal membrane + bending stress created by cross-stream fluid wall temperature differences. This stress is localized within the micro-channel subunit.

The combination of these stresses are limited for BPVC Sec. III Div. 5 Level A and Level B service,

$$P_m \leq S_m \tag{5.36}$$

$$P_L + P_b + Q \leq 3S_m \tag{5.37}$$

Peak stresses are only considered when evaluating fatigue.

$$P_L + P_b + Q + F \leq S_a \tag{5.38}$$

As the micro-channel structure cannot be modeled over the full scale of the heat exchanger, loadings must be resolved with thermohydraulic and orthotropic mechanical models at the full PCHE scale. The results from these models can then be mapped to the various micro-channel SCLs to determine the general primary membrane, local primary membrane, primary bending, secondary, and peak stress. Table 5.5 shows the combinations of model, loading, and stress mapping needed to evaluate each Level A Service stress classification.

Table 5.5: Stress classification within micro-channel subunit

	from loading	uses stress mapping	see Figures
P_m	PCHE model, Pressure Loading	$[\Lambda_\sigma]_m$, SCL membrane stress	5.19b & 5.20b
P_L	PCHE model, Pressure Loading	$[\Lambda_\sigma]_L$, SCL membrane stress	5.19b & 5.20b
P_b	PCHE model, Pressure Loading	$[\Lambda_\sigma]_b$, SCL bending stress	5.22b & 5.23b
Q	PCHE model, Temperature Loading	$[\Lambda_\sigma]_{m+b}$, SCL membrane + bending stress	5.19b-5.19d & 5.19b-5.19d
F	PCHE model, Pressure Loading	$[\Lambda_\sigma]_P$, SCL peak stress	
	Thermohydraulic model, fluid wall temperature difference $\lvert T_{H,wall} - T_{C,wall} \rvert$	$[\Lambda_{\Delta T_{ch.}}]_{m+b}$, SCL membrane + bending	5.19c & 5.20c
The symbols P_m, P_Lm P_b, Q, and F are stress tensors			

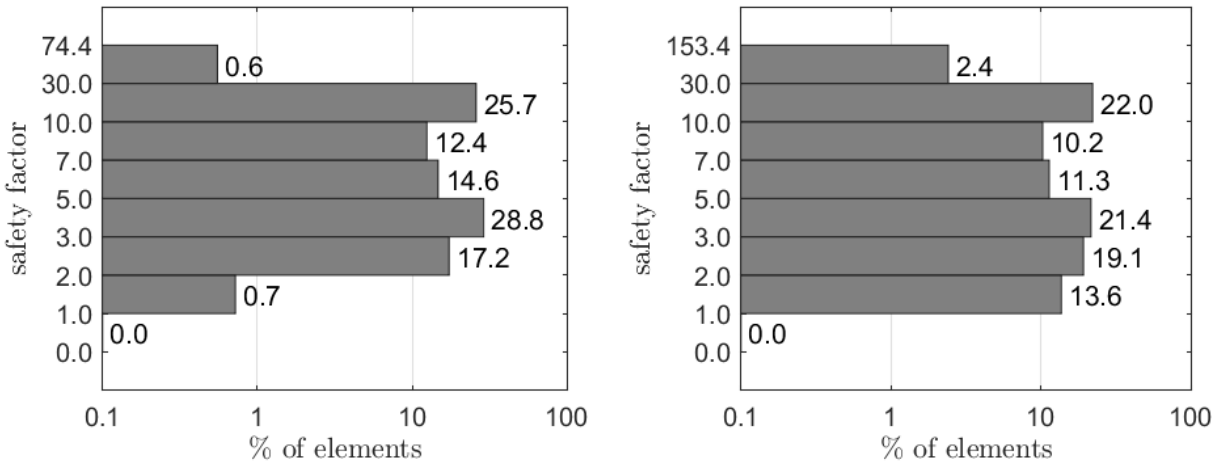

(a) Same-stream SCL **(b)** Cross-stream SCL

Figure 5.24: Distribution of the stress intensity safety factor $\mathrm{SF}_{Sm} = S_m/(P_L + P_b + Q)$ within the PCHE.

The BPVC Sec. III Div. 5 stress intensity in Equation (5.37) can be evaluated from the loadings of the PCHE model. Each component of stress intensity is defined in Table 5.5. By these definitions the stress intesity of each SCL is a combination of the membrane stress due to pressure in the SCL, the maximum bending stress due to pressure in the SCL, the membrane stress due to thermal loading in the SCL, and the maximum bending stress due to thermal loading in the SCL. This is just the combined loading at the SCL as described in Equation (5.1) sans the fluid wall temperature difference term.

A safety factor for evaluating the stress intensity is defined,

$$\mathrm{SF}_{Sm} = \frac{S_m}{P_L + P_b + Q} = \frac{S_m}{\sigma_P + \sigma_{\nabla T}} \tag{5.39}$$

The distribution of this stress intensity safety factor within the micro-channel elements is given for the same-stream and cross-stream SCLs in Figure 5.24.

None of the 28,432 elements of the micro-channel region of the PCHE exceed the stress

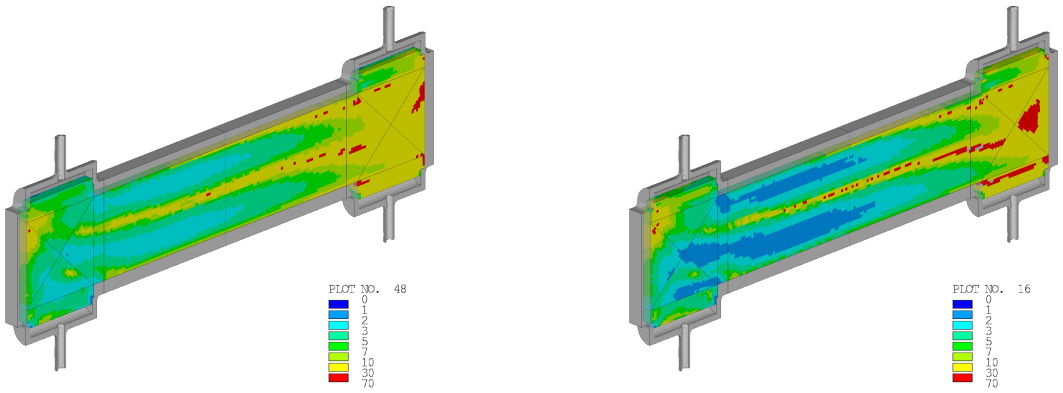

(a) Same-stream SCL **(b)** Cross-stream SCL

Figure 5.25: Stress intensity safety factor $\mathrm{SF}_{Sm} = S_m/(P_L + P_b + Q)$, at SCLs. Elements in dark blue would be above the S_m limits of 316 stainless steel.

intensity limit S_m within either the same-stream or cross-stream wall. Having a larger thickness, the same-stream SCLs have a larger margin of safety than the cross-stream wall.

At the PCHE design conditions only 0.7% of the PCHE's 56,160 same-stream walls have a stress intensity within one S_m of the limit. This amounts to some 393 same-stream walls which are all located within the single-channel regions at the boundary between the micro-channel and solid header walls, see Figure 5.25a. This location is convenient as it is the only bonded micro-channel region that can be inspected externally.

In comparison 13.6% of the PCHE's 51,840 cross-stream walls have a stress intensity within one S_m of the limit. This amounts to some 7,050 cross-stream walls which are all located within the hot end of the counter-flow and cross-flow regions, see Figure 5.25b. Being driven largely by thermal stress within the PCHE, this highest stress intensity region is concentrated in bands above and below the axis of expansion induced bending (nominanlly the x axis). Unfortunately this location is difficult to inspect for failure, as it is buried beneath the solid side walls and first few adjacent micro-channels.

Chapter 6

Airfoil Channel Experimental Performance

6.1 Performance Testing

6.1.1 Pressure Drop Tests

Pressure drop experiments were performed with the Airfoil Printed Circuit Heat Exchanger (PCHE) and Darcy friction factor data was obtained for Reynolds ranging from Re 295 to Re 61480. Pressure drop experiments were performed at room temperature and steady state so as to keep CO_2 properties uniform through the heatexchanger. Pressure data taken in 5 min sets at 2 Hz was the used to calculate the friction factor and Reynolds number of the flow within the airfoil channels.

Darcy friction factor evaluation

The Darcy friction factor of the central channel is calculated from experimental density and pressure drop measurements. The total pressure drop, ΔP, is related to the Darcy friction factor, f_D, as follows,

$$\Delta P = \frac{1}{2} f_D \frac{L}{D_h} \rho v^2 \tag{6.1}$$

where ρ, v, and ΔP are directly measured across the channels of the Airfoil recuperator. Since pressure and temperature do not vary greatly across the channels it is reasonable to assume that ρ is constant along the length of the channels and equal to that measured at the inlet by the Coriolis meter. Along with measuring the density, the Coriolis meter measures mass flow, which when combined with the known cross sectional area of the channels, A_c,

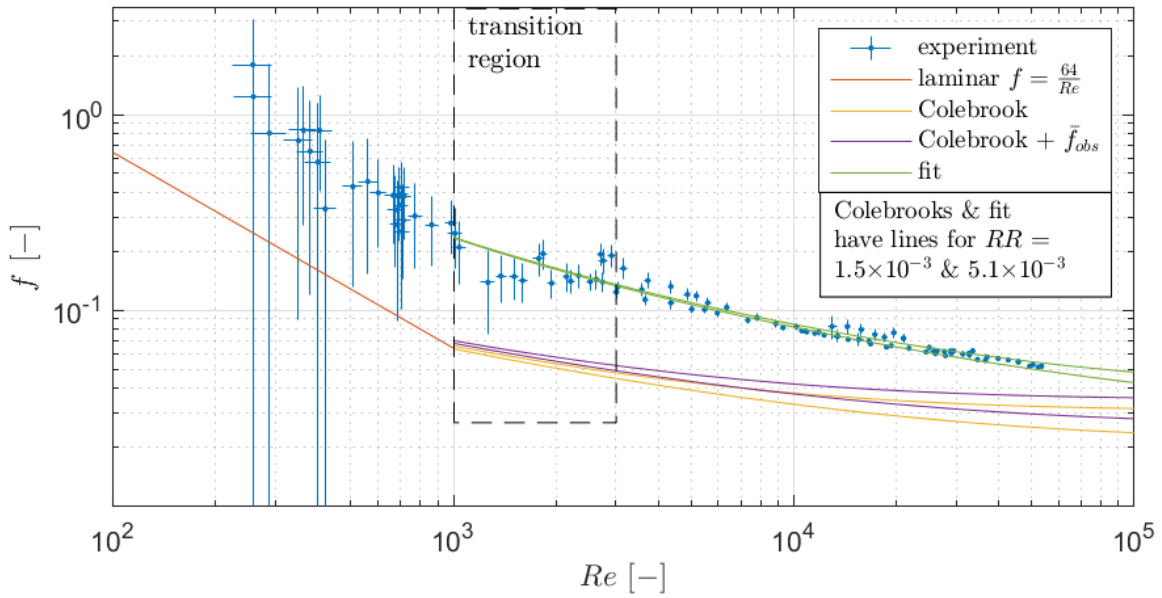

Figure 6.1: Darcy friction factor data and comparison to correlations

leads to an accurate measurement of velocity–i.e. $v = \dot{m}/\rho A_c$. The cross-sectional of the airfoil channels are 375.5 & 300.4 mm^2 for the cold and hot sides respectively. A differential pressure transducer accurately measures the ΔP from header-to-header across the channel.

The Reynolds number of the flow through the channels was also determined. The general form of the Reynolds equation can be reduced to a form utilizing the known experimental mass flow, $\dot{m}$, as follows,

$$Re = \frac{\rho v D_h}{\mu} = \frac{\dot{m} D_h}{A_c \mu} \tag{6.2}$$

where viscosity, μ, is determined using a viscosity correlation provided by Fenghour et. al[43]. When calculating Reynolds of the channels, μ is taken as the viscosity of CO_2 at the state defined by the average temperature within the channels and the density measured at the inlet by the Coriolis meter.

Darcy f results

In order to get a full range of Reynolds numbers, tests had to be run at a variety of pressures. High Reynolds tests used pressures nearer the critical pressure, ranging from 3.5-4.5 MPa, and corresponding densities of 70-150 kg/m^3. Low Reynolds tests had to be performed at lower pressures and densities, as velocity in the system could only be throttled down if the operation point was away from the vapor dome. Otherwise expansion in throttle valves would cause a two phase condition. The low Reynolds points were made at pressures ranging from 1.7-3.0 MPa and ρ of 34-48 kg/m^3.

The resulting Darcy friction factor data is shown in Figure 6.1. Instrument measurement error was propagated through all calculation of Re and f_D. High error in f at low Re resulted from using an oversized, and less accurate, 0-500 kPa differential pressure transducer. Ultimately it was decided not to retake the lower Reynolds data with a more accurate pressure transducer, as the data is far too low in Re to be practically applicable.

The friction factor data is plotted along with standard laminar and turbulent correlations for pipe. A common correlation covering the turbulent-transitionally-rough region of internal flow is the Colebrook equation[28].

$$\frac{1}{\sqrt{f}} = -A\log_{10}\left(\frac{RR}{B} + \frac{C}{Re\sqrt{f}}\right) \qquad \text{with: } A = 2.0 \;\; B = 3.7 \;\; C = 2.51 \tag{6.3}$$

The Colebrook formulation can be compared to experimental airfoil channel data if the relative roughness, RR, of the channels is considered. Optical measurements of similar etched 316 PCHE plates at UW-Madison has found surface roughness to be in the range of 0.0022-0.0076 mm[9][8]. Thus the airfoil channels are expected to be between $RR = 1.5\times10^{-3}$ & 5.1×10^{-3}. The variation in friction factor correlation due to RR is shown in Figure 6.1 as

upper and lower lines representing each roughness.

Experiment results in friction factors that are much larger than bot the Colebrook prediction and the Colebrook prediction plus the expected airfoil drag obstruction term ($\bar{f}_{obs}$=0.0043. This isn't a surprise as the Colebrook relation only accounts for wall-shear losses and the airfoil drag term was estimated base on drag coefficients for airfoils in open flow. As the airfoil-fins are tightly packed, higher than predicted friction factors were anticipated.

A fit was made to the friction factor data within the turbulent regime (Re >3000). The fit was made using Equation 6.3 holding constant RR=33×10^{-3} and A=2, while varying B, and C. Values of B = 0.409 and C= 43.1 yielded a fit with rms of 2.87×10^{-}3. The fit is plotted in Figure 6.1.

6.1.2 Heat Transfer determination

Recuperator performance data at steady-state conditions were obtained for a series of thirteen, 30 minute long tests. A 10 kW annular heater, plumbed between the cold outlet and hot inlet of the recuperator, would be used to heat the recuperator to a steady state condition. This low power system limited the experimental range to hot inlet temperatures of 205 C at mass flows up to 0.1 kg/s.

Mass flow and recuperator channel inlet and outlet conditions were recorded in data logs. Mass flow was measured by a SitransF Corilios meter mounted downstream of the hot outlet. Conditions at the inlets and outlets of both hot and cold CO_2 were measured using a combination of thermocouples and pressure transducers. Each inlet was instrumented with an absolute pressure tranducer and the pressure drop between both hot and cold streams were measured with dedicated differential pressure transducers. Data was read and written to file at a rate of 1 Hz during the duration of each test and then averaged afterwards. The

error in these averaged values accounted for the variance in data as well as the instrument error of the data.

lumped ε-NTU evaluation

Effectiveness NTU methods (ε-NTU) of evaluating heat exchanger performance can be used to determine the heat transfer occurring at the experimental steady state. The simplest method is to lump the airfoil recuperator together as a single counter-flow recuperator of length L = 726.5 mm.

The total heating of the cold and hot CO_2 streams can be determined from the change in CO_2 entropy between the inlets and outlets of the streams.

$$\dot{q}_C = \dot{m}\left(H\left(T_{H,inlet}, P_{H,inlet}\right) - H\left(T_{H,outlet}, P_{H,outlet}\right)\right) \tag{6.4}$$

$$\dot{q}_H = \dot{m}\left(H\left(T_{C,inlet}, P_{C,inlet}\right) - H\left(T_{C,outlet}, P_{C,outlet}\right)\right) \tag{6.5}$$

$$\dot{q} = \frac{1}{2}\left(\dot{q}_C - \dot{q}_H\right) \tag{6.6}$$

where the enthalpy, H, is determined at the specified CO_2 temperature and pressure using the Span and Wagner equation of state[41].

The capacitance flowing through each stream, as well as the capacitance ratio are determined.

$$\dot{C}_C = \frac{\dot{q}_C}{T_{C,outlet} - T_{C,inlet}},\ \dot{C}_H = \frac{\dot{q}_H}{T_{H,outlet} - T_{H,inlet}} \tag{6.7}$$

$$C_R = \frac{min\left(\dot{C}_C, \dot{C}_H\right)}{max\left(\dot{C}_C, \dot{C}_H\right)},\ \dot{C}_{min} = min\left(\dot{C}_C, \dot{C}_H\right) \tag{6.8}$$

Results from Equations 6.4-6.8 are used to find the effectiveness, ε, NTU, and UA for a counter-flow heat exchanger.

$$\varepsilon = \frac{\dot{q}}{\dot{C}_{min}\left(T_{H,inlet} - T_{C,outlet}\right)} \tag{6.9}$$

$$NTU = \begin{cases} ln\left(\frac{1-\varepsilon C_R}{1-\varepsilon}\right) / \left(1 - C_R\right) & \text{for } C_R < 1 \\ \frac{\varepsilon}{1-\varepsilon} & \text{for } C_r = 1 \end{cases} \tag{6.10}$$

$$UA = NTU\, \dot{C}_{min} \tag{6.11}$$

The local heat transfer coefficient can be inferred from an evaluation of the local heat transfer coefficient. As inter-channel wall temperature measurements were not made during all runs, the assumption that the wall temperature can be taken as the mean temperature of both hot and cold CO_2 can be used. In this case the local heat transfer coefficient is,

$$h = \frac{\dot{q}}{A_c(T_f - T_w)} \tag{6.12}$$

$$T_w = \frac{1}{4}\left(T_{H,inlet} + T_{H,outlet} + T_{C,inlet} + T_{C,outlet}\right) \tag{6.13}$$

and Colburn heat transfer coefficient in Equation 2.27 can be rewritten as,

$$j = \frac{hPr^{2/3}A_c}{\dot{C}} = \frac{\dot{q}}{T_f - T_w}\frac{A_c}{A_s}\frac{1}{\dot{C}}Pr^{2/3} \tag{6.14}$$

as the ratio of cross-sectional flow area to surface area to surface area is related to the hydraulic diameter and length, $A_c/A_s = D_h/4L$, the Colburn heat transfer coefficient on both sides can be determined from the NTU.

$$j_C = \frac{\dot{q}_C}{0.5(T_{C,inlet} + T_{C,outlet}) - T_w} \frac{D_h}{4L} \frac{1}{\dot{C}_C} Pr_C^{2/3} \tag{6.15}$$

$$j_H = \frac{\dot{q}_H}{0.5(T_{H,inlet} + T_{H,outlet}) - T_w} \frac{D_h}{4L} \frac{1}{\dot{C}_H} Pr_H^{2/3} \tag{6.16}$$

This lumped evaluation of j only roughly captures the true heat-transfer performance. Performing a single ε-NTU analysis over the entire recuperator neglects the affect of CO_2 property variation. Significant property variation does occur at the low temperature and pressure test conditions (20-210 C, 5.5-8.2 MPa). Furthermore, by modeling the entire length of the airfoil recuperator as being purely counter-flow, the affect of cross-flow regions at the inlets and outlets is lost.

discretized ε-NTU evaluation

The lumped ε-NTU method is improved by breaking the recuperator up into multiple sub heatexchanger sections (subHX). In this fashion a one dimensional discretization of the airfoil recuperator is performed. Each discrete subHX is evaluated using the ε-NTU method for backing out the local Colburn j heattransfer coefficient. In this fashion property variation is reduced as each subHX sees less change in CO_2 temperatures.

The recuperator is broken into 12 subHX sections as outline in Table 6.1. As the airfoil recuperator contains turning cross-flow regions at the CO_2 inlets and outlets, the discretized model is broken into 8 central counter-flow subHX sections and 4 cross-flow regions (2 at either end).

The subHXs are broken up so that the UA of the recuperator is distributed evenly along the recuperator.

$$UA_i = UA \frac{\Delta x}{L} \tag{6.17}$$

Table 6.1: Sub-HX Model Regions

start	end	Δx	flow type
	$[mm]$		
0	44.76	44.76	cross
44.76	89.52	44.76	cross
89.52	157.9	68.43	counter
157.9	226.4	68.43	counter
226.4	294.8	68.43	counter
294.8	363.2	68.43	counter
363.2	431.7	68.43	counter
431.7	500.1	68.43	counter
500.1	568.5	68.43	counter
568.5	637.	68.43	counter
637.	681.7	44.76	cross
681.7	726.5	44.76	cross

Pressure is assumed to drop linearly across the recuperator, while inlet and outlet temperatures are fixed to experimental values.

$$\begin{aligned} P_{C,i} &= P_{C,inlet} - \sum(\Delta x_i/L)\Delta P_C \\ P_{H,i} &= P_{H,inlet} - (1 - \sum(\Delta x_i/L))\,\Delta P_H \end{aligned} \tag{6.18}$$

$$\begin{aligned} T_{C,0} &= T_{C,inlet} \quad T_{C,12} = T_{C,outlet} \\ T_{H,0} &= T_{H,outlet} \quad T_{H,12} = T_{H,inlet} \end{aligned} \tag{6.19}$$

The heat transfered within the i^{th} subHX relates the change in enthalpy in the CO_2 streams.

$$\dot{q}_i = \dot{m}\left(H\left(T_{H,i}, P_{H,i}\right) - H\left(T_{H,i-1}, P_{H,i-1}\right)\right) \tag{6.20}$$

$$\dot{q}_i = \dot{m}\left(H\left(T_{C,i}, P_{C,i}\right) - H\left(T_{C,i-1}, P_{C,i-1}\right)\right) \tag{6.21}$$

and the capacitance flow of the hot and cold sides is

$$\dot{C}_{C,i} = \frac{\dot{q}_i}{T_{C,i} - T_{C,i-1}},\ \dot{C}_{H,i} = \frac{\dot{q}_i}{T_{H,i} - T_{H,i-1}} \tag{6.22}$$

$$C_{R,i} = \frac{min\left(\dot{C}_{C,i}, \dot{C}_{H,i}\right)}{max\left(\dot{C}_{C,i}, \dot{C}_{H,i}\right)},\ \dot{C}_{min,i} = min\left(\dot{C}_{C,i}, \dot{C}_{H,i}\right) \tag{6.23}$$

which allows the calculation of each subHX's NTU,

$$NTU_i = \frac{UA_i}{\dot{C}_{min,i}} \tag{6.24}$$

The heat transfered in each subHX must be solved from the subHX's effectiveness,

$$\dot{q}_i = \varepsilon_i \dot{C}_{min,i} \left(T_{H,i} - T_{C,i-1}\right) \tag{6.25}$$

within the 8 counter-flow sub heatexchanger the effectiveness is determined from the counter-flow relation [24],

$$\varepsilon_i = \begin{cases} \frac{1-e^{-NTU_i(1-C_{r,i})}}{1-C_{R,i}e^{-NTU_i(1-C_{r,i})}} & \text{for } C_R < 1 \\ \frac{NTU_i}{1+NTU_i} & \text{for } C_r = 1 \end{cases} \tag{6.26}$$

within the 4 cross-flow sub heatexchanger the effectiveness is determined from an unmixed fluid cross-flow relation [24],

$$\varepsilon_i = 1 - e^{\left(\frac{NTU_i^{0.22}}{C_{R,i}}\left(e^{-C_{R,i}NTU_i^{0.78}} - 1\right)\right)} \tag{6.27}$$

as with the lumped ε-NTU method, the Colburn heat transfer coefficient can be determined from the $\dot{q}$, the assumption that the wall temperature is the mean of the CO_2 temperatures, and length of the subHX.

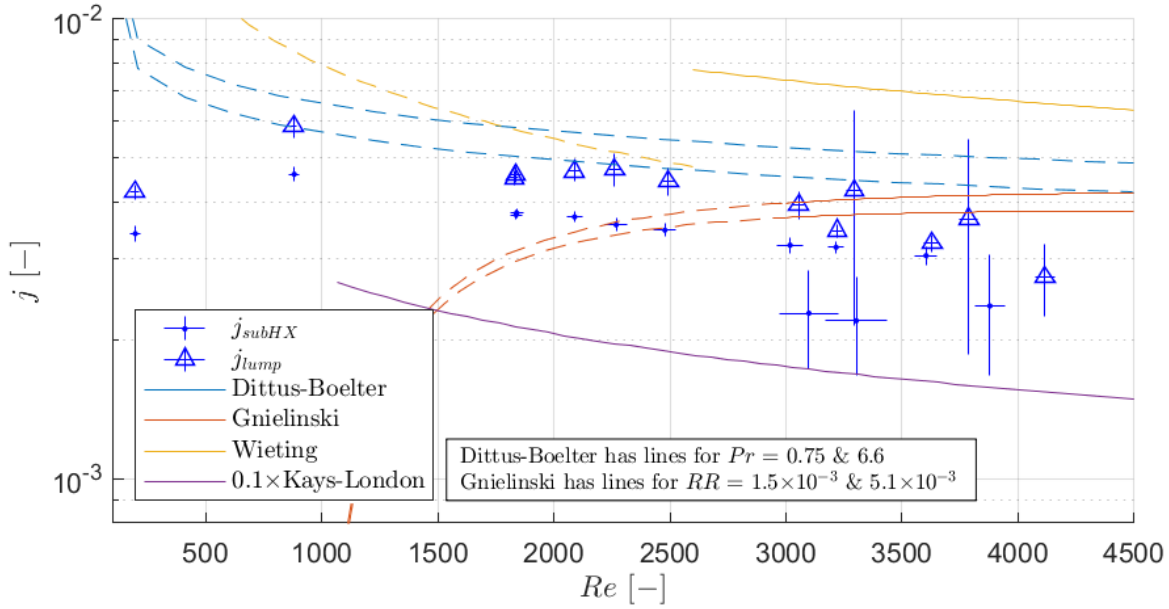

Figure 6.2: Colburn heat transfer coefficients for the cold CO_2 side

$$T_{w,i} = \frac{1}{4}\left(T_{H,i} + T_{H,i-1} + T_{C,i-1} + T_{C,i}\right) \tag{6.28}$$

$$j_{C,i} = \frac{\dot{q}_i}{0.5(T_{C,i} + T_{C,i-1}) - T_{w,i}} \frac{D_h}{4\Delta x_i} \frac{1}{\dot{C}_{C,i}} Pr_{C,i}^{2/3} \tag{6.29}$$

$$j_{H,i} = \frac{\dot{q}_i}{0.5(T_{H,i} + T_{H,i-1}) - T_{w,i}} \frac{D_h}{4\Delta x_i} \frac{1}{\dot{C}_{H,i}} Pr_{H,i}^{2/3} \tag{6.30}$$

Reynolds number within the subHX is found from mass flow as in Equation 6.2, but with μ evaluated at the subHX's mean CO_2 temperatures.

Colburn j results

Colburn j coefficients using both the lumped and discretized subHX methods were found for 13 experimental runs and are shown in Figures 6.2 and 6.3. As with the f calculations, error from the averaging of data and instrumental uncertainty was propagated through the

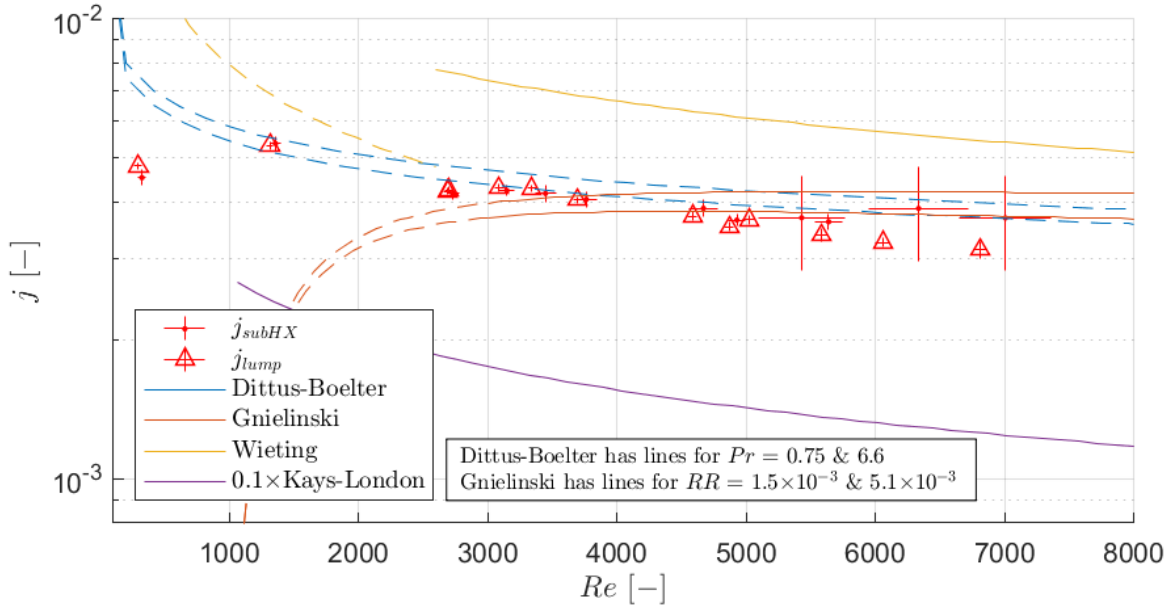

Figure 6.3: Colburn heat transfer coefficients for the hot CO_2 side

calculation of j, with most error being attributable to uncertainty in the measurement of inlet pressures and temperatures.

In Figures 6.2-6.3, j calculated using the lumped method is plotted as $\triangle$ while the mean of the 12 subHX j calculated with the discretized method is plotted as $\cdot$.

The experimental data is compared to various correlations for j, who's solid lines represent their region of applicability while dashed lines represent their application beyond their use. The Dittus-Boelter correlation comes the closest to matching the airfoil data, although it isn't applicable below Re=10000. We would expect the Dittus-Boelter to under-predict the heat transfer of the airfoil channels, as it is a smooth pipe correlation.

A rough flow correlation that relates j to the friction factor, by way of considering the wall-boundary-layer thickness, is the Gnielinski correlation. This is only valid above Re 3000 and within this region gives a slightly higher prediction of j and a trend opposite that of the experimental data. This ill-fit isn't surprising as the Gnielinski correlation assumes straight

but rough walls, while the airfoil channel is convoluted with relatively smooth walls.

Two off-set-fin correlations are presented, the older Wieting correlation, and the Kays-London correlation. Both account for obstructions in the flow, and in doing so would be expected to match airfoil data better than Dittus-Boelter. The Wieting correlation slightly over predicts while the Kays-London correlation grossly over predicts j (it is plotted at a $\times 10$ reduction to fit on the plots).

The lumped and discrete subHX methods of calculating j are far from perfect. It is not unreasonable to assume that they are an inaccurate calculation of the real local heat transfer coefficient. Given that the method results come close to the Dittus-Boelter smooth pipe relation but are far lower than the off-set-fin correlations of Wieting and Kays-London, it can be postulated that these j values are an under prediction of the real local heat-transfer coefficient.

6.2 Fiber Optic Thermal Mapping

The Airfoil recuperator was designed to test a novel method of measuring the thermal gradients within a PCHE. Fiber optic temperature probes are built into the central instrumentation channel shown in Figure 2.4, allowing temperature readings to be made along the length of the recuperator at 0.6125 mm intervals. Eight fiber probes are laid side-by-side as shown in Figure 6.4. In this way a planar map of temperatures can be made within the recuperator.

The fibers read an internal temperature of the PCHE block in real-time, enabling thermal stresses in the block to be determined. By recording thermal transients during cycling tests experimental thermal stress histories can be recorded.

An in house code, FiberMap, for obtaining and interpreting fiber data was created. Data acquisition consists of a couple of purpose built LabView codes that interface with the Luna

ODiSI fiber sensor system to create .csv databases of experimental data. A set of matlab scripts within FiberMap are then used to read and assemble the .csv database, convert fiber data to temperature readings, and create final 2D maps of temperature in the recuperator over time. An example of a temperature map made at a low temperature run is shown in Figure 6.5.

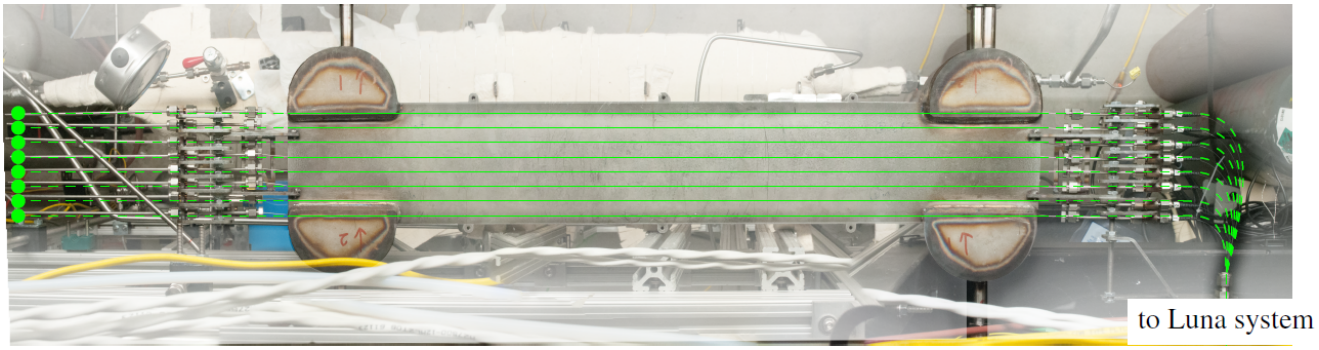

Figure 6.4: Fibers instrumentation of Airfoil recuperator, solid lines are region of measurement

Thermal stress concentrations can be identified in the Airfoil recuperator during high flow, low-efficiency tests. An example of steady state temperature distribution is shown in Figure 6.5. The temperature gradient of this distribution is shown in Figure 6.6.

As mass flow is increased in the recuperator, the bulk of heat transfer shifts toward the hot side and the corresponding hot inlet. At the hot side of the recuperator flow entering from the hot-stream channel inlet enters at a right angle, completing a 90 degree turn into the counterflow portion of the recuperator. Simultaneously cooler flow in the cold-stream channels are leaving the counterflow portion of the recuperator and completing a mirroring 90 degree turn out of the recuperator.

Thermal stress concentrations are clearly visible at the entrance of the hot-stream and exit of the cold-stream (as seen at x = 0.68 in Figure 6.6). These occur because local cross-flow conditions exist within the inlet and outlet of the recuperator.

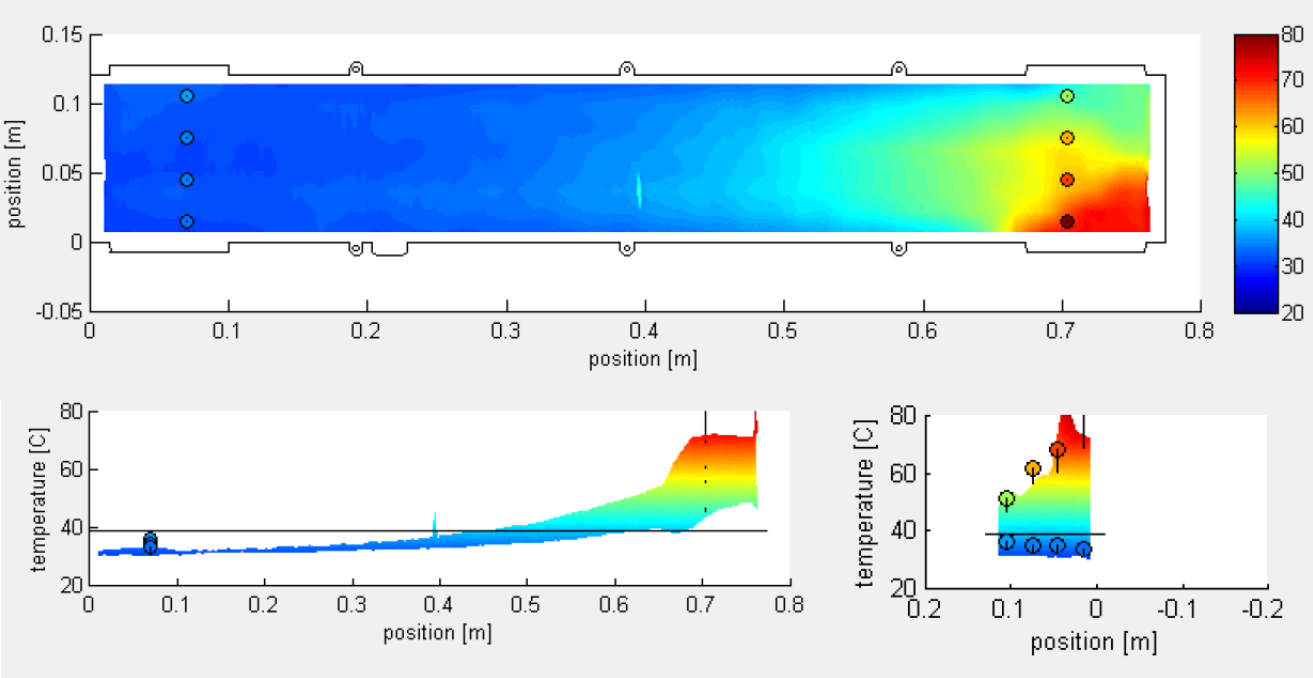

Figure 6.5: Temperature distribution in Airfoil recuperator during a high mass flow test (Re 7500 in hot-stream, Re 4130 in cold-stream). As seen from above (top), in side profile (bottom left), and end profile (bottom right)

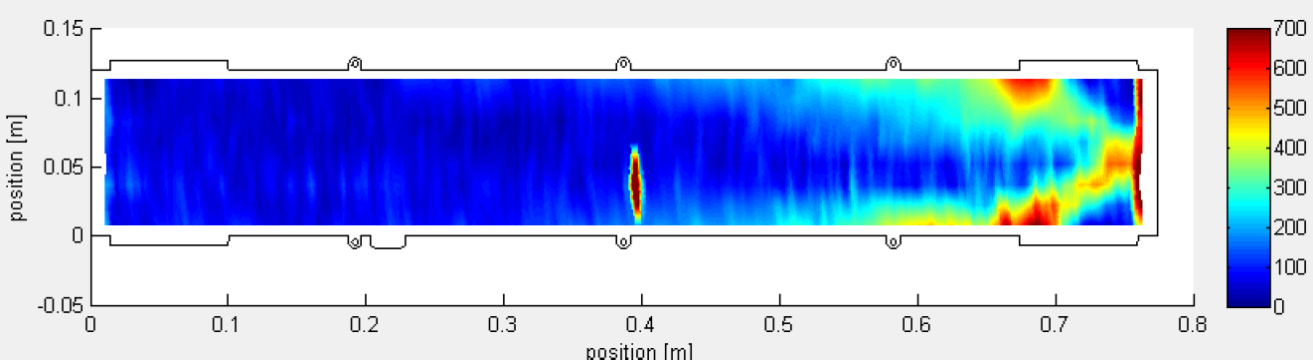

Figure 6.6: Temperature gradient in Airfoil recuperator during a high mass flow test (Re 7500 in hot-stream, Re 4130 in cold-stream). Units are $[K/m]$. Fiber reading noise creates some non-physical gradient readings (located at x = 0.4 and x = 0.78).

Chapter 7

Conclusions

This work established the modeling of Printed Circuit Heat Exchanger (PCHE)s as required for nuclear service certification. Through full component thermohydraulic and mechanical models, a detailed analysis of loadings and stress classification as required by American Society of Mechanical Engineers (ASME) Boiler and Pressure Vessel Code (BPVC) section III Division 5 was made. The modeling is novel in that the PCHE and constituent micro-channels are considered separately. Modeling effort is reduced through simplification of the micro-channel thermohydraulic and structural behavior. Homogenization methods are used to simplify PCHE thermohydraulics and mechanics so that full component analyses can be performed separately from that of the micro-channel.

A custom finite element method for modeling PCHE thermohydraulics was developed. A novel PCHE thermohydraulic model and Finite Element (FE) implementation was developed. Testing of scale PCHEs verified model accuracy. These were purpose designed for measurement of temperature distribution across the entire PCHE. A homogenized structural mechanics model of the PCHE was implemented in commercial ANSYS mechanical FE software. Linear elastic models of PCHE component and structure were used to determine stress intensities within micro-channel walls. All relevant combinations of load (pressure, thermal) and stress (membrane, bending, peak) could be determined everywhere within the PCHE. Full Nuclear Service evaluation is presented for a zig-zag scale PCHE.

Detailed conclusions for parts of this work are as follows:

7.1 Homogenized Thermohydrualic Modeling of PCHEs

A system for modeling the thermohydraulic behavior inside of PCHEs, the Homogenized Heat Exchanger Thermohydraulic (Homogenized Heat Exchanger Thermohydraulics (HHXT)) model, has been developed to simplify modeling of thermal loads for ratcheting and creep fatigue analyses. The HHXT provides a multi-stream heat transfer solution in 2D or 3D for full sized heat exchangers without needing to resolve the specific micro-channel geometries. This is achieved through a finite element solution of a system of coupled non-linear partial differential equations (PDEs) which model the following behavior: core solid thermal conduction, non-linear porous media flow in each fluid stream, thermal advection in each fluid stream, heat transfer between each fluid stream and the core solid, and thermal storage in the core and all fluids.

A 2D counter flow s-CO_2 recuperator problem is presented as a demonstration of the HHXT model. The model is able to model directional change of the flow within a recuperator core where the cold stream enters and exits at the sides of the PCHE and the hot stream enters at the top and bottom. The HHXT model captures both the counter flow and cross flow heat exchange that occurs in this geometry. The model is also shown to correctly resolve the effect of the cross flow region on the distribution of heat transfer.

The ultimate purpose of the HHXT model is to provide realistic boundary conditions for ratcheting and creep fatigue models, by determining channel wall temperature transients throughout a full heat exchanger. On their own, mechanical models cannot scale to a full size heat exchanger as the resulting mesh size would be impractical. Thus mechanical modeling is limited to capturing specific components of the heat exchanger, be it the internal micro-channel structure, solid wall components, or header attachments. For component mechanical models to capture behavior over a full heat exchanger, results from the HHXT model can provide the spatial variation in channel temperatures. The HHXT model would be used

to locate and quantify the largest thermal transients, then a component mechanical model could be used to evaluate the shakedown at these locations.

The HHXT model is being distributed for free within the research community. It has been developed, and is distributed, as a MATLAB® toolbox with functionality familiar to any who have used the MATLAB® PDE toolbox. The current version and supporting documentation can be found at `https://github.com/IanJentz/HHXT`.

7.2 Experimental Validation of Modeling

Pressure drop and heat transfer performance was investigated experimentally with a medium pressure (8-20MPa) CO_2 facility. A scaled test Printed Circuit Heat Exchanger (PCHE) featuring 80° zig-zag micro-channels was built and installed into the CO_2 facility as a high temperature recuperator, heating CO_2 from from 43 to 448°C.

The geometry of the test PCHE is investigated and presented in detail. Optical topology scans of the etched micro-channels were used to reconstruct the PCHE micro-structure, enabling an evaluation of porosity, conductivity, and channel hydraulic diameter. The resulting channel geometry and diffusion bond layout are illustrated and quantified in Figures 2.1-2.4 and Tables 2.4-4.1.

Steady state experiments were performed over a wide range of CO_2 mass flow, from 0.012 to 0.265 kg/s, covering channel Reynolds numbers from 1,790 to 64,200. Mass flow, inlet and outlet temperature, pressures, and pressure drops were measured and reported along with the uncertainty in these measurements. Calculation of total heat transferred in the hot and cold CO_2 sides is reported.

Embedded thermocouples and fiber-optic sensors provided a measure of the temperature distribution within the PCHE. This used a novel method of feeding a fiber-optic temperature probe back-and-forth through 8 instrumentation channels within the PCHE. In this way

temperature within an instrumented plate in the PCHE was measured at 7542 distinct points spread both along and across the plane of flow. These measurements resolved behavior within the PCHE, providing detailed data with which to validate thermodynamic modeling.

A 2D model of the zig-zag PCHE was created. The homogenized heat exchanger thermohydraulic developed by Jentz[1] was used. An overview of which was discussed, with attention paid to the handling of flow and heat transfer. Homogenization of the micro-channel structure using unit cell analysis was presented and the geometry and layout of the model discussed, see Figures 5.4-4.4 and Table 4.2.

The model used existing correlations in prescribing the thermal and hydraulic performance of the micro-channels. Correlations for Fanning friction factor and Colburn heat transfer coefficient described by Moisseytsev et al. were used [13], see Figures 4.1-4.2. Model mass flow most accurately compared to experiment when applying a correction to the 80° friction factor. The correction brought performance closer to that of Moisseytsev et al.'s 105° zig-zag channel. Applied to the model, the correlations predicted mass-flow and heat-transfer to within 20% of experiment, and reproduced internally measured temperature profiles with RMS differences from 22-43°C.

Models using uniform pressure drop boundary conditions allowed for the redistribution of mass flux across the PCHE, resulting in temperature profiles which matched the internal fiber-optic measurement. Flow redistribution was found to be the result of temperature driven CO_2 property variation. This drove mass flux to be higher in colder, denser, CO_2 streamlines, the effect being more pronounced at temperatures below 150°C.

Internal temperature distributions could not be matched when using uniform mass flux boundary conditions. This commonly used condition should not be used when modeling PCHEs as it unnaturally constrains the redistribution of mass flux. Models assuming a uniform mass flux across micro-channels cannot capture the cross-core temperature variation that occurs in practice.

Uniform pressure drop boundary conditions should be used when modeling PCHE thermohydrualics. This boundary condition allows for mass flux redistribution according to density and friction factor variation within the CO_2 streams. Density variation is the primary driver of mass flux variation, with the cold side CO_2 seeing the most variation and the hot side the least. This results in CO_2 and solid core temperature distributions that vary both across and along the heat exchanger. The validity of this solution was verified when looking at the fiber-optic measured internal temperatures of all 60 steady state tests.

7.3 Mechanical Model of PCHE and Section III Loading & Stress Evaluation

Mechanical modelling of a scaled zig-zag PCHE demonstrates the application of ASME BPVC Section III design by analysis rules. Evaluation of micro-channel wall stress was possible through the homogenization of the PCHE micro-channel structure. Linearized membrane, bending, and peak stress components were determined within the same-stream and cross-stream channel walls. These components were found for a combination of primary and secondary loadings. In this fashion a section III analysis of the primary pembrane, primary pending, and secondary loads was made.

The elastic response of the zig-zag PCHE to thermal and mechanical loading was determined using micro-channel homogenization methods first illustrated by Shaw et. al [49]. This involved separate evaluations of the full sized PCHE and its repeating micro-channel structural subunits. The full size PCHE model substitutes an orthotropic material in lieu of the numerous internal micro-channels. Elastic deformation of the micro-channel structure was used to establish the orthotropic stiffness of the structure. The various counter-flow, cross-flow, and single channel micro-channel structural configurations of the zig-zag PCHE were considered.

A thermo-hydrualic model of the zig-zag PCHE provided steady state distributions of temperature within the PCHE solid structure, temperatures and pressures of the hot and cold fluid streams, and the temperature drop between the hot and cold micro-channel walls. These distributions were evaluated at the zig-zag PCHE's designed operating condition of 0.0336 kg/s CO_2 flow, 18 kW heat load. Temperatures at the design condition were 55-428.9 °C from inlet to outlet on the cold CO_2 side and 495.5-69.3 °C from inlet to outlet on the hot CO_2 side. Deformation and thermal expansion of the full scale PCHE was determined using these pressure and temperature distributions.

Stress intensity within the micro-channel walls were evaluated using the ASME BPVC Section III stress linearization approach. Stress classification lines (SCLs) within same-stream and cross-stream micro-channel walls were defined for the counter-flow, cross-flow, and single channel micro-channel configurations. Within micro-channel subunit models, the elastic stress state of the structure was determined given a set of basis deformations and hot-cold thermal expansion loads. Linearization of the elastic stress along the SCLs determined the Membrane, Bending, and Peak stress intensities of the same-stream and cross-stream walls. Stress intensities were normalized by the basis deformations that created them, creating a scaling factor for determining stress intensity from load. Deformation from loading of the full scale PCHE model, combined with the stress intensity scaling factors, was used to determine the membrane, bending, and peak stress intensities within the 56,160 same-stream walls and 51,840 cross-stream walls of the zig-zag PCHE. In this fashion the distribution of micro-channel wall stress throughout the PCHE, along with local areas of elevated wall stress, were determined.

Stress within the heat exchanger was found for a combination of pressurization, differential thermal expansion across the PCHE, and differential thermal expansion between hot and cold micro-channels. Of these, stress from differential thermal expansion of the PCHE was highest. Mass-flow imbalance across the zig-zag PCHE led to a temperature distribu-

tion that was not only hotter on one end than another, but hotter on one side of the PCHE than the other, resulting in thermal expansion containing a degree of bending in the PCHE. Bending of the PCHE due to thermal expansion created local maximum wall membrane stresses located off the bending axis. Stress from pressurization was lower in magnitude but more evenly distributed. Pressurization stresses were uniform within the counter-flow core except at the edges where stiff solid PCHE sides relieved neighbouring micro-channel walls or near inlets/outlets where PCHE headers increased wall loading. Stress from differential expansion between hot and cold micro-channels produced the lowest stress. This stress was concentrated in the same-stream wall which bore the force of the hot-cold channel differential expansion, with little stress appearing in the cross-stream wall.

The safety of the zig-zag PCHE was considered by considering the Section III allowable membrane Stress Intensity, S_m. Allowable S_m for the 316 stainless steel structure accounted for variation in PCHE temperature–i.e. the hot end of the PCHE had a lower S_m. Safety of the micro-channel walls was quantified by considering a safety factor comparing the allowable membrane stress intensity to the total of primary membrane, primary bending, and secondary membrane + bending stress within the same-stream and cross-stream micro-channel walls. None of the 56,160 same-stream walls and 51,840 cross-stream walls exceeded S_m. Of the thinner cross-stream micro-channel walls, 13.6% of the walls had a safety factor between 1 & 2 (all other were above 2). Of the thicker same-stream walls, 0.7% of the walls had a safety factor between 1 & 2 (all other were above 2). The zig-zag PCHE design complied with Section III membrane stress intensity design.

Bibliography

[1] Ian W. Jentz and Mark H. Anderson. Coupled Heat Transfer and Hydraulic Modeling of an Experimental Printed Circuit Heat Exchanger Using Finite Element Methods. *Journal of Thermal Science and Engineering Applications*, 13(3), 2021. doi: 10.1115/1.4048312.

[2] Eugenio Urquiza, Kenneth Lee, Per F. Peterson, and Ralph Greif. Multiscale Transient Thermal, Hydraulic, and Mechanical Analysis Methodology of a Printed Circuit Heat Exchanger Using an Effective Porous Media Approach. *Journal of Thermal Science and Engineering Applications*, 5(4):041011, 2013. ISSN 1948-5085. doi: 10.1115/1.4024712. URL `http://thermalscienceapplication.asmedigitalcollection.asme.org/article.aspx?doi=10.1115/1.4024712`.

[3] V Dostal. A Supercritical Carbon Dioxide Cycle for Next Generation Nuclear Reactors. *Technical Report MIT-ANP-TR-100*, pages 1–317, 2004. doi: MIT-ANP-TR-100.

[4] A Moisseytsev, E Hoffman, and C Grandy. Selection of Core Outlet Temperature and Impacts on Fast Reactor Economics. *Nuclear Technology*, 173(Mar):251–269, 2011.

[5] Justin Figley, Xiaodong Sun, Sai K. Mylavarapu, and Brian Hajek. Numerical study on thermal hydraulic performance of a Printed Circuit Heat Exchanger. *Progress in Nuclear Energy*, 68:89–96, 2013. ISSN 01491970. doi: 10.1016/j.pnucene.2013.05.003. URL `http://dx.doi.org/10.1016/j.pnucene.2013.05.003`.

[6] Sai K. Mylavarapu, Xiaodong Sun, Richard E. Glosup, Richard N. Christensen, and Michael W. Patterson. Thermal hydraulic performance testing of printed circuit heat exchangers in a high-temperature helium test facility. *Applied Thermal Engineering*, 65

(1-2):605–614, 2014. ISSN 13594311. doi: 10.1016/j.applthermaleng.2014.01.025. URL http://dx.doi.org/10.1016/j.applthermaleng.2014.01.025.

[7] G. D. Pérez-Pichel, J. I. Linares, L. E. Herranz, and B. Y. Moratilla. Thermal analysis of supercritical CO 2 power cycles: Assessment of their suitability to the forthcoming sodium fast reactors. *Nuclear Engineering and Design*, 250:23–34, 2012. ISSN 00295493. doi: 10.1016/j.nucengdes.2012.05.011. URL http://dx.doi.org/10.1016/j.nucengdes.2012.05.011.

[8] Alan Kruizenga. *Heat Transfer and Pressure Drop Measurements in Prototypic Heat Exchangers for the Supercritical Carbon Dioxide Brayton Power Cycles*. PhD thesis, University of Wisconsin Madison, 2010.

[9] Matthew Carlson. *Measurement and Analysis of the Thermal and Hydraulic Performance of Several Printed Circuit Heat Exchanger Channel Geometries*. Masters thesis, University of Wisconsin Madison, 2012.

[10] Eric Van Abel. *Computational Stuidies on the Fluid Flow and Heat Transfer of Supercritical Carbon Dioxide in Printed Circuit Heat Exchangers*. PhD thesis, University of Wisconsin Madison, 2011.

[11] Ting Ma, Lei Li, Xiang Yang Xu, Yi Tung Chen, and Qiu Wang Wang. Study on local thermalhydraulic performance and optimization of zigzag-type printed circuit heat exchanger at high temperature. In *Energy Conversion and Management*, volume 104, pages 55–66. Elsevier Ltd, 2015. doi: 10.1016/j.enconman.2015.03.016. URL http://dx.doi.org/10.1016/j.enconman.2015.03.016.

[12] David Southall, Renaud Le Pierres, and Stephen John Dewson. Design considerations for compact heat exchangers. *International Conference on Advances in Nuclear Power Plants, ICAPP 2008*, 3:1953–1968, 2008.

[13] Anton Moisseytsev, James J. Sienicki, D. H. Cho, and M. R. Thomas. Comparison of Heat Exchanger Modeling with Data from CO2-to-CO2 Printed Circuit Heat Exchanger Performance Tests. In *2010 International Congress on Advances in Nuclear Power Plants*, page 10123, San Diego, CA, 2010.

[14] Alon Katz, Shaun R. Aakre, Mark H. Anderson, and Devesh Ranjan. Experimental investigation of pressure drop and heat transfer in high temperature supercritical CO2 and helium in a printed-circuit heat exchanger. *International Journal of Heat and Mass Transfer*, 171:121089, 2021. ISSN 00179310. doi: 10.1016/j.ijheatmasstransfer.2021.121089. URL `https://doi.org/10.1016/j.ijheatmasstransfer.2021.121089`.

[15] In Hun Kim and Hee Cheon No. Physical model development and optimal design of PCHE for intermediate heat exchangers in HTGRs. *Nuclear Engineering and Design*, 243:243–250, 2012. ISSN 0029-5493. doi: 10.1016/j.nucengdes.2011.11.020. URL `http://dx.doi.org/10.1016/j.nucengdes.2011.11.020`.

[16] Ian W. Jentz and Mark H. Anderson. Measurement of Thermohydraulic Performance and Fiber Optic Thermal Mapping in Printed Circuit Heat Exchangers. *Journal of Thermal Science and Engineering Applications*, 12(4), 2020.

[17] Alan Kruizenga. Heat Transfer of Supercritical Carbon Dioxide in Printed Circuit Heat Exchanger Geometries. *Journal of Thermal Science and Engineering Applications*, 3 (September):1–8, 2011. doi: 10.1115/1.4004252.

[18] Hongzhi Li, Alan Kruizenga, Mark Anderson, Michael Corradini, Yushan Luo, Haijun Wang, and Huixiong Li. Development of a new forced convection heat transfer correlation for CO2 in both heating and cooling modes at supercritical pressures. *International Journal of Thermal Sciences*, 50:2430–2442, 2011. doi: 10.1016/j.ijthermalsci.2011.07.004.

[19] Minghui Chen, Xiaodong Sun, Richard N Christensen, Shanbin Shi, Isaac Skavdahl, and Vivek Utgikar. Experimental and numerical study of a printed circuit heat exchanger. *Annals of Nuclear Energy*, 97:221–231, 2016. ISSN 0306-4549. doi: 10.1016/j.anucene.2016.07.010. URL `http://dx.doi.org/10.1016/j.anucene.2016.07.010`.

[20] Anton Moisseytsev and James J. Sienicki. Analysis of Thermal Transients for sCO2 Brayton Cycle Heat Exchangers. In *Proceedings of ASME Turbo Expo 2019*, pages GT2019–90374, Phoenix, 2019. ASME.

[21] Eugenio Urquiza. *Transient Thermal, Hydraulic, and Mechanical Analysis of a Counter Flow Offset Strip Fin Intermediate Heat Exchanger using an Effective Porous Media Approach*. Doctoral thesis, University of California Berkely, 2009.

[22] Franck Pra, Patrice Tochon, Christian Mauget, Jan Fokkens, and Sander Willemsen. Promising designs of compact heat exchangers for modular HTRs using the Brayton cycle. *Nuclear Engineering and Design*, 238(11):3160–3173, 2008. ISSN 00295493. doi: 10.1016/j.nucengdes.2007.12.024.

[23] Idelchik. *Handbook of Hydraulic Resistance*. 1967.

[24] Gregory Nellis and Sanford Kelin. *Heat Transfer*. Cambridge University Press, New York, NY, 1 edition, 2009. ISBN 978-0-521-887107-4.

[25] Herbert Oertel and Ludwig Prandtl. *Prandtl's Essentials of Fluid Mechanics*. Springer, Karlsruhe, DE, 2004.

[26] Frank M. White. *Fluid mechanics*. McGraw-Hill, second edition, 1986. ISBN 0-07-069673-X.

[27] Johann Nikuradse. Stroemungsgesetze in Rauhen Rohren. In *Forschungsheft 361, Teil B*. VDI Verlag., Berlin, 1933.

[28] C. F. Colebrook. Turbulent Flow in Pipes, with Particular Reference to the Transition between the Smooth and Rough Pipe Laws. *J. Inst. Civ. Eng. Lond.*, 11:133–156, 1938.

[29] L. F. Moody. Friction Factors for Pipe Flow. *ASME Trans.*, 66:671–684, 1944.

[30] M. M. El-Wakil. *Nuclear Heat Transpor.* American Nuclear Society, La Grange Park, IL, 3 edition, 1971. ISBN 0-89448-014-6.

[31] W. M. Kays and A. L. London. *Conpact Heat Exchangers.* McGraw-Hill, New York, 2 edition, 1955.

[32] K. L. Hansen, R. M. Kelso, and B. B. Dally. The Effect of Leading Edge Tubercle Geometry on the Performance of Different Airfoils. In *7th World Conference on Experimental Heat Transfer, Fluid Mechanics and Thermodynamics*, Krakow, Poland, 2009. doi: 10.1177/002029407400700404.

[33] Fran P. Incropera and David P. DeWitt. *Fundamentals of Heat and Mass Transfer.* Wiley, Hoboken, 6th edition, 2007. ISBN 978-0-471-45728-2.

[34] A. R. Wieting. Empirical correlations for heat transfer and flow friction characteristics of rectangular offset-fin plate-fin heat exchangers. *Trans. ASME, Journal of Heat Transfer*, 97:488–490, 1975.

[35] Raj M. Manglik and Arthur E. Bergles. Heat transfer and pressure drop correlations for the rectangular offset strip fin compact heat exchanger. *Experimental Thermal and Fluid Science*, 10(2):171–180, 1995. ISSN 08941777. doi: 10.1016/0894-1777(94)00096-Q.

[36] O.C. Zienkiewicz, R.L. Taylor, and P. Nithiarasu. Generalized Flow Through Porous Media. In *The Finite Element Method for Fluid Dynamcis*, chapter 9, pages 274–291. Elsevier, Oxford, 6 edition, 2005. ISBN 0-7506-6322-7.

[37] W Cui, K A Gawecka, D M Potts, D M G Taborda, and L Zdravkovi. A Petrov-Galerkin finite element method for 2D transient and steady state highly advective flows in porous media. *Computers and Geotechnics*, 100(April):158–173, 2018. doi: 10.1016/j.compgeo.2018.04.013.

[38] Jean Donea and Antonio Huerta. Steady Transport Problems. In *Finite Element Methods for Flow Problems*, chapter 2, pages 33–78. Wiley and Sons, West Sussex, 1 edition, 2003. ISBN 0-471-49666-9.

[39] V John and Petr Knobloch. On spurious oscillations at layers diminishing (SOLD) methods for convectiondiffusion equations: part I a review. *Computational Methods Applied Mechanical Engineering*, (196):2197–2215, 2007.

[40] Petr Knobloch. On the choice of the SUPG parameter at outflow boundary layers. *Adv. Comput. Math*, (31):369–389, 2009. doi: 10.1007/s10444-008-9075-6.

[41] R Span and W Wagner. A New Equation of State for Carbon Dioxide Covering the Fluid Region from the Triple-Point Temperature to 1100 K at Pressures up to 800 MPa. *Journal of Physical Chemistry Referance Data*, 25(6), 1996.

[42] V. Vesovic. The Transport Properties of Carbon Dioxide. *Journal of Physical Chemistry Referance Data*, 19(3), 1990.

[43] A. Fenghour, W. A. Wakeham, and V. Vesovic. The Viscosity of Carbon Dioxide. *Journal of Physical Chemistry Referance Data*, 27(1), 1998.

[44] W.C. Kroenke. Classification of finite element stresses according to asme section iii stress categories. pages 107–140, 1974. URL `https://www.scopus.com/inward/record.uri?eid=2-s2.0-0016321835&partnerID=40&md5=2edc0b6a03319367617ec78ecef4d180`.

[45] W.C. Kroenke, G.W. Addicott, and B.M. Hinton. Interpretation of finite element stresses according to asme section iii. *American Society of Mechanical Engineers (Paper)*, (75 -PVP-63), 1975. URL https://www.scopus.com/inward/record.uri?eid=2-s2.0-85069349919&partnerID=40&md5=61cb90803c8cc9f81149fb08a69dd795.

[46] J.L. Gordon. Outcur: An automated evaluation of two-dimensional finite element stresses according to asme section iii stress requirements. *American Society of Mechanical Engineers (Paper)*, (76 -WA/PVP-16), 1976. URL https://www.scopus.com/inward/record.uri?eid=2-s2.0-85069377943&partnerID=40&md5=7ce21ac9b68fc5b9b74718c8c477c2e6.

[47] D. Mackenzie. Stress linearization concepts and restrictions in elastic design by analysis. volume 1A-2017, 2017. doi: 10.1115/PVP2017-65678. URL https://www.scopus.com/inward/record.uri?eid=2-s2.0-85034058512&doi=10.1115%2fPVP2017-65678&partnerID=40&md5=eaeb5cade517e2af84a73b6517144ebc.

[48] Ian W. Jentz and Mark H. Anderson. Coupled Heat Transfer and Hydraulic Modeling of an Experimental Printed Circuit Heat Exchanger Using Finite Element Methods. *Journal of Thermal Science and Engineering Applications*, 12(4), 2020.

[49] *Assessment of Compact Heat Exchanger Design According to the Simplified ASME Analysis Methodologies*, volume Volume 3: Design and Analysis of *Pressure Vessels and Piping Conference*, 08 2020. doi: 10.1115/PVP2020-21547. URL https://doi.org/10.1115/PVP2020-21547. V003T03A033.

Appendix A

Finite Element Formulation for System of Elliptic PDEs

This appendix details the Finite Element (FE) implementation of the homogenized heat exchanger Partial Differential Equation (PDE)s outlined in Section 3.1.

A.1 PDE system

A.1.1 Generalized System

The PDEs can be described as a system of N PDEs of the following form:

$$\underset{N\times N}{[\mathbf{d}]}\frac{\partial\{\mathbf{u}\}}{\partial t}-\nabla\cdot\left(\underset{N\times N\times 3\times 3}{[[\mathbf{c}]]}\otimes\nabla\{\mathbf{u}\}\right)+\underset{N\times N\times 1\times 3}{[\lfloor\mathbf{b}\rfloor]}\otimes\nabla\{\mathbf{u}\}+\underset{N\times N}{[\mathbf{a}]}\{\mathbf{u}\}=\underset{N\times 1}{\{\mathbf{f}\}} \tag{A.1}$$

This is a system of elliptic PDEs that also contains a first order term $[\mathbf{b}]$.

Different implementations of the model choose to define either $\{\mathbf{f}\}$ or $[\mathbf{b}]$, leaving the system with purely elliptical or with mixed elliptical and first order PDEs respectively.

A.1.2 Nonlinear Terms

Nonlinearity exists in all terms of the PDE system (equation A.1). When considering the effect of nonlinearities of the solution we can think of two sources of nonlinear behavior: material and gradient based nonlinearities. The interaction of these nonlinearity sources with terms of the PDEs system is diagramed in Figure A.1.

Material nonlinearities arise from spatial and state variance of the model materials. Fluid

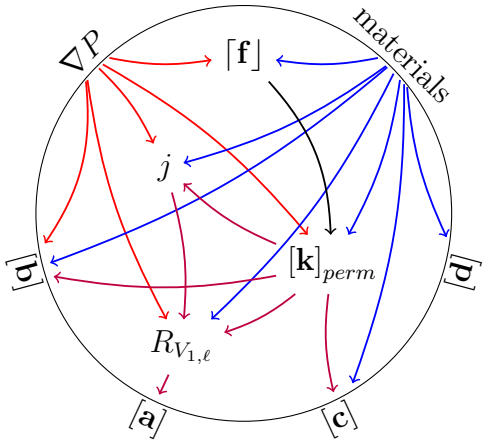

Figure A.1: Nonlinear dependencies in the FE implementation.

and solid properties can vary with temperature and pressure. Channel geometry can vary in position. This affects the values of **d**, **c**, **b**, **a**, and **f**, and thus the solution of the system. However these do not causing instabilities in the solution, thus material nonlinearities are considered weak nonlinearities.

Gradient nonlinearities are strong nonlinearities that tie **c**, **b**, **a**, and **f** terms to the dofs that they operate on. These originate from the ∇P dependency of permeability $[\mathbf{k}]_{perm}$, thermal resistance R_V, and heat advection terms. If the heat advection term is implemented as an **f** contribution, it will also gain ∇T dependency and further nonlinearity.

A.1.3 Boundary Conditions

Boundary conditions for the PDEs are specified for each bounded domain Ω of the problem. The boundary conditions specify a combination of the dofs $\{\mathbf{u}\}$ and their normal derivative on a boundary $\partial\Omega$:

- *Dirichlet:* $[\mathbf{h}]\{\mathbf{u}\} = \{\mathbf{r}\}$ on the boundary $\partial\Omega$.
- *Generalized Neumann:* $\vec{n} \cdot ([[\mathbf{c}]] \otimes \nabla\{\mathbf{u}\}) + [\mathbf{q}]\{\mathbf{u}\} = \{\mathbf{g}\}$ on $\partial\Omega$.

- *Outflow:* $\vec{n} \cdot ([[\mathbf{c}]] \otimes \nabla \{\mathbf{u}\}) - \vec{n} \cdot \lfloor \mathbf{b} \rfloor \{\mathbf{u}\} = 0$ on $\partial\Omega$.

- *Mixed:* A combination of Dirichlet, Generalized Neumann and Outflow.

$\vec{n}$ is the outward unit normal. $\{\mathbf{g}\}$, $[\mathbf{q}]$, $[\mathbf{h}]$, and $\{\mathbf{r}\}$ are functions defined on $\partial\Omega$. Note, traditionally a Neumann condition usually refers to the case $q = 0$.

By default a Generalized Neumann condition of $[\mathbf{q}] = [0]$ and $\{\mathbf{g}\} = \{0\}$ is used at all non-specified boundaries.

A.1.4 Solution Step

Finite element methods are used to approximate the PDE system over a geometry of many domains Ω. The entire problem is composed into a linear system operating on an approximate solution.

$$\underset{NP\times NP}{[\mathbb{K}]} \{\tilde{\mathbf{U}}\} = \underset{NP\times 1}{\{\mathbb{F}\}} \tag{A.2}$$

The unknown vector $\{\tilde{\mathbf{U}}\}$ contains the values of the approximate solution at the mesh points. Its length is the number of dofs in Table 3.1, N, times the number of nodes in the mesh, P.

The approximate solution to the PDE system is found by following these steps:

1. Describe the heat exchanger geometry on the domain Ω and the boundary conditions. The geometry can have many domains, but they must be connected. This is done using the `HHXTmodel` class and Matlab's PDE Toolbox.

2. Set material properties of the problem for each domain Ω of the geometry. Solid material properties must be defined for all Ω while stream properties can be selectively defined. This is done using the `HHXTmodel`.

3. Build a mesh of quadratic triangular/tetrahedral elements on the domain Ω. Matlab's PDE toolbox has mesh generating and refining tools. The mesh is described by three matrices of fixed format that contain information about the mesh points (`p`), the boundary segments (`e`), and the elements (`t`).

4. Provide initial conditions, these can be arbitrary values or previous results. Set the current solution $\{\mathbf{U}\}$ equal to the initial conditions.

5. Construct the linear system using the current solution $\{\mathbf{U}\}$ to evaluate any nonlinear terms. See Appendix A.2.1 for the FE formulation of equation A.1.

6. Solve the linear system to obtain a new solution. This is now the current solution. Advance the solution using partial stepping or a predictor corrector method if desired.

7. Repeat 5-6 until the solution converges.

A.1.5 Construction of Global Matrices

$$\underset{NP\times NP}{[\mathbf{D}]}\{\mathbf{U}\} + \underset{NP\times NP}{[\mathbf{K}]}\{\mathbf{U}\} + \underset{NP\times NP}{[\mathbf{B}]}\{\mathbf{U}\} + \underset{NP\times NP}{[\mathbf{A}]}\{\mathbf{U}\} = \underset{NP\times 1}{\{\mathbf{F}\}} \tag{A.3}$$

The residual used in the method can be derived from equation A.1. Only the spatial terms carry through, as the trial function $\tilde{u}$ is only spatial.

$$\mathcal{R}(\tilde{u}) = -\nabla \cdot \left(\underset{3\times 3}{[c]} \nabla\tilde{u} \right) + \underset{1\times 3}{\lfloor b \rfloor} \nabla\tilde{u} + a\tilde{u} - f \tag{A.4}$$

A.2 FE formulation of PDEs

Formulation of the FE method is given here. First order terms and standard elliptical terms are constructed using Galerkin methods with Petrov stabilisation corrections for the first order terms.

Approximating functions are derived from the shape functions of the element. In our case quadratic shape functions are used. The approximating functions and their derivatives are thus,

$$\tilde{u} = \lfloor \mathbf{N} \rfloor \{\mathbf{u_e}\}\, \tilde{u}_{,x} = \lfloor \mathbf{N}_{,x} \rfloor \{\mathbf{u_e}\}\ etc \tag{A.5}$$

where $\mathbf{u}$ are the dofs given in Tabletab:PDESystem.

A.2.1 Galerkin method

The Galerkin method involves integrating the residual with weights W_i that are related to the approximating function.

$$\begin{aligned} W_i = \frac{\partial \tilde{u}}{\partial \mathbf{u}_{\mathbf{e}_i}} = \mathbf{N}_i \Rightarrow \lfloor \mathbf{W} \rfloor = \lfloor \mathbf{N} \rfloor^T \\ \int_V W_i \mathcal{R} = 0 \Rightarrow \int_V \lfloor \mathbf{N} \rfloor^T \mathcal{R} = 0 \end{aligned} \tag{A.6}$$

Expansion of the residual results in the following terms,

$$\begin{aligned} \mathcal{R}(\tilde{u}) = &- \frac{\partial}{\partial x}\left(\mathbf{c}_{xx}\tilde{u}_{,x} + \mathbf{c}_{xy}\tilde{u}_{,y} + \mathbf{c}_{xz}\tilde{u}_{,z}\right) - \frac{\partial}{\partial y}\left(\mathbf{c}_{yx}\tilde{u}_{,x} + \mathbf{c}_{yy}\tilde{u}_{,y} + \mathbf{c}_{yz}\tilde{u}_{,z}\right) \\ &- \frac{\partial}{\partial z}\left(\mathbf{c}_{zx}\tilde{u}_{,x} + \mathbf{c}_{zy}\tilde{u}_{,y} + \mathbf{c}_{zz}\tilde{u}_{,z}\right) + \left(\mathbf{b}_x\tilde{u}_{,x} + \mathbf{b}_y\tilde{u}_{,y} + \mathbf{b}_z\tilde{u}_{,z}\right) \\ &+ a\tilde{u} - f \end{aligned} \tag{A.7}$$

Each component of the residual can be individually evaluated by the Galerkin integral in equation A.6.

Galerkin of c terms

All of the **c** terms of the residual are integrated the same way. For example taking one of these second order terms,

$$\int_V \lfloor \mathbf{N} \rfloor^T \left(-\frac{\partial}{\partial x} \left(\mathbf{c}_{xx} \tilde{u}_{,x} \right) \right) \tag{A.8}$$

which when integrated by parts in the x direction becomes,

$$\iint \lfloor \mathbf{N} \rfloor^T \left(-\mathbf{c}_{xx} \tilde{u}_{,x} \right) dydz - \int_V \lfloor \mathbf{N}_{,x} \rfloor^T \left(-\mathbf{c}_{xx} \tilde{u}_{,x} \right) \tag{A.9}$$

into which the definition of the derivative of the approximating function from equation A.5 can be substituted to give,

$$\iint \lfloor \mathbf{N} \rfloor^T \left(-\mathbf{c}_{xx} \lfloor \mathbf{N}_{,x} \rfloor \right) dydz \{ \mathbf{u_e} \} - \int_V \lfloor \mathbf{N}_{,x} \rfloor^T \left(-\mathbf{c}_{xx} \lfloor \mathbf{N}_{,x} \rfloor \right) \{ \mathbf{u_e} \} \tag{A.10}$$

This allows the element solution $\{\mathbf{u_e}\}$ to be separated from the volume and surface integrals. Note the surface integral is operating on a boundary normal to the x direction, $\vec{n} = \lfloor 1,\ 0,\ 0 \rfloor^T$.

The steps taken in equations A.8-A.10 can be repeated for all the other 2nd order terms of equation A.7. Combining all of these results in the portion of the Galerkin integral operating on $[\mathbf{c}]$.

$$\int_V \left\lfloor \lfloor \mathbf{N}_{,x} \rfloor^T \lfloor \mathbf{N}_{,y} \rfloor^T \lfloor \mathbf{N}_{,z} \rfloor^T \right\rfloor \underset{3\times 3}{[\mathbf{c}]} \begin{Bmatrix} \lfloor \mathbf{N}_{,x} \rfloor \\ \lfloor \mathbf{N}_{,y} \rfloor \\ \lfloor \mathbf{N}_{,z} \rfloor \end{Bmatrix} \{ \mathbf{u_e} \} - \int_S \lfloor \mathbf{N} \rfloor^T \{ \vec{n} \}^T \underset{3\times 3}{[\mathbf{c}]} \begin{Bmatrix} \lfloor \mathbf{N}_{,x} \rfloor \\ \lfloor \mathbf{N}_{,y} \rfloor \\ \lfloor \mathbf{N}_{,z} \rfloor \end{Bmatrix} \{ \mathbf{u_e} \} \tag{A.11}$$

These integrals are all in Cartesian space (x, y, z). In order to use Gaussian Quadrature to integrate these over an element, it is necessary to transform into element space (r, s, t). This is done by finding the Jacobian [**J**] within the element and using it to calculate the spatial derivatives of the field variables, [**B**].

$$\underbrace{\begin{Bmatrix} \lfloor \mathbf{N}_{,x} \rfloor \\ \lfloor \mathbf{N}_{,y} \rfloor \\ \lfloor \mathbf{N}_{,z} \rfloor \end{Bmatrix}}_{[\mathbf{B}]} = [\mathbf{J}]^{-1} \underbrace{\begin{Bmatrix} \lfloor \mathbf{N}_{,r} \rfloor \\ \lfloor \mathbf{N}_{,s} \rfloor \\ \lfloor \mathbf{N}_{,t} \rfloor \end{Bmatrix}}_{[\mathbf{N},]} \tag{A.12}$$

which when applied to equation A.11 gives the following form of the integrals

$$\int_V [\mathbf{B}]^T [\mathbf{c}] [\mathbf{B}] \{\mathbf{u_e}\} - \int_S \lfloor \mathbf{N} \rfloor^T \underbrace{\{\vec{n}\}^T [\mathbf{c}] [\mathbf{B}]}_{\lfloor f_B \rfloor} \{\mathbf{u_e}\} \tag{A.13}$$

where now only [**c**] and $\vec{n}$ maintain their Cartesian values.

Note that a boundary integral must be taken in this case.

Galerkin of a and f terms

The same analysis can be performed for the a and f terms in equation A.7. The Galerkin integration in this case is quite simple.

$$\int_V \lfloor \mathbf{N} \rfloor^T a\tilde{u} - \int_V \lfloor \mathbf{N} \rfloor^T f \tag{A.14}$$

substituting in the definition of the approximating function,

$$\int_V \lfloor \mathbf{N} \rfloor^T a \lfloor \mathbf{N} \rfloor \{\mathbf{u_e}\} - \int_V \lfloor \mathbf{N} \rfloor^T f \tag{A.15}$$

Since there was no need to integrate by parts, we are not left with boundary integrals

for the a and f terms.

Galerkin of b terms

The same analysis is performed on the **b** term of equation A.7. The Galerkin integral of this portion of the residual is,

$$\int_V \lfloor \mathbf{N} \rfloor^T \left(\mathbf{b}_x \tilde{u}_{,x} + \mathbf{b}_y \tilde{u}_{,y} + \mathbf{b}_z \tilde{u}_{,z} \right) \tag{A.16}$$

substituting in the definition of the approximating function,

$$\int_V \lfloor \mathbf{N} \rfloor^T \left(\mathbf{b}_x \lfloor \mathbf{N}_{,x} \rfloor + \mathbf{b}_y \lfloor \mathbf{N}_{,y} \rfloor + \mathbf{b}_z \lfloor \mathbf{N}_{,z} \rfloor \right) \{ \mathbf{u_e} \} \tag{A.17}$$

This is then transformed into element space using the definition of $[\mathbf{B}]$ in equation A.12.

$$\int_V \lfloor \mathbf{N} \rfloor^T \lfloor \mathbf{b} \rfloor [\mathbf{B}] \{ \mathbf{u_e} \} \tag{A.18}$$

where $\lfloor \mathbf{b} \rfloor$ is still in Cartesian coordinates.

Integration using Gaussian Quadrature

The full Galerkin integral of the residual is the combination of equations A.13, A.15, and A.18.

$$\begin{aligned} \int_V [\mathbf{B}]^T [\mathbf{c}] [\mathbf{B}] \{ \mathbf{u_e} \} - \int_S \lfloor \mathbf{N} \rfloor^T \{ \vec{n} \}^T [\mathbf{c}] [\mathbf{B}] \{ \mathbf{u_e} \} + \int_V \lfloor \mathbf{N} \rfloor^T \lfloor \mathbf{b} \rfloor [\mathbf{B}] \{ \mathbf{u_e} \} \\ + \int_V \lfloor \mathbf{N} \rfloor^T a \lfloor \mathbf{N} \rfloor \{ \mathbf{u_e} \} - \int_V \lfloor \mathbf{N} \rfloor^T f = 0 \end{aligned} \tag{A.19}$$

When using Gaussian Quadrature to evaluate these integrals, the Jacobian and spatial derivatives will have to be evaluated at different points within the element volume, $i = \lfloor r,\, s,\, t \rfloor^T$. As the spatial derivatives are not constant in quadratic elements, the evaluation of $[\mathbf{J}_i]$ and $[\mathbf{B}_i]$ at point i will vary with choice of i. Integration of equation A.13 using Gaussian Quadrature results in summation of Gauss points both within the volume of the element, i, and over surface points j.

$$\begin{aligned}
&\sum_i \left([\mathbf{B}_i]^T [\mathbf{c}_i] [\mathbf{B}_i] \right) J_i W_i \{\mathbf{u_e}\} - \sum_j \left(\lfloor \mathbf{N}_j \rfloor^T \{\vec{n}\}^T [\mathbf{c}_j] [\mathbf{B}_j] \right) J_j W_j \{\mathbf{u_e}\} \\
&+ \sum_i \left(\lfloor \mathbf{N}_i \rfloor^T \lfloor \mathbf{b}_i \rfloor [\mathbf{B}_i] \right) J_i W_i \{\mathbf{u_e}\} + \sum_i \left(\lfloor \mathbf{N}_i \rfloor^T a_i \lfloor \mathbf{N}_i \rfloor \right) J_i W_i \{\mathbf{u_e}\} \\
&= \sum_i \left(\lfloor \mathbf{N}_i \rfloor^T f_i \right) \\
&\textit{in a 3D tetrahedral element,} \\
&J_i = \tfrac{1}{6} \|\mathbf{J}_i\| \textit{ and } J_j = \tfrac{1}{2} \|\mathbf{J}_j\| \\
&\textit{in a 2D triangular element,} \\
&J_i = \tfrac{1}{2} \|\mathbf{J}_i\| \textit{ and } J_j = \|\mathbf{J}_j\|
\end{aligned} \tag{A.20}$$

In a three dimensional mesh, the volume integration occurs over points i within a tetrahedral volume, and the surface integration occurs over points j on all triangular surfaces. Gaussian quadrature points and weights for integration over a tetrahedral volume and integration over a triangular surface are given in Tables A.3 and A.2 respectively. In a two dimensional mesh this changes, with the volume integration being over a triangular element and the surface integration taken over element edges. The edges use linear Gauss quadrature, with points and weights given in Table A.1.

Applying equation A.20 to a 10 node tetrahedral element gives us element matrices for one PDE.

Table A.1: Selected Formulas for Numerical Integration over an Edge

No. of points	Degree of precision	Coordinates r_i	Weights W_i
1	1	$\frac{1}{2}$	1.0
2	2	$\frac{3-\sqrt{3}}{6}, \frac{3+\sqrt{3}}{6}$	$\frac{1}{2}$
3	3	$\begin{cases} \frac{1}{2} \\ \frac{5-\sqrt{15}}{10}, \frac{5+\sqrt{15}}{10} \end{cases}$	$\begin{matrix} \frac{4}{9} \\ \frac{5}{18} \end{matrix}$

Table A.2: Selected Formulas for Numerical Integration over a Triangular Area

No. of points	Degree of precision	Coordinates (r_i, s_i)	Weights W_i
1	1	$\left(\frac{1}{3}, \frac{1}{3}\right)$	1.0
3	2	$\left(\frac{2}{3}, \frac{1}{6}\right), \left(\frac{1}{6}, \frac{1}{6}\right), \left(\frac{1}{6}, \frac{2}{3}\right)$	$\frac{1}{3}$
3	2	$\left(\frac{1}{2}, 0\right), \left(0, \frac{1}{2}\right), \left(\frac{1}{2}, \frac{1}{2}\right)$	$\frac{1}{3}$
4	3	$\begin{cases} \left(\frac{1}{3}, \frac{1}{3}\right) \\ \left(\frac{3}{5}, \frac{1}{5}\right), \left(\frac{1}{5}, \frac{1}{5}\right), \left(\frac{1}{5}, \frac{1}{3}\right) \end{cases}$	$\begin{matrix} -\frac{27}{48} \\ \frac{25}{48} \end{matrix}$

$$\left(\underset{10\times10}{[\mathbf{k_e}]} + \underset{10\times10}{[\mathbf{b_e}]} + \underset{10\times10}{[\mathbf{a_e}]} \right) \underset{10\times1}{\{\mathbf{u_e}\}} = \underset{10\times1}{\{\mathbf{f_e}\}} \tag{A.21}$$

where each matrix is defined by the $[\mathbf{c}]$ and $\lfloor \mathbf{b} \rfloor$ matrices and a and f constants of PDE n; which come from the PDE system matrices of equation A.1,

This is repeated for $n = 1...N$ PDEs within the system

Table A.3: Selected Formulas for Numerical Integration over a Tetrahedral Volume

No. of points	Degree of precision	Coordinates (r_i, s_i, t_i)	Weights W_i
1	1	$\left(\frac{1}{4}, \frac{1}{4}, \frac{1}{4}\right)$	1.0
3	2	$(a, b, b), (b, b, b), (b, b, a), (b, a, b)$ where $a = \frac{5+3\sqrt{5}}{20}, b = \frac{5-\sqrt{5}}{20}$	$\frac{1}{4}$
4	3	$\begin{cases} \left(\frac{1}{4}, \frac{1}{4}, \frac{1}{4}\right) \\ \left(\frac{1}{2}, \frac{1}{6}, \frac{1}{6}\right), \left(\frac{1}{6}, \frac{1}{6}, \frac{1}{6}\right), \left(\frac{1}{6}, \frac{1}{6}, \frac{1}{2}\right), \left(\frac{1}{6}, \frac{1}{2}, \frac{1}{6}\right) \end{cases}$	$\begin{matrix} -\frac{4}{5} \\ \frac{9}{20} \end{matrix}$

A.2.2 Streamline Upwind Petrov Galerkin Formulation

The first order **b** terms introduce instability in a purely Galerkin approach. Instability can be eliminated through the introduction of a stabilization term.

$$\underbrace{\int_V W\mathcal{R}(u)dV}_{Galerkin} + \underbrace{\int_V \mathcal{P}(W)\tau\mathcal{R}(u)dV}_{Stabilization} = 0 \tag{A.22}$$

When consulting literature the terms in the stabilization integral are generally defined for mass transport applications; where the advective factor is taken as a velocity in $\left[\frac{m}{s}\right]$. This differs from our application where the advective factor is the enthalpy advection with units of $\left[\frac{W}{m^2-K}\right]$. To aid

For advective problems the stabilization function is taken as the projection of the advecting velocity, $\mathbf{v}$, on the gradient of the weights, W. The relationship between the weights and approximating functions in equation A.6 can be applied,

$$\mathcal{P}(W) = \mathbf{v}\cdot\nabla W = \mathbf{v}\cdot\nabla\mathbf{N} = \lfloor\mathbf{v}\rfloor[\mathbf{B}] \tag{A.23}$$

$$\mathcal{P}(W) = \mathbf{b}\cdot\nabla W = \mathbf{b}\cdot\nabla\mathbf{N} = \lfloor\mathbf{b}\rfloor[\mathbf{B}] \tag{A.24}$$

this corresponds to a perturbation of the approximating functions in the upwind direction of the streamline defined by $\mathbf{v}$; hence the this method is known as the Streamline Upwind Petrov Galerkin (SUPG) method.

Choice of the stabilization parameter,τ, in equation A.22 plays a major role. In FE methods the parameter has to be calculated at every step and for each element. For quadratic elements τ is a stabilization coefficient matrix, and for linear elements τ is a scalar. Furthermore the definition changes for 1D, 2D, and 3D meshes.

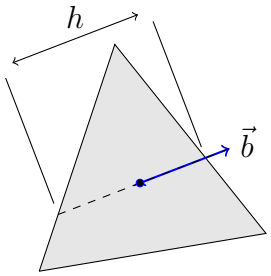

Figure A.2: Determining the streamline length within a 2D element.

A simple 1D formulation of τ can be used in 2D and 3D if the path length, h, and Peclet number, Pe, of the streamline within the element is determined,

$$\tau = \frac{h}{2\,|\mathbf{b}|}\left(coth(Pe) - \frac{1}{Pe}\right) \tag{A.25}$$

here h is found within each element as shown in figure A.2.

The Peclet number is also determined within each element.

$$Pe = \frac{|\mathbf{b}|\,h}{2\alpha} \tag{A.26}$$

where α is the thermal diffusivity of the fluid in the streamline direction. If fluid conductivity is orthotropic the diffusivity would also have to be calculated from the conductivity given in the $\mathbf{c}$ term,

$$\alpha = \frac{1}{\rho c_p}\left|[\mathbf{c}]\,\frac{\{\mathbf{b}\}}{|\mathbf{b}|}\right| \tag{A.27}$$

Insertion of the residual into the stabilization integral in Equation A.22 results in,

$$\int_V [\mathbf{B}]^T \lfloor \mathbf{b} \rfloor^T \tau \left(-\nabla \cdot ([\mathbf{c}]\,\nabla\tilde{u}) + \lfloor \mathbf{b} \rfloor \cdot \nabla\tilde{u} + a\tilde{u} - f\right) dV \tag{A.28}$$

This is numerically integrated using Gaussian Quadrature.

Appendix B

Measurements made in the zig-zag test PCHE

This appendix contains data from the recuperation experiments performed on the zig-zag test heat exchanger. The experiment and methodology used in obtaining this data is described in Section 4.1.1. Table B.1 contains averaged experimental measurements taken during each 2 min logging period. Table D.2 contains the measured mass flow rate along with hot and cold inlet and outlet pressures, temperatures, and pressure drop. Table B.2 contains the total heat flux of the hot and cold CO_2 sides of the recuperator for all mass flow rates. Uncertainty in inlet/outlet condition measurement is propagated into the calculation of heat transfer. Table B.3 contains output of the thermohydraulic model which is compared to experiment in Section 4.3.3.

B.1 Zig-zag Operating Conditions

Table B.1: Experimental Data: Measurements at Recuperator Inlets and Outlets

Run	$T_{H,in}$ (C)	$T_{H,out}$ (C)	$T_{C,in}$ (C)	$T_{C,out}$ (C)	$P_{H,in}$ (MPa)	$P_{C,in}$ (MPa)	ΔP_H (kPa)	ΔP_C (kPa)
1	451.3 ± 1.8	63.6 ± 1.7	54.9 ± 1.0	397.6 ± 1.5	12.0 ± 0.0	12.1 ± 0.1	4.0 ± 0.3	2.7 ± 0.3
2	451.1 ± 1.8	64.1 ± 1.7	55.4 ± 1.0	396.5 ± 1.6	12.1 ± 0.0	12.2 ± 0.0	3.9 ± 0.4	2.7 ± 0.4
3	454.0 ± 1.8	64.2 ± 1.7	55.3 ± 1.0	400.0 ± 1.4	12.1 ± 0.0	12.2 ± 0.0	5.3 ± 0.4	3.6 ± 0.3
4	456.2 ± 1.8	63.9 ± 1.7	54.5 ± 1.0	403.6 ± 1.6	12.0 ± 0.0	12.1 ± 0.0	6.6 ± 1.0	4.5 ± 0.4
5	458.1 ± 1.8	64.2 ± 1.7	54.4 ± 1.0	406.3 ± 1.5	12.0 ± 0.0	12.2 ± 0.0	8.2 ± 1.0	5.6 ± 0.4
6	459.5 ± 1.8	63.5 ± 1.7	53.7 ± 1.0	407.3 ± 1.5	11.9 ± 0.0	12.1 ± 0.0	10.4 ± 0.7	6.9 ± 0.3
7	460.4 ± 1.8	62.5 ± 1.7	53.1 ± 1.0	407.1 ± 1.5	11.7 ± 0.0	12.0 ± 0.0	12.5 ± 1.8	8.4 ± 0.4
8	460.8 ± 1.8	63.3 ± 1.7	53.7 ± 1.0	407.5 ± 1.4	11.8 ± 0.0	12.1 ± 0.0	13.1 ± 0.4	8.5 ± 0.4
9	496.0 ± 1.9	69.9 ± 2.0	57.2 ± 1.0	435.7 ± 1.6	11.6 ± 0.1	11.7 ± 0.1	14.5 ± 5.8	9.2 ± 2.3
10	462.6 ± 1.8	63.2 ± 1.7	53.9 ± 1.0	407.4 ± 1.4	11.9 ± 0.1	12.2 ± 0.0	14.8 ± 2.7	10.0 ± 0.3
11	463.4 ± 1.8	62.5 ± 1.7	53.5 ± 1.0	406.4 ± 1.4	11.7 ± 0.1	12.2 ± 0.0	18.4 ± 1.5	11.7 ± 0.3
12	510.0 ± 1.8	61.4 ± 1.7	50.6 ± 1.0	447.6 ± 1.4	11.0 ± 0.0	11.2 ± 0.0	21.1 ± 2.3	12.9 ± 2.3
13	464.7 ± 1.8	62.8 ± 1.7	53.6 ± 1.0	404.9 ± 1.6	11.7 ± 0.0	12.2 ± 0.1	22.3 ± 0.8	13.9 ± 0.6
14	495.5 ± 1.9	69.3 ± 1.9	55.0 ± 1.0	428.9 ± 1.8	11.4 ± 0.1	11.5 ± 0.1	31.8 ± 6.9	20.5 ± 1.9
15	465.7 ± 1.8	62.8 ± 1.7	52.9 ± 1.0	401.4 ± 1.8	11.5 ± 0.0	12.2 ± 0.0	29.3 ± 2.5	17.9 ± 0.6
16	510.0 ± 1.9	63.3 ± 1.7	50.5 ± 1.0	441.9 ± 1.6	11.0 ± 0.1	11.2 ± 0.1	34.9 ± 2.8	22.0 ± 2.5
17	466.8 ± 1.8	63.4 ± 1.7	52.6 ± 1.0	399.0 ± 1.5	11.3 ± 0.1	12.2 ± 0.0	37.6 ± 4.2	22.5 ± 0.7
18	463.6 ± 1.8	64.6 ± 1.7	53.6 ± 1.0	395.9 ± 1.5	11.5 ± 0.1	12.4 ± 0.1	37.5 ± 3.9	22.6 ± 0.6
19	508.0 ± 1.8	65.5 ± 1.7	50.3 ± 1.0	436.3 ± 1.6	11.0 ± 0.0	11.2 ± 0.1	47.3 ± 3.6	29.1 ± 2.5
20	467.3 ± 1.8	64.3 ± 1.7	52.3 ± 1.0	395.5 ± 1.5	11.1 ± 0.1	12.2 ± 0.1	47.6 ± 1.8	27.4 ± 0.7
21	504.2 ± 1.8	66.7 ± 1.8	50.1 ± 1.0	430.0 ± 1.6	11.0 ± 0.0	11.3 ± 0.0	57.8 ± 2.6	35.1 ± 2.2
22	493.9 ± 1.9	71.6 ± 1.8	52.9 ± 1.1	419.8 ± 1.7	11.0 ± 0.1	11.4 ± 0.1	58.7 ± 7.5	36.9 ± 1.8
23	467.5 ± 1.8	65.1 ± 1.7	52.1 ± 1.0	392.2 ± 1.5	10.9 ± 0.1	12.2 ± 0.1	56.6 ± 6.0	32.3 ± 0.7
24	487.3 ± 1.8	72.7 ± 1.8	47.6 ± 1.0	394.8 ± 1.9	10.0 ± 0.1	10.9 ± 0.1	164.9 ± 12.0	95.0 ± 2.5
25	460.3 ± 1.8	57.7 ± 1.7	49.8 ± 1.0	346.3 ± 2.0	8.0 ± 0.0	12.9 ± 0.1	185.3 ± 3.5	66.4 ± 1.0
26	443.5 ± 1.8	108.7 ± 1.8	72.2 ± 1.1	368.4 ± 1.8	11.8 ± 0.0	12.6 ± 0.1	158.0 ± 7.2	98.4 ± 3.1
27	378.5 ± 1.8	53.2 ± 1.7	46.4 ± 1.0	277.8 ± 2.3	8.7 ± 0.0	12.2 ± 0.1	156.7 ± 3.7	65.3 ± 1.2
28	380.8 ± 1.8	54.0 ± 1.7	47.1 ± 1.0	279.5 ± 2.5	8.8 ± 0.0	12.3 ± 0.1	160.0 ± 3.5	66.6 ± 1.0
29	433.8 ± 1.8	94.3 ± 1.7	61.4 ± 1.0	354.6 ± 1.7	10.3 ± 0.0	11.4 ± 0.1	193.1 ± 7.3	115.1 ± 3.0
30	440.6 ± 1.8	109.8 ± 1.7	73.1 ± 1.1	364.4 ± 1.9	11.8 ± 0.0	12.7 ± 0.1	179.5 ± 6.8	111.0 ± 3.4
31	500.4 ± 1.8	125.0 ± 2.0	85.2 ± 1.0	414.8 ± 2.1	17.4 ± 0.0	18.1 ± 0.0	163.7 ± 62.0	102.8 ± 36.2
32	431.8 ± 1.8	94.4 ± 1.7	61.4 ± 1.0	350.6 ± 1.7	10.3 ± 0.0	11.4 ± 0.1	221.2 ± 7.1	129.4 ± 2.8
33	438.4 ± 1.8	110.5 ± 1.7	73.5 ± 1.1	358.9 ± 1.8	11.8 ± 0.1	12.9 ± 0.1	211.0 ± 8.2	128.5 ± 3.5
34	430.0 ± 1.8	95.6 ± 1.8	62.2 ± 1.1	347.6 ± 2.2	10.2 ± 0.0	11.5 ± 0.1	249.1 ± 7.6	144.1 ± 2.9
35	436.6 ± 1.8	111.5 ± 1.8	74.2 ± 1.1	356.0 ± 2.7	11.7 ± 0.0	13.0 ± 0.1	243.9 ± 7.8	146.1 ± 3.4
36	486.1 ± 1.8	94.3 ± 2.2	57.3 ± 1.2	387.4 ± 2.6	9.6 ± 0.0	11.3 ± 0.1	360.7 ± 12.7	192.7 ± 4.4
37	428.6 ± 1.8	97.4 ± 1.8	63.5 ± 1.1	343.9 ± 2.3	10.2 ± 0.0	11.6 ± 0.1	282.6 ± 7.1	161.3 ± 3.0
38	497.9 ± 1.8	129.3 ± 1.9	85.2 ± 1.0	406.4 ± 2.6	16.8 ± 0.1	17.9 ± 0.0	243.9 ± 89.7	140.3 ± 36.4
39	427.7 ± 1.8	97.2 ± 1.7	63.7 ± 1.0	343.3 ± 2.4	9.9 ± 0.0	11.7 ± 0.1	364.4 ± 7.9	199.9 ± 3.3
40	488.0 ± 1.9	106.2 ± 1.8	65.2 ± 1.0	388.3 ± 3.0	9.8 ± 0.0	12.0 ± 0.1	436.8 ± 11.1	231.4 ± 3.8
41	435.3 ± 1.8	112.6 ± 1.8	75.0 ± 1.1	353.4 ± 2.9	11.6 ± 0.0	13.1 ± 0.1	291.1 ± 8.0	171.4 ± 3.5
42	490.5 ± 1.8	130.4 ± 1.8	85.3 ± 1.0	395.6 ± 2.9	16.4 ± 0.1	17.8 ± 0.0	299.2 ± 101.8	169.6 ± 38.4

Continued on next page

Table B.1 – *Continued from previous page*

Run	$T_{H,in}$ (C)	$T_{H,out}$ (C)	$T_{C,in}$ (C)	$T_{C,out}$ (C)	$P_{H,in}$ (MPa)	$P_{C,in}$ (MPa)	ΔP_H (kPa)	ΔP_C (kPa)
43	491.8 ± 1.9	114.2 ± 1.8	70.9 ± 1.1	392.9 ± 2.6	10.0 ± 0.0	12.3 ± 0.1	476.0 ± 9.5	251.8 ± 3.3
44	428.6 ± 1.8	95.9 ± 1.7	63.0 ± 1.0	342.6 ± 2.4	9.6 ± 0.0	11.7 ± 0.1	430.7 ± 8.7	227.2 ± 3.2
45	432.1 ± 1.9	92.0 ± 1.9	61.0 ± 1.1	341.3 ± 2.4	9.4 ± 0.0	11.7 ± 0.1	471.1 ± 9.1	240.9 ± 3.6
46	434.5 ± 1.8	111.0 ± 1.7	73.9 ± 1.0	347.9 ± 2.8	11.3 ± 0.0	13.2 ± 0.1	399.2 ± 9.5	222.6 ± 4.1
47	483.8 ± 1.9	130.1 ± 1.8	85.0 ± 1.0	386.7 ± 2.7	16.2 ± 0.1	17.8 ± 0.0	335.2 ± 105.5	189.4 ± 39.1
48	477.5 ± 1.9	129.7 ± 1.8	84.8 ± 1.0	378.4 ± 2.9	16.1 ± 0.1	17.8 ± 0.0	367.7 ± 109.6	204.9 ± 38.7
49	470.1 ± 2.0	129.6 ± 1.8	84.9 ± 1.0	368.4 ± 3.1	15.9 ± 0.1	17.8 ± 0.0	414.5 ± 108.8	222.2 ± 38.9
50	460.4 ± 2.1	129.8 ± 1.8	85.5 ± 1.0	355.0 ± 2.8	15.7 ± 0.1	18.0 ± 0.0	487.7 ± 105.4	256.0 ± 42.5
51	449.8 ± 2.1	129.9 ± 1.8	86.2 ± 1.0	341.8 ± 2.6	15.6 ± 0.1	18.1 ± 0.0	548.8 ± 99.1	289.6 ± 49.5
52	487.2 ± 2.5	141.4 ± 1.8	91.1 ± 1.0	366.5 ± 2.5	15.5 ± 0.1	18.4 ± 0.0	636.8 ± 95.7	327.1 ± 62.4
53	469.5 ± 2.5	141.0 ± 1.8	92.3 ± 1.0	349.0 ± 2.1	15.3 ± 0.1	18.5 ± 0.1	707.0 ± 87.3	361.3 ± 70.7
54	454.8 ± 2.5	139.6 ± 1.8	92.2 ± 1.0	335.0 ± 2.2	15.2 ± 0.1	18.6 ± 0.1	760.9 ± 77.5	383.0 ± 75.0
55	438.6 ± 2.5	138.1 ± 1.8	92.4 ± 1.1	320.0 ± 2.0	15.1 ± 0.0	18.8 ± 0.1	827.7 ± 71.9	411.5 ± 83.4
56	421.0 ± 2.6	136.9 ± 1.8	93.1 ± 1.1	306.1 ± 2.3	15.2 ± 0.0	19.1 ± 0.1	871.2 ± 64.9	431.8 ± 92.8
57	404.9 ± 2.6	135.9 ± 1.8	93.8 ± 1.1	292.8 ± 2.4	15.3 ± 0.0	19.4 ± 0.1	937.5 ± 61.8	460.1 ± 104.9
58	387.5 ± 2.8	134.8 ± 1.8	94.6 ± 1.1	279.3 ± 2.9	15.4 ± 0.0	19.7 ± 0.1	990.3 ± 57.4	483.6 ± 115.6
59	371.4 ± 2.9	131.6 ± 1.8	95.0 ± 1.1	265.8 ± 2.8	15.5 ± 0.0	20.1 ± 0.1	1046.5 ± 63.1	507.6 ± 127.2
60	397.0 ± 3.4	134.0 ± 2.1	101.5 ± 1.1	288.0 ± 4.2	14.7 ± 0.1	20.1 ± 0.1	1261.6 ± 73.1	594.9 ± 156.9

Table B.2: Experimental Data: Measured Mass Flow and Heat Transferred

Run	$\dot{m}$ (kg/s)		$\dot{q}_H$ (kW)		$\dot{q}_C$ (kW)	
1	0.012 29	± 0.000 263	−6.420	± 0.161	6.131	± 0.147
2	0.012 30	± 0.000 272	−6.423	± 0.165	6.113	± 0.150
3	0.014 24	± 0.000 319	−7.491	± 0.194	7.161	± 0.177
4	0.016 14	± 0.000 329	−8.509	± 0.205	8.216	± 0.188
5	0.018 06	± 0.000 470	−9.541	± 0.277	9.270	± 0.260
6	0.020 13	± 0.000 460	–10.690	± 0.280	10.415	± 0.261
7	0.022 23	± 0.000 630	–11.852	± 0.370	11.535	± 0.348
8	0.022 50	± 0.000 412	–11.973	± 0.268	11.644	± 0.244
9	0.022 91	± 0.000 420	–12.586	± 0.274	12.060	± 0.256
10	0.024 68	± 0.000 410	–13.209	± 0.279	12.777	± 0.249
11	0.026 92	± 0.000 535	–14.448	± 0.343	13.942	± 0.311
12	0.027 68	± 0.001 05	−16.159	± 0.642	15.632	± 0.621
13	0.029 42	± 0.000 662	–15.789	± 0	15.201	± 0
14	0.033 57	± 0.000 339	–18.341	± 0.269	17.666	± 0.273
15	0.033 94	± 0.000 800	–18.111	± 0.484	17.481	± 0.450
16	0.035 14	± 0.001 26	−20.271	± 0.757	19.664	± 0.737
17	0.038 29	± 0.000 833	–20.274	± 0.504	19.666	± 0.472
18	0.038 69	± 0.000 821	–20.300	± 0.495	19.647	± 0.462
19	0.040 85	± 0.001 17	−23.140	± 0.703	22.640	± 0.697
20	0.042 34	± 0.001 35	−22.160	± 0.749	21.645	± 0.723
21	0.045 29	± 0.000 968	–25.268	± 0.595	24.870	± 0.600

Continued on next page

Table B.2 – *Continued from previous page*

Run	$\dot{m}$ (kg/s)		$\dot{q}_H$ (kW)		$\dot{q}_C$ (kW)	
22	0.045 60	± 0.000 371	–24.329	± 0.306	23.839	± 0.352
23	0.046 89	± 0.000 996	–24.273	± 0.580	23.853	± 0.562
24	0.075 56	± 0.000 879	–38.500	± 0.551	38.961	± 0.694
25	0.075 67	± 0.000 418	–36.420	± 0.358	35.606	± 0.408
26	0.076 30	± 0.000 862	–31.142	± 0.443	30.858	± 0.460
27	0.077 71	± 0.000 549	–31.585	± 0.442	30.999	± 0.447
28	0.078 58	± 0.000 589	–32.130	± 0.455	31.373	± 0.468
29	0.083 40	± 0.000 709	–34.155	± 0.412	33.881	± 0.483
30	0.084 40	± 0.000 822	–34.018	± 0.443	33.635	± 0.469
31	0.087 30	± 0.000 931	–42.040	± 0.581	41.029	± 0.549
32	0.091 67	± 0.000 576	–37.238	± 0.396	36.899	± 0.486
33	0.095 31	± 0.001 01	−38.027	± 0.521	37.402	± 0.544
34	0.1004	± 0.000 537	–40.314	± 0.410	39.903	± 0.538
35	0.1060	± 0.000 606	–41.849	± 0.436	41.178	± 0.536
36	0.1070	± 0.000 308	–49.684	± 0.446	49.437	± 0.719
37	0.1086	± 0.000 715	–43.072	± 0.468	42.321	± 0.603
38	0.1099	± 0.001 11	−51.369	± 0.671	50.413	± 0.687
39	0.1130	± 0.000 681	–44.444	± 0.465	44.123	± 0.616
40	0.1153	± 0.000 536	–51.940	± 0.459	50.939	± 0.653
41	0.1202	± 0.000 575	–46.964	± 0.466	46.230	± 0.609
42	0.1230	± 0.001 20	−55.883	± 0.719	54.684	± 0.767
43	0.1235	± 0.000 567	–54.894	± 0.490	53.458	± 0.621

Continued on next page

Table B.2 – *Continued from previous page*

Run	$\dot{m}$ (kg/s)		$\dot{q}_H$ (kW)		$\dot{q}_C$ (kW)	
44	0.1242	± 0.000 547	−48.928	± 0.466	48.774	± 0.647
45	0.1260	± 0.000 672	−50.644	± 0.528	50.226	± 0.746
46	0.1277	± 0.000 654	−49.681	± 0.499	48.877	± 0.646
47	0.1310	± 0.001 28	−58.397	± 0.754	56.960	± 0.792
48	0.1380	± 0.001 38	−60.406	± 0.795	58.685	± 0.855
49	0.1475	± 0.001 45	−63.126	± 0.834	60.982	± 0.909
50	0.1614	± 0.001 48	−66.876	± 0.868	63.960	± 0.919
51	0.1724	± 0.001 46	−69.004	± 0.887	65.372	± 0.912
52	0.1805	± 0.001 37	−77.049	± 0.934	71.803	± 0.908
53	0.1916	± 0.001 28	−77.545	± 0.937	71.712	± 0.854
54	0.2004	± 0.001 17	−77.817	± 0.934	71.757	± 0.856
55	0.2116	± 0.001 04	−78.382	± 0.937	72.003	± 0.845
56	0.2204	± 0.000 936	−77.384	± 0.976	71.114	± 0.915
57	0.2323	± 0.000 794	−77.413	± 1	71.012	± 0.959
58	0.2430	± 0.000 850	−76.380	± 1.098	70.112	± 1.113
59	0.2544	± 0.000 814	−76.331	± 1.179	69.132	± 1.149
60	0.2646	± 0.001 04	−85.304	± 1.387	75.265	± 1.571

B.1.1 thermodynamic model results

Table B.3: Model Data

Run	$T_{H,out}$ (C)	$T_{C,out}$ (C)	$\dot{m}_H$ (kg/s)	$\dot{m}_C$ (kg/s)	$\dot{q}_H$ (kW)	$\dot{q}_C$ (kW)	$\bar{Re}_H$ $(-)$	$Re_{std,H}$ $(-)$	$\bar{Re}_C$ $(-)$	$Re_{std,C}$ $(-)$
1	68.8	397.8	0.011 28	0.011 52	−5.745	5.747	1855	238	1557	308
2	68.8	395.8	0.011 25	0.011 58	−5.740	5.742	1844	235	1561	308
3	69.4	395.5	0.013 22	0.013 63	−6.770	6.772	2165	276	1831	374
4	67.9	388.8	0.014 97	0.015 80	−7.749	7.753	2464	318	2125	455
5	68.6	390.2	0.016 87	0.017 72	−8.730	8.736	2780	359	2377	515
6	69.0	392.4	0.019 03	0.019 75	−9.836	9.842	3142	409	2640	583
7	67.5	384.7	0.021 07	0.022 37	−10.969	10.976	3493	458	2991	683
8	69.6	392.5	0.021 46	0.022 20	−11.057	11.065	3554	466	2969	659
9	73.9	440.2	0.020 99	0.020 85	−11.113	11.124	3459	522	2863	568
10	68.4	382.8	0.023 30	0.024 98	−12.147	12.156	3860	504	3333	757
11	69.9	389.7	0.025 76	0.026 79	−13.292	13.302	4286	569	3571	809
12	70.8	447.4	0.025 09	0.024 85	−13.963	13.978	4160	674	3350	775
13	70.5	390.2	0.028 48	0.029 48	−14.654	14.666	4746	634	3921	890
14	72.8	420.5	0.032 65	0.033 77	−17.408	17.425	5462	834	4658	1003
15	70.0	385.8	0.032 87	0.034 24	−16.910	16.924	5525	754	4542	1058
16	70.4	430.1	0.033 72	0.034 77	−18.851	18.869	5642	907	4708	1132
17	69.7	381.7	0.037 44	0.039 26	−19.231	19.247	6342	885	5198	1231
18	70.6	378.4	0.037 78	0.039 76	−19.247	19.264	6381	869	5256	1221
19	71.4	422.4	0.039 77	0.041 05	−21.916	21.940	6692	1086	5565	1338
20	69.8	380.3	0.042 07	0.043 86	−21.477	21.496	7189	1035	5789	1387
21	71.6	414.3	0.044 59	0.046 19	−24.301	24.329	7534	1218	6252	1512
22	72.3	407.5	0.045 42	0.047 54	−24.047	24.073	7708	1216	6560	1482
23	70.8	362.4	0.046 21	0.049 68	−23.284	23.308	8016	1187	6552	1589
24	68.1	368.9	0.077 64	0.084 30	−40.463	40.512	13 660	2346	11 518	2911
25	63.9	324.9	0.076 87	0.083 96	−36.649	36.685	14 814	2932	10 134	2931

Continued on next page

Table B.3 – *Continued from previous page*

Run	$T_{H,out}$ (C)	$T_{C,out}$ (C)	$\dot{m}_H$ (kg/s)	$\dot{m}_C$ (kg/s)	$\dot{q}_H$ (kW)	$\dot{q}_C$ (kW)	$\bar{Re}_H$ $(-)$	$Re_{std,H}$ $(-)$	$\bar{Re}_C$ $(-)$	$Re_{std,C}$ $(-)$
26	108.4	366.4	0.081 22	0.084 97	−34.116	34.159	13 911	1934	12 342	1839
27	56.3	257.0	0.079 69	0.088 17	−31.904	31.933	15 606	2331	10 779	3169
28	57.4	260.4	0.080 70	0.088 94	−32.440	32.469	15 728	2341	10 879	3151
29	98.2	334.9	0.085 35	0.091 70	−35.191	35.242	15 111	2313	13 769	2088
30	108.5	362.2	0.087 37	0.091 65	−36.221	36.266	14 986	2068	13 315	1941
31	133.1	413.7	0.097 36	0.1008	−47.054	47.112	14 688	1493	12 523	1876
32	95.0	339.5	0.092 12	0.097 93	−38.194	38.247	16 391	2525	14 633	2284
33	108.3	357.7	0.095 58	0.1005	−39.233	39.282	16 430	2263	14 585	2091
34	94.2	339.9	0.098 31	0.1043	−40.570	40.625	17 542	2709	15 550	2437
35	108.7	354.4	0.1034	0.1088	−41.975	42.028	17 805	2453	15 777	2220
36	89.0	377.5	0.1128	0.1208	−54.295	54.364	20 059	3718	17 436	3423
37	94.1	339.9	0.1052	0.1115	−42.959	43.015	18 836	2919	16 629	2602
38	135.8	413.9	0.1177	0.1182	−55.069	55.141	17 977	1954	14 778	2150
39	92.6	334.4	0.1197	0.1278	−48.513	48.575	21 648	3433	19 026	2984
40	98.6	382.8	0.1250	0.1337	−58.159	58.236	21 925	3975	19 427	3379
41	109.0	350.2	0.1136	0.1201	−45.613	45.671	19 618	2721	17 385	2408
42	135.1	403.5	0.1311	0.1323	−59.877	59.956	20 223	2225	16 643	2383
43	107.6	389.9	0.1302	0.1388	−59.433	59.513	22 577	4043	20 211	3327
44	91.2	331.0	0.1293	0.1386	−52.466	52.532	23 544	3833	20 576	3265
45	88.7	329.3	0.1343	0.1446	−55.453	55.521	24 614	4130	21 343	3515
46	107.7	341.0	0.1331	0.1420	−52.938	53.002	23 271	3347	20 492	2880
47	133.9	394.2	0.1397	0.1422	−62.815	62.897	21 712	2379	17 918	2563
48	133.5	387.4	0.1470	0.1496	−64.900	64.984	22 972	2508	18 868	2685
49	134.2	382.1	0.1564	0.1571	−67.165	67.252	24 580	2683	19 824	2780
50	133.9	370.7	0.1711	0.1725	−71.215	71.307	27 137	2946	21 779	3002
51	132.7	356.8	0.1837	0.1882	−74.266	74.360	29 409	3139	23 794	3230
52	142.5	389.4	0.1910	0.1951	−82.518	82.625	30 139	3689	24 616	3220
53	140.3	370.9	0.2034	0.2103	−83.690	83.796	32 498	3839	26 643	3354
54	137.8	356.5	0.2128	0.2211	−84.268	84.374	34 326	3922	28 008	3483

Continued on next page

Table B.3 – *Continued from previous page*

Run	$T_{H,out}$ (C)	$T_{C,out}$ (C)	$\dot{m}_H$ (kg/s)	$\dot{m}_C$ (kg/s)	$\dot{q}_H$ (kW)	$\dot{q}_C$ (kW)	$\bar{Re}_H$ $(-)$	$Re_{std,H}$ $(-)$	$\bar{Re}_C$ $(-)$	$Re_{std,C}$ $(-)$
55	135.7	339.9	0.2244	0.2353	−85.061	85.172	36 556	3992	29 736	3641
56	134.2	323.8	0.2334	0.2467	−84.083	84.195	38 333	3930	31 116	3713
57	133.3	309.0	0.2448	0.2608	−83.890	84.000	40 494	3897	32 705	3824
58	132.4	293.7	0.2549	0.2734	−82.593	82.696	42 436	3775	34 073	3941
59	131.5	279.9	0.2653	0.2861	−81.453	81.546	44 414	3648	35 345	4129
60	138.2	299.0	0.2747	0.3005	−88.211	88.308	46 180	4635	37 743	3743

Appendix C

Mechanical model results tables

This Appendix contains further results from the zig-zag micro-channel subunit analysis discussed in Section 5.2.

C.1 results of the micro-channel subunit models

C.1.1 deformation and elasticity of the subunits

Table C.1: Deformations and Stresses of the cross-flow subunit model

	subunit dimensions			
	1 (x)	2 (y)	3 (z)	
length (mm)	7.24	7.24	3.00	
area (mm^2)	21.7	21.7	52.4	
	deformation (μm)			**reaction (kN)**
	1 (x)	2 (y)	3 (z)	
tension 1	**14.484**	-4.405	-1.587	5.270
tension 2	-4.438	**14.484**	-1.597	5.309
tension 3	-2.697	-2.694	**6.000**	8.958
shear 12	-0.013	**14.484**	0.000	1.470
shear 23	0.000	0.008	**14.484**	0.567
shear 31	**6.000**	0.000	0.117	3.058
	strain (mm/m)			**stress (MPa)**
	1 (x)	2 (y)	3 (z)	
tension 1	**2.000**	-0.608	-0.529	242.6
tension 2	-0.613	**2.000**	-0.532	244.4
tension 3	-0.372	-0.372	**2.000**	170.8
shear 12	-0.002	**2.000**	0.000	67.6
shear 23	0.000	0.001	**2.000**	26.1
shear 31	**2.000**	0.000	0.039	58.3

Table C.2: Deformations and Stresses of the counterflow channel subunit model

subunit dimensions				
	1 (x)	2 (y)	3 (z)	
length (mm)	7.24	6.56	3.00	
area (mm^2)	19.7	21.7	47.5	
	deformation (μm)			**reaction (kN)**
	1 (x)	2 (y)	3 (z)	
tension 1	**14.484**	-4.195	-1.543	4.956
tension 2	-4.327	**13.128**	-1.364	5.112
tension 3	-2.879	-2.467	**6.000**	9.248
shear 12	-0.003	**14.484**	0.000	1.278
shear 23	0.000	-0.018	**13.128**	0.557
shear 31	**6.000**	0.000	0.000	2.841
	strain (mm/m)			**stress (MPa)**
	1 (x)	2 (y)	3 (z)	
tension 1	**2.001**	-0.639	-0.514	251.8
tension 2	-0.598	**2.001**	-0.455	235.3
tension 3	-0.398	-0.376	**2.000**	194.7
shear 12	0.000	**2.001**	0.000	65.0
shear 23	0.000	-0.003	**2.001**	25.6
shear 31	**2.000**	0.000	0.000	59.8

C.1.2 mapping of linearized stress components for the counterflow subunit

Table C.3: Deformations and Stresses of the single channel subunit model

	subunit dimensions			
	1 (x)	2 (y)	3 (z)	
length (mm) 7.24	6.56	6.00		
area (mm^2) 39.4	43.5	47.5		
	deformation (μm)			**reaction (kN)**
	1 (x)	2 (y)	3 (z)	
tension 1	**14.484**	-4.086	-1.773	12.689
tension 2	-4.389	**13.128**	-1.733	13.629
tension 3	-3.098	-2.819	**12.000**	11.214
shear 12	-0.002	**14.484**	0.000	3.184
shear 23	0.000	-0.002	**13.128**	1.660
shear 31	**12.000**	0.000	0.000	3.931
	strain (mm/m)			**stress (MPa)**
	1 (x)	2 (y)	3 (z)	
tension 1	**2.000**	-0.622	-0.295	322.2
tension 2	-0.606	**2.000**	-0.289	313.7
tension 3	-0.428	-0.429	**2.000**	235.9
shear 12	0.000	**2.000**	0.000	80.8
shear 23	0.000	0.000	**2.000**	38.2
shear 31	**2.000**	0.000	0.000	82.7

Continued on next page

Continued from previous page

Counterflow micro-channel, same-stream SCL : $\sigma_{\text{scl}} = [\Lambda]\sigma$

$[\Lambda_\sigma]$

Table C.4: Stress transforms for the Counterflow micro-channel at the Same-Stream Stress Classification Line

Counterflow micro-channel, same-stream SCL : $\sigma_{\text{scl}} = [\Lambda]\sigma$

$[\Lambda_\sigma]$

Membrane

$$\begin{bmatrix} 1.1711 & 0.091268 & 0.35477 & -0.29585 & -0.43504 & 0.18916 \\ 0.10348 & 1.1443 & 0.31932 & -0.073083 & -1.5693 & 0.014726 \\ 0.0044425 & 0.014146 & 2.4293 & -0.1287 & 0.019436 & 0.21216 \\ 0.12293 & 0.027191 & 0.10978 & 1.5119 & -0.11361 & 0.066662 \\ -0.00026242 & 0.016934 & 0.0094508 & -0.039048 & 2.3382 & 0.2987 \\ -0.0082075 & 0.0041999 & -0.0029418 & -0.051955 & 0.30029 & 2.5299 \end{bmatrix}$$

Bending (Inside)

$$\begin{bmatrix} -0.004669 & 0.00081217 & 0.023053 & 0.45163 & 1.3752 & -2.8527 \\ 0.0035227 & 0.020036 & 0.039063 & 0.14503 & 4.3098 & -1.1463 \\ 0.010772 & 0.022141 & 0.020845 & 0.23018 & 0.51285 & -3.5681 \\ 0.0018577 & 0.011212 & -0.0056415 & 0.21794 & -0.99098 & 0.32027 \\ -0.13662 & 0.74617 & 0.014198 & -0.61014 & -0.65453 & 0.0040192 \\ -0.62456 & 0.15029 & -0.0086087 & 1.0803 & -0.054227 & -0.084299 \end{bmatrix}$$

Continued on next page

Continued from previous page

Counterflow micro-channel, same-stream SCL : $\sigma_{\text{scl}} = [\Lambda]\sigma$

$[\Lambda_\sigma]$

Bending (Outside)

$$\begin{bmatrix} 0.004669 & -0.00081217 & -0.023053 & -0.45163 & -1.3752 & 2.8527 \\ -0.0035227 & -0.020036 & -0.039063 & -0.14503 & -4.3098 & 1.1463 \\ -0.010772 & -0.022141 & -0.020845 & -0.23018 & -0.51285 & 3.5681 \\ -0.0018577 & -0.011212 & 0.0056415 & -0.21794 & 0.99098 & -0.32027 \\ 0.13662 & -0.74617 & -0.014198 & 0.61014 & 0.65453 & -0.0040192 \\ 0.62456 & -0.15029 & 0.0086087 & -1.0803 & 0.054227 & 0.084299 \end{bmatrix}$$

Membrane+Bending (Inside)

$$\begin{bmatrix} 1.1664 & 0.092081 & 0.37782 & 0.1558 & 0.94016 & -2.6635 \\ 0.107 & 1.1643 & 0.35838 & 0.071949 & 2.7405 & -1.1316 \\ 0.015214 & 0.036286 & 2.4502 & 0.10148 & 0.5323 & -3.356 \\ 0.12479 & 0.038403 & 0.10414 & 1.7298 & -1.1046 & 0.38694 \\ -0.13688 & 0.76311 & 0.023649 & -0.64918 & 1.6837 & 0.30273 \\ -0.63274 & 0.15449 & -0.011551 & 1.0283 & 0.24606 & 2.4457 \end{bmatrix}$$

Membrane+Bending (Center)

$$\begin{bmatrix} 1.1711 & 0.091268 & 0.35477 & -0.29585 & -0.43504 & 0.18916 \\ 0.10348 & 1.1443 & 0.31932 & -0.073083 & -1.5693 & 0.014726 \\ 0.0044425 & 0.014146 & 2.4293 & -0.1287 & 0.019436 & 0.21216 \\ 0.12293 & 0.027191 & 0.10978 & 1.5119 & -0.11361 & 0.066662 \\ -0.00026242 & 0.016934 & 0.0094508 & -0.039048 & 2.3382 & 0.2987 \\ -0.0082075 & 0.0041999 & -0.0029418 & -0.051955 & 0.30029 & 2.5299 \end{bmatrix}$$

Continued on next page

Continued from previous page

Counterflow micro-channel, same-stream SCL : $\sigma_{\text{scl}} = [\Lambda]\sigma$

$[\Lambda_\sigma]$

Membrane+Bending (Outside)

$$\begin{bmatrix} 1.1758 & 0.090455 & 0.33172 & -0.74748 & -1.8103 & 3.0418 \\ 0.099956 & 1.1242 & 0.28025 & -0.21811 & -5.8793 & 1.161 \\ -0.0063294 & -0.0079953 & 2.4085 & -0.35888 & -0.49344 & 3.7803 \\ 0.12107 & 0.015979 & 0.11542 & 1.294 & 0.87734 & -0.25361 \\ 0.13636 & -0.72923 & -0.0047476 & 0.57109 & 2.9927 & 0.29468 \\ 0.61635 & -0.14609 & 0.0056667 & -1.1322 & 0.35451 & 2.6142 \end{bmatrix}$$

Peak (Inside)

$$\begin{bmatrix} 0.3091 & 0.2338 & 0.86595 & -1.0299 & 2.0482 & -2.8634 \\ 0.086583 & 0.46209 & 0.84933 & -0.85623 & 3.3446 & -1.1648 \\ 0.49151 & 0.85051 & 2.6629 & -1.9866 & 7.5426 & -6.0077 \\ 0.0039889 & 0.022796 & 0.18447 & 0.080672 & 0.37909 & -0.17388 \\ -0.39082 & 0.69123 & 0.77246 & -0.14951 & 3.5054 & 0.13615 \\ -0.64341 & 0.50855 & -0.62241 & 0.62815 & -0.070375 & 2.988 \end{bmatrix}$$

Peak (Center)

$$\begin{bmatrix} -0.049567 & -0.051064 & -0.10428 & 0.19289 & -0.11719 & 0.010423 \\ -0.029719 & -0.089906 & -0.10708 & 0.18017 & -0.11729 & -0.010545 \\ -0.028188 & -0.048277 & -0.26074 & 0.12856 & -0.24991 & -0.015709 \\ 0.019347 & 0.02061 & -0.0075805 & -0.074134 & 0.015653 & -0.00038595 \\ 0.00024648 & -0.011434 & -0.0057564 & 0.010332 & -0.57738 & -0.26662 \\ 0.0070274 & -0.0045923 & 0.0017458 & 0.046112 & -0.18226 & -0.24834 \end{bmatrix}$$

Continued on next page

Continued from previous page

Counterflow micro-channel, same-stream SCL : $\sigma_{\text{scl}} = [\Lambda]\sigma$

$[\Lambda_\sigma]$

Peak (Outside)

$$\begin{bmatrix} 0.30307 & 0.16629 & 0.76672 & -1.1374 & -0.92137 & 2.6701 \\ 0.02392 & 0.49426 & 0.78569 & -0.84729 & -2.911 & 1.1081 \\ 0.41921 & 0.69311 & 2.3627 & -2.1426 & -4.7945 & 6.0426 \\ -0.033552 & 0.047451 & 0.15447 & 0.071226 & -0.49602 & 0.18249 \\ 0.3643 & -0.66162 & -0.708 & 0.053968 & 4.2859 & 0.21587 \\ 0.62492 & -0.409 & 0.5681 & -1.1012 & 1.2962 & 3.0079 \end{bmatrix}$$

Total (Inside)

$$\begin{bmatrix} 1.4755 & 0.32588 & 1.2437 & -0.87411 & 2.9883 & -5.5269 \\ 0.19359 & 1.6264 & 1.2077 & -0.78428 & 6.0852 & -2.2965 \\ 0.50671 & 0.88677 & 5.1131 & -1.8851 & 8.075 & -9.3637 \\ 0.12877 & 0.0612 & 0.28861 & 1.8106 & -0.72551 & 0.21306 \\ -0.5277 & 1.4543 & 0.7961 & -0.79869 & 5.1891 & 0.43886 \\ -1.2762 & 0.66306 & -0.63395 & 1.6565 & 0.17568 & 5.4336 \end{bmatrix}$$

Total (Center)

$$\begin{bmatrix} 1.1215 & 0.040204 & 0.25049 & -0.10295 & -0.55223 & 0.19958 \\ 0.073762 & 1.0543 & 0.21224 & 0.10709 & -1.6866 & 0.0041811 \\ -0.023746 & -0.034129 & 2.1686 & -0.00014252 & -0.23047 & 0.19645 \\ 0.14228 & 0.0478 & 0.1022 & 1.4378 & -0.097961 & 0.066278 \\ -1.5941e-05 & 0.0055009 & 0.0036946 & -0.028715 & 1.7608 & 0.032079 \\ -0.0011802 & -0.00039258 & -0.001196 & -0.0058429 & 0.11802 & 2.2816 \end{bmatrix}$$

Continued on next page

Continued from previous page

Counterflow micro-channel, same-stream SCL : $\sigma_{\text{scl}} = [\Lambda]\sigma$

$[\Lambda_\sigma]$

Total (Outside)	$\begin{bmatrix} 1.4788 & 0.25675 & 1.0984 & -1.8848 & -2.7317 & 5.7119 \\ 0.12388 & 1.6185 & 1.0659 & -1.0654 & -8.7902 & 2.2691 \\ 0.41286 & 0.68511 & 4.7712 & -2.5015 & -5.2879 & 9.8229 \\ 0.08752 & 0.06343 & 0.26989 & 1.3652 & 0.38135 & -0.07112 \\ 0.50067 & -1.3909 & -0.71272 & 0.62506 & 7.2785 & 0.51055 \\ 1.2412 & -0.55506 & 0.57374 & -2.2334 & 1.6507 & 5.6222 \end{bmatrix}$

Table C.5: Fluid-wall thermal stress transforms for the Counter-flow micro-channel

Counter-flow micro-channel: $\sigma_{\text{scl}} = [\Lambda]\Delta T_{ch.}$		
	same stream SCL: $[\Lambda_{\Delta T_{ch.}}]$	**cross stream SCL:** $[\Lambda_{\Delta T_{ch.}}]$
Membrane	$\begin{Bmatrix} -1.3598 \\ -1.3117 \\ -0.026401 \\ -0.079316 \\ -0.0085687 \\ 0.010587 \end{Bmatrix}$	$\begin{Bmatrix} 0.068896 \\ 0.062529 \\ -0.18713 \\ -0.012199 \\ 0.0050417 \\ -0.0056576 \end{Bmatrix}$
Bending (Inside)	$\begin{Bmatrix} -0.044855 \\ -0.054754 \\ -0.047374 \\ 0.019482 \\ -0.68353 \\ 0.55205 \end{Bmatrix}$	$\begin{Bmatrix} -2.9967 \\ -3.1202 \\ -0.14333 \\ 0.32473 \\ 0.0028492 \\ -0.0022001 \end{Bmatrix}$

Continued on next page

Continued from previous page

Counter-flow micro-channel: $\sigma_{\text{scl}} = [\Lambda]\Delta T_{ch.}$

same stream SCL: $[\Lambda_{\Delta T_{ch.}}]$ **cross stream SCL:** $[\Lambda_{\Delta T_{ch.}}]$

Bending (Outside)	$\begin{Bmatrix} 0.044855 \\ 0.054754 \\ 0.047374 \\ -0.019482 \\ 0.68353 \\ -0.55205 \end{Bmatrix}$	$\begin{Bmatrix} 2.9967 \\ 3.1202 \\ 0.14333 \\ -0.32473 \\ -0.0028492 \\ 0.0022001 \end{Bmatrix}$
Membrane+Bending (Inside)	$\begin{Bmatrix} -1.4046 \\ -1.3664 \\ -0.073778 \\ -0.059835 \\ -0.69209 \\ 0.56266 \end{Bmatrix}$	$\begin{Bmatrix} -2.9278 \\ -3.0577 \\ -0.33047 \\ 0.31254 \\ 0.0078909 \\ -0.0078579 \end{Bmatrix}$
Membrane+Bending (Center)	$\begin{Bmatrix} -1.3598 \\ -1.3117 \\ -0.026401 \\ -0.079316 \\ -0.0085687 \\ 0.010587 \end{Bmatrix}$	$\begin{Bmatrix} 0.068896 \\ 0.062529 \\ -0.18713 \\ -0.012199 \\ 0.0050417 \\ -0.0056576 \end{Bmatrix}$

Continued on next page

Continued from previous page

Counter-flow micro-channel: $\sigma_{\text{scl}} = [\Lambda]\Delta T_{ch.}$

same stream SCL: $[\Lambda_{\Delta T_{ch.}}]$ **cross stream SCL:** $[\Lambda_{\Delta T_{ch.}}]$

Membrane+Bending (Outside)	$\begin{Bmatrix} -1.3149 \\ -1.2569 \\ 0.020974 \\ -0.098801 \\ 0.67495 \\ -0.54148 \end{Bmatrix}$	$\begin{Bmatrix} 3.0656 \\ 3.1827 \\ -0.043801 \\ -0.33694 \\ 0.0021926 \\ -0.0034576 \end{Bmatrix}$
Peak (Inside)	$\begin{Bmatrix} -1.6082 \\ -1.5505 \\ -2.8434 \\ -0.29713 \\ -0.63663 \\ 0.50798 \end{Bmatrix}$	$\begin{Bmatrix} -0.43148 \\ -0.5298 \\ 0.31942 \\ 0.2457 \\ -0.012012 \\ 0.011296 \end{Bmatrix}$
Peak (Center)	$\begin{Bmatrix} 0.37788 \\ 0.3671 \\ 0.35263 \\ 0.052401 \\ 0.001038 \\ 0.00096081 \end{Bmatrix}$	$\begin{Bmatrix} 0.11214 \\ 0.12873 \\ -0.056512 \\ -0.049933 \\ 0.0012369 \\ -0.0015124 \end{Bmatrix}$

Continued on next page

Continued from previous page

Counter-flow micro-channel: $\sigma_{\text{scl}} = [\Lambda]\Delta T_{ch.}$

same stream SCL: $[\Lambda_{\Delta T_{ch.}}]$ **cross stream SCL:** $[\Lambda_{\Delta T_{ch.}}]$

Peak (Outside)	$\begin{Bmatrix} -1.3364 \\ -1.225 \\ -2.2766 \\ -0.32789 \\ 0.47461 \\ -0.4205 \end{Bmatrix}$	$\begin{Bmatrix} -0.12749 \\ -0.13794 \\ 0.045859 \\ 0.036852 \\ -0.0036054 \\ 0.0049768 \end{Bmatrix}$
Total (Inside)	$\begin{Bmatrix} -3.0128 \\ -2.917 \\ -2.9172 \\ -0.35697 \\ -1.3287 \\ 1.0706 \end{Bmatrix}$	$\begin{Bmatrix} -3.3593 \\ -3.5875 \\ -0.011047 \\ 0.55821 \\ -0.0041212 \\ 0.003438 \end{Bmatrix}$
Total (Center)	$\begin{Bmatrix} -0.98185 \\ -0.94458 \\ 0.32623 \\ -0.026918 \\ -0.007531 \\ 0.011547 \end{Bmatrix}$	$\begin{Bmatrix} 0.18104 \\ 0.19125 \\ -0.24365 \\ -0.062131 \\ 0.0062788 \\ -0.00717 \end{Bmatrix}$

Continued on next page

Continued from previous page

Counter-flow micro-channel: $\sigma_{\text{scl}} = [\Lambda]\Delta T_{ch.}$

same stream SCL: $[\Lambda_{\Delta T_{ch.}}]$ **cross stream SCL:** $[\Lambda_{\Delta T_{ch.}}]$

Total (Outside)	$\begin{Bmatrix} -2.6512 \\ -2.4819 \\ -2.2557 \\ -0.4267 \\ 1.1496 \\ -0.96199 \end{Bmatrix}$	$\begin{Bmatrix} 2.9381 \\ 3.0448 \\ 0.0020594 \\ -0.30008 \\ -0.0014126 \\ 0.0015193 \end{Bmatrix}$

Appendix D

Air-foil heat exchanger performance results

D.1 Pressure drop experiment results

This appendix contains data from the pressure drop experiments performed on the Airfoil test heat exchanger from 6/1/2017 to 6/22/2017. The experiment and methodology used in obtaining this data is described in Section 6.1.1. Table D.1 contains averaged experimental measurements taken during each 10 min logging period. Table D.2 contains the Darcy friction factor, f, and Reynolds number, Re, calculation results. Two values of f are present, one just assuming core friction, and one including minor losses in the headers as described by the Kays & London relation in Equation 2.20.

D.2 Pressure drop data

-

Table D.1: Airfoil average pressure drop experiment measurements

Test Date	ΔP [psi]	$\dot{m}$ [kg/s]	ρ [kg/m^3]	T [C]
6/1/2017	1.04 ± 0.062	0.059 72 ± 0.0010	102.5 ± 0.54	4.587± 0.15
	0.821 ± 0.039	0.056 98 ± 0.000 99	111.9 ± 0.39	6.208± 0.12
	0.725 ± 0.039	0.054 00 ± 0.0010	117.6 ± 0.58	7.285± 0.12
	0.620 ± 0.038	0.049 91 ± 0.000 95	124.4 ± 0.44	8.297± 0.12
	0.521 ± 0.038	0.045 86 ± 0.000 84	129.9 ± 0.55	9.163± 0.11
	1.16 ± 0.040	0.062 75 ± 0.000 82	94.96 ± 0.45	2.839± 0.18
	1.16 ± 0.040	0.062 75 ± 0.000 82	94.96 ± 0.45	2.839± 0.18
	1.65 ± 0.040	0.073 57 ± 0.000 91	82.14 ± 0.68	2.556± 1.1
	1.89 ± 0.038	0.077 48 ± 0.000 66	76.60 ± 0.54	3.610± 0.24
	2.13 ± 0.039	0.080 72 ± 0.000 53	73.44 ± 0.42	2.499± 0.12
	2.40 ± 0.039	0.084 10 ± 0.000 43	69.18 ± 0.34	1.701± 0.071
	2.46 ± 0.040	0.084 77 ± 0.000 42	69.71 ± 0.32	2.220± 0.11
	2.49 ± 0.040	0.085 33 ± 0.000 43	70.38 ± 0.33	1.847± 0.14
6/12/2017	0.616 ± 0.074	0.040 11 ± 0.0012	83.91 ± 0.51	17.45 ± 1.6
	1.26 ± 0.022	0.088 20 ± 0.0017	148.5 ± 0.37	23.49 ± 0.44
	4.17 ± 0.021	0.1654 ± 0.0013	132.2 ± 0.82	24.34 ± 0.46
	1.80 ± 0.023	0.1076 ± 0.0015	149.6 ± 0.45	23.43 ± 0.43

Continued on next page

Table D.1 – *Continued from previous page*

Test Date	ΔP [psi]	$\dot{m}$ [kg/s]	ρ [kg/m^3]	T [C]
6/13/2017	4.31 ± 0.022	0.1777 ± 0.0013	146.3 ± 0.45	21.78 ± 0.33
	1.88 ± 0.044	0.1141 ± 0.0014	159.4 ± 0.53	23.15 ± 0.48
	1.90 ± 0.015	0.1140 ± 0.0014	160.5 ± 0.50	23.24 ± 0.47
	2.34 ± 0.014	0.1284 ± 0.0015	158.5 ± 0.47	23.15 ± 0.40
	2.67 ± 0.014	0.1380 ± 0.0015	157.4 ± 0.49	22.85 ± 0.43
	3.02 ± 0.015	0.1475 ± 0.0015	156.1 ± 0.44	22.74 ± 0.38
	3.39 ± 0.016	0.1576 ± 0.0015	155.3 ± 0.45	22.49 ± 0.38

Continued on next page

Table D.1 – *Continued from previous page*

Test Date	ΔP [psi]	$\dot{m}$ [kg/s]	ρ [kg/m^3]	T [C]
6/13/2017	3.39 ± 0.016	0.1576 ± 0.0015	155.3 ± 0.45	22.49 ± 0.38
	4.02 ± 0.015	0.1735 ± 0.0014	153.7 ± 0.56	22.08 ± 0.34
	4.43 ± 0.013	0.1836 ± 0.0013	153.5 ± 0.78	21.94 ± 0.35
	1.94 ± 0.016	0.1189 ± 0.0018	175.6 ± 0.78	20.50 ± 0.92
	1.67 ± 0.014	0.096 99 ± 0.0013	135.3 ± 0.38	23.86 ± 0.40
	3.33 ± 0.015	0.1173 ± 0.000 87	89.00 ± 0.41	27.45 ± 0.28
	3.17 ± 0.012	0.1102 ± 0.000 76	83.59 ± 0.17	26.38 ± 0.23
	2.66 ± 0.012	0.087 37 ± 0.000 61	65.38 ± 0.088	26.60 ± 0.25
	1.02 ± 0.012	0.051 97 ± 0.000 67	71.69 ± 0.11	24.65 ± 0.32
	1.33 ± 0.012	0.060 37 ± 0.000 67	70.51 ± 0.12	24.67 ± 0.39
	1.65 ± 0.012	0.067 94 ± 0.000 70	69.60 ± 0.10	24.18 ± 0.29
	2.04 ± 0.012	0.076 32 ± 0.000 69	67.87 ± 0.096	24.82 ± 0.25
	2.32 ± 0.013	0.081 42 ± 0.000 66	66.69 ± 0.12	25.57 ± 0.25
	0.0705 ± 0.0090	0.008 638 ± 0.000 30	73.83 ± 0.12	25.22 ± 0.34
	0.148 ± 0.0087	0.015 29 ± 0.000 34	73.95 ± 0.11	25.30 ± 0.27
	0.178 ± 0.0084	0.017 55 ± 0.000 33	73.71 ± 0.11	25.23 ± 0.37
	0.216 ± 0.0088	0.019 90 ± 0.000 36	73.64 ± 0.12	24.76 ± 0.28
	0.0838 ± 0.0098	0.009 154 ± 0.000 25	73.93 ± 0.13	25.43 ± 0.28
	0.0738 ± 0.0089	0.008 498 ± 0.000 23	73.49 ± 0.099	25.07 ± 0.29
	0.0850 ± 0.0093	0.009 900 ± 0.000 24	73.50 ± 0.12	24.90 ± 0.28
	0.102 ± 0.0086	0.011 67 ± 0.000 24	73.44 ± 0.10	24.68 ± 0.28
	0.165 ± 0.0083	0.016 20 ± 0.000 29	73.30 ± 0.11	24.74 ± 0.34
	0.131 ± 0.0093	0.013 65 ± 0.000 26	73.06 ± 0.11	24.96 ± 0.33
	0.714 ± 0.026	0.042 05 ± 0.0013	70.91 ± 0.14	24.80 ± 0.28
	0.918 ± 0.038	0.048 43 ± 0.0016	70.30 ± 0.16	24.60 ± 0.29
	0.295 ± 0.0086	0.024 39 ± 0.000 44	72.03 ± 0.077	24.86 ± 0.29
	0.456 ± 0.0086	0.031 83 ± 0.000 54	71.39 ± 0.083	24.99 ± 0.35
	0.718 ± 0.0095	0.042 01 ± 0.000 64	70.44 ± 0.14	24.99 ± 0.38
	0.358 ± 0.0092	0.027 72 ± 0.000 52	71.37 ± 0.089	24.99 ± 0.33
	0.582 ± 0.0094	0.036 97 ± 0.000 59	70.56 ± 0.093	25.04 ± 0.39

Continued on next page

Table D.1 – *Continued from previous page*

Test Date	ΔP [psi]	$\dot{m}$ [kg/s]	ρ [kg/m^3]	T [C]
6/14/2017	1.95 ± 0.011	0.057 75 ± 0.000 42	43.01 ± 0.051	27.49 ± 0.24
	0.160 ± 0.0086	0.013 44 ± 0.000 28	47.83 ± 0.036	26.82 ± 0.60
	0.0445 ± 0.0079	0.005 476 ± 0.000 22	48.19 ± 0.034	25.41 ± 0.28
	0.0754 ± 0.0080	0.008 057 ± 0.000 19	48.22 ± 0.034	24.54 ± 0.27
	0.123 ± 0.0083	0.010 96 ± 0.000 20	48.21 ± 0.031	24.56 ± 0.35
	0.0496 ± 0.0082	0.005 621 ± 0.000 15	48.30 ± 0.034	24.55 ± 0.25
	0.0621 ± 0.0080	0.007 141 ± 0.000 17	48.15 ± 0.034	24.42 ± 0.25
	0.0797 ± 0.0082	0.008 402 ± 0.000 17	48.04 ± 0.034	24.39 ± 0.26
	0.0520 ± 0.0087	0.006 577 ± 0.000 15	48.02 ± 0.037	24.26 ± 0.28
	0.723 ± 0.011	0.033 00 ± 0.000 41	45.93 ± 0.065	24.85 ± 0.31
	0.734 ± 0.011	0.033 42 ± 0.000 42	45.91 ± 0.063	24.61 ± 0.29
	0.809 ± 0.012	0.035 28 ± 0.000 44	45.64 ± 0.057	24.59 ± 0.26
	1.22 ± 0.012	0.044 24 ± 0.000 45	44.43 ± 0.058	24.78 ± 0.26
	1.60 ± 0.013	0.051 45 ± 0.000 43	43.28 ± 0.068	24.95 ± 0.31
	0.910 ± 0.011	0.037 62 ± 0.000 42	45.11 ± 0.066	24.92 ± 0.32
	0.199 ± 0.0083	0.015 35 ± 0.000 25	46.76 ± 0.032	24.41 ± 0.26
	0.236 ± 0.0091	0.016 75 ± 0.000 25	46.61 ± 0.031	24.41 ± 0.25
	0.271 ± 0.0085	0.018 26 ± 0.000 27	46.38 ± 0.042	24.65 ± 0.30
	0.379 ± 0.0088	0.022 44 ± 0.000 31	45.95 ± 0.031	24.66 ± 0.27
	0.569 ± 0.0086	0.028 48 ± 0.000 34	45.27 ± 0.042	24.88 ± 0.31
	0.710 ± 0.0086	0.032 27 ± 0.000 38	44.82 ± 0.038	24.76 ± 0.29
	0.158 ± 0.0082	0.011 11 ± 0.000 20	34.44 ± 0.031	24.79 ± 0.24
	0.0229 ± 0.010	0.003 835 ± 0.000 18	34.69 ± 0.032	24.47 ± 0.23
	0.0293 ± 0.0078	0.004 178 ± 0.000 15	34.63 ± 0.034	24.20 ± 0.25
	0.0350 ± 0.0081	0.004 572 ± 0.000 15	34.58 ± 0.032	23.81 ± 0.25
	0.0537 ± 0.0087	0.005 889 ± 0.000 16	34.53 ± 0.034	23.66 ± 0.25
	0.0923 ± 0.0082	0.007 643 ± 0.000 18	34.45 ± 0.028	23.68 ± 0.24
	0.117 ± 0.0083	0.009 116 ± 0.000 20	34.34 ± 0.036	23.95 ± 0.26
	0.0376 ± 0.0081	0.004 841 ± 0.000 16	34.39 ± 0.035	23.85 ± 0.23
	0.0719 ± 0.0091	0.006 704 ± 0.000 17	34.24 ± 0.032	24.03 ± 0.27

Continued on next page

Table D.1 – *Continued from previous page*

Test Date	ΔP [psi]	$\dot{m}$ [kg/s]	ρ [kg/m^3]	T [C]
6/15/2017	0.132 ± 0.0079	0.009 239 ± 0.000 17	32.99 ± 0.024	25.47 ± 0.25
	0.0245 ± 0.0084	0.003 156 ± 0.000 14	33.23 ± 0.031	24.71 ± 0.24
	0.0272 ± 0.0088	0.003 062 ± 0.000 15	33.20 ± 0.032	24.23 ± 0.24
	0.0289 ± 0.0084	0.002 976 ± 0.000 13	33.18 ± 0.031	23.87 ± 0.23
	0.0219 ± 0.0083	0.002 611 ± 0.000 12	33.17 ± 0.031	23.59 ± 0.23
	0.009 76 ± 0.0097	0.001 207 ± 0.000 11	33.23 ± 0.034	23.21 ± 0.25
	0.0127 ± 0.0083	0.000 777 0 ± 0.000 10	33.24 ± 0.033	22.91 ± 0.23
	0.009 65 ± 0.0083	0.001 057 ± 0.000 100	33.17 ± 0.032	22.73 ± 0.21
	0.009 98 ± 0.0079	0.001 144 ± 0.000 10	33.10 ± 0.033	22.63 ± 0.23
	0.006 22 ± 0.0077	0.001 266 ± 0.000 097	33.03 ± 0.030	22.60 ± 0.23
	0.0153 ± 0.0100	0.001 691 ± 0.000 11	32.96 ± 0.034	22.63 ± 0.23
	0.0160 ± 0.0077	0.002 038 ± 0.000 11	32.90 ± 0.030	22.65 ± 0.23
	0.0137 ± 0.0092	0.002 057 ± 0.000 11	32.86 ± 0.031	22.50 ± 0.25
	0.0157 ± 0.0077	0.002 149 ± 0.000 11	32.83 ± 0.034	22.36 ± 0.23
	0.0194 ± 0.0088	0.002 321 ± 0.000 11	32.78 ± 0.034	22.34 ± 0.24

Continued on next page

Table D.1 – *Continued from previous page*

Test Date	ΔP [psi]	$\dot{m}$ [kg/s]	ρ [kg/m^3]	T [C]
6/22/2017	0.007 06 ± 0.0086	0.000 862 2 ± 0.000 10	32.97 ± 0.035	20.54 ± 0.23
	0.008 73 ± 0.0084	0.000 773 7 ± 0.000 098	32.89 ± 0.032	20.56 ± 0.23
	0.0117 ± 0.0080	0.001 517 ± 0.000 099	32.82 ± 0.035	20.56 ± 0.24
	0.0154 ± 0.0071	0.001 802 ± 0.000 099	32.76 ± 0.035	20.54 ± 0.24
	0.0183 ± 0.0077	0.001 993 ± 0.000 11	32.70 ± 0.034	20.55 ± 0.22
	0.0193 ± 0.0077	0.002 065 ± 0.000 11	32.62 ± 0.037	20.52 ± 0.23
	0.0181 ± 0.0080	0.002 099 ± 0.000 11	32.55 ± 0.037	20.53 ± 0.23
	0.0207 ± 0.0084	0.002 099 ± 0.000 11	32.48 ± 0.035	20.51 ± 0.24
	0.0228 ± 0.0076	0.002 116 ± 0.000 11	32.40 ± 0.036	20.49 ± 0.23
	0.0210 ± 0.0082	0.002 140 ± 0.000 11	32.33 ± 0.035	20.47 ± 0.23
	0.0136 ± 0.0081	0.002 112 ± 0.000 11	32.26 ± 0.036	20.45 ± 0.23
	0.0118 ± 0.0077	0.001 085 ± 0.000 10	32.18 ± 0.037	20.46 ± 0.23
	0.0148 ± 0.0072	0.001 210 ± 0.000 10	32.11 ± 0.035	20.44 ± 0.22

D.3 Friction factor results

D.3.1 Core friction factor results

Table D.2: Airfoil channel friction factor measurements

Test Date	Re [−]	f_D [−] (no minor losses)	f_D [−] (Kays-London minor losses)
6/1/2017	19 704 ± 333	0.0767 ± 0.0053	0.0744 ± 0.0053
	18 481 ± 322	0.0727 ± 0.0043	0.0703 ± 0.0043
	17 320 ± 324	0.0752 ± 0.0049	0.0728 ± 0.0049
	15 808 ± 302	0.0796 ± 0.0058	0.0772 ± 0.0058
	14 375 ± 262	0.0826 ± 0.0068	0.0802 ± 0.0068
	21 015 ± 273	0.0719 ± 0.0031	0.0695 ± 0.0031
	21 015 ± 273	0.0719 ± 0.0031	0.0695 ± 0.0031
	25 025 ± 309	0.0645 ± 0.0023	0.0621 ± 0.0023
	26 418 ± 226	0.0620 ± 0.0017	0.0596 ± 0.0017
	27 715 ± 181	0.0616 ± 0.0014	0.0592 ± 0.0014
	29 074 ± 150	0.0603 ± 0.0012	0.0579 ± 0.0012
	29 240 ± 145	0.0614 ± 0.0012	0.0590 ± 0.0012
	29 450 ± 149	0.0619 ± 0.0012	0.0595 ± 0.0012
6/12/2017	12 971 ± 395	0.0826 ± 0.011	0.0802 ± 0.011
	25 788 ± 501	0.0616 ± 0.0026	0.0592 ± 0.0026
	49 395 ± 384	0.0517 ± 0.000 90	0.0493 ± 0.000 90
	31 423 ± 426	0.0597 ± 0.0018	0.0573 ± 0.0018
6/13/2017	52 391 ± 380	0.0513 ± 0.000 80	0.0489 ± 0.000 80
	32 848 ± 417	0.0592 ± 0.0020	0.0568 ± 0.0020
	32 751 ± 416	0.0603 ± 0.0016	0.0579 ± 0.0016
	37 009 ± 437	0.0577 ± 0.0014	0.0553 ± 0.0014
	39 878 ± 425	0.0567 ± 0.0013	0.0543 ± 0.0013
	42 721 ± 427	0.0557 ± 0.0012	0.0533 ± 0.0012
	45 737 ± 424	0.0545 ± 0.0011	0.0521 ± 0.0011

Continued on next page

Table D.2 – *Continued from previous page*

Test Date	Re [−]	f_D [−] (no minor losses)	f_D [−] (Kays-London minor losses)
6/13/2017	45 737 ± 424	0.0545 ± 0.0011	0.0521 ± 0.0011
	50 535 ± 402	0.0527 ± 0.000 88	0.0503 ± 0.000 88
	53 520 ± 395	0.0518 ± 0.000 81	0.0494 ± 0.000 81
	33 583 ± 497	0.0620 ± 0.0019	0.0596 ± 0.0019
	28 875 ± 378	0.0618 ± 0.0017	0.0594 ± 0.0017
	36 573 ± 273	0.0554 ± 0.000 90	0.0530 ± 0.000 90
	34 685 ± 238	0.0560 ± 0.000 80	0.0536 ± 0.000 80
	27 949 ± 194	0.0585 ± 0.000 86	0.0562 ± 0.000 86
	16 633 ± 215	0.0695 ± 0.0020	0.0671 ± 0.0020
	19 340 ± 214	0.0659 ± 0.0016	0.0636 ± 0.0016
	21 818 ± 226	0.0638 ± 0.0014	0.0614 ± 0.0014
	24 497 ± 220	0.0612 ± 0.0012	0.0588 ± 0.0012
	26 100 ± 212	0.0600 ± 0.0010	0.0576 ± 0.0010
	2754 ± 94	0.179 ± 0.026	0.177 ± 0.026
	4872 ± 109	0.121 ± 0.0089	0.118 ± 0.0089
	5595 ± 106	0.109 ± 0.0066	0.107 ± 0.0066
	6355 ± 114	0.103 ± 0.0056	0.101 ± 0.0056
	2916 ± 79	0.190 ± 0.024	0.188 ± 0.024
	2712 ± 74	0.193 ± 0.026	0.191 ± 0.026
	3160 ± 76	0.164 ± 0.020	0.162 ± 0.020
	3728 ± 77	0.142 ± 0.013	0.139 ± 0.013
	5174 ± 92	0.119 ± 0.0073	0.116 ± 0.0073
	4358 ± 83	0.132 ± 0.011	0.130 ± 0.011
	13 461 ± 425	0.0735 ± 0.0054	0.0711 ± 0.0054
	15 522 ± 510	0.0707 ± 0.0055	0.0683 ± 0.0055
	7799 ± 140	0.0916 ± 0.0042	0.0892 ± 0.0042
	10 178 ± 173	0.0826 ± 0.0032	0.0802 ± 0.0032
	13 445 ± 205	0.0737 ± 0.0025	0.0713 ± 0.0025
	8864 ± 165	0.0856 ± 0.0039	0.0832 ± 0.0039
	11 830 ± 188	0.0772 ± 0.0028	0.0748 ± 0.0028

Continued on next page

Table D.2 – *Continued from previous page*

Test Date	Re [−]	f_D [−] (no minor losses)	f_D [−] (Kays-London minor losses)
6/14/2017	18 741 ± 136	0.0647 ± 0.0010	0.0624 ± 0.0010
	4355 ± 90	0.109 ± 0.0074	0.107 ± 0.0074
	1782 ± 73	0.184 ± 0.036	0.182 ± 0.036
	2630 ± 61	0.144 ± 0.017	0.141 ± 0.017
	3576 ± 64	0.127 ± 0.0097	0.125 ± 0.0097
	1834 ± 50	0.195 ± 0.034	0.192 ± 0.034
	2332 ± 54	0.151 ± 0.021	0.148 ± 0.021
	2744 ± 56	0.139 ± 0.015	0.137 ± 0.015
	2149 ± 50	0.148 ± 0.026	0.146 ± 0.026
	10 780 ± 134	0.0784 ± 0.0023	0.0760 ± 0.0023
	10 924 ± 137	0.0775 ± 0.0023	0.0751 ± 0.0023
	11 535 ± 145	0.0763 ± 0.0022	0.0739 ± 0.0022
	14 469 ± 149	0.0709 ± 0.0016	0.0686 ± 0.0016
	16 828 ± 142	0.0673 ± 0.0013	0.0649 ± 0.0013
	12 292 ± 138	0.0746 ± 0.0019	0.0722 ± 0.0019
	5017 ± 81	0.101 ± 0.0053	0.0989 ± 0.0053
	5474 ± 82	0.101 ± 0.0049	0.0984 ± 0.0049
	5967 ± 89	0.0969 ± 0.0042	0.0946 ± 0.0042
	7334 ± 103	0.0889 ± 0.0032	0.0865 ± 0.0032
	9306 ± 111	0.0816 ± 0.0023	0.0792 ± 0.0023
	10 552 ± 124	0.0785 ± 0.0021	0.0761 ± 0.0021
	3658 ± 66	0.113 ± 0.0072	0.111 ± 0.0072
	1263 ± 60	0.139 ± 0.063	0.136 ± 0.063
	1378 ± 49	0.150 ± 0.041	0.147 ± 0.041
	1509 ± 48	0.149 ± 0.036	0.146 ± 0.036
	1945 ± 53	0.137 ± 0.024	0.135 ± 0.024
	2524 ± 59	0.140 ± 0.014	0.138 ± 0.014
	3008 ± 67	0.124 ± 0.010	0.122 ± 0.010
	1598 ± 52	0.142 ± 0.032	0.139 ± 0.032
	2212 ± 55	0.141 ± 0.019	0.138 ± 0.019

Continued on next page

Table D.2 – *Continued from previous page*

Test Date	Re [−]	f_D [−] (no minor losses)	f_D [−] (Kays-London minor losses)
6/15/2017	3037 ± 54	0.132 ± 0.0091	0.129 ± 0.0091
	1040 ± 46	0.210 ± 0.074	0.208 ± 0.074
	1010 ± 49	0.247 ± 0.084	0.245 ± 0.084
	983 ± 43	0.279 ± 0.085	0.276 ± 0.085
	863 ± 40	0.274 ± 0.11	0.271 ± 0.11
	400 ± 36	0.572 ± 0.58	0.569 ± 0.58
	257 ± 34	1.80 ± 1.3	1.80 ± 1.3
	351 ± 33	0.736 ± 0.65	0.733 ± 0.65
	379 ± 35	0.649 ± 0.53	0.647 ± 0.53
	420 ± 32	0.329 ± 0.41	0.327 ± 0.41
	561 ± 37	0.455 ± 0.30	0.452 ± 0.30
	676 ± 37	0.326 ± 0.16	0.323 ± 0.16
	683 ± 35	0.274 ± 0.19	0.272 ± 0.19
	713 ± 37	0.288 ± 0.14	0.285 ± 0.14
	771 ± 38	0.303 ± 0.14	0.301 ± 0.14
6/22/2017	288 ± 34	0.804 ± 1.00	0.802 ± 1.00
	258 ± 33	1.23 ± 1.2	1.23 ± 1.2
	507 ± 33	0.428 ± 0.30	0.426 ± 0.30
	602 ± 33	0.398 ± 0.19	0.396 ± 0.19
	666 ± 38	0.387 ± 0.17	0.385 ± 0.17
	690 ± 36	0.380 ± 0.16	0.378 ± 0.16
	701 ± 36	0.344 ± 0.16	0.342 ± 0.16
	701 ± 37	0.392 ± 0.16	0.390 ± 0.16
	707 ± 36	0.425 ± 0.15	0.422 ± 0.15
	715 ± 36	0.381 ± 0.15	0.379 ± 0.15
	706 ± 38	0.253 ± 0.15	0.251 ± 0.15
	363 ± 34	0.832 ± 0.56	0.829 ± 0.56
	405 ± 34	0.831 ± 0.43	0.829 ± 0.43

D.4 Heat transfer experiment results

This appendix contains data from the heat transfer experiments performed on the airfoil test heat exchanger from 7/26/2017 to 8/10/2017. The experiment and methodology used in obtaining this data is described in detail in Section 6.1.2. Tables D.3, D.4, and D.5 contain averaged experimental measurements of mass flow, cold side temperatures and pressures, and hot side temperatures and pressures respectively. These values are the average of data points taken during each 30 min logging period. Recuperator effictiveness, NTU, and UA, as determined by the gross-UA evaluation of recuperator data (Sec. 6.1.2) are given in Table D.6. Results of the gross-UA evaluation of Re and j are given for the cold and hot side of the recuperator in Table D.7 and Table D.8 respectively. Results from the 1D discretization method of calculating j, as described in Section 6.1.2, are given for the cold and the hot side in Table D.9 and Table D.10 respectively.

D.4.1 Heattransfer data

Table D.3: average experimental mass flow measurements in airfoil recuperator

Test Date	$\dot{m}$ [kg/s]		
7/26/17 tst 2	0.004 421	±	0.000 46
7/26/17 tst 3	0.020 96	±	0.000 36
7/26/17 tst 4	0.049 43	±	0.000 59
7/26/17 tst 5	0.077 15	±	0.000 54
7/26/17 tst 6	0.087 57	±	0.000 78
7/26/17 tst 7	0.1033	±	0.000 70
8/10/17 tst 1	0.043 52	±	0.000 53
8/10/17 tst 2	0.043 33	±	0.000 49
8/10/17 tst 3	0.053 78	±	0.000 57
8/10/17 tst 4	0.059 51	±	0.000 56
8/10/17 tst 5	0.073 41	±	0.000 57
8/10/17 tst 6	0.080 25	±	0.000 74
8/10/17 tst 7	0.096 65	±	0.0010

Table D.4: average experimental measurements in headers of cold CO_2 side of airfoil recuperator

Test Date	$T_{C_{in}}$ [C]	$T_{C_{out}}$ [C]	$P_{C_{in}}$ [psi]	ΔP_C [psi]
7/26/17 tst 2	24.02 ± 0.24	102.08 ± 0.82	866.5 ± 7.2	0.0218 ± 0.000 28
7/26/17 tst 3	21.70 ± 0.86	152.03 ± 0.84	852.6 ± 8.0	0.0789 ± 0.0010
7/26/17 tst 4	21.94 ± 0.82	143.75 ± 1.0	846.3 ± 7.7	0.367 ± 0.0048
7/26/17 tst 5	32.77 ± 1.0	134.26 ± 1.1	909.9 ± 9.3	1.02 ± 0.013
7/26/17 tst 6	36.09 ± 1.4	125.72 ± 1.4	973.8 ± 11	1.28 ± 0.017
7/26/17 tst 7	38.09 ± 1.7	82.29 ± 1.4	1161 ± 16	1.02 ± 0.013
8/10/17 tst 1	20.74 ± 0.59	152.46 ± 1.0	806.6 ± 11	0.321 ± 0.11
8/10/17 tst 2	20.68 ± 0.55	152.49 ± 0.94	800.6 ± 11	0.302 ± 0.094
8/10/17 tst 3	22.52 ± 0.84	143.96 ± 0.95	868.8 ± 13	0.592 ± 0.13
8/10/17 tst 4	24.42 ± 0.88	142.39 ± 0.93	890.8 ± 13	0.728 ± 0.14
8/10/17 tst 5	28.63 ± 1.1	134.49 ± 0.96	948.3 ± 13	0.824 ± 0.14
8/10/17 tst 6	31.78 ± 1.2	113.23 ± 1.2	1066 ± 17	0.651 ± 0.16
8/10/17 tst 7	37.96 ± 1.4	97.84 ± 1.4	1217 ± 21	0.674 ± 0.23

Table D.5: average experimental measurements in headers of hot CO_2 side of airfoil recuperator

Test Date	$T_{H_{in}}$ [C]	$T_{H_{out}}$ [C]	$\rho_{H_{out}}$ [kg/m^3]	ΔP_H [psi]
7/26/17 tst 2	148 ± 0.67	28.3 ± 0.15	105.8 ± 0.41	0.0508 ± 0.056
7/26/17 tst 3	204 ± 0.26	33.1 ± 0.24	103.9 ± 0.38	0.184 ± 0.060
7/26/17 tst 4	197 ± 0.24	39.8 ± 0.22	106.5 ± 0.33	0.855 ± 0.063
7/26/17 tst 5	184 ± 0.61	51.7 ± 0.20	74.24 ± 0.52	2.38 ± 0.11
7/26/17 tst 6	176 ± 0.88	52.6 ± 0.32	71.10 ± 0.70	2.98 ± 0.073
7/26/17 tst 7	132 ± 1.3	44.3 ± 0.43	120.6 ± 0.67	2.39 ± 0.069
8/10/17 tst 1	204 ± 0.32	42.0 ± 0.24	97.44 ± 0.31	0.819 ± 0.032
8/10/17 tst 2	205 ± 0.18	42.1 ± 0.19	96.30 ± 0.31	0.822 ± 0.033
8/10/17 tst 3	202 ± 0.18	39.1 ± 0.29	110.2 ± 0.34	1.05 ± 0.033
8/10/17 tst 4	200 ± 0.19	42.4 ± 0.20	105.1 ± 0.36	1.28 ± 0.036
8/10/17 tst 5	193 ± 0.37	45.3 ± 0.52	95.25 ± 0.37	1.93 ± 0.060
8/10/17 tst 6	189 ± 0.42	39.0 ± 0.50	125.4 ± 0.73	1.77 ± 0.042
8/10/17 tst 7	172 ± 1.1	44.4 ± 0.49	141.7 ± 0.85	2.14 ± 0.038

D.4.2 Recuperator effectiveness, *NTU*, and *UA*

Table D.6: Effectiveness, *NTU*, and *UA* of airfoil recuperator

Test Date	ε [–]	*NTU* [–]	*UA* [–]
7/26/17 tst 2	0.9111 ± 0.0070	4.944 ± 0.19	25.4 ± 2.8
7/26/17 tst 3	0.9223 ± 0.0081	5.941 ± 0.22	140.4 ± 5.8
7/26/17 tst 4	0.8873 ± 0.0072	4.666 ± 0.13	261.6 ± 8.2
7/26/17 tst 5	0.8736 ± 0.0060	4.119 ± 0.12	340.6 ± 10
7/26/17 tst 6	0.8828 ± 0.0086	4.084 ± 0.17	381.4 ± 16
7/26/17 tst 7	0.9202 ± 0.043	3.906 ± 0.87	489.9 ±110
8/10/17 tst 1	0.8795 ± 0.0066	4.661 ± 0.13	226 ± 6.7
8/10/17 tst 2	0.8768 ± 0.0065	4.611 ± 0.12	222.1 ± 6.1
8/10/17 tst 3	0.8893 ± 0.012	4.595 ± 0.19	281.7 ± 12
8/10/17 tst 4	0.8883 ± 0.011	4.482 ± 0.18	301.5 ± 12
8/10/17 tst 5	0.8916 ± 0.012	4.306 ± 0.20	351.6 ± 16
8/10/17 tst 6	0.9108 ± 0.048	4.057 ± 0.90	383.6 ± 85
8/10/17 tst 7	0.9366 ± 0.049	4.188 ± 0.93	496.2 ±110

D.5 j results

D.5.1 Gross-UA calculation of j

Table D.7: Gross-UA calculation of j in cold CO_2 side of airfoil recuperator

Test Date	Re_C [−]	$\dot{C}_C$ [W/K]	$\dot{q}_C$ [W]	j_C [−]
7/26/17 tst 2	193 ± 20	7.001 ± 0.73	546.6 ± 57	0.004 200 ± 0.000 15
7/26/17 tst 3	878 ± 15	29.96 ± 0.78	3905 ± 120	0.005 840 ± 0.000 34
7/26/17 tst 4	2088 ± 25	70.76 ± 1.5	8619 ± 220	0.004 663 ± 0.000 22
7/26/17 tst 5	3221 ± 24	107.8 ± 1.5	10 940 ± 250	0.003 461 ± 0.000 11
7/26/17 tst 6	3630 ± 34	128.7 ± 2.5	11 540 ± 400	0.003 251 ± 0.000 14
7/26/17 tst 7	4117 ± 40	241.8 ± 22	10 690 ±1400	0.002 747 ± 0.000 50
8/10/17 tst 1	1835 ± 23	59.13 ± 1.1	7788 ± 170	0.004 587 ± 0.000 17
8/10/17 tst 2	1828 ± 21	58.48 ± 1.1	7709 ± 160	0.004 510 ± 0.000 15
8/10/17 tst 3	2262 ± 25	79.04 ± 2.4	9598 ± 330	0.004 698 ± 0.000 39
8/10/17 tst 4	2493 ± 24	87.98 ± 2.4	10 380 ± 340	0.004 439 ± 0.000 31
8/10/17 tst 5	3054 ± 25	112.4 ± 3.3	11 900 ± 450	0.003 933 ± 0.000 27
8/10/17 tst 6	3294 ± 34	157.9 ± 18	12 860 ±1600	0.004 241 ± 0.0021
8/10/17 tst 7	3788 ± 39	243.6 ± 27	14 590 ±1800	0.003 678 ± 0.0018

Table D.8: Gross-UA calculation of j in hot CO_2 side of airfoil recuperator

Test Date	Re_H [−]	$\dot{C}_H$ [W/K]	$\dot{q}_H$ [W]	j_H [−]
7/26/17 tst 2	296 ± 31	5.139 ± 0.53	−615.9 ± 64	0.004 788 ± 0.000 092
7/26/17 tst 3	1312 ± 23	23.64 ± 0.41	−4037 ± 71	0.005 311 ± 0.000 11
7/26/17 tst 4	3085 ± 37	56.07 ± 0.67	−8828 ± 110	0.004 297 ± 0.000 082
7/26/17 tst 5	4869 ± 35	82.70 ± 0.59	−10 980 ± 94	0.003 528 ± 0.000 079
7/26/17 tst 6	5580 ± 50	93.40 ± 0.84	−11 510 ± 130	0.003 386 ± 0.000 11
7/26/17 tst 7	6809 ± 48	125.4 ± 0.89	−11 000 ± 180	0.003 149 ± 0.000 13
8/10/17 tst 1	2698 ± 33	48.48 ± 0.59	−7871 ± 98	0.004 247 ± 0.000 072
8/10/17 tst 2	2686 ± 30	48.17 ± 0.55	−7831 ± 90	0.004 222 ± 0.000 065
8/10/17 tst 3	3338 ± 35	61.31 ± 0.65	−10 010 ± 110	0.004 280 ± 0.000 077
8/10/17 tst 4	3693 ± 35	67.26 ± 0.64	−10 600 ± 100	0.004 039 ± 0.000 071
8/10/17 tst 5	4586 ± 36	81.65 ± 0.64	−12 100 ± 110	0.003 724 ± 0.000 085
8/10/17 tst 6	5022 ± 46	94.53 ± 0.88	−14 140 ± 150	0.003 657 ± 0.000 084
8/10/17 tst 7	6058 ± 56	118.5 ± 1.1	−15 080 ± 150	0.003 266 ± 0.000 075

D.5.2 1D recuperator discretization calculation of j

Table D.9: 1D discretized calculation of j in cold CO_2 side of airfoil recuperator

Test Date	Re_C [−]	$\dot{q}_C$ [W]	j_C [−]
7/26/17 tst 2	196 ± 20	2448 ± 41	0.003 411 ± 0.000 14
7/26/17 tst 3	881 ± 22	1794 ± 28	0.004 595 ± 0.000 16
7/26/17 tst 4	2089 ± 34	1348 ± 24	0.003 711 ± 0.000 100
7/26/17 tst 5	3216 ± 32	2214 ± 35	0.003 187 ± 0.000 093
7/26/17 tst 6	3604 ± 47	947.2 ± 17	0.003 055 ± 0.000 13
7/26/17 tst 7	3879 ± 66	1272 ± 23	0.002 374 ± 0.000 70
8/10/17 tst 1	1839 ± 29	1319 ± 16	0.003 784 ± 0.000 091
8/10/17 tst 2	1837 ± 27	1113 ± 12	0.003 749 ± 0.000 082
8/10/17 tst 3	2268 ± 46	939.3 ± 11	0.003 566 ± 0.000 12
8/10/17 tst 4	2478 ± 47	1014 ± 12	0.003 472 ± 0.000 11
8/10/17 tst 5	3018 ± 55	754.4 ± 9.3	0.003 220 ± 0.000 13
8/10/17 tst 6	3099 ± 125	754.4 ± 9.3	0.002 290 ± 0.000 55
8/10/17 tst 7	3303 ± 133	558.9 ± 6.9	0.002 205 ± 0.000 53

Table D.10: 1D discretized calculation of j in hot CO_2 side of airfoil recuperator

Test Date	Re_H [−]	$\dot{q}_H$ [W]	j_H [−]
7/26/17 tst 2	323 ± 34	2448 ± 41	0.004 517 ± 0.000 18
7/26/17 tst 3	1356 ± 40	1794 ± 28	0.005 360 ± 0.000 19
7/26/17 tst 4	3148 ± 60	1348 ± 24	0.004 233 ± 0.000 12
7/26/17 tst 5	4927 ± 63	2214 ± 35	0.003 653 ± 0.000 100
7/26/17 tst 6	5637 ± 105	947.2 ± 17	0.003 621 ± 0.000 14
7/26/17 tst 7	7005 ± 355	1272 ± 23	0.003 692 ± 0.000 85

Continued on next page

Table D.10 – *Continued from previous page*

Test Date	Re_H [−]	$\dot{q}_H$ [W]	j_H [−]
8/10/17 tst 1	2731 ± 46	1319 ± 16	0.004 184 ± 0.000 11
8/10/17 tst 2	2728 ± 42	1113 ± 12	0.004 138 ± 0.000 097
8/10/17 tst 3	3446 ± 82	939.3 ± 11	0.004 173 ± 0.000 17
8/10/17 tst 4	3762 ± 83	1014 ± 12	0.004 053 ± 0.000 15
8/10/17 tst 5	4668 ± 110	754.4 ± 9.3	0.003 874 ± 0.000 16
8/10/17 tst 6	5428 ± 332	754.4 ± 9.3	0.003 695 ± 0.000 85
8/10/17 tst 7	6333 ± 387	558.9 ± 6.9	0.003 872 ± 0.000 89